UNIVERSITAT DE BARCELONA

# Development of optical tools for biological applications based on acousto-optic technology

Raúl Bola Sampol

Tesi doctoral

# Development of optical tools for biological applications based on acousto-optic technology

Raúl Bola Sampol

Dr. Mario Montes Usategui i Dra. Estela Martín Badosa


UNIVERSITAT DE BARCELONA

# Development of optical tools for biological applications based on acousto-optic technology

Programa de doctorat en Física

Autor/a: Raúl Bola Sampol

Director/a: Dr. Mario Montes Usategui i Dra. Estela Martín Badosa

Tutor/a: Dr. Artur Carnicer Gonzalez

Lloc on s'ha dut a terme la tesi

Facultat de Física


UNIVERSITAT DE BARCELONA

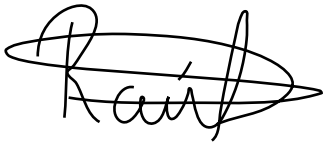

This thesis is dedicated to the most important person in my life

# Resum

Per poder garantir l'avanç de les ciències de la vida, amb la gran repercussió a la salut mundial que això comporta, és important anar millorant les eines amb les quals els científics (especialment els biòlegs) desenvolupen els experiments, podent així millorar la quantitat i el volum de les dades extretes. Amb noves eines, els investigadors poden desenvolupar i dissenyar nous experiments que proporcionin informació rellevant sobre l'estudi i la comprensió de molts processos cel·lulars i malalties.

La tesi tracta sobre el desenvolupament de dos sistemes òptics amb gran aplicació en el camp de la biologia, ambdues basades en un element modulador de llum comú, els deflectors acusto-òptics (AODs). El AODs són dispositius totalment analògics, on s'utilitzen ones acústiques per poder modular i deflectar un làser amb una gran precisió i velocitat. A la primera part, s'explica el desenvolupament d'un sistema d'atrapament òptic i mesura de força. El sistema permet atrapar i manipular, de manera estable, múltiples objectes, així com realitzar oscil·lacions controlades. Al mateix temps, el sistema és totalment compatible amb mesura de forces per canvis de moment. Tot això permet paral·lelitzar experiments a l'interior cel·lular de manera totalment invasiva, oferint informació sobre les propietats mecàniques de diverses estructures biològiques.

A la segona part, es presenta una nova forma d'entendre i utilitzar aquests dispositius: l'holografia acusto-òptica. Mitjançant la generació de senyals acústiques complexes, els AODs permeten projectar patrons de llum arbitraris, més enllà del seu ús principal com a deflectors làser. Això porta al desenvolupament d'un nou microscopi confocal, totalment programable i sense elements mecànics o mòbils. El microscopi permet projectar una infinitat de patrons de llum estructurada, per tal d'obtenir reconstruccions d'alta qualitat a centenars d'imatges per segon. Aquesta nova plataforma de microscòpia d'estat sòlid, permet investigar i implementar una infinitat de maneres d'imatge, per adaptar-se a les necessitats de cada experiment i / o mostra.

# Abstract

To ensure progress in the field of biomedicine and drug development, it is essential to keep improving the equipment needed to carry out most of the experiments. With better tools, scientists can be more efficient, increasing the quality and volume of collected data from biological samples. At the same time, these tools should offer enough flexibility to adapt to new protocols and experiments.

Among all the tools used in cell biology laboratories, photonic technology is the most popular, since it is considered a non-invasive technique, being fully compatible with living samples. The work done in this thesis focuses on the development of two optical tools with great applicability in the field of cell biology: an optical trapping and force measurement system and a novel and flexible confocal microscopy unit. The combination of both apparatus will allow biologists to manipulate and measure forces inside living cells, while providing high contrast visualization of the specimen in real-time. Both technologies share the same light modulator element: an acousto-optic deflector (AOD).

AODs are diffractive devices that use mechanical waves to deflect an incident beam of light with extreme precision and speed (in the kilohertz to megahertz range). Despite being developed in the 30s, their full potential has not been exploited until now. During the thesis, I have carried out a thorough study of the AOD properties, culminating in a new way to understand and use these devices: the acousto-optic holography (AOH). With slight modifications in the control electronics, these devices can be used in the same way as a full complex spatial light modulator. With this new approach, AODs can project arbitrary light patterns and scanning schemes, going beyond their main application as pure beam deflectors.

Incorporating AODs in an optical trapping system allows generating multiple stable optical traps through time multiplexing a single laser beam, catching and manipulating a plurality of objects at the same time. This scheme also allows synchronizing the laser position with a force measurement system based on direct momentum changes, being able to address single object information.

The optical trapping system developed in the first half of this thesis has been used to perform controlled oscillations, as well as measure the response force, in a variety of situations. It has been employed to obtain information about the mechanical properties of some biological structures, such as the cellular cytoskeleton or in active gels of tubulin bundles.

Second, focusing on acousto-optic holography, the thesis presents a new confocal microscope concept: the programmable array microscope, which serves as the start-

ing point for a new generation of solid-state digital microscopes. This new concept proposes eliminating all the mechanical and mobile elements of conventional microscopes and replacing them with fully programmable elements. Specifically, it proposes eliminating the physical "pinhole" and motorized scanning systems, thus resulting in a very flexible device.

The prototype allows the projection of an infinity of structured light patterns at high speeds to produce high-quality reconstructions. Given the high degree of flexibility, this new solid-state microscope can implement multiple imaging modes that can adapt to the needs of each experiment and/or sample. Apart from implementing already existing techniques, the prototype allows the investigation of new imaging modes and smart scanning schemes. These new modes aim to extract sample information more efficiently, faster, or at a higher resolution.

The thesis details the entire development process of the prototype, both in the optomechanical design, the generation of lighting patterns and scanning schemes. Regarding the confocal filtering part, we present two different solutions. First, we present a set of new image processing algorithms that take advantage of our flexible illumination system. Then, we provide the development of a custom and flexible camera module that allows arbitrary pixel reading.

Finally, with the same technology, two different paths have been explored in the field of super-resolution. On the one hand, the confocal system has been adapted for the parallelization of STED microscopy, speeding up the capture process and presenting promising first results. On the other hand, we have explored computational strategies based on deep learning that allow the recovery of high frequencies. This allows the observation of fine structures well beyond the diffraction limit barrier.

# Contents

# Chapter 1

# Introduction

## 1.1 Optical tools for life sciences applications

The great discoveries over the last decades have increased both complexity and variety of essays and experiments carried out in most cellular biology laboratories. To ensure the progress of the studies in this field, the advances in biomedicine must go hand in hand with improvements to the technological tools used for studying biological systems. There is a growing need for faster and more reliable ways to extract valuable information from the studied samples. Then, it is necessary that these tools, such as microscopy or micromanipulation systems, become increasingly robust, efficient, and above all, flexible and easy to use.

It is at this point where a need for convergence between three different disciplines arises: biomedicine, physical sciences, and engineering. The main objective of bringing all these fields of study together is to equip researchers with innovative apparatus and tools, specifically designed to improve the quality of their studies [1]. But the development of such tools should not exclusively focus on improving the existing devices, incrementally enhancing existing features, such as making them faster or more sensitive. Technologists also have to provide novel and flexible tools, opening a wide range of possibilities for researchers.

With new tools, researchers can develop and design new experiments that provide relevant information on the study and understanding of many cellular processes, thereby having a direct consequence in the study of most diseases. Helping to provide faster drug development methods. As an example, most human diseases (cancer, diabetes, kidney and heart diseases or degenerative diseases) are due, among other factors, to dysfunctions or failures in intracellular transport. Or to synaptic dysfunction, in the case of neurodegenerative diseases. So the implementation of tools and devices that allow and help studying these mechanisms in a systematic way creates a significant influence in society and a direct impact on health. In the long term, the understanding and possible cure of these diseases would also have an economic impact, particularly

in the field of the biopharmaceutical industry.

Drug development is a time and resources consuming process that proceeds through several stages until culminating in approval for clinical use. The vast majority of these assays are based on the cellular responses to different compounds or external stimuli, such as mechanical stress, light, or changes in concentration. Such cellular responses are usually captured in the form of an image or external signal and subsequently analyzed to obtain relevant information. In many cases, it is a brute force process based on trial and error, where small compound libraries are screened for selecting potential candidates. This high-throughput analysis has been usually carried out on cultured cells propagated in two-dimensions. However compelling evidence suggests that the microenvironment conditions of 2D cell cultures differ from the real physiological conditions and are not representative of the complex environment of cells forming a tissue. This discrepancy is also present between in vivo and in vitro essays, in which the external conditions can differ to that of the living organism. Due to all this, the development of new non-invasive tools that allow several experiments to be carried out in parallel, quickly, efficiently and accurately is of great value. In addition, it is highly appreciated that such devices accommodate the wide variety of sample types that biologists are faced with.

Among the technological tools for research in cellular biology or biomedicine, devices based on photonic technology are widely popular [2]. Photonics is considered a key enabling technology and a particularly research-intensive industry. One of the main benefits of these techniques is their great compatibility with living specimens. Optical methods are considered non-invasive processes, with all the advantages that this entails: preservation of the internal cell structure, ensuring the excellent condition of the cells for long periods of time and less laborious and expensive sample preparation processes. It should be mentioned that systems based on lasers and photonic technology are also being used at the hospital level as high precision surgical devices, to make incisions or close wounds. Today many of the eye diseases are being diagnosed and treated with laser based systems. Typical vision problems such as myopia or presbyopia are treated with fully automated laser surgery systems.

When talking about optical tools for applications in biology, it is normally understood as such accessories or attachments to an existing and widely accepted commercial system, the inverted optical microscope. That is considered an essential tool for daily use in any cell biology laboratory, which researchers are highly familiar with.

Within the most widely used photonic systems with great application in cell biology, mainly we can find confocal microscopy units and manipulation systems, and to a lesser extent, optogenetics systems [3]. Being the confocal microscopy unit the most widely used and one of the most important, since it allows to visualize with great quality, three-dimensional large systems such as embryos or even tissues. On the other hand, non-invasive micromanipulation systems, such as optical tweezers, allow manipulating and measuring forces at the cellular level, providing valuable information of the mechanical properties of cells or even single proteins. And finally also mention optogenetic systems, mostly used in neuroscience, where light is patterned and directed to specific areas of neuronal cells, to activate certain processes or light-

sensitive probes. Such light stimulation is considered more specific and selective than electrical stimulation techniques.

## 1.2 Thesis overview

Taking a look at the optical design and construction of these optical tools, it is observed that all of them are based around an essential component, a spatial light modulator (SLM), whose purpose is to shape both the phase and amplitude of an incoming laser wavefront in order to reshape, redirect or divide the laser for many different purposes. Additionally we find motorized optomechanical elements, such as galvanometric mirrors or rotating discs (Nipkow disk), especially in most confocal microscopy units, to steer or scan the laser at any point over the microscope's field of view. However, the aforementioned key elements suffer from several inherent problems. On the side of spatial light modulators, there is a clear trade off between modulation speed and overall light efficiency, resulting in two different sets of devices: liquid crystal based SLMs, limited to video rates, or Deformable Micromirror Devices (DMDs) with very low diffraction efficiencies. On the other hand, the mechanical scanners can suffer from facet errors, the requirement of realignment because of bearing wear and inertia due to moving masses.

Acousto-optic (AO) devices are very interesting solid state components capable of diffracting and modulating a laser light beam at very high-speeds (generally in the 10s/100s KHz region). AO cells were first investigated in the 1930s, but they saw very little practical application (several failed attempts were made to implement it in various fields), mainly due to technological limitations of that time. They have gone unnoticed during all these years until the technology needed for growing large, high-quality, artificial crystals matured. Reason why nowadays AO devices are used in a huge variety of optical systems.

Following this trend, and with the aim of removing all moving mechanical elements from optical assemblies, this thesis has centered on the study and implementation of acousto-optic devices. Specifically acousto-optic deflectors (AODs), for its incorporation as a key component, in the construction of two optical tools with great impact in cellular biology: a micromanipulation optical trapping system and a novel confocal microscopy unit. The huge light efficiency, speed, positioning accuracy and lack of inertia make AODs a good platform to build and design a wide variety of optical systems.

On the micromanipulation side, the ability to simultaneously apply and measure external forces in a plurality of optical traps is highly valued [4, 5, 6]. The incredible speed of modulation of AO devices allows the generation of multiple optical traps by fast steering the laser beam. The temporal distribution of the laser energy also implies that the trapped object information is also distributed in time. Allowing single object measurements by precisely synchronizing the laser position with the measurement apparatus. Additionally, the fast positioning of the system also allows to perform controlled perturbations, providing meaningful information on the study

of the mechanical properties of cell membranes or other living systems.

The first part of this thesis focuses on the technical design of a high-precision trapping system fully compatible with a direct force momentum apparatus. With the aim of being able to generate, and measure forces, in multiple stable traps simultaneously. Demonstrating later on, the great utility of the setup in a variety of challenging situations, specially when manipulating and measuring inside living specimens.

On the other hand, in fluorescence microscopy for life science applications there is always a huge compromise between different image quality indicators, such as frame-rate, resolution, signal-to-noise ratio (SNR), field of view or photodamage. Forcing the end users to prioritize one of these parameters to the detriment of the others. This commitment is inherent to the laser steering and modulation technology of the systems and, until the date, it cannot be done within the same device. Imposing the user to use a set of over-specialized devices, each of them satisfying a very niche need.

In this thesis, the meticulous study of AODs, together with the hard work carried out in the laboratory and the extensive experience in digital holography of the research group has culminated with a new way of understanding the AODs. Treating and using them in the same way as a regular wavefront shaping device, enabling the use of digital holography techniques. This fancy, but not common, use of AODs allows the projection of arbitrary light patterns, going beyond their main use as beam deflectors, and having an impact in many different fields.

In the scope of this thesis, this holographic technique has been applied and tested first in optical tweezers applications with good results, demonstrating stable and permanent optical traps configurations but without finding great applicability. And then in confocal microscopy, where we believe that the ability to arbitrarily (and very quickly) modulate different intensity patterns is of immense interest and has great potential.

This is the main reason why the second part of the thesis is focused on the development of a new fully programmable laser confocal microscopy system. Capable of projecting arbitrary light patterns into a fluorescent sample, with which a high resolution and contrast image is later obtained. Under this scheme the AODs replace all the moving elements and allow to implement a infinity of excitation patterns and scanning protocols, since AODs do not suffer from inertia.

The development of the flexible lightning system goes hand in hand with a spatial filtering system, which adapts to the previously generated lighting pattern. Removing the out-of-focus light of thick samples which permits high-quality 3D reconstructions of the sample. In the system developed in this thesis, such confocal filtering system is based on a custom designed camera allowing partial and arbitrary sensor reading. The combination of these two components results in very a versatile microscopy system. Offering different imaging modes depending on the sample and user requirements, all within the same optical setup,.

For example it can implement most common schemes such as single-point scanning, multi-point scanning or line-scanning, to name a few. But, due to the programmable

nature of the device, it also allows us to design and implement new imaging or scanning modes that optimize a particular image quality indicator. Showing schemes to reduce the imaging time, and later on demonstrating scanning procedures that can extract higher spatial resolution.

This idea of a programmable microscope combining the capabilities of nearly all confocal techniques in a single device is very appealing and has been pursued since 1993, when IBM defined this concept under the name of the programmable array microscope (PAM). Actually, the PAM concept goes beyond the imitation of already existing techniques. The illumination patterns of a regular confocal microscope have been demonstrated to be not optimal for obtaining the best section strength [7]. Thus, the implementation of a fully working PAM would allow to investigate optimized excitation and scanning schemes that maximize some quality criteria of a microscopic image, such as sectioning strength, imaging speed or photodamage (in terms of reduced light dose).

However, the experimental implementation of a PAM is very challenging and the reality is that there is not a single commercially available PAM unit. Mainly due to the lack of a light modulator element capable of generating all light patterns efficiently and at high speed. The designs that have come closest to the PAM objective use a DMD for pattern generation [8, 9]. However, these devices have proven not to be ideal for this application, because of their low and pattern depending efficiency, pixelation artifacts and low contrast caused by a strong non-modulated order [10]. Most of the improvements in current PAMs are based on simply using faster and more pixelated DMD devices, offering a higher resolution and arbitrariness of the generated patterns.

Thus, the PAM prototype presented in this doctoral thesis involves a totally different approach. Instead of a DMD or an SLM, we use a slightly modified pair of acousto-optic devices together with the generation of arbitrary and complex acoustic signals. To excite a fluorescent sample with a variety of ligthning patterns and being able to switch them in the tens of kilohertz range.

Additionally, in the last chapters we wanted to go one step further. Motivated by the great boom in super-resolution microscopy, we tested the flexibility of our PAM system for the generation of exotic light patterns and their implementation on a super-resolution system based on the RESOLFT concept (REversible Saturable OpticaL Fluorescence Transitions).

In this context, the doctoral thesis has focused mainly on purely technical aspects. Explaining all the technical development carried out, and the difficulties arising from the incorporation of AODs into a fully functional PAM optical system, together with their own practical experimental solutions.

The structure of my thesis coincides with the chronological order and the natural evolution of the experiments and developments. What has ended up in the creation of two different optical systems for two different applications: optical trapping and confocal microscopy. Reason why this thesis is divided into two different parts corresponding to chapters 1-3 and 4-6 respectively.

The structure of my PhD thesis can be summarized as follows:

- Chapter 1 describes the technical development carried out to build an optical trapping system based on AODs. We study and describe the working principle of acousto-optic devices, the concept of optical tweezer and force measurement system. Then, we explain how AODs can be used to generate multiple stable optical traps while being compatible with quantitative force measurements. At the end, we describe the optical setup and all the technical details regarding alignment and control of AODs.

- In chapter 2 the capabilities of the optical trapping system are presented. Different experiments are shown both in synthetic samples as well as biological systems. Demonstrating the high speed of the system and its complete compatibility with calibration-free force measurements. Finally we describe a new protocol to measure the complete optical force profile of any object, which has been used to study the robustness of light-momentum force measurements.

- In chapter 3 we demonstrate how the same pair of AODs can be used to generate multiple static optical traps, describing a particular algorithm to generate them. We introduce the new concept of acousto-holographic optical traps. At the end we show external force measurement experiments, that demonstrate stable trapping and its compatibility with direct force measurements.

- In Chapter 4 we present a new confocal microscopy system based on holography with AODs. we describe the optical setup and all the technical details regarding the design and alignment processes. Then, the generation of arbitrary light patterns is shown. Different features of such light patterns are analyzed, describing the algorithms used to generate them. Finally the sample scanning and image acquisition protocols are described.

- Chapter 5 describes all the image processing techniques we used to filter the out-of-focus light from thick fluorescent samples. Explaining how to combine the set of images that the optical setup in chapter 4 produces, into a single confocal image. Next, we go one step forward and explain the development process of a new custom camera that takes care of the confocal filtering, implementing the image processing techniques into the camera itself.

- In chapter 6 we tested the capabilities of our microscopy system for super resolution microscopy. First, we introduce the concept of super-resolution microscopy and we review different supe-resolution techniques. Then we tested the flexibility of AODs for the generation of exotic light patterns, and their incorporation on a real RESOLFT experimental setup. Finally, we propose a new super resolution mode based on a trained neural network, able to extract high-frequency information using the same setup described in chapters 4 and 5. Working with regular fluorophores instead of reversable proteins.

This PhD thesis aims to serve as a starting point and inspiration for the development of a whole series of new devices based on laser modulation. One of the long-term

goals of this manuscript is to help future optical technology developers to incorporate AODs as a modulation element. This manuscript aims to serve as a compilation of different design strategies someone has to follow for the best possible implementation of AODs in an optical system. Not only for biological applications but in other fields of industry such as laser material processing or image projection. Basically in any situation where the suppression of all moving parts supposes a great advantage and provides new functionality.

# Chapter 2

# Design of an AOD based optical trapping setup

Experiments with biological samples, especially those of cell mechanics, are increasingly complex. Several of these experiments require dynamic manipulation of many objects at the same time, or to grasp large and bulky objects from different locations in order to have greater control. Just as challenging as manipulating is to quantify the local forces acting in each position, being extremely difficult to measure inside living organisms [11, 12, 13, 14, 15]. Mainly due to the uncertainty and variability of the experimental parameters, necessary for a correct calibration of the optical trap and consequent force measurement.

All of this forced the creation of a universal and calibration-free force measurement method, in which the measurement of the light momentum of the trapping beam allows for direct determination of optical forces [16]. The implementation of this technique into a single beam optical system is rather complicated. Fortunately it has been successfully implemented by our group [17, 18], showing to be very precise, calibration-free, independent on the sample geometry and the trapping beam aberrations [19].

The next chapter is centered on the development of a single beam optical system totally compatible with the aforementioned direct momentum change method. Enabling stable trapping of multiple objects and allowing precise single object force measurements, which will be demonstrated in chapter 4.

Firstly, a study and description of acousto-optic modulators is done, explaining the physical principle of operation. Doing a classification of the types of acousto-optic modulators, emphasizing on the acousto-optic deflectors, used throughout this doctoral thesis. After that, the concept of optical trapping is described, reviewing different calibration and force measurement methods. Then, we introduce the concept of time-shared optical tweezers (TSOT) and its compatibility with a calibration-free force measurement system. Several technical considerations regarding the use of

AODs are exposed, explaining how to generate artifact-free trap configurations. As well as the description of a back-aperture stationary scanning system for improving both the trapping efficiency and the force measurement precision. Finally, the entire synchronization process between the acoustic wave and the sensor of the measuring device is explained.

## 2.1 Acousto-optic devices

Basically, all acousto-optic (AO) devices are based on the interaction between two propagating waves within the same medium: an acoustic wave, described by the Newton's second law for mechanical waves, and an optical wave, whose propagation within the acousto-optic medium is described by Maxwell's equations. Thus, the way to relate the propagation of both waves within a medium finds a solution with the opto-elastic effect or simply known as AO effect. The opto-elastic effect explains how a mechanical wave, normally of ultrasonic frequency, can affect the propagation of light within a transparent medium. It establishes the relationship between the deformation of a material due to strain $S_j$ and its corresponding effect on light, in the form of an acoustically induced refractive index change $\Delta n_i$:

$$\Delta n_i = p_{ij} S_j \tag{2.1}$$

Where $p_{ij}$ is known as the elasto-optic coefficient tensor and is specific to each material, since it depends on the crystalline structure. Both strain and refractive index change are direction dependent magnitudes, defined by rank 2 symmetric tensors with 6 different elements. In the most general case, where materials are both optically and acoustically anisotropic, a deformation of the material in an arbitrary direction can cause a refractive index change in a completely different direction. To take all possible combinations into account, the elasto-optic coefficient is represented by a 6x6 square matrix with 36 independent values. However, point group symmetry conditions often reduce this number and fortunately all calculations become simpler. As an example, the AO devices used throughout this thesis are based on paratellurite ($TeO_2$). For high precision deflectors these devices are designed to work with a slow shear wave mode where only $p_{11}$ and $p_{12}$ are relevant.

Normally the most common way to see an acousto-optic device is in the form of a Bragg cell, figure 2.1 shows the main parts constituting such device. The acoustic wave, normally in the MHz range, is generated by the actuation of a piezoelectric transducer ($LiNbO_3$) deposited on one of the AO medium surfaces, perpendicular to the propagation direction of light. On the opposite side of the transducer there is a sound absorber to prevent acoustic reflections that can cause standing wave effects. The piezoelectric transducer, it is sandwiched between two gold electrodes, where the ground electrode is bonded to the crystal and the other one limits the movement of the transducer. The AO medium crystal is commonly covered with an anti-reflection coating designed for the particular wavelength of operation. Finally, an RF circuit is placed between the transducer and the RF generator, whose purpose is to match the respective impedance avoiding power return losses.

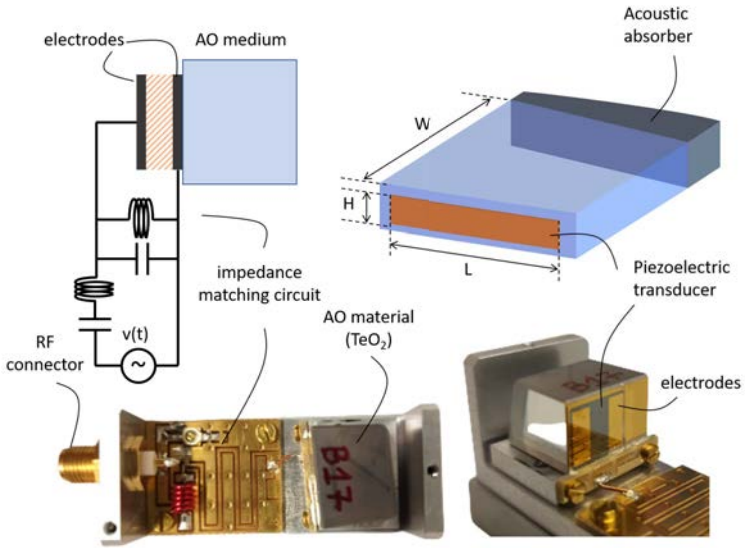


**Figure 2.1:** Scheme and pictures showing the constitution of a $TeO_2$ based AO device

From a first look at the piezoelectric transducer from figure 2.1 two things can be deduced. On one hand, to maximize the acousto-optic interaction, the height H of the transducer has to be greater than the size of the input beam. On the other hand, the length L of the transducer affects both the extension and the divergence of the acoustic wavefront. Both having a great impact on the further performance of the acousto-optic device, as we will see in the following sections.

### 2.1.1 Bragg diffraction

The most simple case to explain the working principle of and AO device is to assume an isotropic AO medium where the piezoelectric transducer is driven by a sinusoidal RF signal of frequency $f$. Assuming both acoustic and optical plane waves, and linearity between the electrical signal $V(t)$ and the transducer movement. The strain wave $S(x,t)$ and it corresponding refractive index modulation $n(x,t)$ can be written of the form:

$$S(x,t) = S_0 \cos(\Omega t - K_A x)) \tag{2.2}$$

$$\Delta n(x,t) = -\frac{1}{2} p n^3 S(x,t) \tag{2.3}$$

$$n(x,t) = n - \Delta n_0 \cos(\Omega t - K_A x)) \tag{2.4}$$

Where $\Omega = 2\pi f$ is the acoustic angular frequency, $K_A = 2\pi/\Lambda$ is the acoustic wavevector, being $\Lambda = v_A/f$ the acoustic wavelength (or induced grating spacing) and $v_A$ the acoustic speed inside the AO medium. Since we are assuming only isotropic materials, both $\Delta n_0$ and $S_0$ are just scalar magnitudes, which simplifies the relationship between them as seen in equation 2.3.

The refractive index modulation $n(x,t)$ is then seen by an incoming light wave of wavelength $\lambda_0$ inciding the AO crystal with and angle $\theta$, as a phase-only diffraction grating of period $\Lambda$. Which then causes a first diffracted order to appear, as a result of constructive interference at the same angle of the incoming beam. Part of the light which has not been modulated (also known as zero-order) is just transmitted and propagates through the crystal with a refractive index $n$ (the DC component of the refractive index modulation).

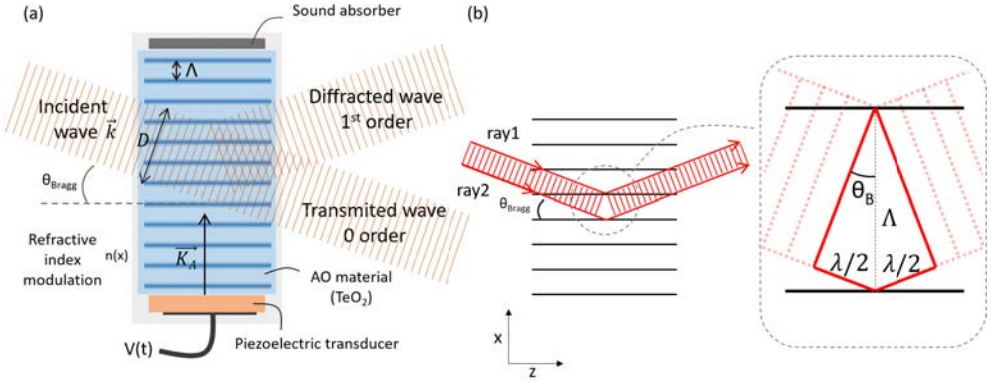


**Figure 2.2:** (a) Scheme showing the working principle of Bragg diffraction in an AO device. (b) Ray tracing for an incident beam fulfilling the Bragg condition

To calculate the intensity distribution of the diffracted outcoming wave, one can simply calculate the total reflectance caused by the grating, that can be expressed as the sum of individual reflectances at each acoustic wavefront:

$$r = \int_{-\frac{D}{2\cos\theta}}^{+\frac{D}{2\cos\theta}} r dr = \int_{-\frac{D}{2\cos\theta}}^{+\frac{D}{2\cos\theta}} e^{i2kxsin\theta} \frac{dr}{dx} dx = ir_0 \,\mathrm{sinc}\left[(2k\sin\theta - K_A)\frac{D}{2\pi\cos\theta})\right] e^{+i\Omega t} \tag{2.5}$$

The term $exp(i2kxsin\theta)$ accounts for the phase difference between the incident and reflected wavefronts and the factor $dr/dx$ can be extracted from the Fresnel coefficients ($dr/dx = (dr/dn)(dn/dx)$). The first surprising conclusion from equation 2.5 is that the frequency of the diffracted beam can be controlled by changing the acoustic frequency $\Omega$. The frequency of the diffracted wave is then $\omega_d = \omega_i \pm \Omega$ (the sign depends on the acoustic propagation direction). However, this slight wavelength mistmach is normally neglected since common laser line-widths are greater than $\Omega$.

If we then analyze the intensity distribution resulted from the acousto-optic interaction, i.e. calculating $|r|^2$, we can see that the intensity of the diffracted beam drastically vanishes when changing the incidence angle $\theta$. From equation 2.5 the Bragg condition can be defined as the incidence angle that maximizes $|r|^2$. This happens when $2ksin\theta = K_A$ from where we can deduce the Bragg angle as:

$$\theta_B = \sin^- 1 \left( \frac{\lambda_0 f}{2nv_A} \right) \tag{2.6}$$

The same result can be obtained if we consider an optical path difference of $m\lambda$ between ray1 and ray2 in figure 2.2. Schematically, the Bragg condition can be represented in the momentum space as an energy and momentum transfer between and incident light wave defined by $\vec{k_i}$ and the acoutic wavevector $\vec{K_A}$. The result after the interaction is a diffracted wave defined by $\vec{k_d} = \vec{k_i} + \vec{K_A}$ and $\vec{\omega_d} = \vec{\omega_i} + \vec{\Omega}$ (energy and momentum conservation), as seen in figure 2.4

As already deduced, the Bragg condition is highly sensitive to changes on either wavelength $\lambda_0$, acoustic frequency $f$ or incidence angle $\theta$. Allowing the design of devices to modulate the intensity, deflect the diffracted beam or filter different wavelengths. This thesis has focused on the study of acousto-optic deflectors, in which a change on the frequency of the driving frequency causes a change on the deflection angle. This can be seen in equation 2.6, where for small angles ($sin\theta \approx \theta$) any change in acoustic frequency is proportional to the angle of the diffracted beam outside the medium

$$\Delta f = \frac{v_A}{\lambda_0} \Delta\theta \tag{2.7}$$

Note that we are assuming an ideal acoustic plane wave, infinitely extense. In reality, the finite size of both the transducer $L$ and the incoming laser beam $D$ are limiting the area of actuation for the Bragg diffraction to occur. When the incidence beam enters the interaction area (defined by $L$ and $D$), light is diffracted in the same way as a regular thin grating, causing the appearance of many diffraction orders (0,±1,±2,±3,...). However, all these orders can interfere with each other during propagation along the interaction area. For very particular conditions, all diffraction orders interfere in phase reinforcing only one order (in addition to non-modulated or DC order, that is blocked afterwards).

This is just an intuitive way to see the phenomenon, to have an exact solution one has to solve the coupled-wave equation for isotropic media. Hopefully, W.R. Klein and B.D. Cook [20] provided a numerical solution to it, where two different diffraction regimes were observed depending on the interaction extension.

As seen in figure 2.3 two different interaction regimes are established: the Raman-Nath regime, where light is diffracted in the same way as by a thin diffraction grating. And the Bragg regime that has already been explained, resulting in a very strong first order. To define in which regime each AO device is working, normally a quality parameter of the AO interaction is used, which is given by:

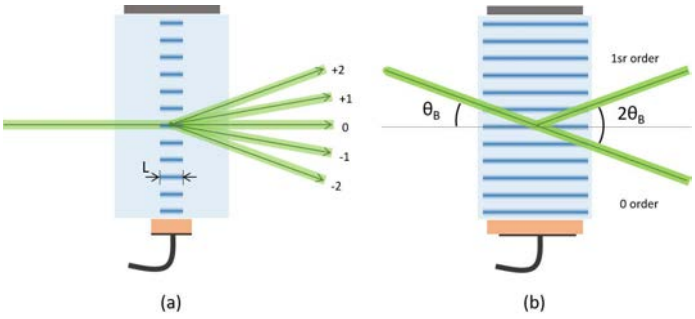


**Figure 2.3:** (a) Raman-Nath regime (b) Bragg regime

$$Q \equiv \frac{K_A^2 L}{k \cos\theta} \approx \frac{K_A^2 L}{k} = \frac{2\pi L \lambda_0}{\Lambda^2 n} \tag{2.8}$$

Where $Q \to \infty$ implies Bragg diffraction and $Q \to 0$ implies Raman-Nath interaction. In the real world, however, AO devices always have a finite transducer length which translates to a finite value of $Q$. Therefore, the generally accepted quantitative standard for entering the Bragg regime is given by $Q = 4\pi$. The vast majority of AO devices are designed to work under Bragg condition, since almost all the incoming laser energy is transferred to the first diffracted order (typical values can reach up to 95% efficiency).

Once the Bragg condition is satisfied, it is convenient to define the diffraction efficiency $\eta$ as a function of the acoustic power $P_a$, as the intensity ratio between the first diffracted order $I$ and the incident laser beam $I_0$.

$$P_a = \frac{\rho v_A^3 S_0^2 H L}{2} \tag{2.9}$$

$$\eta = \frac{I}{I_0} = \sin^2\left[\frac{\pi}{\lambda_0 \cos\theta_B}\sqrt{\frac{M_2 L}{2H} P_a}\right] \tag{2.10}$$

$$M_2 = \frac{n_i^3 n_d^3 p^2}{\rho v_A^3} = \frac{n^6 p^2}{\rho v_A^3} \tag{2.11}$$

Where $\rho$ is the material density. The quantity $M_2$ is an AO figure of merit and depends exclusively on the media properties. Note that $M_2$ is also written for anisotropic birefringent materials (being $n_i$ and $n_d$ the refractive index seen by the incoming and diffracted waves), which are the most commonly used for efficient and high bandwidth AO devices, and that will be explained later.

Just taking a look at equation 2.10, one can we can extract several conclusions for the design of an efficient Bragg cell. Choosing an AO material a $M_2$ figure of merit

as high as possible is important. The design of the piezoelectric transducer directly affects the efficiency and one should make the transducer as elongated as possible ($L \uparrow$ and $H \downarrow$). However $H$ should not be smaller than the beam size, otherwise the beam would not be completely diffracted. Smaller wavelengths also increase the diffraction efficiency, or in other words, for smaller wavelengths the power needed to drive the AO device is less.

The most important aspect regarding the Bragg diffraction effiency is that it changes with the acoustic power $P_a$ as $sin^2$, until it reaches its maximum value and saturates. So, for low acoustic power one can assume linearity between diffraction efficiency $\eta$ and $P_a$ and a linear amplitude modulator is obtained.

When AO interaction was first investigated in the 1930s only isotropic materials such as water or glass were studied. In this materials, the incident and diffracted waves polarization states remain untouched. However, the vast majority of AO devices are based on birefringent materials. Here, the refractive index now depends on the direction as well as the polarization of the light beam. In general, the refractive indices of the incident and diffracted light beams are different, and the AO interaction no longer can be explained as diffraction through a phase grating.

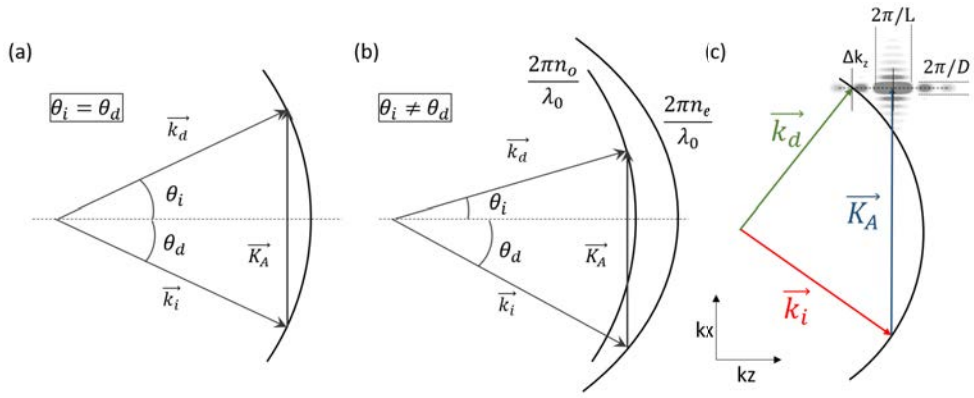


**Figure 2.4:** Acousto-optic wavevector diagram for (a) isotropic and (b) anisotropic materials. (c) Scheme showing the Bragg condition mismatch

Another observation of the anisotropic AO effect is that the incidence and diffracted angles are no longer equal $\theta_i \neq \theta_d$. Depending on how the crystal is cutted, i.e depending where the optical axis is pointing at, birefringence breaks the symmetry in the momentum space. Then the Bragg condition needs to be defined for both $\theta_i$ and $\theta_d$, which has to be solved numerically (since $n_i$ and $n_d$ also depend on the propagation direction).

$$\sin\theta_i = \frac{\lambda_0}{2n_i v_A}\left\{f + \frac{v_A^2}{\lambda_0^2 f}(n_i^2 - n_d^2)\right\} \tag{2.12}$$

$$\sin\theta_d = \frac{\lambda_0}{2n_d v_A}\left\{f - \frac{v_A^2}{\lambda_0^2 f}(n_i^2 - n_d^2)\right\} \tag{2.13}$$

As seen in figure 2.4(b) the incoming laser beam propagates with $n_e$ and the acousto-optic effect can be seen as a momentum transfer process between the ordinary and extraordinary waves inside the birefringent material. From which we can conclude that AO interaction is changing the polarization state of the diffracted wave. Since, in a birefringent device, the polarization state of the diffracted beam is orthogonal to that of the incident and undiffracted light (corresponding to ordinary and extraordinary waves), both the undiffracted and scattered light can be simply blocked by an analyzer. What gives them a higher dynamic range.

The anisotropic AO interaction implies that from now on, the Bragg condition fulfillment also depends on the polarization state of the input beam. For an efficient Bragg diffraction, the incoming polarization state needs to be parallel to the acoustic wave propagation direction $\vec{K_A}$. And if not, just the corresponding component will be diffracted, whereas the others will be transmitted and not diffracted, acting as a polarization analyzer (figure 2.5(c)).

In figure 2.5 we show experimental diffraction efficiency curves as a function of the injected RF electric signal power (RMS value). The curves correspond to the devices used throughout this doctoral thesis and basically are two different sets of 2 AODs each. One set designed for near-IR ($\lambda_0$ = 1064 nm) and another custom AOD set designed to work in the visible part of the spectrum ($\lambda_0$ = 532 nm or 473 nm). Each AOD is deflecting the beam only in one axis, so for a bi-dimensional laser scanner we need to put two orthogonally arranged AODs, one after the other. Under this configuration we note that the diffraction efficiency is quadratic for the whole set, since the total efficiency is the product of $\eta_1\eta_2$. Additionally, the polarization state remains the same (rotated 180 degrees) due to each AO cell rotates the polarization by $90^{\text{o}}$. The wavelength dependence in equation 2.10 is also demonstrated experimentally in figure 2.5(b). Where although the maximum accepted RF power for the visible AOD set is 1.2 W, as opposed to 2.2 W for the near-IR AOD, the effiency is higher.

### 2.1.2 Acousto-optic deflectors

In the real world neither the acoustic wave or the input beam are infinitely extense, which means that their corresponding vectors in the momentum space $\vec{K_A}$ and $\vec{k}$ are not perfectly defined. The finite sizes of both the transducer and the optical window of any AO device, introduce an uncertainty in $\vec{K_A}$ and $\vec{k}$ which is caused by the diffraction of the corresponding windows of sizes $L$, $H$ and $D$. Such uncertainty can be expressed as sinc($Lk_x$),sinc($Hk_y$) and sinc($Dk_z$) respectively. This can be seen in figure 2.4(c), where the acoustic and optical waves are not just points but rather diffraction spots in momentum space.

The scheme from figure 2.4(c) helps us to define the concept of phase mismatch. That is defined as $\Delta k = |\vec{k_d} - \vec{K_A} - \vec{k_i}|$ and represents how far the actual condition is from

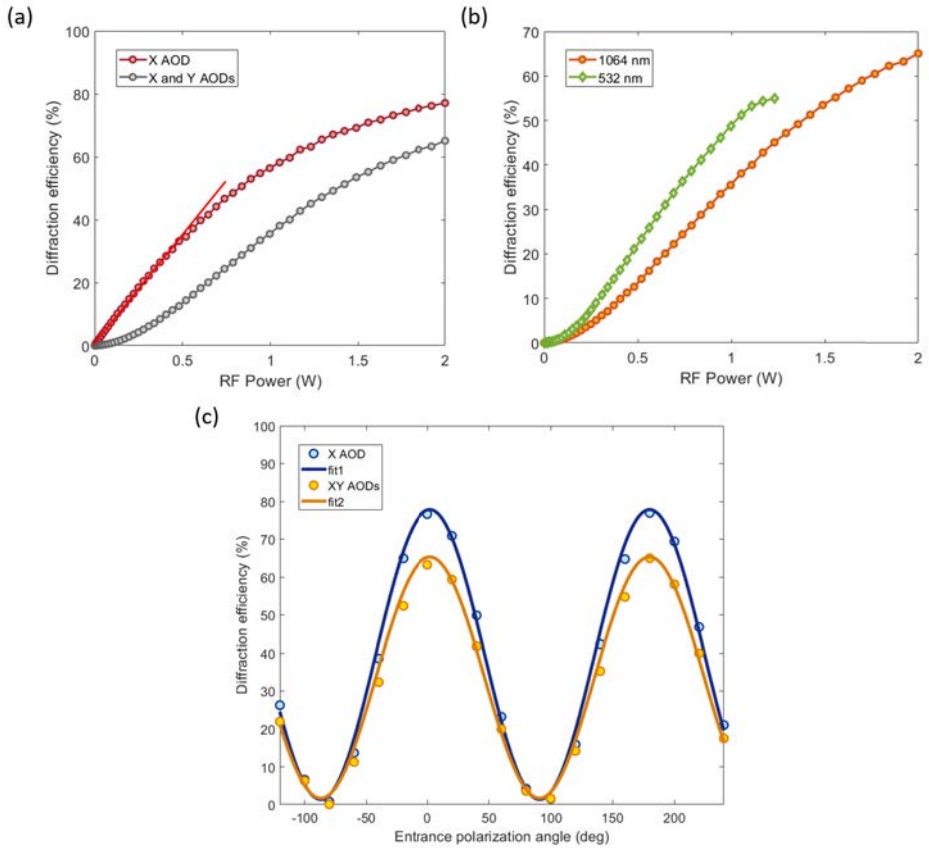


**Figure 2.5:** Experimental efficiency curves for the different acousto-optic deflectors used through this thesis. (a) Diffraction efficiency as a function of the driving signal RF power (proportional to the acoustic power $P_a$). Comparing between one AOD and two consecutive AODs. (b) Diffraction as a function of RF power. Comparing between two different sets of XY deflectors, specifically designed for either near IR (1064 nm) or visible light (532 nm). (c) Diffraction as a function of the input beam polarization angle for both a single AOD and two consecutive AODs.

perfect Bragg diffraction, where diffraction efficiency is maximized. As in most optical interference phenomena, a phase mismatch affects the overall intensity of the resulted pattern. The consequences of such non-ideal conditions are clear and particularly in an AO device $\Delta k$ affects the overall efficiency $\eta$ of the form:

$$\left[\frac{\sin(\Delta kL/2)}{(\Delta kL/2)}\right]^2 \tag{2.14}$$

The concept of phase mismatch is crucial for the construction of AO devices. When

designing an AO device, specially AODs, it is sought that a Bragg condition fulfillment over the widest range of acoustic frequencies possible, known as the Bragg bandwidth $\Delta f$.

The benefits of working with high-bandwidth AO devices are several. Since the Bragg condition is fulfilled for a wide range of frequencies, different AO devices can be designed for very particular applications. These devices can be classified according to a parameter $c = \Delta\phi/\Delta\theta_A$. Where $\Delta\phi$ is the divergence of the diffracted beam and $\Delta\theta_A$ corresponds to the divergence of the acoustic wave. Using this parameter $c$ we can classify AO devices in 3 categories: acousto-optic deflectors (AODs) (for $c << 1$), acousto-optic modulators (AOMs) (for $c \approx 1$) and acousto-optic tunable filters (AOTFs) (for $c >> 1$).

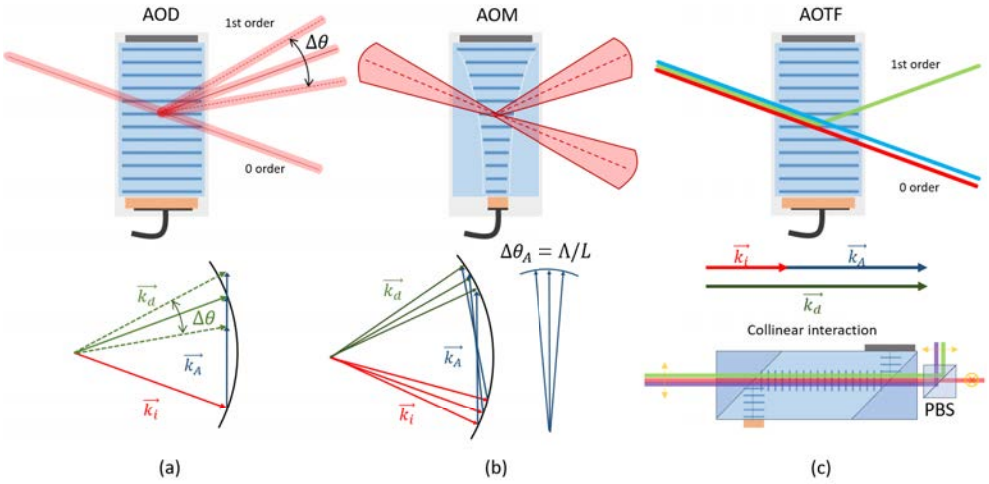


**Figure 2.6:** Scheme of the working principle for: (a) acousto-optic deflector, (b) acousto-optic modulator and (c) acousto-optic tunable filter (working in collinear interaction).

In an AOTF, the wavelength for which the Bragg condition is satisfied can be tuned by selecting a particular acoustic frequency $f$. Acting as highly programmable optical notch filters. A change in $f$ is translated into a change on the diffracted wavelength, while keeping the same angle. In order to fulfill such condition, the acoustic wave needs to propagate as parallel as possible to the incident beam in a collinear interaction way. The experimental implementation of this is difficult, as can be seen in figure 2.6(c). Additionally, $c >> 1$ implies that ATOFs can diffract, and therefore accept, high diverging laser beams. They can modulate, not only single beams, but extense images. For example, they are used in fluorescence microscopes to change between different fluorescence channels, eliminating motorized filter wheels.

On a counterpart, AOMs are designed for high speed modulation. To achieve that, the are designed for very small beam diameters. A smaller beam waist implies a shorter transition time, and therefore a higher modulation frequency. In some models the

incoming laser is focused inside the crystal, where the acousto-optic interaction takes part, figure 2.6(b). On top of that, AOMs are designed to work with a longitudinal acoustic wave, which is around 6 times faster than the shear-mode of AODs or AOTFs. However, to propperly diffract a divergent laser beam, the acoustic wave also has to be diverging, see en in figure 2.6 (b). Since each $\vec{k_i}$ component has to interact with its own $\vec{K_A}$ acoustic component.

This thesis focuses on the use of AODs in two different optical setups, so from now on we will focus only on this devices. AODs are highly precise and very fast in the positioning of the diffracted beam. A high-bandwidth in an AOD is translated into a higher maximum deflection angle. For the particular applications of this thesis, this would correspond to a larger field of action of the optical trap, or larger field-of-view for the confocal microscope.

When talking about the performance of an AOD, normally three important performance parameters are used: diffraction efficiency $\eta$, modulation frequency or response time $\tau$ and resolution or number of resolvable spots $N$. On one hand, for the modulation speed of an AOD, this only depends on the speed of sound inside the AO medium and the input beam diameter. The transition or modulation time $\tau$ is defined as the time it takes for the acoustic wave to cross, and therefore modulate, the incident beam $\tau = D/v_A$. A more realistic definition of $\tau$ is $0.65D/v_A$, which takes into account the Gaussian distribution of the beam. Note that this formula is only valid when the beam size is smaller thant the entrance window of the AOD, otherwise instead of $D$ we should use the AOD entrance window apperture $A$. On the other hand, the spatial resolution or number of resolvable points is defined by how many spots can be created simultaneously inside the deflection window, depending on a resolution criteria. Then $N = \Delta\theta/\Delta\phi$ is defined as the ratio between the total scan angle $\Delta\theta$ and the divergence of the diffracted laser beam $\Delta\phi$. $N$ can be also defined as a function of experimental parameters as $N = \tau\Delta f$.

Both AODs and AOTFs are designed to work under a shear-wave mode. This acoustic propagation mode is characterized by being slower than the regular longitudinal wave. For $TeO_2$, the acoustic speed for the shear-wave is around 650 m/s whereas for longitudinal wave is 4000 m/s. The slower propagation speed of shear waves provides them with high precision. A slower wave or an overfilling of the entrance window result in an higher $\tau$ value, increasing $N$.

In a regular design of an AOD, the acoustic wave is considered a plane wave and both the incident and diffracted beams are almost collimated. Then, the design of an AOD normally is a process of maximizing the diffraction efficiency and bandwidth by changing the transducer geometry and cutting the AO crystal along some preferred crystalline directions. For some particular applications it is also common to use multiple transducers, in the same way as in phased array antennas, which results in higher deflection angles. In this case, the extra deflection angle is not caused by Bragg diffraction, but by an induced linear phase between the different transducers.

When we buy an AOD and use it for the first time, one realizes that its operation is different than expected based on theory. For this reason, I would like to point out two

minor phenomena, which I consider important when introducing such devices into an optical system.

In any ray diagram explaining the Bragg condition, it is always observed that the incident and diffracted beams are always forming an angle between them. Ideally, to simplify any alignment process, it is convenient that the incoming and outgoing diffracted beams are parallel. AO devices manufacturers already take this into account by cutting and polishing the exit surface appropriately. As can be seen in figure 2.7(b), the angle $\gamma$ is chosen in such a way the incident and diffracted beams are parallel. Of course, this is only valid for a given acoustic frequency $f_c$. Thus, we define the central frequency of the AOD as that acoustic frequency for which, entering perpendicular to the first surface, the diffracted beam is not being deflected at all with respect the incident beam.

Theoretically, the value of $f_c$ should correspond to the center of the acoustic bandwidth, but in practice it depends exclusively on each particular device. AOD manufacturers provide the value of $f_c$ for a single wavelength and with a huge tolerance which can be up to a 30% of the total bandwidth. So, it is recommended to measure it before the alignment of the optical system, since $f_c$ will define the optical axis. Using a wrong value of $f_c$ would introduce a twist on the optical axis of our already aligned optical system. Additionally, the wedget face and the fact that the AO medium is almost 2cm in thickness, introduce an offset on the diffracted beam which has to be corrected afterwards (as we will discuss later).

The second important aspect is the diffraction efficiency curve. When changing the acoustic frequency in an AOD, the diffracted beam is deflected at an angle proportional to $f$. However, the diffraction efficiency is not constant allover the acoustic bandwidth $\Delta f$. This results in non-constant power throughout the microscope's field-of-view.

Such efficency curves are explained in figure 2.8: each acoustic frequency introduces its own phase-mismatch $\Delta k$, which then affects the overall diffraction efficiency as in equation 2.14. The efficiency curves can be compensated by modulating the acoustic power $P_a$, as in equation 2.10. It is worth mentioning that the efficiency curve can be changed depending on the user needs. By simply changing the entrance angle to the AOD, the efficiency curve changes its shape. Being able to choose between a high maximum efficiency or a less-efficient flatter curve, the latter being much easier to compensate.

## 2.2 Optical tweezers

In this section we briefly introduce the concept of optical trapping, describing the optical forces and the use of the optical trap as a force sensor. We describe some of the most used force measurement methods, based on trap calibration, and the difficulty of implementation in the cellular environment. Finally we present the direct force measurement method, based on light momentum changes, which will be incorporated later on in the experimental setup of this thesis.

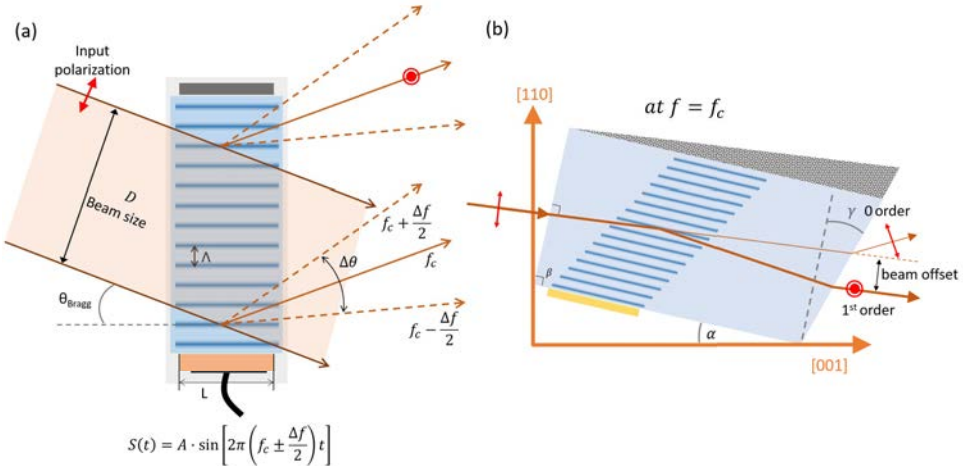


**Figure 2.7:** (a) Scheme of the working principle for an acousto-optic deflector. (b) Geometric constitution of a real acousto-optic deflector.

### 2.2.1 Introduction to optical tweezers

Optical tweezers are highly-focused laser beams capable of exerting forces in the piconewton (pN) range. The principle behind this force is the radiation pressure effect, which results from the momentum transfer between light (photons) and matter. The radiation pressure effect can be observed on a large scale in space and it is the reason why the tails of comets are more elongated as they approach the sun. The same effect was observed by A. Ashkin on a microscopic scale [21, 22], where he noticed two different contributions acting on high-refractive index dielectric particles ($n_{particle} > n_{water}$): the scattering force and the gradient force. The first one accelerates the particle in the direction of the laser propagation, and the second one always points towards the center of the laser beam (in all three dimensions). When these two forces are compensated propperly, specially in the axial direction, the particle's movement is confined to a small region of the space we call "optical trap".

Stable optical trapping was first achived by using two counter-propagating laser beams (where two focusing lenses are needed), and later by focusing the laser using a single high-numerical aperture (NA) microscope objective. Being single-beam optical traps the most used worldwide. Due to its easy implementation in an inverted microscope, and the possibility to use laser modulation elements to steer or generate several traps at the same time.

To describe the optical forces acting on a particle, there exist numerous theoretical approaches that can be classified into two different regimes depending on the particle size. If the particle is larger than the wavelength of the trapping laser $\lambda$, the optical force is explained by the momentum exchanged caused by each ray refracted at the surface of the particle [23] (Mie regime). On the other side, particles smaller than $\lambda$ are considered electric dipoles, for which both scattering and gradient force expressions

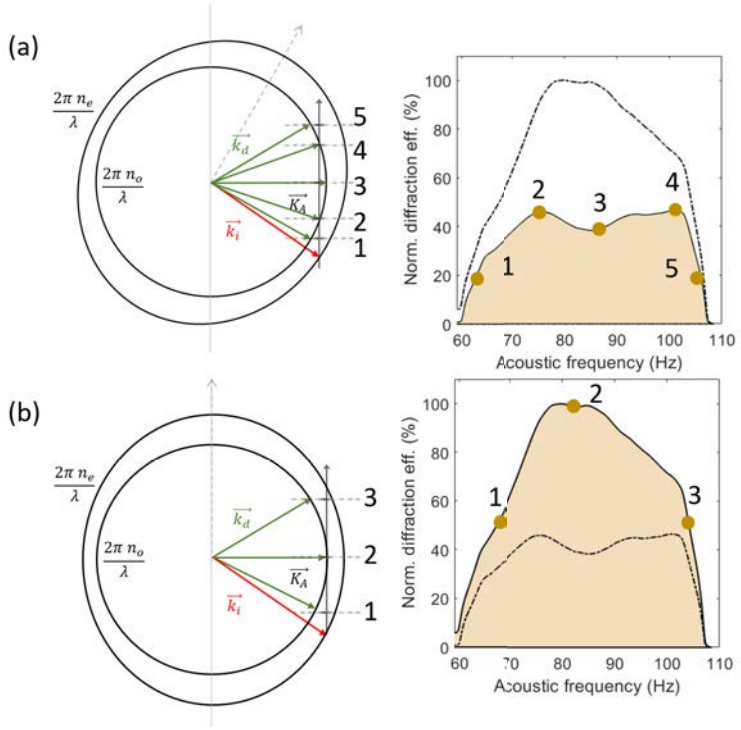


**Figure 2.8:** Momentum diagram and experimental diffraction efficiency curves of an acousto-optic deflector based on $TeO_2$. By changing the AO crystal angle we can obtain a flatter curve (a) or a higher maximum efficiency (b).

can be found [24] (Rayleigh regime). The common size of particle ranges from 0.2 to 10 $\mu m$. Trapping lasers are typically in the near-IR range (980-1200 nm), benefiting from the low absorption coefficient of water in that window. Which allows to perform experiments inside living cells without causing any damage or extra heat [25, 26].

In any of the cases the optical trap can be approximated, around the center of the laser distribution, as a harmonic potential. Within this region, the optical force can be assumed to be linear as the particle is displaced from its equilibrium position. Additionally, the optical force becomes proportional with the trap power, since power is proportional to the number of photons exchanging momentum with the trapped particle. The optical force can be expressed as follows:

$$F = -\kappa \Delta x \tag{2.15}$$

Being $\kappa$ the trap stiffness, a calibration factor which has to be previously known for accurate force measurements, and $\Delta x$ the particle displacement with respect its equilibrium position, considered at the focus of the laser. The negative sign indicates that the optical force is a restoring force, it always opposes to any external action.

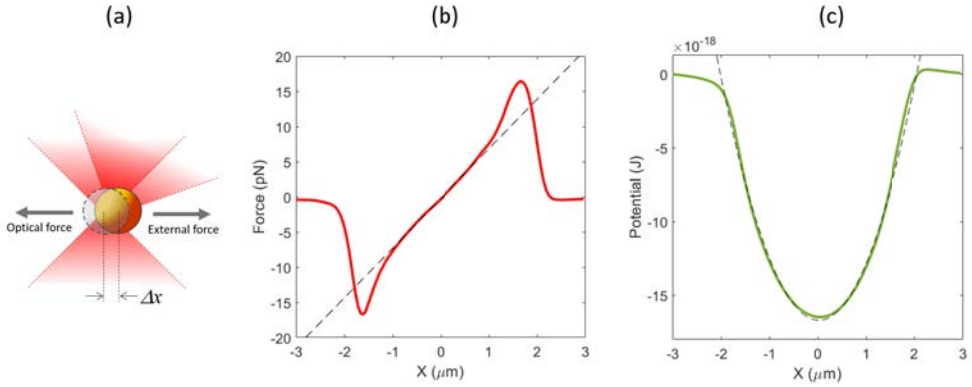


**Figure 2.9:** (a) Cartoon of an optical trap when an external force is applied. And experimental force profile (b) and its corresponding calculated potential (c) for a 3-$\mu m$ polystyrene microsphere trapped with a 1064 nm and 10 mW laser.

Optical tweezers find their niche application in cell biology [27, 28, 29]. Optical trapping is considered a non-invasive technique for studies in cellular mechanics. Allowing to penetrate inside living cells, or even embryonic tissue, to trap, manipulate and exert perturbations [30]. However, the most important aspect of optical trapping is the possibility for quantitative force measurements. During the last decade, optical tweezers have provided lots of valuable data that helped the study of many biological processes. Biological properties of molecular motors have been studied with optical traps, both on in vitro essays [31, 32] and in embryonic tissue [33] using lipid droplets as probes. Additionally, the mechanical properties of cell membranes have been also studied with optical tweezers, by deforming and measuring tensions on the cell membrane [34, 35].

### 2.2.2 Optical force measurements: stiffness calibration and direct force momentum method

The fact that the optical trap can be approximated by Hooke's law implies it can be used to measure forces in the same way as using a micro-dynamometer. When an external agent is exerting a constant force into the particle, this one moves towards a new equilibrium position. Where the optical force compensates the external force. Once the trap stiffness is known, the external exerted force can be measured by knowing the position at which the particle has moved.

In this way, force measurement is a two-step process where first, we need to know the stiffness (calibration process) and then, track the particle's position over time. As a result of this, the force measurement precision depends on the reliability of both the calibration method and the position measurement technique.

Within the position measurement techniques, we can distinguish two different ap-

proaches: laser-based methods and image-based methods. A very common and standardized laser-based method is back-focal-plane interferometry (BFPI), which is able to track sub-nanometer particle displacements in all three dimensions [36]. The implementation of this technique is based on an optical system that collects the forward scattered light with a high-NA condenser lens, whose back-focal-plane is then imaged (by means of a relay lens) into a quadrant photo-diode (QPD). The intensity pattern at the QPD plane is an interference pattern resulting from two contributions: the light scattered by the particle and the light that has not interacted. Gittes *et al.* demonstrates that the center of mass of such interferogram is proportional to the position of the particle. The particle position is calculated as $x = \beta S_x$ , where $\beta$ is the proportionality factor (given in $\mu m/V$) and $S_x$ the QPD voltage (x-coordinate channel). $\beta$ factor can be measured through scanning the trap position across the particle, either by moving the stage or fast scanning using AODs [37]. In the next chapter, we will describe a new and more robust method to calibrate $\beta$ also using AODs.

Figure 2.10(a) and (b) shows the trajectory of a 3-$\mu m$ polystyrene bead trapped with two different laser powers. As we can see from either the position traces or histograms, by increasing 10-fold the laser power, the particle's movement is more restricted. The resulted calibrated stiffness $\kappa$ is also 10 times higher, demonstrating in figure 2.10(d) the linearity between trapping power and $\kappa$.

On the image-based techniques side, video tracking is commonly used to know the particle's position over time for further calibration of the trap stiffness [38], at the cost of reduced temporal resolution. High-speed cameras can reach frame rates of a few kilohertz, compared to the hundreds of kilohertz of QPDs. Additionally, camera-based detection systems are dependent on an off-line calibration, and they need to process large data streams. However, they allow the parallelization of experiments, being able to simultaneously measure at many positions.

Concerning calibration techniques, this ones can be classified whether they are considered passive or active methods. On the passive approach, stiffness is obtained by analyzing the thermal diffusion (Brownian motion) of the trapped object [39]. Assuming a quadratic potential well (harmonic oscillator) the thermal fluctuations can be applied to the equipartition theorem:

$$\frac{1}{2}\kappa_B T = \frac{1}{2}\kappa \left\langle x^2 \right\rangle \tag{2.16}$$

Where $\left\langle x^2 \right\rangle$ is the trapped object variance, which can be calculated from the position histogram (as seen in figure 2.10(b)). Note that $\kappa$ only depends on the sample's temperature $T$. Thus, the equipartition theorem calibration method can provide a first order approximation of the forces. However, if we know additional experimental parameters, such as the buffer viscosity or the probe geometry, a more precise calibration method can be applied. If such parameters are known, the power spectrum analysis [40] compares the thermal fluctuations with the hydrodynamic forces acting on the particle. From which, assuming a purely viscous medium, an expression for

the position power spectrum can be deduced:

$$m\ddot{x} + \gamma\dot{x} + \kappa x = \sqrt{2k_B T\gamma} \tag{2.17}$$

$$P(f) = \frac{1}{T_{meas}} |x(f)|^2 = \frac{k_B T}{\gamma\pi^2(f_c^2 + f^2)} \tag{2.18}$$

Where $\gamma$ is called the friction coefficient and depends on both the medium viscosity and the object geometry, for an spherical particle (radius $R$) is $\gamma = 6\pi\eta R$. The power spectrum can be easily calculated by Fourier transforming the particle'recording the particle trajectory (by means of BFPI). As seen in equation 2.18, for purely viscous medium $P(f)$ is a Lorentzian function where the cutoff frequency $f_c$ is proportional to the stiffness $\kappa$. Figure 2.10(c) and (d) show different power spectrum curves, as well as the fitted Lorentzian distributions and corresponding stiffness, for the same microshpere increasing the trapping power.

Another approach to trap calibration is by applying controlled forces and measuring the particle response for different values of the applied force. This method is called the drag-force calibration. The external force is applied by moving either the sample (with a piezoelectric stage) or the trap position (with a fast laser steering system). The Stokes-drag force relates the movement of the piezoelectric stage with the applied force into an spherical object of the form $F_{drag} = 6\pi\eta R v_{fluid}$. Where $v_{fluid}$ is the relative velocity between the object and the medium and corresponds to the piezoelectric stage speed ($v_{fluid} = \dot{x_{stage}}$). Controlled drag forces are commonly used to test the precision of other calibration techniques, as we will show in the next chapter.

The trap stiffness $\kappa$ depends on almost all experimental parameters; it depends on the object geometry, refractive index (both from the object and the buffer), temperature, laser power, optical aberrations, etc. If we want the most accurate measurement possible, trap calibration has to be performed *in situ*, on the same object we will use later on and under the exact same experimental conditions. If a new particle is trapped, or any external condition has changed, the trap has to be calibrated again. On top of this, remember that $\kappa$ is defined only around the center of the optical trap, where force is proportional to position. This limits the range of motion for reliable measurements. Measuring displacements greater than the linear zone usually result on an overestimation in the force measurement.

Following this reasoning, the quantification of forces inside complex environments such as living cells, is still a challenge due to strong difficulties on stiffness calibration. In the intracellular environment, trap calibration is challenged by three main factors. First, all the aforementioned and most commonly used, calibration methods are only applicable for viscous media. But the cell cytoplasm is not a viscous system like pure water. It is an always changing mixture of organelles, vesicles, microtubules, etc. Modeled as a viscoelastic medium. Second, the shape of the cellular components can differ from perfect spheres (assumed by most calibration methods). And finally, the cell is alive. Which implies that the movement of a particle inside such a chaotic

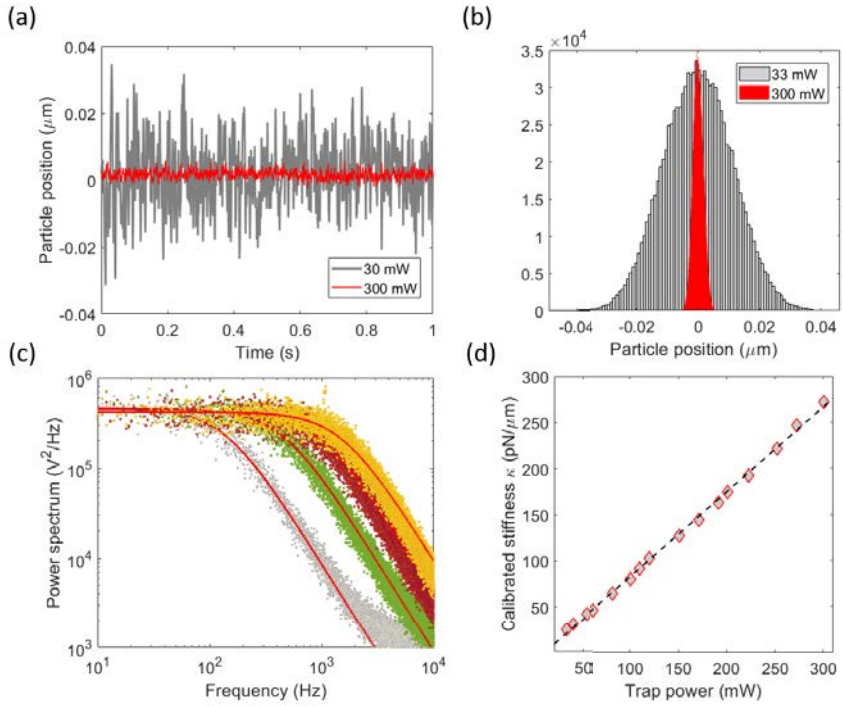


**Figure 2.10:** Example of trap calibration process for a 3-$\mu m$ polystyrene microsphere, for different trapping laser power. (a) Position traces for 33 and 300 mW tracked using BFPI. (b) Position histogram of traces in (a). (c) Power spectrum curves for 4 different laser powers, corresponding to 33mW (grey), 100 mW (green), 200 mW (magenta) and 300 mW (Yellow). (d) Calibrated stiffness from Lorentzian fittings for 16 different laser powers, demonstrating linearity between $\kappa$ and trap power.

environment is very difficult to model and predict, making the calibration process even more challenging (or even impossible).

Fortunately, there is a force measurement technique that is not based on a calibration process, with all the advantages that this entails. Rather than approximating the optical force like a spring, this technique directly measures the change in momentum of photons as they interact with the trapped object. This technique is called the direct force measurement method, and its implementation allows calibration-free and sample-independent force measurements. Since the force is measured in a straightforward manner.

The first implementation of the direct force measurement method was done by S. Smith *et. al* on a counter-propagating optical trapping setup [16]. The apparatus senses the momentum exchange for both trapping beams by using two different position sensitive detectors (PSD), placed at the BFP of each of the objective lenses

[41, 42]. The measurement of changes in light momentum in a single-beam high-NA optical trap is more challenging than in the counter-propagating case. A. Farre *et. al* successfully solved all technical difficulties regarding its implementation [17, 18].

The direct force measurement apparatus constitution is quite similar to a BFPI system. However, for single beam optical traps, two necessary conditions have to be satisfied in order to propperly measure force. First of all, the collection of all the scattered light is a must. This means that the condenser lens NA has to be higher than the trapping beam, and the refractive index of the medium. $NA > n_{medium}$ means that the condenser captures all light propagating towards the sensor, even rays traveling at $90^{o}$. Secondly, the lateral momentum of photons $p_x$ needs to be proportional to the x position in the PSD sensor. This is achieved by using a condenser lens fulfilling the Abbe sine condition ($x = f'nsin\theta = \frac{\lambda_0 f' p_x}{h}$, where $f'$ is the apparatus effective focal length, and $h$ is the Planck's constant) and placing the PSD at a conjugated plane of the condenser's BFP. The force signal $(F_x, F_y)$ and the trap power $P_{trap}$ are given by the following expressions:

$$F_x = \frac{R_D}{\psi f'_C}(Sx - Sx_0) = \alpha(Sx - Sx_0) \tag{2.19}$$

$$P_{trap} = \frac{S_{SUM}}{\psi} \tag{2.20}$$

Where $\psi$ is the PSD sensitivity and $R_D$ is the PSD radius. $Sx$ and $S_{SUM}$ are the PSD x-position and total intensity channels. As we can see in equation 2.19, the net force value is proportional to the PSD voltage $Sx$ signal through a constant $\alpha$. The important conclusion is that $\alpha$ is determined only by the optical parameters of the apparatus. Another interesting aspect is that the apparatus is an optimized version of a regular BFPI system. In summary, the conditions for which $x = \beta Sx$ are less restrictive than those that imply that $F_x = \alpha Sx$. Then, a good method to assess whether the device is configured for precise calibration-free measurements is to check the next equality:

$$F = \kappa x = \kappa\beta(Sx - Sx_0) = \alpha(Sx - Sx_0) \tag{2.21}$$

Within the linear region of the trap, we always can find a proportionality factor between force and the PSD signal $\kappa\beta$. However, both $\kappa$ and $\beta$ are strongly dependent on the experimental conditions, while $\frac{R_D}{\psi f'_C} = \alpha$ only depends on macroscopic apparatus parameters. The result of fulfilling all these conditions is a force measurement apparatus that, no matter which object or environment one is dealing with, directly provides a precise force value. F. Català *et. al* precisely analyzes the robustness of the method for both exotic beams and irregular samples, reporting an error of less than 10% [19]. The force measurement apparatus used through this thesis is schemed in figure 2.11. Since all the forward scattered light is captured, the apparatus also serves as a high-precision trap power sensor. This latter feature will be used to determine light losses in chapter 3. Finally, the value $Sx_0$ corresponds to the voltage reading

when no object is trapped, and from now on is called the initial momentum of the trap. And it is related to the aberrations of the trapping beam or scattering caused by the medium itself. One of the goals of this chapter is to design a laser steering system in which $Sx_0$ remains always constant.

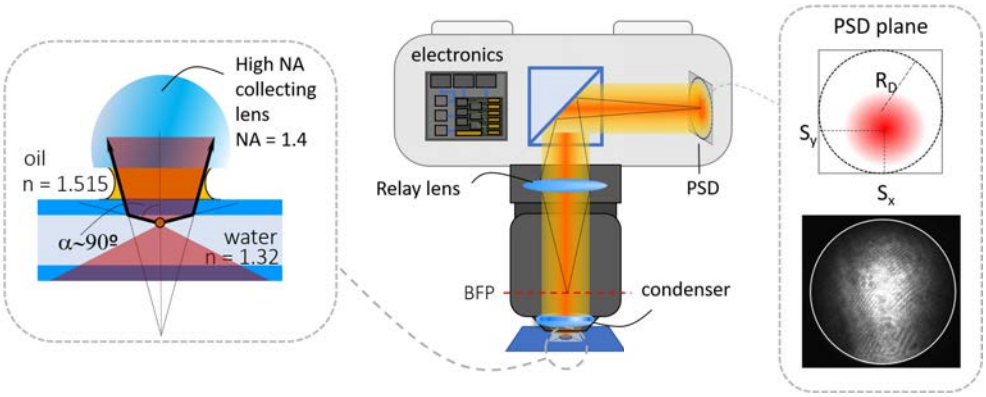


**Figure 2.11:** Scheme of the direct force measurement system. On the left we show the collection of all the forward scattered light. On the right we show the intensity distribution at the PSD plane when no particle is trapped.

## 2.3 Acousto-optic deflectors for optical tweezers

The main objective of incorporating AODs into an optical trapping setup, is to deflect the laser beam very precisely and very fast. Such fast deflections of the trapping beam correspond, if aligned properly, to precise steering of the optical trap at any desired position.

As seen in previous sections, a single AOD deflects the laser beam along the propagation direction of the acoustic wave. So, in order to position the optical trap in two dimensions we need two orthogonally arranged acousto-optic deflectors. Each of them taking care of the deflection of the laser beam in one axis, thereby controlling the position of the trap at any position of the microscope field of view. From now on we will refer each one-dimensional AOD as "AODx" and "AODy", referring to their respective directions of deflection.

When talking about the precision of an AOD, it is common to talk about the number of resolvable spots an AOD can generate. However, in this chapter we are using the AODs as simple deflectors. In this case, the positioning precision of the system is given by the minimum step a single spot can be shifted. Since AODs are considered analog devices, i.e. the crystal is a continuous medium with no pixels, the minimum angle the AOD can deflect a laser beam is mainly defined by the RF signal generator. In other words, the minimum step we can shift the optical trap $\delta x$ is proportional to the minimum step in frequency our electronics is able to reproduce $\delta f$. Nevertheless,

the position precision can be affected depending on the Bragg cell construction. As an example, S. Block *et. al* reported a systematic positioning error (of around 2 nm) due to acoustic stationary wave effects arising from small back-reflections at the sound absorber [43].

In this section we show how a single pair of AODs can stably trap multiple particles at the same time, by means of a time-sharing approach. The dynamics of a trapped particle under such conditions (a flashing trap) is described. Then, we analyze the performance of AODs when driven at high-speeds, specially when approaching the speed modulation limit. The propagating nature of the acoustic wave causes the appearance of intensity artifacts, which are described, analyzed and quantified in this section. Final solutions to minimize or reduce such artifacts is provided.

### 2.3.1 Multiple trap generation through time-sharing

There is a growing interest in the use of more than one trap for micromanipulation. Many experiments require manipulation of objects using multiple optical traps, together with the measurement of their positions or the forces exerted on them. For example, this is the case when we wish to measure forces at different adhesion sites [14], study multi-particle interactions in colloidal science [13], hold pairs of DNA strands [12], measure forces exerted by the growth cones of differentiating neurons [11], or more generally, grasp large samples or those with complex geometries, such as red blood cells [15], from several sides to measure their mechanical properties [**?**].

The main idea behind the generation of multiple optical traps is to divide the trapping laser source into different beams, each of them at different positions, being able to trap several objects simultaneously. Another idea could be to merge several independent laser sources into the same optical path, i.e. the same objective lens. In order to divide the laser beam several methods can be proposed, such as using a microlens array, generating several beams with multiple beamsplitters (BSs), through interferometric techniques, etc. All these methods suppose fixed trap patterns, and they not offer dynamic control over each trap. Changing the position of the traps would mean to physically move some parts and realign the system.

Being able to move the trap position also allows to apply controlled oscillations and perturbations to the system, to further extract quantitative information. If trap positions are permanent, the external forces have to be applied by means of motorized or piezoelectric stages or complex microfluidic systems.

The use of spatial light modulators (SLMs) to shape the incoming beam for the dynamic generation of arbitrary light patterns is a common way to obtain multiple optical traps in so called holographic optical tweezers (HOTs) [44]. In this technique, previously calculated computer generated holograms (CGHs) are displayed on the SLM screen, which is placed at the BFP of the objective lens. Being able to modulate the phase of the laser wavefront and create almost any desired trap configuration at the sample plane. Allowing three-dimensional control over the trap positions and also the generation of complex beams with exotic force profiles, such as vortexes or cogwheels.

But HOTs suffer from two drawbacks: low modulation speed and incompatibility with laser-based force detection techniques. On one side, the liquid crystal displays found in most SLMs systems are limited to video rates (typically around 60 Hz). On the other side, since the laser is divided into different beams, the light scattered by all the particles merges into a single-intensity pattern at the back focal plane (BFP) of the collection lens.

Following a different approach, multiple optical traps can be created using a time-sharing technique. If we consider that the traps generated with HOTs are analogous to the fingers of our hands, here we only have a single finger capable of moving very fast. In time-sharing optical tweezers (TSOTs), the laser beam is not modulated spatially but in time. By changing the trap position at very high-rates, one can trap and manipulate different objects simultaneously. The successful implementation of TSOTs relies on the use of a high-speed device to arbitrarily move the trap between the desired positions. Appart from AODs, which are the object of study of this thesis, TSOTs have also been implemented by using galvanometric mirrors [45], DMDs or electro-optic modulators [43].

Figure 2.12 (a) shows the trapping scheme of 6 different objects with TSOTs. The trapping laser beam is visiting cyclically all 6 microspheres, trapping one object at each time. It is then fair to say, that each object is strictly trapped only 1/6th of the time, photons are only exchanging momentum when the laser incides into the particle. From the point of view of each individual particle, the laser is flashing with a duty cycle of 1:6. However, the laser flickering can affect the dynamics of the trapped object, the faster the switching frequency the more stable trapping we get. To give a comprehensive understanding to this effect, we can incorporate the laser flickering into Lavengin's equation (describing the Brownian motion of a trapped particle) as follows:

$$m\frac{\partial^2 x(t)}{\partial t^2} + \gamma\frac{\partial x(t)}{\partial t} + \kappa(t)x(t) = F_{random}(t) \tag{2.22}$$

Where $m$ is the particle's mass, $\gamma$ the friction coefficient and $F_{random}(t)$ is the external random force describing the Brownian motion, which depends on temperature $T$. As we can see in equation 2.17 the flickering of the laser is described as a time-dependent quadratic potential well, resulting in a time-dependent trap stiffness. Although the laser flickering has to be modeled with $\kappa(t)$ following a square wave, like in figure 2.12(a). We assumed, for simplicity in calculations, that $\kappa(t) = \frac{\kappa_0}{2}\left[1 + sin(2\pi f_{TS} t)\right]$.

Where $\kappa_0$ corresponds to the stiffness we would obtain for continuous-wave trapping, and $f_{TS}$ is the time-sharing frequency. By numerically solving equation 2.22, we obtain the particle's trajectory $x(t)$, from which we can calculate the power spectrum to know if it responds to laser flickering. This is shown in figure 2.12(d), where we compare the power spectrum betwen continuous trapping and TSOTs for a 3-$\mu m$ microsphere at room temperature, $f_{TS} = 10kHz$ and $\kappa_0 = 100pN/\mu m$. By looking at the power spectrum we can conclude that the particle is stably trapped, see figures 2.12(d) and (e). It behaves in the same way as trapped with half the laser power, i.e. half the trap stiffness, which exactly corresponds to the average value of $\kappa(t)$:

$$\kappa_{eff} = \langle\kappa(t)\rangle = \kappa_0/2 \tag{2.23}$$

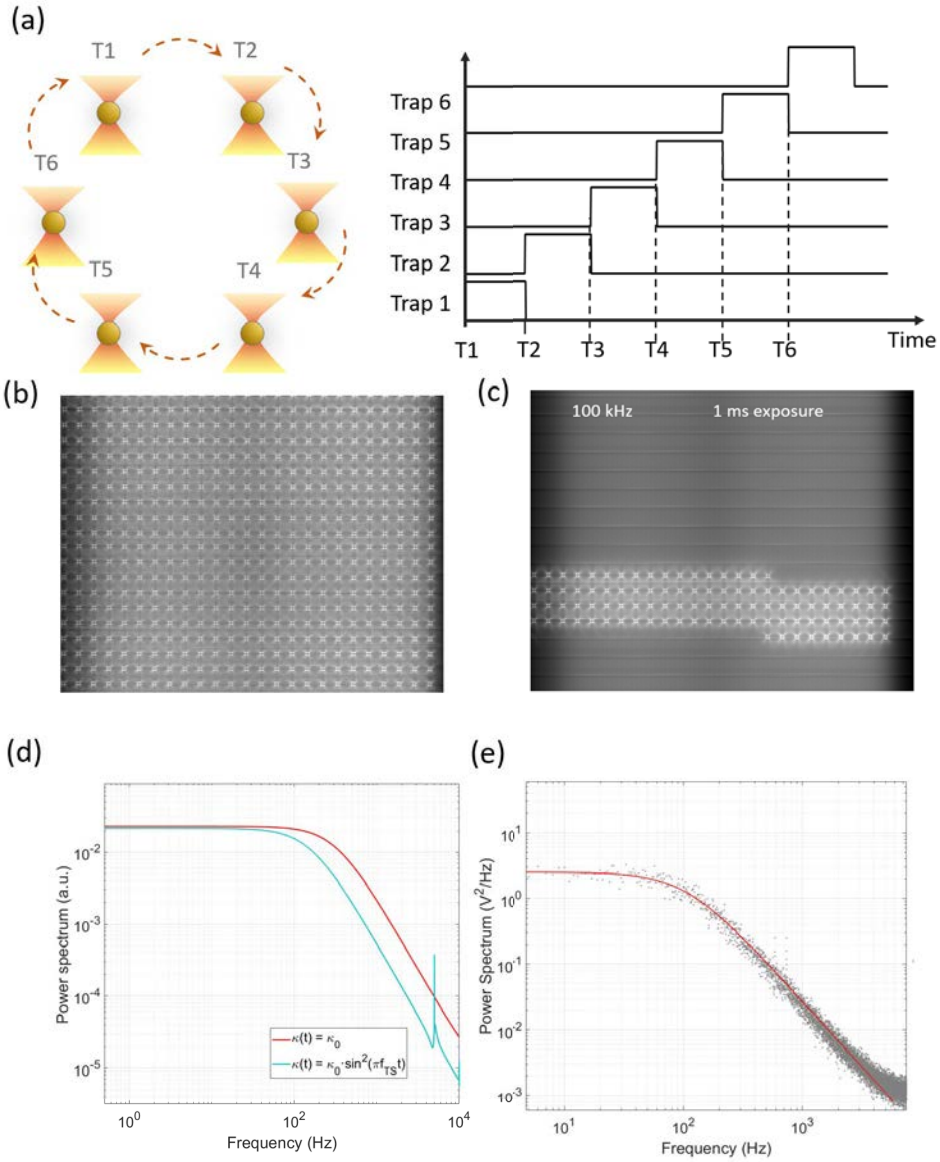


**Figure 2.12:** (a) Explanatory scheme of the generation of multiple optical traps through time-sharing. (b) 625 optical traps aranged in a 25x25 grid generated with fast laser steering. The image corresponds to the reflection on the glass-water interface of the sample. (c) Low exposure image of the same configuration in (b), demonstrating that traps are not permanent. (d) Simulated power spectrum for a 3-$\mu m$ microsphere with a static trap (red curve) and with a time-shared trap. (e) Experimental power spectrum of a 3-$\mu m$ polystyrene microsphere trapped with TSOT at 30 kHz, demonstrating stable trapping. Note that the sampling frequency is 15 kHz (half of $f_{TS}$), due to another particle was trapped at the same time.

Being $\kappa_{eff}$ the effective trap stiffness. Even though this simulation only takes into account a sinusoidal laser fluctuation, it helps us to understand that the particle is responding to an average potential well (an average stiffness). A more detailed Monte Carlo simulation was done by Yuxuan *et. al*, where they assumed $\kappa(t)$ to follow a square wave (a much more realistic approach). They calculated the effective stiffness of the trapped particle for different trapping duty cycles of the square wave [46]. Assuming the same laser power in all positions, a duty cycle of 1:N is analogous to have N different laser positions. From which we can conclude that the stiffness for each particle has to be scaled accordingly:

$$\kappa_{eff} = \kappa_0 \frac{P_i}{\sum_1^N Pi} \left[1 - e^{(-f_{SW}/f_c)}\right] \tag{2.24}$$

$$\kappa_i = \kappa_0 \frac{P_i}{\sum_1^N Pi} = \frac{\kappa_0}{N} \tag{2.25}$$

The particle's diffusion time is given by the cutoff frequency $f_c$ of its power spectrum, which for typical laser power values it sits between 100 Hz and 1 kHz. Note that as the number of trapped elements increases, the switching frequency $f_{SW}$ and the duty ratio scale as $1/N$ ($f_{SW} = f_{TS}/N$). Then, each particle will be stabily trapped if $f_{SW} >> f_c$, since the laser switch is faster than the particle's response time, preventing particles from scaping. In this scenario, the effective stiffness of each trap scales with $1/N$, equation 2.25. However, as $N$ increases $f_{SW}$ decreases and the particle's stability is compromised. Resulting in a much lower $\kappa_{eff}$ (equation 2.24) that can affect the precision of force measurements. As an example, W. H. Guilfort *et. al* demonstrates precise measurement at only 6 different positions [47].

### 2.3.2 [redacted]

[redacted]

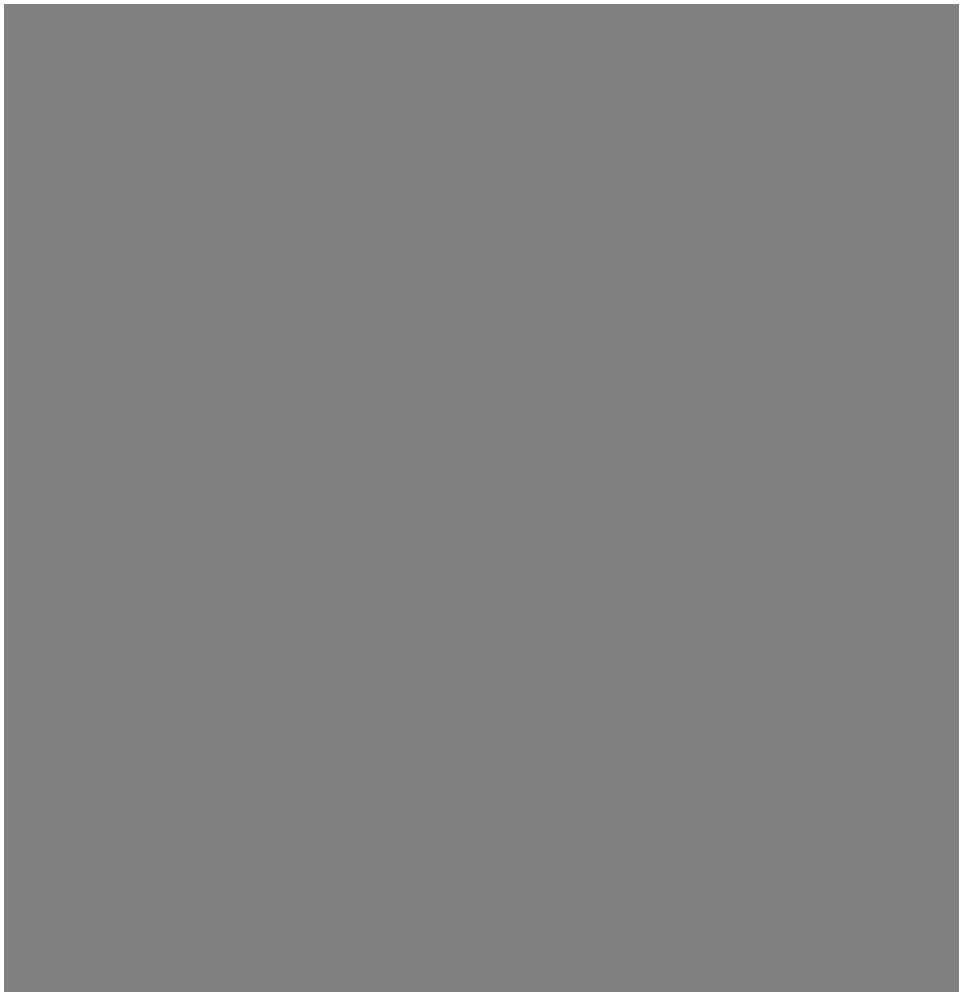

### 2.3.3

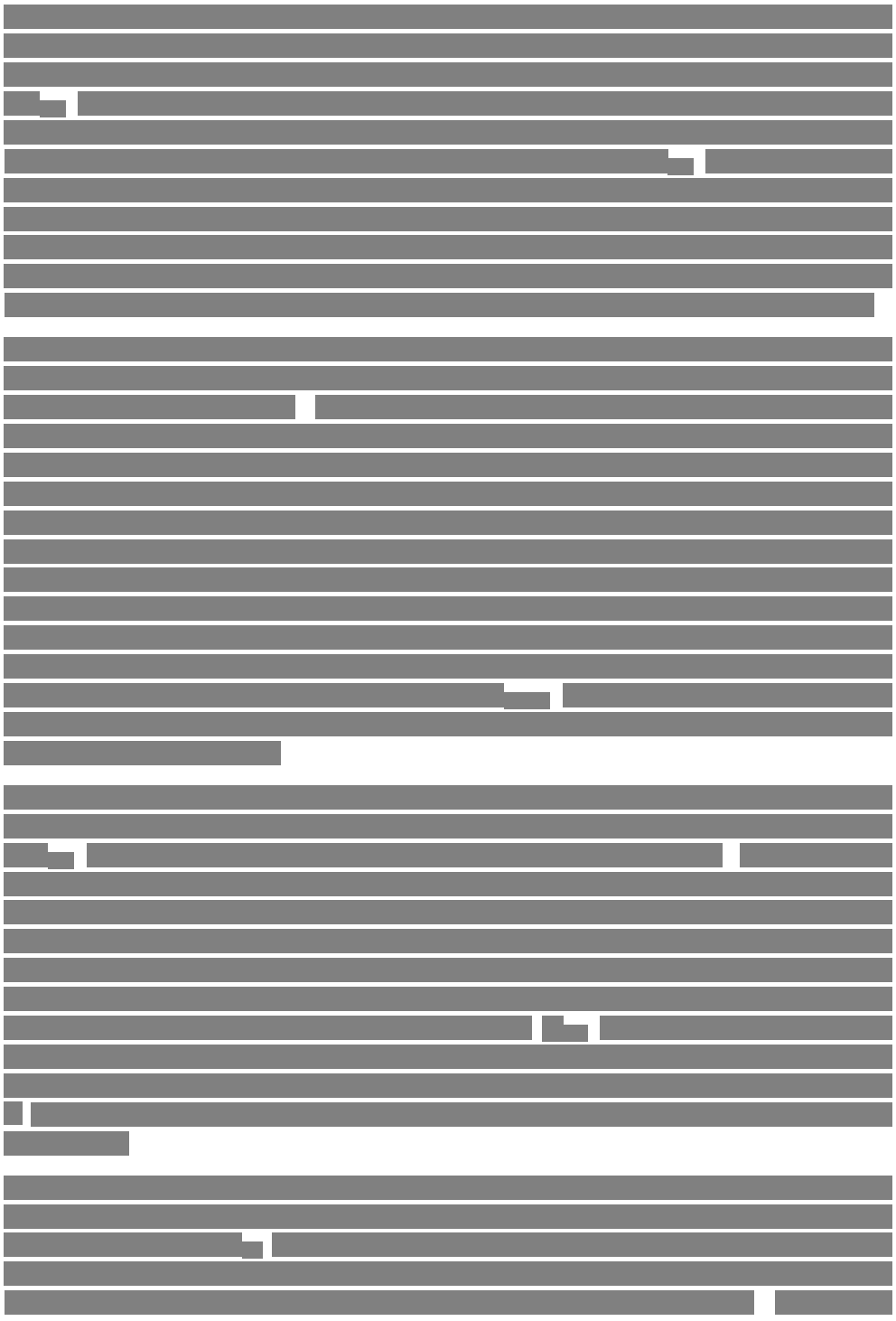

## 2.4 Design an alignment of an AOD based optical trapping setup

This part is devoted to the whole optical design process of a flexible micromanipulation system using AODs as the main modulation element. The incorporation of the AODs into the optical setup introduce several constrains that will be explained through the section. Additionally we show the incorporation of a simple BFP stationary beam steering system that improves the quality of direct force measurements throughout the entire field of view.

### 2.4.1 Description of the optical trapping setup

The optical micromanipulation setup design and used in this thesis is shown in figure 2.18. The optical setup was built around a commercial inverted microscope (Nikon Eclipse TE-2000E) and is composed of 3 different parts: the beam adaptation part, the beam modulation system and the pupil matching part.

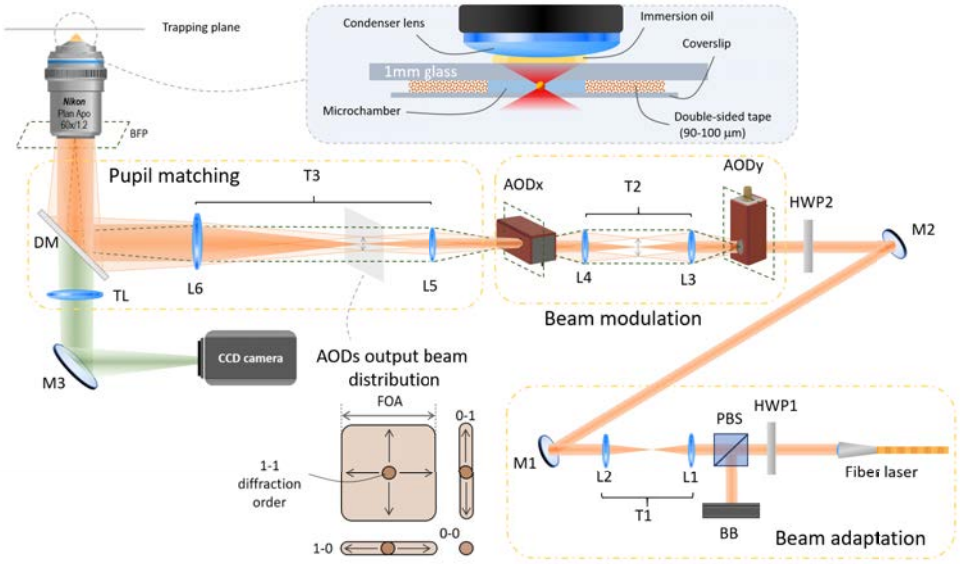


**Figure 2.18:** Scheme of the AOD-based optical trapping setup.

The fiber laser (IPG YLM-5-1064-LP) generates a continous wave, linearly polarized Gaussian beam $TEM_{00}$, at a wavelength of 1064nm and up to 5W of output power. At the end of the fiber there is a collimation head with a small lens inside, which sends the the optical fiber core plane to infinity, generating a perfectly collimated laser beam of 5.1mm in diameter (measured through the knife-edge method).

The fiber laser is usually working at high power, at 1.5-2W, in order to improve power

and polarization stability. The power control of the laser beam in this part is done through a half wave-plate (HWP1), a polarizing beam splitter (PBS) and a beam block (BB). After that, since the collimator head of the laser is fixed, a telescope (T1) composed of lenses $L1$ and $L2$ is used to change the convergence or divergence degree of the laser beam before entering the AODs. The reason to that is because, even though AOD theory assumes a perfectly collimated laser beam, we experienced that a slightly convergent beam enhances the AODs diffraction efficiency and flattens the efficiency map, allowing to increase a little bit the field of action of the optical trap.

Before entering the modulation part, a second half wave-plate (HWP2) allows control over the polarization state that inputs the first AODy, in order to maximize the diffraction efficiency. The laser beam is redirected to the entrance window of the AOD-based steering system by means of mirrors M1 and M2. The use of two mirrors between the beam adaptation and beam modulation parts, gives us enough degrees of freedom to propperly align the system, as we will see in section 2.4.3.

The modulation part is composed of two orthogonally aranged AODs, AODx and AODy respectively, (AA Optoelectronics, DTSXY-400-1064). The original configuration of the two AODs brings them together in the same mount. However, as we will explain in section 2.4.2, this configuration is not ideal for a precision steering system. It introduces aberrations, specially for high deflection angles, affecting force measurements and trapping efficiency. Instead, the original mount provided by manufacturer has been replaced by two 3D-printed mount designs, allowing to separate both AODs by means of a 4f relay system (telescope T2, composed of lenses $L3$ and $L4$). The non-diffracted order of each AOD is blocked by means of a 3D-printed aperture, covered with carbon paper which absorbs and diffuses the zero-order. Allowing only the first-diffracted order of each AOD (what we call the "1-1" order) to pass through the aperture. All zero-orders (0-0,1-0 and 0-1) are blocked at the focal plane of $L5$, where the laser beam is focused and all 4 diffraction orders are well separated.

On the pupil matching part, after being modulated, the laser beam is expanded by means of telescope T3 (lenses $L_5$ and $L_6$) that conjugates each AOD plane with the microscope objetive's back aperture. The telescope T3 is designed so that the laser beam slightly overfills the aperture. The laser beam enters the inverted microscope through one of the rear fluorescence ports. Then, a dichroic mirror (DM) reflects the laser beam up towards the microscope objective (Nikon Plan Apo 60x 1.2 NA or Nikon Plan Fluor 100x 1.3 NA), which then focuses the laser at its focal plane, creating the optical trap inside the microchamber.

The optical setup allows micromanipulation of the sample, while being fully compatible with brightfield, phase contrast, DIC and any kind of fluorescence imaging. For brightfield imaging, the sample is homogeneously illuminated through a condenser lens from above, and the focal plane of the infinity corrected objective lens is imaged into a CCD camera placed at one of the imaging ports (Qimaging, QICAM 12-bit, 1392x1040 pixels, $4.65\mu m$/pixel and 20 Hz maximum fame-rate at full frame) by means of a tube lens (TL, $f_{TL} = 200mm$).

To allow force measurement experiments, the illumination system is substituted by

a direct force detection system (Impetux Optics, Lunam T-40i), which its NA=1.4 condenser lens collects all the $\lambda$=1064nm forward scattered light while illuminating the sample for brightfield imaging. Moreover, a piezoelectric platform (Piezosystems Jena, TRITOR 102 SG) is placed at the microscope stage to extert controlled drag forces at the trapped particles. A data acquisition card (National Instruments, NI-DAQ 6229 USB) allows both modulation and monitoring (MOD1, MOD2, MON1, MON2 analog channels) of the piezoelectric platform position by using a custom Labview software.

Regarding sample preparation, all optical trapping experiments have been performed on microchambers composed of: a coverslip of $\sim 150 - 170\mu m$ in thickness (Deltalab nr.1 or 1.5, depending on the application) and a 1mm-thick microscope slide (Deltalab), sandwiched with a 90-$\mu m$ double-sided tape in between. Before mounting, a 1x1cm square hole is created at the center of the scotch tape, thereby creating a 1cm x 1cm x 90$\mu m$ cavity, which is then filled with a water dilution of microspheres of different sizes (0.61-5$\mu m$) and materials (polystyrene, silica or melamine resin), depending on the experient.

### Design trade-offs and constrains

During the design process several decisions have been made in order to satisfy the specifications of the micromanipulation system. Such specifications were:

- The field of action (FOA) of the generated optical trap has to cover most of the microscope field of view (FOV). Which for the CCD camera used is 80.6x107.8$\mu m$.
- In order to generate multiple stable optical traps, the modulation speed of the AOD-based steering system has to be at least 100kHz.
- The system must work with the two available high-NA microscope objectives, which have different back aperture sizes.

All these requirements can be fulfilled by choosing the proper combination of lenses of the system ($L_{1\rightarrow 6}$). The requirements can be mathematically written as equations, relating each specification as a function of the focal length $f_{1\rightarrow 6}$. Apart from the specifications, the physical apertures of the elements and their mounts have to be considered, such as the objective lens back aperture or the AOD entrance window. As an example, the laser beam diameter after the AODs is limited to 7.5mm (entrance window size).

Regarding the field of view, one of the major limiting factors is the small deflection angle of AODs with respect of its competitors galvanometric mirrors. The specifications of our AODs are listed in table 2.1. The deflection angle of our particular system is $49mrad$ ($\pm 1.4^{o}$) whereas typical galvanometric mirror systems can reach up to $\pm 12^{o}$. To overcome this issue, one can reduce the magnification of T3 ($f_6/f_5$), increasing the angular magnification, which then results in a larger FOA.

| | AOD specifications |
|---|---|
| Operating wavelength ($\lambda$) | 1064nm |
| Material | $TeO_2$ ($v_A$ = 650 m/s) |
| Central frequency ($f_c$) | 75MHz (tol: -3MHz/+5MHz) |
| Bandwidth ($\Delta f$) | 30MHz (75MHz $\pm$ 15MHz) |
| Max. power density | 5W/$mm^2$ |
| Max accepted RF power | 2.2W |
| Active aperture | 7.5mm |
| Max. deviation angle ($\Delta\theta$) | 49mrad |
| Optical transmission | >96% |
| Incidence polarization | Linear perpendicular |
| Incidence Bragg angle | Close to optical autocollimation |

**Table 2.1:** Specification of the near-IR AODs used in the optical setup.

$$FOA(\mu m) = f_{obj}\left[\sin(\theta_{max}\frac{f_5}{f_6}) - \sin(\theta_{min}\frac{f_5}{f_6})\right] \approx \Delta\theta(mrad)\frac{f_5}{f_6}\frac{f_{TL}}{M_{obj}} \tag{2.28}$$

Being $f_{obj}$ and $M_{obj}$ the focal length and magnification of the microscope objective. If we reduce the magnification of T3, then the back aperture of the microscope objective will not be overfilled by the Gaussian intensity distribution, resulting on a very low stiffness $\kappa$, since the effective NA would be $NA_{eff} = NA_{obj}OF$. Being $OF$ the overfilling factor, defined as follows:

$$OF = \frac{\phi}{\phi_{obj}} = \frac{f_2 f_4 f_6}{f_1 f_3 f_5}\frac{\phi_0}{\phi_{obj}} \tag{2.29}$$

Where $\phi_0$ is the beam diameter at the exit of the fiber laser, and $\phi$ its size at the BFP of the objective, whose back aperture diameter is $\phi_{obj}$. The trapping efficiency is defined as $Q = \frac{c}{n}\frac{F}{P}$, and is a measure of the force (in pN) exerted per unit of power (in mW). $Q$ typically increases with the objective lens numerical apperture and decreases in the presence of aberrations.

The ideal case is to have $OF = 1$, lower values result in low trapping efficiency, whereas for very high values we start to see diffraction effects due to the pupil size (big side-lobes of the point spread function (PSF)).

The setup needs to be designed for the two available microscope objectives: a 100x with $\phi_{obj} = 5mm$ and a 60x $\phi_{obj} = 8mm$. However it is preferable to optimize the design for the water immersion one, since the collar correction ring compensates for the spherical aberration introduced by the refractive index mismatch between coverglass and water. Allowing to trap particles through the entire microchamber volume. Instead, for the oil immersion objective, the spherical aberration increases as we move deeper into the sample. The spherical aberration results into a bigger spot size (larger PSF's FWHM), diminishing the gradient force, $Q$, and thereby restricting the axial trapping region to only 10-15$\mu m$ (instead of 90$\mu m$).

The solution to this is to set $\phi = 8mm$ ($OF = 1$ for the water immersion objective), under these conditions $OF \approx 1.6$. Even though the $OF$ factor is not the optimum, the numerical aperture for the oil immersion objective is higher, resulting into a similar trapping efficiency for both objective lenses. However, the total light efficiency decreases from 91% to 53% when using the oil immersion, since most part of the Gaussian beam distribution is blocked by the objective's physical aperture. On top of that, we need to account for the optical transmittance of the microscope objective which is around ∼60% at $\lambda = 1064nm$.

For the part of the AODs, the maximum modulation frequency only depends on the laser beam diameter at the entrance of the AO cell:

$$f_{TS} = \frac{1}{\tau} = \frac{v_A f_1}{\phi_0 f_2} \tag{2.30}$$

By looking at equations 2.28, 2.29 and 2.30, we can clearly see that there is a trade off between field of action and modulation speed. For example, if we reduce the laser beam at the entrace of AODs from 5.1mm to 1mm (the minimum accepted by the manufacturer), a higher number of particles would be stabily trapped since $f_{TS}$ would be 650kHz. However, to ensure efficient trapping, i.e. $OF \approx 1$, the magnification of T3 would have to decrease accordingly, reducing the field of action from $102\mu m$ to $20\mu m$.

Another constrains arising from the alignment process, is that the beam diameter has to under-fill the AOD entrance window, there has to be enough clearance to correct for the lateral shift introduced by the thick (and of high refractive index) piece of AO medium (see figure 2.7). Otherwise the intensity distribution of the trapping beam would be asymmetric, affecting trapping quality.

With all the specifications and constrains, the lens selection for the construction of the system, is shown in the next table:

| $f_1$ | $f_2$ | $f_3$ | $f_4$ | $f_5$ | $f_6$ |
|---|---|---|---|---|---|
| 80mm | 80mm | 50mm | 50mm | 100mm | 160mm |

**Table 2.2:** Focal length of each lens of the optical setup.

And the system specifications:

| | Nikon Plan Apo 60x 1.2 NA | Nikon Plan Fluor 100x 1.3 NA |
|---|---|---|
| Field of action | $102.08\mu m$ | $61.25\mu m$ |
| Overfilling | 1.02 | 1.63 |
| Modulation frequency | 127.5kHz | 127.5kHz |

**Table 2.3:** Optical setup specifications for two different microscope objectives.

### 2.4.2 Pivot plane conjugation: initial momentum compensation

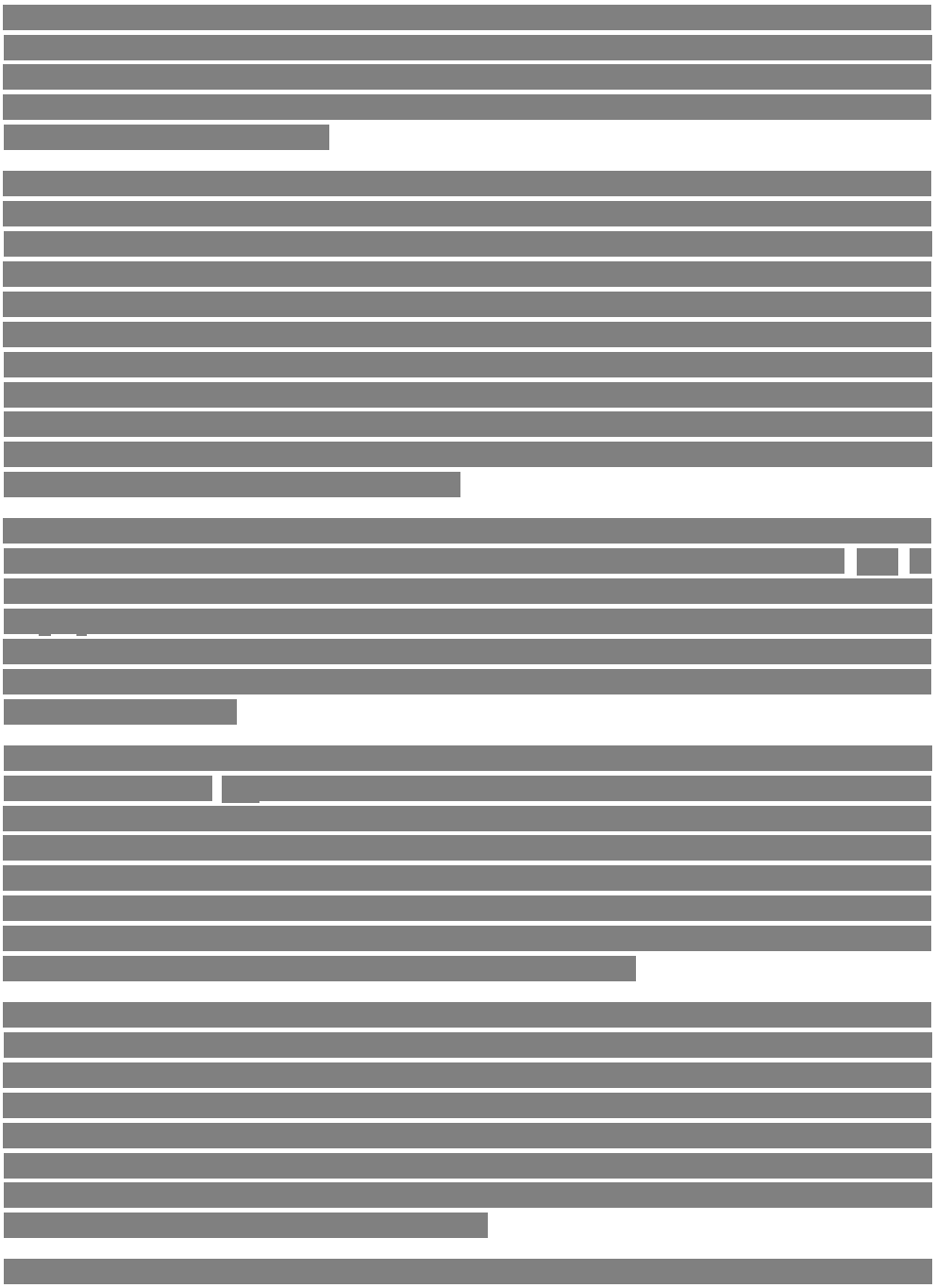

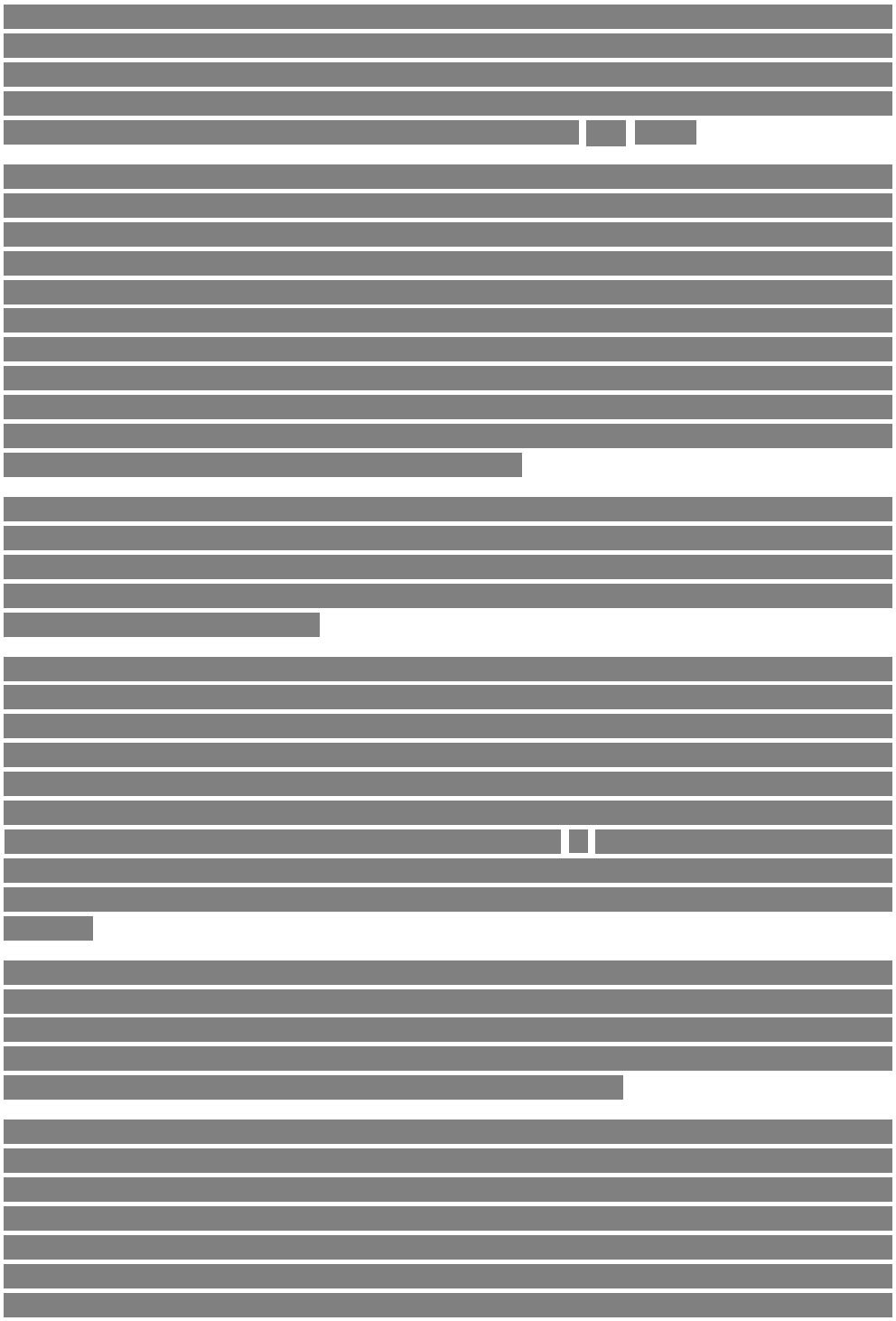

### 2.4.3 Comments on alignment protocol

### 2.4.4 Control software and electronics

To drive the AODs, we used a direct digital synthesizer and power amplifier unit (DDSPA) (AA Optoelectronics, DDSPA-D8b), which generates high-power (up to 2 Watts of RMS power) sinusoidal RF signals, and sends them to the piezoelectric transducer of each AOD. Even though the DDSPA can be controlled through a USB 2.0 interface, we have chosen to control the DDSPA with a PCI data acquisition card (National Instruments, NI-DAQ PCI-6229) and two connection boxes (National Instruments, SCB-68) to digitally code the frequency and amplitude of the sinusoidal RF signals. The use of a PCI card extremely increases the data badnwidth over USB 2.0. Allowing to change the trap position up to 250kHz (limited by the internal digital-to-analog converter), which permits to generate multiple TSOTs.

Since the deflection angle of the AODs is proportional to the input RF frequency, the position of the optical trap $(x_{trap}, y_{trap})$ in the sample plane can be calculated as follows:

$$(x_{trap}, y_{trap}) = \frac{(\theta_H - \theta_L)}{(F_H - F_L)} \frac{f_5 f_{TL}}{f_6 M_{obj}} [(F_x, F_y) - F_c] \tag{2.31}$$

Where the acoustic frequencies are denoted with uppercase $F's$ and focal lengths with lowercase $f's$. $F_H$ and $F_L$ correspond to highest and lowest frequencies of the acoustic

bandwidth, which then causes the laser beam to be deflected $\theta_H$ and $\theta_L$ respectively. The center of coordinates is chosen to be the center of the CCD camera, the trap would be at the center when $(F_x, F_y) = (F_c, F_c)$, being $F_c$ the AOD central frequency. The proportionality factor between acoustic frequency and position is assumed to be constant allover the FOV. This $\mu m/MHz$ factor is calibrated by tracking the position of 4 particles trapped simultaneously at the 4 corners of the FOV. However if the system is well aligned, we always see that the calibration factor never differs more than 1% from its nominal value, calculated from the system specifications (AOD specifications and different focal lengths).

The trap positioning accuracy of the optical system depends exclusively on the RF signal generator used to drive the AODs, specifically on its frequency resolution. In our case, the amplitude and frequency information are controlled digitally through a DB44 connector. The amplitude is coded with 8-bit resolution, whereas the frequency can be encoded in 15, 23 or 31 bits respectively. This means that the minimum step in frequency is given by $500\text{MHz}/2^n$, being 500MHz the DDSPA maximum output frequency, defining the theoretical positioning resolution:

| | Nikon Plan Apo 60x 1.2 NA | Nikon Plan Fluor 100x 1.3 NA |
|---|---|---|
| 15 bits | 51.92nm | 31.15nm |
| 23 bits | $2.03\mathring{A}$ | $1.22\mathring{A}$ |
| 32 bits | $3.9 \times 10^{-3}\mathring{A}$ | $2.3 \times 10^{-3}\mathring{A}$ |

**Table 2.4:** Positioning accuracy depending on the DDSPA digital resolution.

The data acquisition card has 3 different digital output ports: one with 32 connections (P0) and two with 8 connections each (P1 and P2). However, only P0 can access the internal clock of the card, P1 and P2 are restricted by the computer's CPU. This implies that we have very fast control over the trap position, but the trapping power can not be modulated at $f_{TS}$. If we had high-speed control over the amplitude, the efficiency maps of figures 2.20(c) and (d) could be compensated, resulting in a constant stiffness $\kappa$ allover the field of view for the same output laser power.

With all this, the amplitude of each channel is coded in ports P1 and P2. The position at the sample, i.e $F_x$ and $F_y$, is coded using connections P0.0-P0.14 and P0.15-P0.29 respectively. Then ports P0.30 and P0.31 are used for synchronization with the force measurement apparatus when needed. Note that, due to the limited number of connections of the card, our positioning accuracy is restricted to 51.92nm.

For the generation of multiple optical traps through time-sharing, the N coordinates of the N traps, are set into a cyclic buffer that is reproduced in FIFO mode at the specified time-sharing frequency $f_{TS}$. In this way, assuming 3 different optical traps, the acoustic frequencies generated by the DDSPA would be ($Fx1$, $Fx2$, $Fx3$, $Fx1$, $Fx2$, $Fx3$, $Fx1$, ...) for the x-channel, and its corresponding for the y-channel, which are sent simultaneously to the AODs. Mention that, in order to measure the force value at each position, a TTL pulse is sent to the force sensing apparatus every time the acoustic frequency changes.

Regarding the control of multiple optical traps, different Labview control software have been programmed depending on the needs of each experiment. In all of them the CCD camera is controlled with Micromanage 1.4, an open source program that allows us to write Java-based routines and image processing algorithms. We programmed a small routine that reads the desired trap position and sends it to our Labview program, which in turn generates the corresponding acoustic frequencies to drive the AODs. In the program, the user can create N different traps by clicking at N different positions of the field of view, or use predefined geometrical shapes where a trap will be created at each corner. In order to change the position of any trap, the user can just "click and drag" the corresponding image point and the trap moves accordingly. At the same time, the force sensing apparatus is connected to the computer through USB 3.0 and controlled also using Labview routines.

In order to perform controlled oscillations or to have a precise control over the different particle trajectories, each trap position can be modulated independently. To implement it, the trajectory of each particle $(x_i(t), y_i(t))$ is previously calculated either following a straight line, triangular signal or sinusoidally. Each trajectory is translated into its corresponding acoustic frequency $(F_i(t)), F_i(t))$. Finally, the frequency trajectories of each particle are then interleaved sequentially from trap 1 to N. Figure 2.22(d) shows three 3-$\mu m$ polystyrene microspheres, where the particle in the middle is oscillating sinusoidally at 50Hz and 7.5$\mu m$ amplitude. Figures 2.22(b) and (c) show the independent manipulation of 4 microspheres and a 5-$\mu m$ wide and 30-$\mu m$ long polystyrene cylinder. For the cylinder case, 15 different traps were created along the direction of the user drawn line.

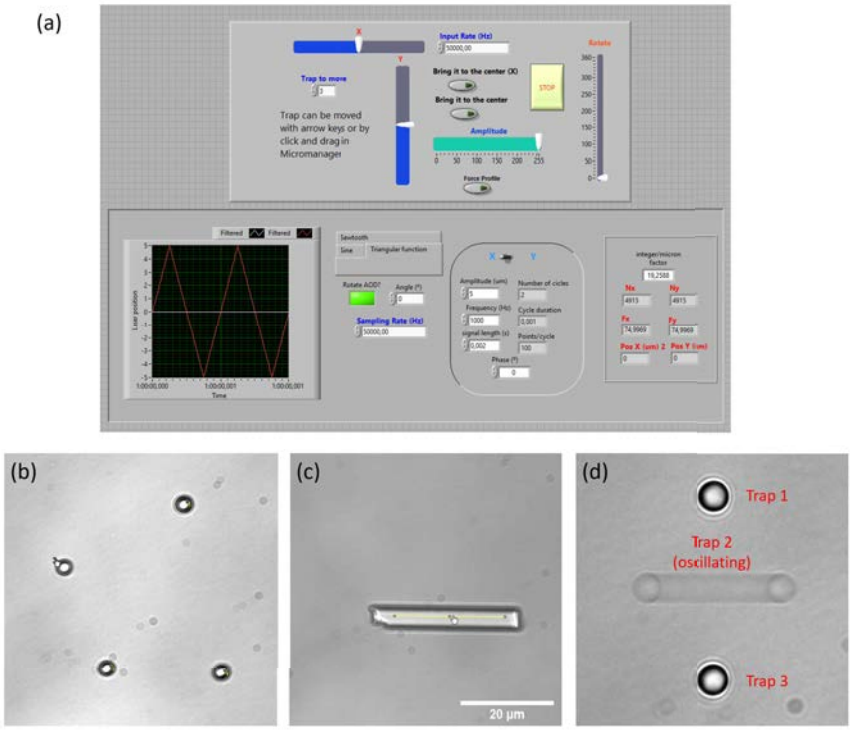


**Figure 2.22:** (a) Front end of the Labview user interface to generate different optical traps. (b) Manipulation of four 3-$\mu m$ microspheres and a polystyrene cylinder(c). (d) Three trapped particles where the center one is oscillating at 50Hz. The image is the average over a time series.

# Chapter 3

# Capabilities portfolio of the AOD-based optical trapping setup

The optical micromanipulation unit designed in this thesis supposes a very useful tool, with which to carry out new experiments, impossible to date. The optical setup described in the previous chapter combines, for the first time, a high-end AOD-based steering and trap generation system, with all the benefits of a calibration-free and sample-independent force measurement device. Bringing these two features together makes the system suitable for a wide variety of biological applications. Especially for quantitative force measurements inside living specimens, where the *a priori* knowledge of the sample parameters is crucial for an accurate trap stiffness calibration, affecting to the corresponding force values. Additionally, the fact that force measurements are independent of the sample geometry, allows the user to perform experiments inside living cells, by trapping and manipulating their own organelles, membranes and vesicles. Without the need of injection of microshperes of other external and artificial bodies, that can affect the integrity of the cell structure, and thereby the validity of the obtained results.

The parallelization of multiple experiments is the main feature of the system. The generation of multiple optical traps at different locations by means of fast steering, allows us to grasp and manipulate multiple objects, or extense and irregular samples, such as big cells or cell aggregates. While at the same time, the force and position information is recorded for each of the generated traps. In this chapter we show different experiments demonstrating the manipulation and precise force measurement capabilities of the system. The experiments have been performed in synthetic samples, mainly water dilutions of microspheres, as well as some tests in living specimens.

In the first part of the chapter we demonstrate individual trap force measurements by applying controlled oscillations. Regarding controlled oscillations, we explain and demonstrate the benefits of laser-driven ones compared to driving the stage. We explain the implementation of the active-passive trap calibration method on a laser-

driven basis, which allows calibrating the trap inside viscoelastic media. Then, we propose a new robust force profiling method that allows us to measure, in real time, the complete optical force profile. Providing useful information on how the optical force profile is affected by changing the experimental conditions (such as particle size, refractive index or beam aberrations), as well as quantifying the backscattered light losses, which can affect the precision of force measurements. Finally, the system capabilities are put to the test in an active gel based on tubulin bundles and kinesin aggregates, in which we did a preliminary study on its mechanical propperties.

## 3.1 Real-time simultaneous single object force measurements

To demonstrate the possibility of the optical system on addressing single object information, we generated multiple optical traps and measured the force signal upon applying a controlled drag force by moving the piezoelectric stage.

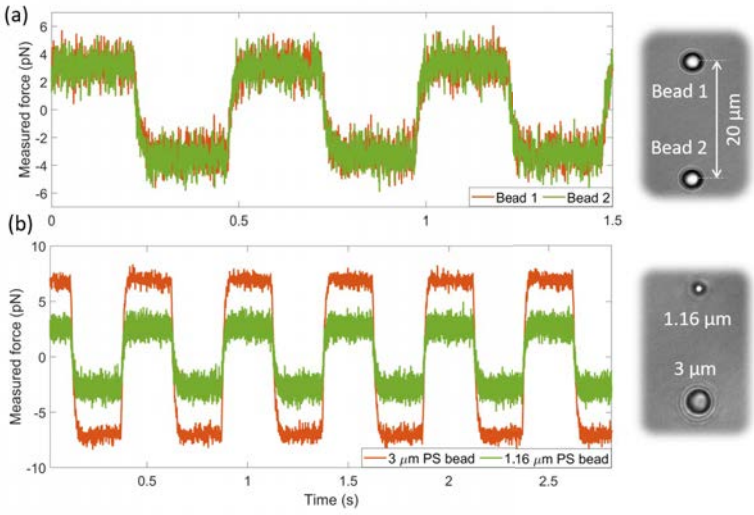


**Figure 3.1:** Individual trap force signals of two time-sharing optical traps. (Top) 3-$\mu m$ polystyrene beads separated by 20$\mu m$ and (bottom) 1.16-$\mu m$ and 3$\mu m$ polystyrene beads.

Under these conditions, if the microchamber is propperly attached to the piezoelectric stage, its controlled movement is translated into fluid velocities exerting hydrodynamic forces on each of the trapped particles. The exerted force on each object depends on the flow velocity, the buffer viscosity and the geometry, specifically in the cross section in the direction of the fluid. For the spherical particles we measured on, the exerted drag force is:

$$F_{drag}(t) = 6\pi\eta(T)Rv_{flow}(t)b = 6\pi\eta R\frac{dx_{S,L}(t)}{dt}b \tag{3.1}$$

$$b = \frac{1}{1 - \frac{9R}{16h} + (\frac{R}{2h})^3} \tag{3.2}$$

Where $\eta(T)$ is the buffer viscosity, which depends on the ambient temperature, $v_{flow}$ is the fluid velocity and $x_{S,L}(t)$ in this case corresponds to the piezoelectric stage trajectory, controlled and monitored by means of the NI-DAQ. $b$ is known as the Faxén factor accounting for the coveslip's surface interaction, neglected in all this thesis since experiments are performed at $\sim 40\mu m$ from the bottom. Then, the applied external force can be controlled by changing both the frequency and amplitude of the oscillations. Equation 3.1 is exclusive for spherical particle, where drag force is independent of the direction, but for example in figure 2.22(c) the cylinder has to be defined with two different friction coefficients $\parallel$ and $\perp$.

Figure 3.1 shows two drag-force experiments. The piezoelectric stage position is driven by a triangular signal, resulting in a constant force within half the range of a period, which then changes its direction and thereby the sign of the applied force. Since the piezo stage is modulated by a triangular signal, the corresponding hydrodynamic force can be modeled by a square-wave of the same period, i.e. the derivative of the input triangular signal. In both experiments, two time-shared traps are generated at $f_{TS} = 15kHz$, the traps are separated $20\mu m$ along the y-axis in order to avoid hydrodynamic interaction between them.

In the first experiment shown in figure 3.1(a), two identical 3-$\mu m$ polystyrene microspheres are trapped, while the piezo stage is driven at 2Hz and $8\mu m$ in amplitude. In that case the theoretical applied force for each particle is 3.80pN, for which we measured 3.61pN and 3.52pN, corresponding to an error of 5% and 7.4% respectively. The measured absolute force is calculated as the half-difference between the two constant-force plateaus, which automatically cancels out the initial momentum of the beam. Due to $f_{TS} = 15kHz$ each trap was sampled at 7.5kHz, and the value of each plateau is the average over 1000 data points, which eliminates the zero-mean Gaussian noise due to Brownian motion.

The second experiment shows a similar scenario, but here the trapped particles are of different diameter, 1.16 and $3\mu m$ respectively, and therefore the applied force is also different (3/1.16 times larger for the $3\mu m$ microsphere). In this case the piezo stage is driven at also 2Hz but $15\mu m$ in amplitude. The theoretical forces are $F_{1.16\mu m} = 2.62pN$ and $F_{3\mu m} = 6.78pN$, for which we measured 2.68pN (2.3% error) and 6.89pN (1.6% error) respectively. An appreciable difference in the noise level in the constant force plateau is observed, due to the Brownian motion is greater for smaller particles.

Both experiments demonstrate that individual forces can be measured by propper synchronization between the trap generation and the force measurement device. Comment that this experiment can be exclusively done with our system. If instead of

TSOT we would have used a HOT approach, the force measurement apparatus would have measured the sum of both forces.

The use of a piezoelectric platform to apply controlled oscillations is not ideal due to several reasons. First of all it has slow frequency response curve, limiting the maximum frequency of the applied oscillations. It also causes that the stage is not responding instantly, it takes some time to reach the desired constant velocity, due to the stage needs to accelerate. This acceleration can be seen on any of the force traces in figure 3.1, especially in the transition time between a positive to a negative force value. But the major disadvantage of stage driven oscillations is that the force is applied to all the particles at once, is impossible to individually control the applied force on each particle.

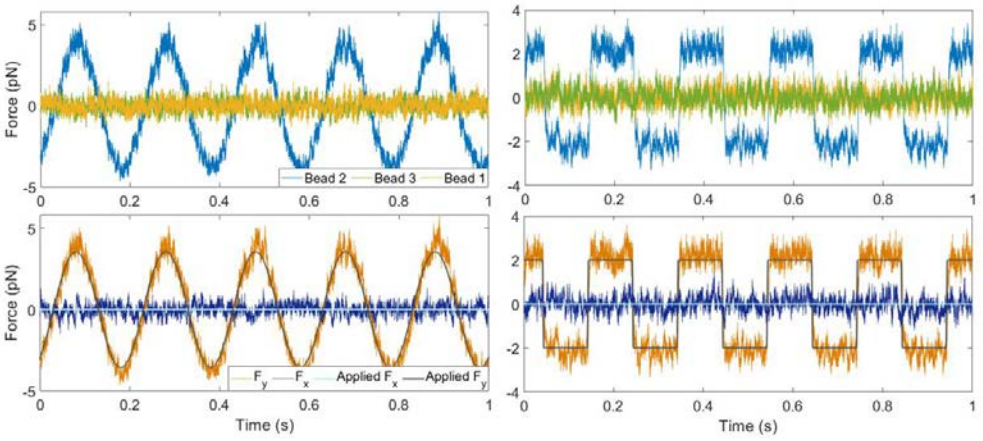


**Figure 3.2:** Single trap force signals for three different $3\mu m$ microspheres. Traps 1 and 3 are always kept static, while trap number 2 is oscillating at 5Hz and $3\mu m$ in amplitude. The experiments from the left and right correspond to a sinusoidal and triangular-wave oscillations. Force traces for the three different trapped microspheres are shown at the top, and a comparison between the X and Y channel is presented at the bottom. The applied force curves are calculated from the derivative of the laser position nominal values.

To overcome such issue, by moving the trap position itself we benefit from more precise and individual control over the exerted forces. Thanks to the AOD-based steering system, the trap can be positioned and moved much faster than the trapped object response time. As opposed to galvo-mirrors or the piezo stage, where in both cases physical elements have to be moved to exert forces. Additionally, since it takes almost no time for the trap to move (it only takes $\tau$), we can assume that the external optical force is applied instantly. If we move the trap from position $x_0$ (equilibrium position) to $x_1$ the instant external force would be $F_{ext} = \kappa(x_0 - x_1)$, and then we can go back to $x_0$ before the particle even responds to any to this changes.

Thus, to demonstrate the flexibility of our system while being fully compatible with calibration-free direct force measurements, we performed the same kind of drag force

experiment but in a laser-driven approach. Instead of moving the platform, here the laser position of each individual trap is modulated independently, allowing controlled forces to be exerted on one or more objects at the same time. If the laser oscillation frequency is kept below the cutoff frequency of the power spectrum, each particle will move following the same path as the corresponding optical trap. However, if the laser is swept fast enough, particles will no longer be trapped and will diffuse away during the oscillation time.

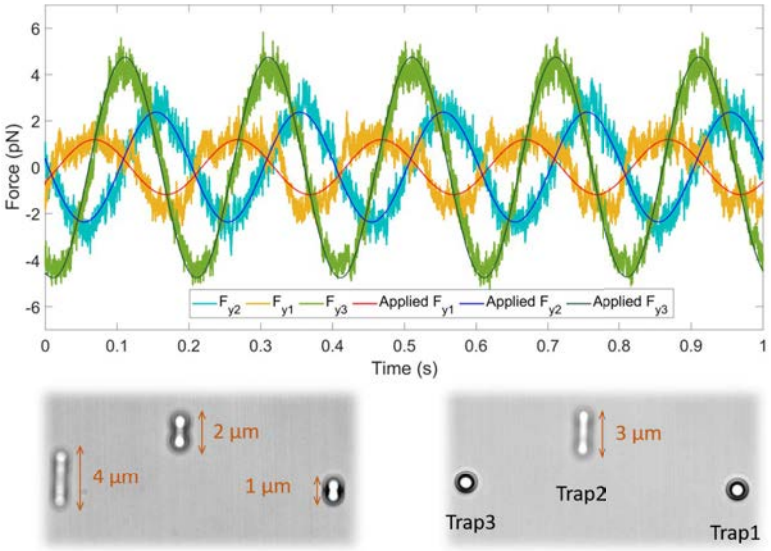


**Figure 3.3:** Measured force traces, and theoretical applied force curves, for three trapped particles. All three optical traps were oscillating at 5Hz and 1, 2 and 4$\mu m$ respectively. The images at the bottom show the movement of the trapped particles when each trap is oscillating (left) and when only moving the central one (right).

This is what is shown in figure 3.2. In this experiment, three horizontally distributed optical traps were generated trapping 3-$\mu m$ polystyrene microspheres. Then, traps 1 and 3 were kept static while trap 2 was oscillating along the y-axis either sinusoidally or following a triangular wave, as in the stage-driven experiment. Since the oscillation is vertical, only the AODy is constantly changing the acoustic frequency. As can be seen in the force traces, the only non-zero force signal is the one corresponding to the y-component force of trap number 2, which is in good agreement with the theoretical value of the applied force. For this laser-driven case, the theoretical drag force signal is calculated in the same way as in equation 3.1, taking the derivative of the trap position $dx_L(t)/dt$, which is directly obtained from the previously calculated acoustic frequencies, equation 2.31. It is easy to see, that in the case of sinusoidal oscillations, the laser position and applied force signals are two sinusoidal functions with a phase difference of $\pi/2$, due water is a purely viscous medium.

The zero-force signal corresponding to the x-component of the force indicates perfect

alignment between each AOD axis and the PSD sensor axis. The zero-force signal from traps 1 and 3 demonstrates good synchronization between the DDSPA and the force sensing apparatus, otherwise we would see lower force values or force signal leaking from trap 2 to the other ones. Note that, on the triangular-wave oscillation the transition from positive to negative constant force values is much faster than on the stage-driven case. The only transition we see is due to the microsphere's response time to the change of laser direction.

Finally, in figure 3.3 we show the case where we apply external forces on each of the three microspheres. The traps were oscillated sinusoidally at 5Hz for all three particles, but with different amplitudes: 1, 2 and $4\mu m$ respectively. In that way, $F_2 = 2 \times F_1$ and $F_3 = 2 \times F_2$, since all three beads are of the same size. The measured force trace for each individual trap perfectly overlaps with the corresponding theoretical value, demonstrating the compatibility of our system with the direct force measurements.

## 3.2 Active passive calibration and rheological studies

The quantification of intracellular forces has remained a challenge due to complications on trap stiffness calibration inside complex media, as is the cell cytoplasm. The interior of a cell is an heterogeneous mixture that contains both viscous and elastic components. The cytosol provides the viscous behaviour, whereas several rigid structures, such as actin and tubulin filaments, give the mechanical consistency to the cell, forming the cytoskeleton. Due to all of this, the behaviour of a particle inside such a viscoelastic medium, differs a lot to the same microscopic particle embedded in pure water or other known viscous buffers.

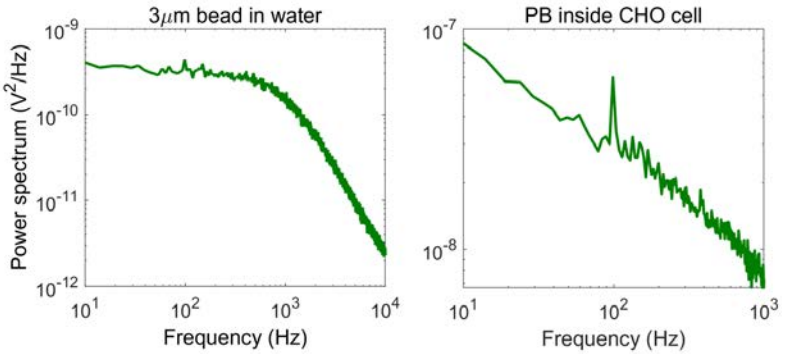


**Figure 3.4:** Power spectrum for a $3\mu m$ trapped particle in water (left) and a protein body inside a Chinese Hamster Ovary (CHO) cell.

Here, the external forces are no longer hydrodynamic, and we can distinguish two components: a hydrodynamic force proportional to the fluid velocity (like in pure

water), and an elastic component which is proportional to the relative position within the cytoplasm. Since the particle is embedded in a web-like structure, the force acting on the particle changes from point to point. This elastic behavior can be incorporated into a generalized Langevin equation (equation 2.17) by assuming that the friction retardation coefficient $\tilde{\gamma}$ is a complex number instead of a real quantity, where the real part accounts for the viscous behaviour (dissipative processes) and the imaginary part for the elastic processes. All this causes that the power spectrum of a trapped particle in such a chaotic medium can no longer be approximated by a Lorentzian function. Making it very difficult to calibrate the trap through the power spectrum analysis. Figure 3.4 compares the power spectrum of a particle in pure water, with a trapped $\sim 1\mu m$ spherical protein body inside a living chinese hamster ovary (CHO) epithelial cell. Note that in the case of the cell, the characteristic plateau at low frequencies disappears. Due to the cell cytoskeleton, a new elastic component appears with another characteristic frequency, enhancing the low frequency range and making it very difficult to identify the cutoff frequency corresponding to the trap stiffness.

In this scenario, a passive calibration of the trap would involve modeling both the elastic and viscous components of the cell cytoplasm [50]. As well as the geometry and size of the trapped objects, which as they are elements of the cell interior, most are below the diffraction limit. All these needed variables for calibration are not consistent from cell to cell, neither within the same cell type.

To solve this problem, active-passive calibration was proposed by M. Fischer and K. Berg-Sorensen [51], later tested on a viscoelastic gel [52] and finally demonstrated its performance in living cells [53]. In this method the viscoelastic properties of the medium, as well as the object geometry, are assumed unknown, and therefore the external thermal agitation forces $F_{rand}(t)$. This means that the thermal fluctuations do not offer enough information about the system response function, from which to extract the trap stiffness. The system response function $\chi(\omega)$ relates the particle position when an external force is applied: $x(\omega) = \chi(\omega)F_{ext}(\omega)$. Note that on a viscous medium, $F_{ext} = F_{rand}$ and this is completely known, then $\chi(\omega)$ can be measured just by analyzing the power spectrum $|x(\omega)|^2$.

On the active-passive calibration, the system response function is measured over a wide range of individual frequencies by comparing the measured thermal fluctuations with the measured system response upon controlled perturbations. In other words, due to the thermal forces acting on the particle are *a priori* unknown, we measure the system response function by analyzing how the system responds to known stimuli. We can distinguish two scenarios corresponding whether no external force is applied to the system (passive part) and when applying an external perturbation (active part). The equations describing both the active and passive parts are:

$$-\omega^2 m x_P(\omega) = -i\tilde{\gamma_P}(\omega)x_P(w) - \kappa x_P(\omega) + F_{rand}(\omega) \tag{3.3}$$

$$-\omega^2 m x_A(\omega) = -i\tilde{\gamma_A}(\omega)x_A(w) - \kappa x_A(\omega) + F_{rand}(\omega) + F_{ext}(\omega) \tag{3.4}$$

$$P_P(\omega) = \left\langle |x_P(\omega)|^2 \right\rangle = \frac{2k_B T Re\left\{\tilde{\gamma_P}\right\}}{|\kappa + i\omega\gamma_P(\omega) - \omega^2 m)|^2} \tag{3.5}$$

Being $x_{A,P}$ the particle position for the active and passive parts, $F_{rand}$ the thermal agitations and $F_{ext}$ the applied external force. The friction retardation coefficient is defined as $\tilde{\gamma}_{P,A} = \gamma_{1P,A} + i\omega\gamma_{2P,A}$. External perturbations are typically applied by oscillating the piezo stage or by moving the laser, in the same way as in the previous section. If the external force is applied by means of the piezoelectric platform $F_{ext}(t) = \tilde{\gamma}(\omega) i\omega x_s(\omega)$, whereas if the laser moves $F_{ext}(\omega) = \kappa x_L(\omega)$. Being $x_S(t)$ and $x_l(t)$ the piezo stage and laser positions.

Note that for the passive part, only thermal fluctuations are acting on the system, so the average of the particle positions is $\langle x_P(\omega)\rangle = 0$, and thereby the active part $\langle x_A(\omega)\rangle = \chi(\omega) F_{ext}(\omega)$. Assuming $\tilde{\gamma_P}(\omega) = \tilde{\gamma_P}(\omega) = \tilde{\gamma}(\omega)$, and knowing that $\chi(\omega) = \frac{1}{\kappa + i\omega\tilde{\gamma}(\omega) - m\omega^2}$, the following expression is obtained:

$$\chi''(\omega) = \frac{\omega}{2k_B T} P(\omega) \tag{3.6}$$

Where $\chi''$ is the imaginary part of the system response function. Thus, when the stage or the laser are driven of the form $A_{s,l} sin(\omega t + \phi_{s,l})$, the particle position would also be a sinusoidal function, $A_p sin(\omega t + \phi_p)$ which can tracked by means of BFPI. The stiffness is calculated as follows:

$$\kappa - \omega^2 m = \frac{2k_B T}{P(\omega)} \frac{A_p}{\omega A_s} \sin(\Delta\phi) \tag{3.7}$$

$$\kappa = \frac{2k_B T}{P(\omega)} \frac{A_p}{\omega A_L} \sin(\Delta\phi) \tag{3.8}$$

Being $\Delta\phi$ the phase delay between the particle and the stage (equation 3.7) or between the particle and the laser (equation 3.8). The active-passive method provides an stiffness value for each frequency, and typically the average value over the whole range is taken.

Appart from the trap stiffness, the active-passive method is widely used to measure the mechanical properties of the medium. Once the stiffness is known, the system response function $\chi(\omega)$ can be calculated, from which the complex friction retardation coefficient $\tilde{\gamma}(\omega)$ is obtained, providing information of both the viscous and elastic components of the medium. Note that $\tilde{\gamma}(\omega)$ depends on the object geometry, which difficults comparison between different cells. If we assume that most intracellular bodies are spherical, we can calculate the G-modulus $G(\omega) = \frac{i\omega\gamma(\omega)}{6\pi R}$. This last magnitude only depends on the medium's mechanical properties.

In the laboratory, the calibration is performed by oscillating the piezo stage at different frequencies between 5 and 70Hz, limited by the piezo stage frequency response

function, with an oscillation amplitude between 0.5 and $2\mu m$ (depending on the laser power). In the calibration process, the active and passive parts are alternated in 1 second intervals, each time increasing the driving frequency of the active part. The particle position is obtained in volts by recording the $Sx$ and $Sy$ PSD channels of the direct force momentum apparatus. To obtain the position of the particle in physical units, the $\beta(\mu m/V)$ proportionality factor is calibrated by video tracking when applying a high amplitude driving oscillation. The piezo stage position is obtained by means of the monitoring channel. All active signals are analyzed and fitted with sinusoidal functions to extract $A_p$, $\phi_p$, $A_s$ and $\phi_s$, whereas the power spectra for each of the passive time-series are averaged to reduce noise on $P(\omega)$.

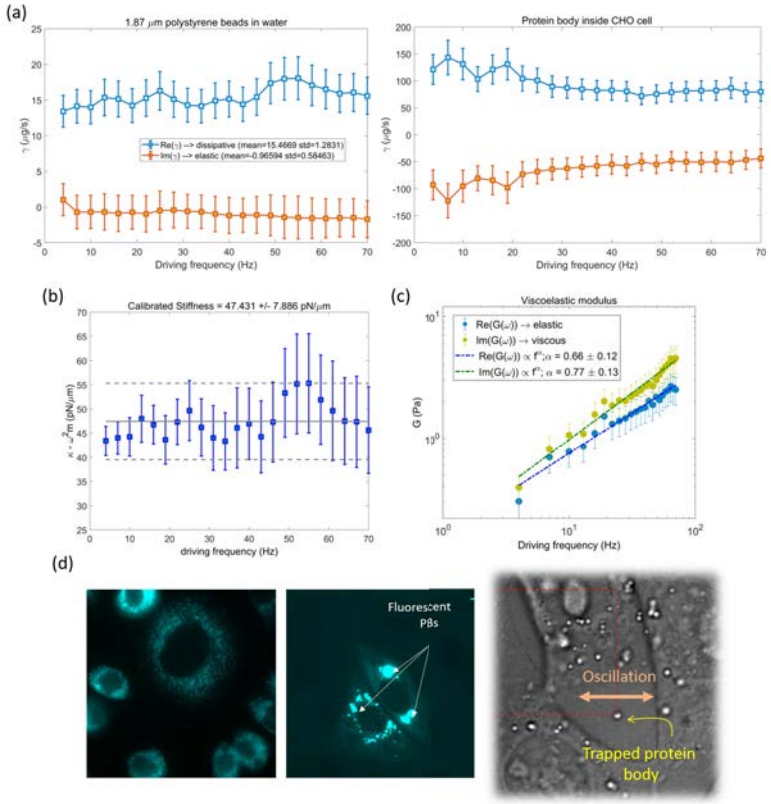


**Figure 3.5:** Results from a stage-driven active-passive calibration for a protein body inside a living CHO cell. (a) Measured friction retardation coefficient, compared to water (left). (b) Calibrated stiffness. (c) Measured shear modulus of the cell cytoplasm. (d) Epifluorescence and brighfield images of the artificially induced protein bodies.

Figure 3.5 shows the results of the active-passive calibration method on a protein body inside the cytoplasm of a Chinese Hamster Ovary (CHO) epithelial cell. As can be seen, the friction retardation coefficient $\tilde{\gamma}(\omega)$ presents both an elastic part and a

viscous part of the same order of magnitude, corroborating the cell cytoplasm's viscoelastic nature. Also, the friction coefficient is frequency dependent getting bigger at low frequencies. To test the validity of the method, the same active-passive calibration is also performed on a 1.87-$\mu m$ polystyrene microshpere embedded in water. As expected, the measured friction retardation coefficient reports an almost null elastic part. The viscous part is constant for the whole frequency range, and in good agreement with the theoretical value of $\gamma = 14.8\mu g/s$ (calculated as $\gamma = 6\pi\eta R$). Figure 3.5(c) shows both the elastic and viscous parts of the G-modulus of the cell cytoplasm, which follows a power law $\propto f^{\alpha}$ also observed with other techniques such as AFM indentation [54, 55, 56].

For the calibrated stiffness we can see that it remains more or less constant over the frequency range. The calibrated stiffness was $\kappa = 47.43 \pm 7.8pN$, corresponding to a $\pm 15\%$ error. The main source of error comes from a noisy power spectrum, which can be improved by increasing the recording time. Also the camera-based $\beta$ calibration contributes to the huge error-bars, affecting the final result.

Regarding experiments inside living cells, the active-passive calibration method was performed on different samples of a transfected CHO cell line expressing self-fluorescent (cyan fluorescent protein (CFP)) protein bodies [57]. Due to their high refractive index and size, they become optimal trapping targets for active-passive calibration, see figure 3.5(d). CHO cells were cultured first on 60mm petri dishes for two weeks. Before the experiment, around 2000 cells were taken out during culture passage and placed on a sterile 170$\mu m$ coverslip with growth medium for 24 hours, until they attach to the glass surface, expand and start to divide. Finally, a microchamber using two-sided scotch tape is mounted, filling the whole volume with growth medium. The experiments were performed within the next hour until biological activity starts to decrease.

### 3.2.1 Transition from stage driven to laser driven active passive calibration

For active-passive calibration to be as accurate as possible, there are several things to consider. The amplitude of the stage oscillation has to be big-enough to produce an appreciable change on the voltage signal. On the active part, the signal-to-noise ratio (SNR) increases with the oscillation amplitude or the laser intensity, due to the thermal fluctuations are reduced when increasing power. Additionally, the applied external force has to fall within the linear region of the optical trap. Otherwise, the particle would move outside of the linear zone, causing a deformation of the sinusoidal position signal $Sx$, affecting the fitted $A_p$ value, thereby ending up with a wrong calibration. So, if the oscillation amplitude remains constant over the whole process, the applied force is linearly increasing with driving frequency. This is good for improving the SNR, but we risk working outside of the linear zone. It is preferable to reduce the amplitude of the oscillation as the frequency increases, in this way the SNR remains constant and we make sure to work in the linear zone.

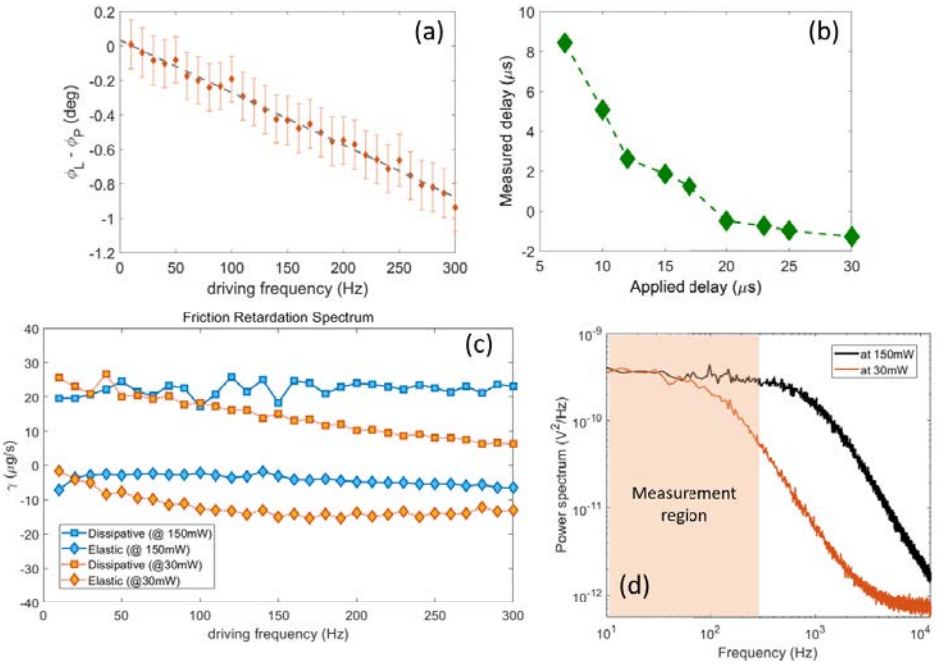


**Figure 3.6:** (a) Fitted phase of a stucked 5-$\mu m$ particle as a function of the driving frequency. The non-constant phase denotes the presence of a constant time-delay between the laser and the particle. (b) Measured delay as a function of the applied delay, when the measured delay is zero the system is assumed synchronized. (c) Friction retardation coefficient for a 3-$\mu m$ microsphere in water at low power (30mW) and high-power (150mW). The fact that the particle is not feeling the optical force at high frequencies results in an underestimation of the forces. (d) Passive power spectrum for the two cases of (c).

In this section we describe the experimental implementation of laser-driving active-passive calibration. The transition from driving the piezo stage to driving the laser improves the overall quality of the measurements due to several factors. The first thing to note, is that by moving the trap instead of the stage we remove any inertial term from the calibration equation 3.7. The fact that the applied external force is hydrodynamic, introduces a mass-dependent term ($-\omega^2 m$), *a priori* unknown for intracellular organelles. This factor becomes significant at the high-frequency range, where the calibration accuracy is higher. However, if the external force is exerted by the laser movement, the inertial term disappears. Enabling rheological studies at a higher frequency range, which is neither limited by the piezo stage response function.

Laser-driving active-passive calibration has been implemented in our setup by means of a Labview program that takes care of driving the laser and reading all the PSD signals. The oscillations are programmed in the same way as in section 3.1, allowing also

to perform active-passive calibration, as well as measuring the mechanical properties, in different locations at the same time. Since the cell interior is a constantly changing structure, it is preferable that all measurements are carried out in the shortest time possible.

The laser-driving scheme implemented in this thesis follows the same sequential approach as in the stage-driven case. Both active and passive parts are recorded sequentially in $\sim 1$ second intervals. The difference here is that the oscillation frequency is not limited by the stage, and it can be up to 2kHz (defining the oscillation period with at least 10 sample points). However, mention that the flexibility of the system allows us to implement other smart scanning schemes such as the one developed by J.R. Stauton and B. Blehm [58], where the trap position is oscillated at multiple frequencies at the same time, allowing to measure all the desired frequencies in just one shot. Another possibility is to move the trap following a square-wave, i.e. switch the laser between two very close positions. In both schemes, the system transfer function can be measured simultaneously by doing a Fourier analysis of the signals, instead of testing individual frequencies one by one.

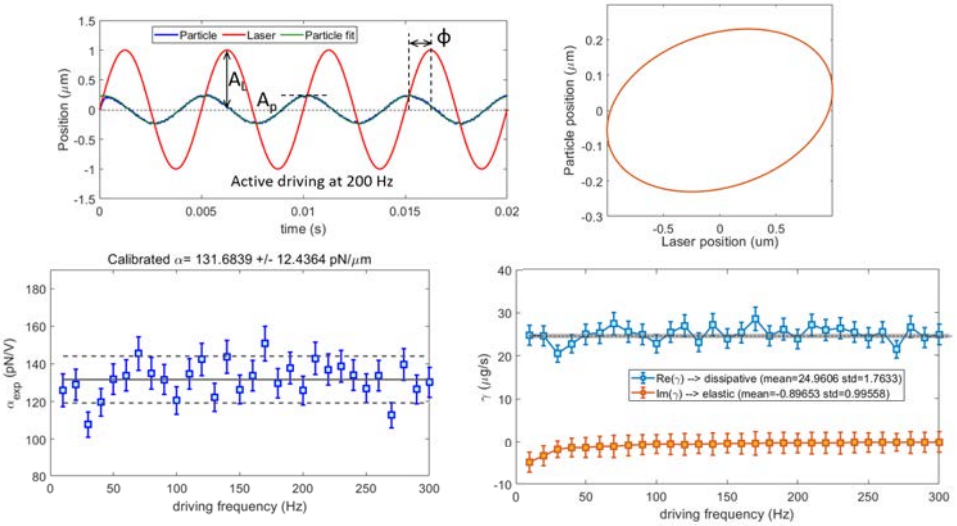


**Figure 3.7:** Obtained results summary of the laser-driving active-passive calibration on a 3-$\mu m$ polystyrene microsphere in water.

A correct measurement of the time delay (phase delay $\Delta\phi$) between the laser and the particle position is crucial for an accurate calibration. Compared to the stage-driving case, where the stage position is obtained by the piezo monitoring signal, here one has to rely on the nominal value of the laser. Which, due to the acoustic wave transition between the AOD transducer and the laser beam, is not synchronized with the actual movement of the laser.

Hence, this time delay has to be first measured and then compensated, either exper-

imentally, by delaying the PSD digitization or mathematically during data analysis. A constant time-delay $t_0$ between the laser and the particle results in $\phi_P - \phi_L = \Delta\phi - 2\pi f t_0$, which causes the stiffness value to change following $\kappa(\omega) \propto sin(\Delta\phi - \omega t_0)$.

Figure 3.6(a) and (b) shows the experiment we designed to precisely measure such delay. To calibrate $t_0$, a 5-$\mu m$ polystyrene microsphere is attached to the microchamber coverslip in order to prevent the particle to move when scanning the laser, since the particle position is the reference signal. Then, all active oscillations are performed, recording the particle position information through the $Sx$ PSD signal. The phase delay between the laser and the particle is obtained from sinusoidal fittings to both signals. The measured time-delay is obtained from the slope of the linear fitting to the fitted phase vs driving frequency curve, figure 3.6(a). In our setup, the time-delay is compensated electronically by delaying the PSD digitization. Due to limitations in the electronics of the DDSPA, delay compensation is done on a trial and error basis, until the delay measured by the system is zero, figure 3.6(b).

Once the laser is perfectly synchronized, the maximum frequency at which the optical trap can be calibrated is, in principle, just limited by the AODs transition time. However, for oscillations faster than the power spectrum's cutoff frequency, the particle starts to not be totally trapped. The particle is not completely following the laser movement and can diffuse away during the oscillation time. The measured $A_p$ would be lower, resulting on an underestimation of the trap stiffness $\kappa$.

This behavior is shown in figure 3.6(b) and (c), where we reduced the laser power, i.e. the trap stiffness, until the cutoff frequency falls within the active-passive frequency range. In this case, both $\tilde{\gamma}(\omega)$ and $\kappa(\omega)$ decrease with the driving frequency. The measured values are lower than the same measured at 5-times the laser power, where the tested frequencies are within the power spectrum plateau.

To test the implementation of the method, laser-driving active-passive calibration was performed on 3-$\mu m$ polystyrene microspheres embeded in pure water. The results are shown in figure 3.7. As expected, the measured friction retardation coefficient remains constant for the whole frequency range, with a null elastic component. The viscous component is in good agreement with the theoretical value of $\gamma = 23.75 \mu g/s$. Regarding the stiffness calibration, we see almost no variation over the calibration bandwidth. In this particular experiment, the $\beta(\mu m/V)$ factor was not calibrated and the whole data analysis was performed assuming $\beta = 1\mu/V$. By doing this, the obtained stiffness is given in $pN/V$, from now on $\alpha_{exp}$ since are the same units as the $\alpha$ factor of the force measurement device. Note that the calibrated $pN/V$ factor is obtained from the active-passive calibration, whereas the $\alpha$ factor of the apparatus only depends on macroscopic variables (such as its effective focal lenght).

Then, $\alpha_{exp} = \alpha$ only if the device satisfies the conditions for direct force measurement, explained in section 2.2.2. In our particular case $\alpha_{exp} = 131 pN/V$ and $\alpha = 123.25 pN/V$. This means that all the recorded $Sx$ signals correspond, not only to the particle position ($\beta Sx$), but also to the external applied force ($\alpha Sx$), since $\alpha = \kappa\beta$.

### 3.2.2 [redacted]

[redacted]

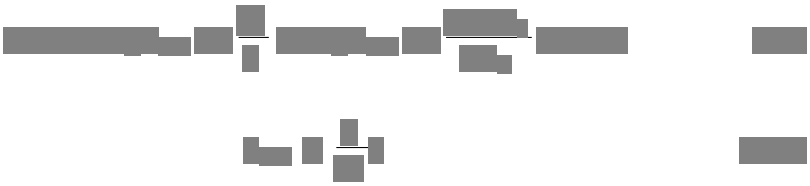

[redacted]

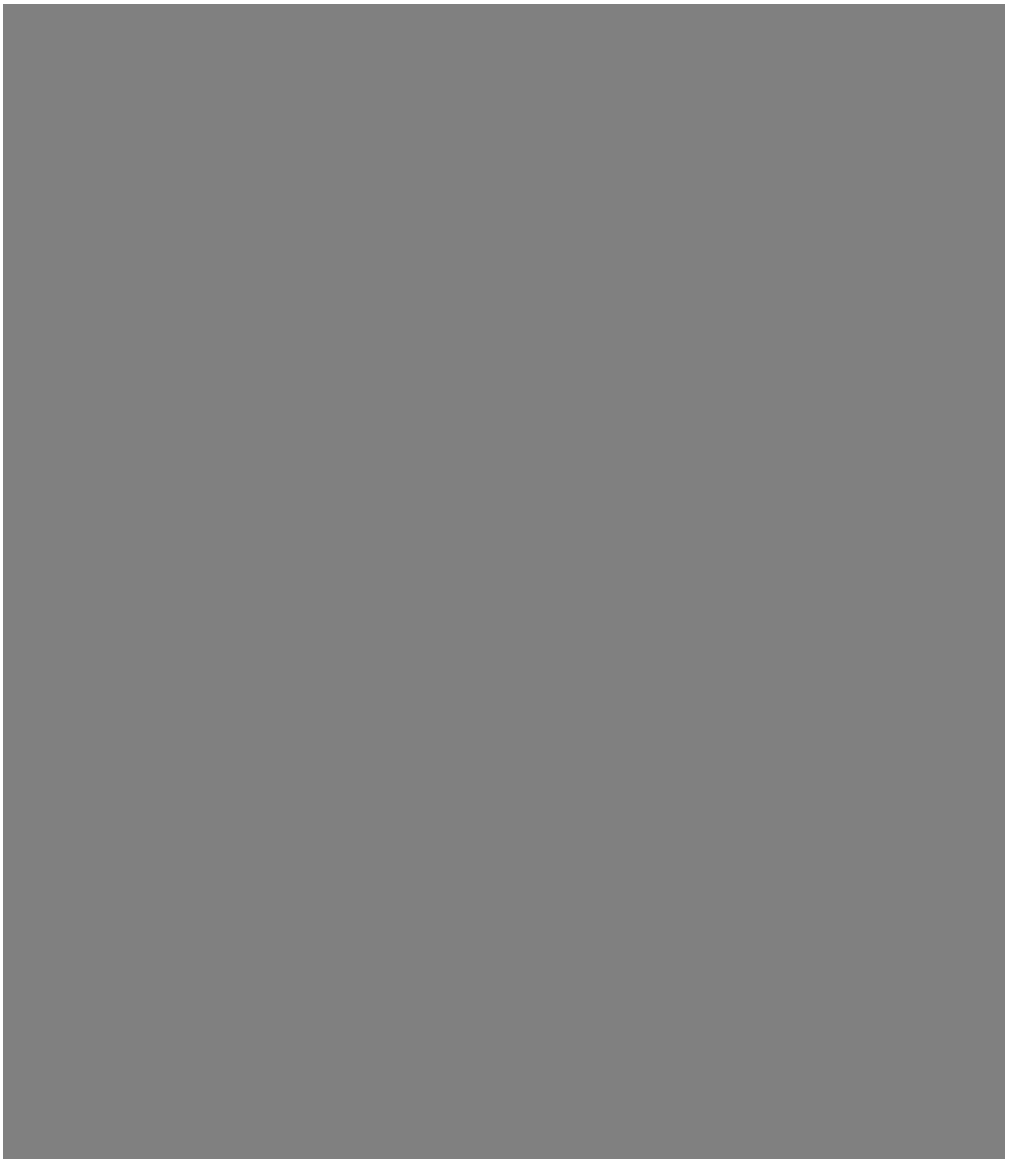

## 3.3 Real time force profiling and backscattered light loss determination

No matter how accurate the calibration method is, the measured force values are only valid in the region where the trap stiffness is defined. Such linear zone is not abrupt, and its extension is uncertain. Depending on the particle geometry, refractive index or beam aberrations, the shape of the force profile changes, and with it the extension for which the force measurements are valid. All this causes that, especially on the intracellular environment where optical properties of targets are *a priori* unknown, the error in the estimate of the maximum force one can apply can be substantial. In practice, the estimation of forces is done on a simulation basis by guessing the geometry and refractive index. In figure 3.9 we show the experimental force profile of polystyrene microspheres in water of different size (1.16 and $3\mu m$ respectively). As we can see, particles on the Mie regime present a better defined linear zone (limited by drastic change on the slope close to the particle's edge), whereas for the Rayleight regime the force profile is smoother. If the maximum force is estimated just by an stiffness calibration, this difference on the force profile shape results on an overestimation and underestimation of the maximum force for Rayleight and Mie particles respectively, as indicated in the figure.

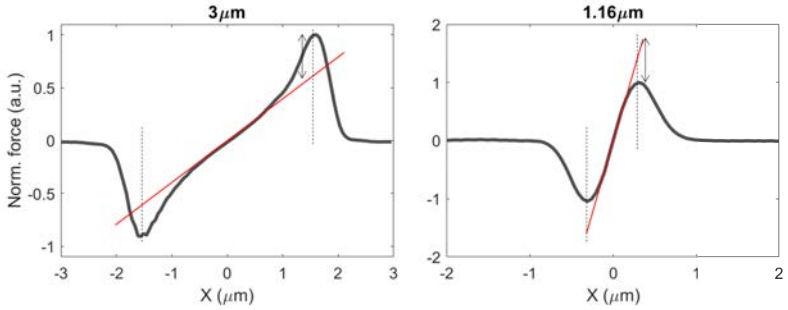


**Figure 3.9:** Experimental complete force profile for a 3-$\mu m$ (left) and 1.16-$\mu m$ (right) microsphere in water.

A new technique for directly measuring the force profile is presented in this section. Benefiting from the fast AOD-based steering system and its compatibility with a direct force momentum apparatus, the micromanipulation setup is able to measure the complete force profile. This allows the possible user to know at any time, not only the instantaneous force, but also the maximum force the optical trap is capable of exerting.

To put an example, a substantial force is required to deform a cell membrane, which in many cases cannot be achieved due to the low relative refractive index. In this case, it would be better to use high-index artificial particles as handles instead of moving the membrane itself. Additionally, the knowledge of the complete force profile offers a better control over the forces to be exerted. Allowing, for example, the implementation of force clamp routines [59].

### 3.3.1 Force profiles through fast scanning

At a first glance, the idea of measuring the force profile is straightforward, one simply needs to scan either the optical trap or the object along a desired direction, while reading the value given by the measurement system. This scanning strategy is commonly used to obtain the positional calibration $\beta(\mu m/V)$ factor in a BFPI system. A water dilution of microspheres is left to dry on top of the coverslip, that stick to the glass surface once the solvent evaporates. The sample is then scanned by moving the piezoelectric platform, while synchronously monitoring the stage's position and the voltage of the BFPI system. Then, from the measured curve one can extract the $\beta$ factor from a linear fitting around $x_{trap} = 0$, as well as the extension of the linear region (that limits the measurement area).

So, the complete force profile can be obtained directly by replacing the BFPI system with a direct force measurement sensor, based on detection of changes of light momentum. In this way, the recorded voltage is always proportional to the net force, regardless of the particle position. However, in this piezo scanning approach the particle is not actually trapped, is stucked to the glass surface, which may be on a different axial position. Such mismatch between the image plane and the trapping plane can affect the measured force profile.

So, it is preferable that the force profile is measured under the same experimental conditions as in the further experiment. The force profile has to be measured while the particle is trapped. The experimental way to implement this is to scan the optical trap along the object with the AODs. K. C. Vermeulen *et. al.* demonstrate the experimental implementation of AOD-based scanning to obtain the calibration positional factor $\beta$ [37]. The position of the trap is moved from $x_1$ to $x_2$ following a triangular signal, resulting in scanning the object back and forth. In order to avoid the particle to diffuse away during the oscillation time, they kept the oscillation amplitude within the linear zone and repeat the process in short time-bursts.

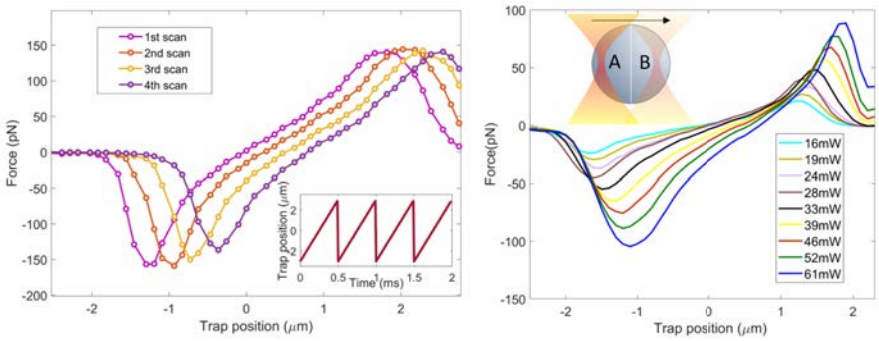


**Figure 3.10:** Experimental force profiles of a 3-$\mu m$ microsphere obtained from fast optical trap scans. (left) The particle moves towards the scanning direction. (right) The optical force profile becomes asymmetric when increasing the trapping power.

In principle, if the scanning speed is high enough the particle is not feeling the optical

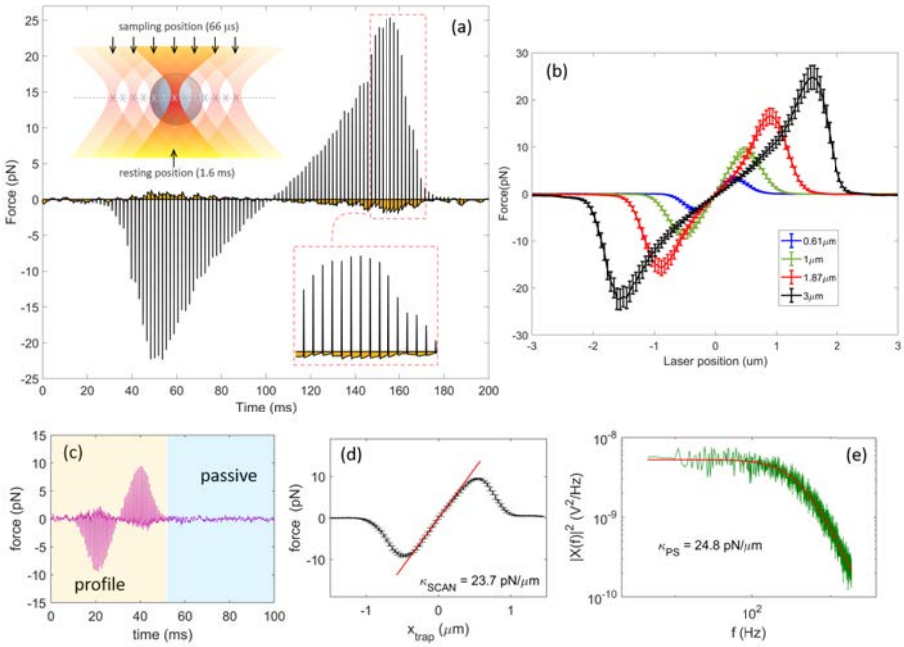


**Figure 3.11:** Implementation of the trap-stepping scanning approach. To test the validity of the method, the stiffness obtained from the measured force profile is compared to the calibrated stiffness by means of power spectrum analysis. The error-bars of all force profiles correspond to the standard deviation over 100 different experiments.

trap potential well, but this is never the case. During the implementation process, we noticed that even scanning the optical trap in the 2-3kHz range, the particles still felt the optical force. Instead of diffusing away, particles followed the laser movement. This effect can be seen in figure 3.10, where the trap position is modulated with a sawtooth signal. After 4 consecutive scans in which the trap was moved from $x_{trap}$=-2.9$\mu m$ to $x_{trap}$=2.9$\mu m$ in 500$\mu s$, we observe that the particle has shifted 0.938$\mu m$ towards the scanning direction (around 300nm per scan). This particle movement when scanning, implies that the measured force profile depends on the laser power. Appart from the known linearity between power and force, the measured force profile also changes in shape when increasing trapping power. The force profile becomes asymmetric, the first part of the force profile becomes wider and the second part narrower, figure 3.10(left). Since the particle is moving towards the laser direction, the optical trap stays more time in the first half of the sphere than in the second. The absolute laser position $x_{trap}$ is not proportional to the relative position $x_{trap} - x_p$. Resulting in a deformation of the x-axis, and thereby the force profile.

Mention that in figure 3.10(left) the laser power was high (93mW). One possible solution would be to use lower trapping power and scale the force profile according

to the desired power, neglecting any absorption or heating effect [26]. The use of a symmetric triangular signal would also minimize the error in trap position, due to the particle will move in opposite directions, averaging the effect.

Here, we propose a much robust scanning scheme that allows us to measure the complete force profile very accurately. The scanning strategy consists on time-sharing the optical trap between two positions (at $f_{TS}$), one of them is always placed at the equilibrium position ($x_{trap} = 0$) for M time-sharing clock cycles, whereas the other trap is swept over the scanning direction, staying at each position for just 1 clock cycle. Then returning to the central position for another M cycles, repeating the process until the entire measuring range is covered. Note that this laser-stepping scanning scheme can only be implemented with AODs, due to the random accessibility on the laser position. As opposed to galvo scanners, the laser is "jumping" between $x_{trap} = 0$ and the sampling position, without visiting any intermediate position.

A set of TTL pulses synchronized with the time-sharing clock are sent to the force measurement apparatus, which takes a force value once the PSD is fully charged. With this laser-stepping scanning approach, the first trap ensures the particle to be static at its equilibrium position at $x_{trap} = 0$, preventing the particle diffusing away, while the second one is visiting the desired sampling position for the time required to fully charge the PSD.

The raw force signal obtained using this approach is shown in figure 3.11(a), where $M = 25$ and $f_{TS} = 15kHz$. The laser stays 1.6ms at the equilibrium position and $66\mu s$ at each sampling position. The final force profile is obtained as follows: $F[n] = F_{raw}[n(M+1)]$, where $F[n]$ is the $n^{th}$ data point of the final profile. Note that this is equivalent as assuming M+1 different time-sharing traps and taking the signal of the $M + 1^{th}$.

The time it takes to measure a complete force profile is $\frac{N(M+1)}{f_{TS}}$. Where $N$ is the number of sample points of the desired force profile. Regarding $f_{TS}$, this is chosen to be as high as possible and is limited by the PSD response time ($f_{TS} < 25kHz$). Regarding the error in the force profile, we experimentally observe that it depends on the number of photons exchanging linear momentum during the sampling stage, that is either increasing laser power or reducing $f_{TS}$ (increasing the visitation time). During $1/f_{TS}$ the particle feels the optical force and starts to move towards the sampling position, just after this, the trap returns to the equilibrium position, for which the particle is no longer centered. This phenomenon can be seen in figure 3.11(a) (orange shaded area), just after the sampling step the sensor measures a small negative force value, which becomes significant at the extremes of the force profile where the exerted force is higher. There has to be enough time between samples ($M \uparrow$) so that the particle can relax towards the center of the trap. Otherwise there will be a small uncertainty in the position of the particle, apart from thermal fluctuations, getting larger at the force profile extremes.

All the reported force profiles in this thesis correspond to the average over 100 different consecutive profiles, and errorbars to the standard deviation. Averaging the force profiles removes zero-mean Gaussian noise due to thermal agitations. To test the

validity of the force profile, passive detection signals are recorded after each scan in order to validate trap stiffness calibration from stepping (3.11(d)) with power spectrum analysis, 3.11(e), showing a maximum discrepance of 5%. This test ensures that the PSD is fully charged, hence the system measures the correct force value. Using higher $f_{TS}$ values would result in a more stable particle, but a scaled down force profile readout (see figure 2.17(c)).

### 3.3.2 Implications of measuring the complete force profile

Force profiles obtained with such method provide great information over the optical forces one can exert. Apart from the optical force, the $S_{SUM}$ channel of the PSD also offers information of the number of photons reaching the detector ($P = S_{SUM}/\psi$).

One of the main sources of error in beam momentum measurements is the amount of light captured. By definition, the use of an oil-immersion condenser lens with an NA (NA=1.4) higher than the medium's refractive index (typically $n_{water}$=1.33), ensures that all forward scattered light reaches the detector. As long as targets are within the working distance, even scattered rays traveling at $90^{\text{o}}$ inside the medium are captured by the measurement apparatus. Nevertheless, back-scattered light still escapes the detection system for single beam optical traps. The error arising from missing photons that propagate in the backward direction is known to be small in several cases of practical interest, such as microspheres of different sizes and materials or glass micro-cylinders [19], but has not been systematically analyzed. Although low backscattering is partly indicating that the error in momentum measurements will be small, one needs to specifically determine the amount of momentum information lost alongside backward-propagating photons.

Commonly backscattering is calculated as $P/P_0$, where $P_0$ is the power value readout for an empty trap. The amount of backscattered light scales proportionally with the relative refractive index. Assuming a perfect spherical object, the angular distribution is symmetric at the equilibrium position, for which lost photons do not carry momentum information. However, when an external force is applied, the angular distribution of such backscattered light depends on the new equilibrium position. Thus, depending on the particle position, the geometry or even beam aberrations, the measured force could either be overestimated or underestimated.

The measurement of both the optical force profile and the profile of lost light, allows us to know and estimate the committed error over the whole force range. Thanks to fast and precise particle scanning, we see that backscattering is not a constant value, but rather a curve.

Figure 3.12(a) and (b) show the optical force profile, as well as backscattering profiles, for polystyrene beads of different sizes. The curves are compared with finite difference time domain (FDTD) simulations [1], see figure Figure 3.12(c) and (d). The FDTD simulation can emulate the precision of lateral force measurements by splitting the

[1] We thank F. Català for adapting Lumerical simulation software to be able to split the forward-backward contributions and subsequently perform the FDTD simulations.

forward- and backward-scattered light momentum contribution. Once the field has been propagated, optical forces are obtained by integrating the Maxwell stress tensor (MST) over a surface surrounding the particle. In this way, any field with a positive axial component is propagated to infinity, contributing to the apparatus measurement. Whereas fields with negative axial components correspond to backscattered light, which can be collected to determine losses.

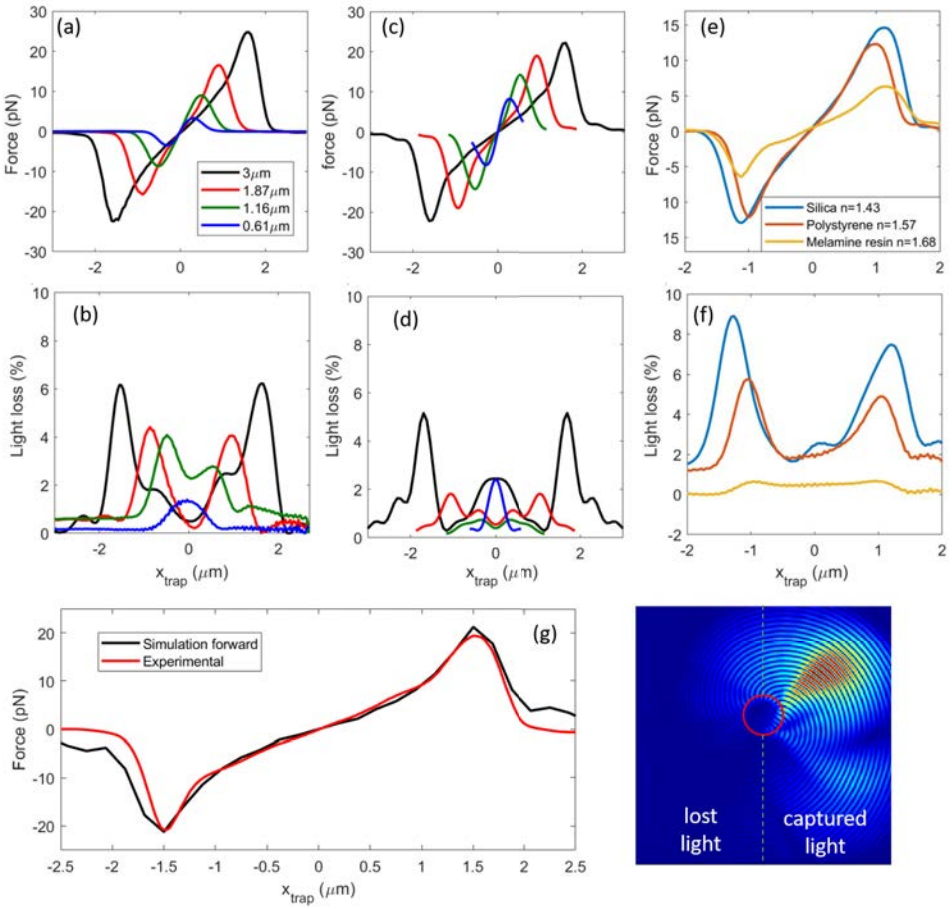


**Figure 3.12:** Experimental (a, b, e and f) and simulated (c and d) optical force profiles. (a, b, c, d) Polystytene beads of different sizes. (e and f) 2-$\mu m$ microspheres of different refractive index. (g) comparison between the experimental and simulated force profiles for a 3-$\mu m$ polystyrene microsphere. The bottom-right image corresponds to the simulated electric field distribution when the laser is at the particle's radius, showing total internal reflection at the particle's edge.

Interestingly, both simulated and experimental force profiles show the transition between the Rayleigh ($0.61\mu m$) and Mie regimes ($1.87\mu m$ and $3\mu m$). Note that small beads present a single centered light loss peak, while large particles show a double

peak around the particle radius. The interpretation of this is that, small particles feel a constant electric field that becomes higher at the center, hence producing higher scattering. Whereas for bigger particles the whole Gaussian distribution enters the particle, so that rays impacting at the edges of the sphere tend to be more internally-reflected. This can be seen in the field distribution of figure 3.12(g).

For small particles, the lost light has almost no momentum information, and thereby the error made when measuring is minimum and constant throughout the entire range. On the contrary, both FDTD simulations and experimental curves for large particles show that light losses become higher at the edge. The momentum distribution of lost photons near the particle edge has a greater contribution to the measured force values. Close to the border, lost photons are more valuable than in the center, contributing to an underestimation of the force value in this region. Figure 3.12(g) shows the comparison between the experimental and simulated force profile for a 3-$\mu m$ polystyrene microsphere trapped using an oil-immersion objective at 10mW. The simulated profile is calculated just using the forward scattered field, imitating the measuring device. Both force profiles are in good agreement, with the exception of the tails (attributed to simulation boundary effects).

Following this reasoning for Mie particles, targets of different refractive index have been also analyzed in figures 3.12(e) and (f). As expected, all three backscattering curves show a double peak around the particle radius. Apart from the expected increase on the optical force, the amount of lost light also increases. Thus, one can expect that measurements with high refractive index particles suffer from greater uncertainty, especially near the escape force.

For the whole range of situations analyzed, the accuracy of the methods falls within $\pm 5\%$, with the exception of high-refractive-index targets. All this establishes an inherent trade-off between, the amount of force one can apply and the measurement error, that in none of the analyzed cases exceeds $\pm 10\%$ (melamine resin in water).

Apart from providing useful information about the forces one can apply, and estimate the committed error, these force profiles allow to have a better understanding on how different experimental parameters affect the optical force. In figure 3.13 two problematic situations have been measured. On one side, figure 3.13(a) shows the force profile for the same 3-$\mu m$ polystyrene microsphere embedded in different buffers of increasing refractive index, from $n_{medium} = 1.29$ (fluorinated oil) to $n_{medium} = 1.47$ (glycerol). As expected, either the escape force and the stiffness increase with the relative refractive index between the object and the medium. A comment on this experiment is that, here the relative refractive index is increased by using a low-index buffer, not a high-index target. The silicon-oil experiment marks the limit for which the force measurement apparatus fulfills the conditions for correct light momentum detection, established in section 2.2.2. Even neglecting the backscattered light contribution, if $n_{medium} > NA_{condenser}$ part of the forward scattered light will not reach the detector. Steeper rays, those carrying most momentum information, will be lost, affecting the accuracy of force measurements in the same way as backscattered light.

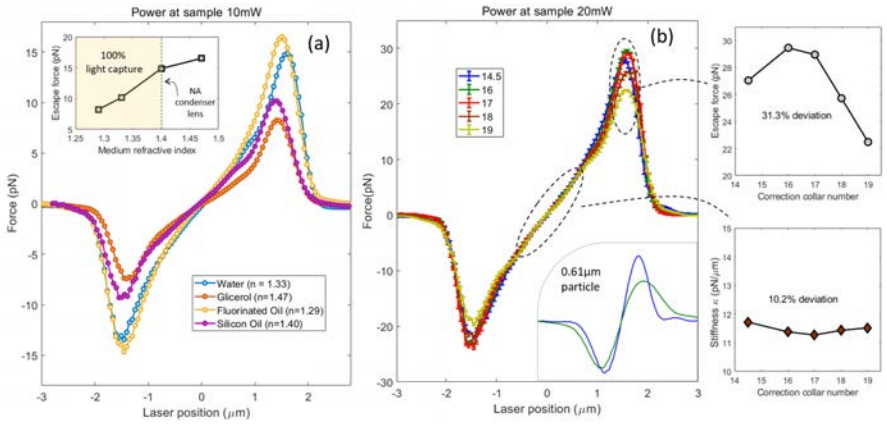


**Figure 3.13:** Experimental complete force profiles for a 3-$\mu m$ polystyrene bead. (a) immersed in buffers of increasing refractive index. (b) for different degrees of spherical aberration, introduced by misplacing the correction ring of the water immersion objective.

On the other side, figure 3.13(b) shows the force profiles for the same 3-$\mu m$ polystyrene microsphere embedded in water, for different degrees of beam aberrations. When trapping an organelle inside the cell cytoplasm, the refractive index mismatch between the cytoplasm and the microscope objective's immersion medium, introduces spherical aberration into the trapping beam, which gets worse as the trap moves deeper into the sample. In this experiment, we introduce, on purpose, an increasing degree of spherical aberration by rotating the correction collar of our water immersion objective. The correction collar is designed to compensate spherical aberration introduced by the coverglass thickness, using a wrong value introduces unwanted spherical aberration.

The results of this experiments surprisingly corroborate the results shown by S. R. Dutra and N. B. Viana, on the robustness of trap stiffness with respect to beam aberrations [60]. In our case, we see that 0.61-$\mu m$ particles are more vulnerable to spherical aberration. Force profiles for small particles show lower stiffness as soon as aberrations are introduced, up to the point where the particle escapes from the trap, due to excessively low gradient force and trap stiffness $Q$. On the other side, bigger particles (3-$\mu m$) were stability trapped over the whole range. By taking a look at the force profiles we observe almost no variance on trap stiffness, whereas the escape force decreases as the beam is being aberrated. Showing an optimum spot of maximum force at 16, corresponding to the nominal value for our 170-$\mu m$ thick coverslip. This result indicates that, for Mie particles, beam aberrations affect the optical force profile mostly at the edges. One possible explanation to this is that: on presence of spherical aberration the effective PSF's FWHM gets larger, for which the particle starts a transition to Rayleigh regime, reason why the double-stiffness profile is less prominent. This hypothesis could also explain why experimental and simulated optical force profiles differ, especially near the escape force, while stiffness values are very consistent. We attribute this to an aberration-free simulated beam, which inadequately describes the reality.

## 3.4 Studying the mechanical properties of active tubulin bundles

The micromanipulation and force measurement capabilities of our optical trapping platform are demonstrated in this section. Here, the optical setup is used to study an active gel system composed of different intracellular structures, such as cytoskeleton filaments (tubulin) and molecular motors (kinesins). The flexibility on trap manipulation offered by the AOD-based steering system, allows us to trap and deformate different active tubulin bundles, while simultaneously record the total force signal by means of the beam momentum method. This section details a set of experiments developed in collaboration with the Soft Condensed and Self Assembled Materials (SOCSAM) group of the Chemistry Faculty of the University of Barcelona.

The optical micromanipulation system is used to obtain meaningful information at two different stages. On the one hand, while external energy is being injected into the system (in the form of adenosine triphosphate or ATP), the system is out of equilibrium, constantly moving and evolving. Here, optical tweezers are used to measure the order of magnitude of the local forces that dominate the dynamic evolution of the system at a larger scale. This forces are the result of cooperation of many kinesins that cause deformation and buckling of tubulin filaments. On the other hand, once ATP is depleted, and the system is under control (not constantly moving), optical tweezers are used to manipulate and deformate these structures. In this case, recorded force signals can be analyzed and interpreted to extract interesting mechanical properties of tubulin and kinesin assemblies. Interestingly, even though this system seems very chaotic at nano and micrometer level (thousands of molecular motors exerting forces), a knowledge of the mechanical properties at these scales can help to describe the behavior and future evolution of the system at a much larger scale [61, 62, 63].

The particular system is an active gel preparation of microtubules, where 1-2$\mu m$ tubulin filaments (bovine brain tubulin) are mixed with a depleting agent (polyethyleneglycol or PEG) that causes the formation of microtubule aggregations or bundles. Separately, kinesin-1 motor proteins are incubated in the presence of streptavidin which leads to motor protein clusters containing 2 kinesins each (on average). The tubulin bundles are then mixed with the kinesin-kinesin complexes, which act as cross-linkers between different bundles, thereby creating a consistent gel. When ATP is aded to the system, kinesins start to move along microtubules with opposite polarity causing microtubules to slide and bend, due to local shear forces caused by the molecular motor action (figure 3.14). When confining the movement of bundles in two dimensions, the chaotic behavior of this system can be controlled and predicted through changes in preparation or through external stimuli [61, 62, 63].

However, even though the bi-dimensional active gel is the most interesting system for the group, the collective forces that cause this bundles to flow are orders of magnitude higher than typical optical forces. Moreover, once ATP is depleted, the viscoelastic parameters of such dense bundle network are outside the measurement range, the system is too rigid. Several active-passive calibration experiments were made by in-

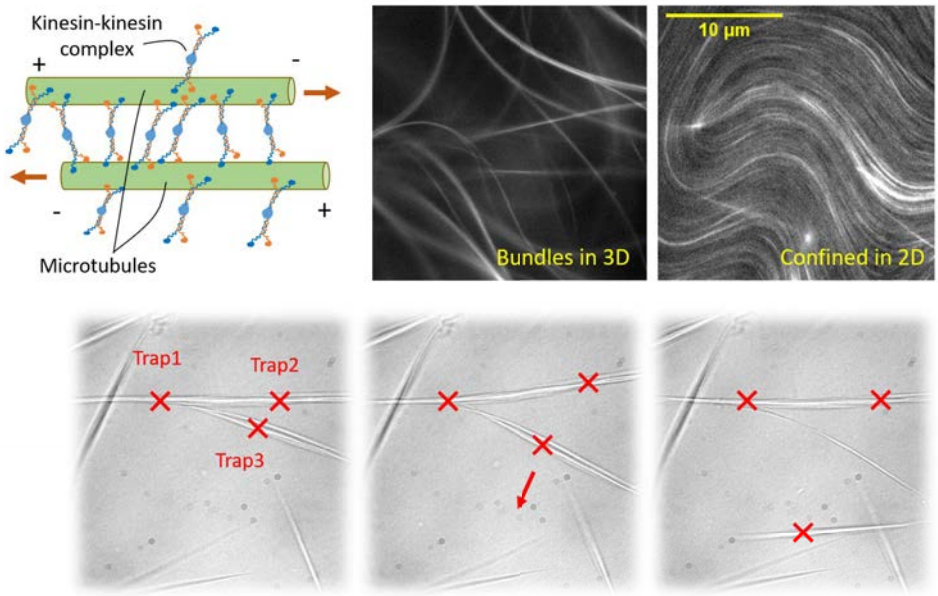


**Figure 3.14:** Description of the active gel constitution and fluorescence images of the tubulin bundles (tubulin is labeled with mCherry). On the bottom we show the manipulation of a tubulin bundle with three optical tweezers, the bundle is pulled down until it breaks into several thinner bundles.

jecting 3-$\mu m$ beads inside the 2D active gel. All of them failed because the material could not be deformed in the direction perpendicular to the bundles, while in the parallel direction, measurements reported the viscosity of water and almost null elastic components. Because of this, the experiments and results shown in this section correspond to 3D bundle aggregates immersed in water, as can be seen in figure 3.14.

Instead of confining them in 2D, bundles are let to move in all three dimensions. In such low concentration, individual tubulin bundles are easy to identify, characterize and manipulate. Figure 3.14 shows the dynamic manipulation of a bundle aggregate with three different time-shared optical traps. By pulling down trap number 3 we are able to deform, "unbundle" and break the aggregate into several thinner bundles. Thus demonstrating that is possible to exert forces into such tubulin bundles.

Figure 3.15(a) shows the complete optical force profile of three randomly selected bundles and its corresponding backscattering curves, all of them obtained using the same method described in section 3.3. The optical force profiles show a very low trapping efficiency, reporting a maximum force of ∼65pN at 500mW of trapping power. Note that the same force value can be achieved on a 3-$\mu m$ polystyrene bead at just 43mW, corresponding to an 11-fold increase on trapping efficiency. Even though several studies estimate the refractive index of tubulin to be 2.3-2.9 [64], our bundles

are not entirely composed of tubulin. They are aggregates of many thin filaments with kinesins in between and PEG gluing everything together. This results in an effective refractive index much lower than pure tubulin. Another hypothesis is that trapping laser light is highly scattered by the individual filaments forming the bundle, in such a way that only few photons are exerting gradient forces, whereas the most part are just forward scattered and not contributing to lateral force. Comment that all reported force profiles correspond to the perpendicular direction of the bundle, in the parallel direction the optical force is null, due to the refractive index is almost constant. Moving the optical trap alongside the bundle is not causing any force, if the optical trap is static, the bundle can slide.

Optical force profiles are also used to estimate the bundle thickness, calculated as the distance between the positive and negative force peaks. This method supposes a better estimation than camera based, due to most bundles are below the diffraction limit. Regarding the precision of force measurements, the lost-light curves from figure 3.15(b) show a very low backscattering. Indicating that, even though the optical forces are low, they can be directly measured without the need of spherical probes or calibrating the trap.

To have a better control of the bundles, force measurements have been performed in two stages: while the system is being active, and when ATP is depleted, usually after 6 hours minimum. The activity time will depend on both the ATP and kinesin concentrations. During the first hour, the system behaves in a turbulent manner, observing bundles bending and buckling very fast, measuring maximum speeds up to $50\mu m/\text{s}$, situation where optical forces are almost negligible. The combination of very low trapping efficiency and the high forces originated from many kinesins acting in a cooperating manner, force the use of very high laser powers, which could increase the local temperature by 10K. In this way, depending on the bundle thickness, remaining ATP concentration and laser power, we observed two situations: the active bundle escapes from the optical trap, or it remains at the trap position all the time.

These two situations are shown in experiments of figures 3.15(d) and (e) respectively, where the optical trap was always placed at the center of the field of view and we waited until a bundle crosses the optical trap. In the first situation, the inertia of the bundles and the optical force preventing its advance, cause the bundles to bend in the same way as a fishing rod. Which accumulates elastic potential energy until it exceeds the escape force of the trap. Then the bundle returns to its initial shape and continues to advance. Note that different escape forces are measured because each bundle is different, this can be seen in the second experiment of figure 3.15(d), where the first measured escape force is lower due to a thinner bundle, which is confirmed from the video images.

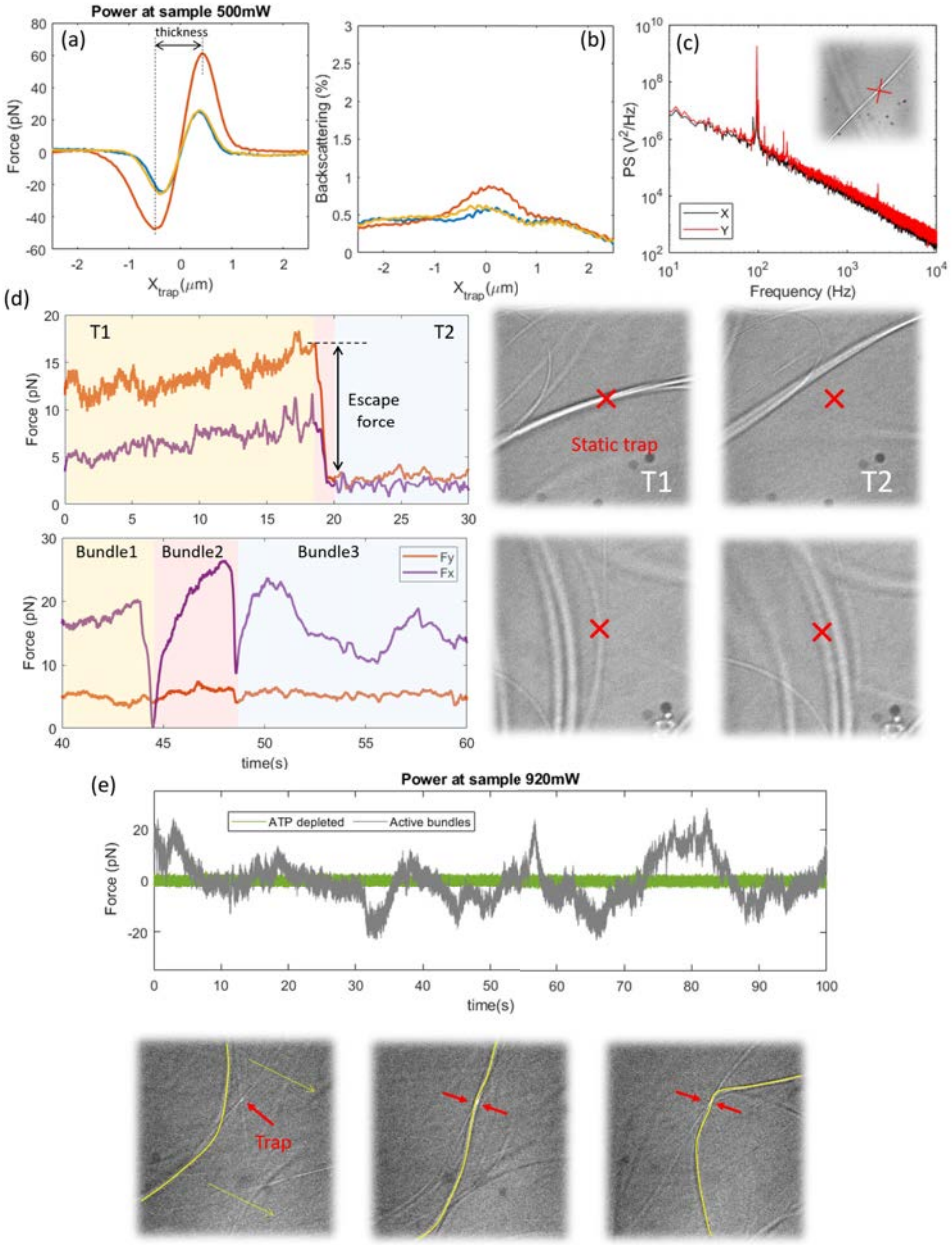


**Figure 3.15:** Optical force profiles (a) and backscattering curves (b) of three different trapped tubulin bundles (c) Passive power spectrum of a randomly selected bundle, the absence of a plateau at low frequencies shows the elastic properties of tubulin bundles. (d) Bundle trapping experiment where the bundles escape from the optical trap, observed in the force traces as a drastic force jump. (e) The same experiment as in (d), but doubling the laser power and thereby preventing bundles to escape from the trap. Forcing the bundles to bend or break.

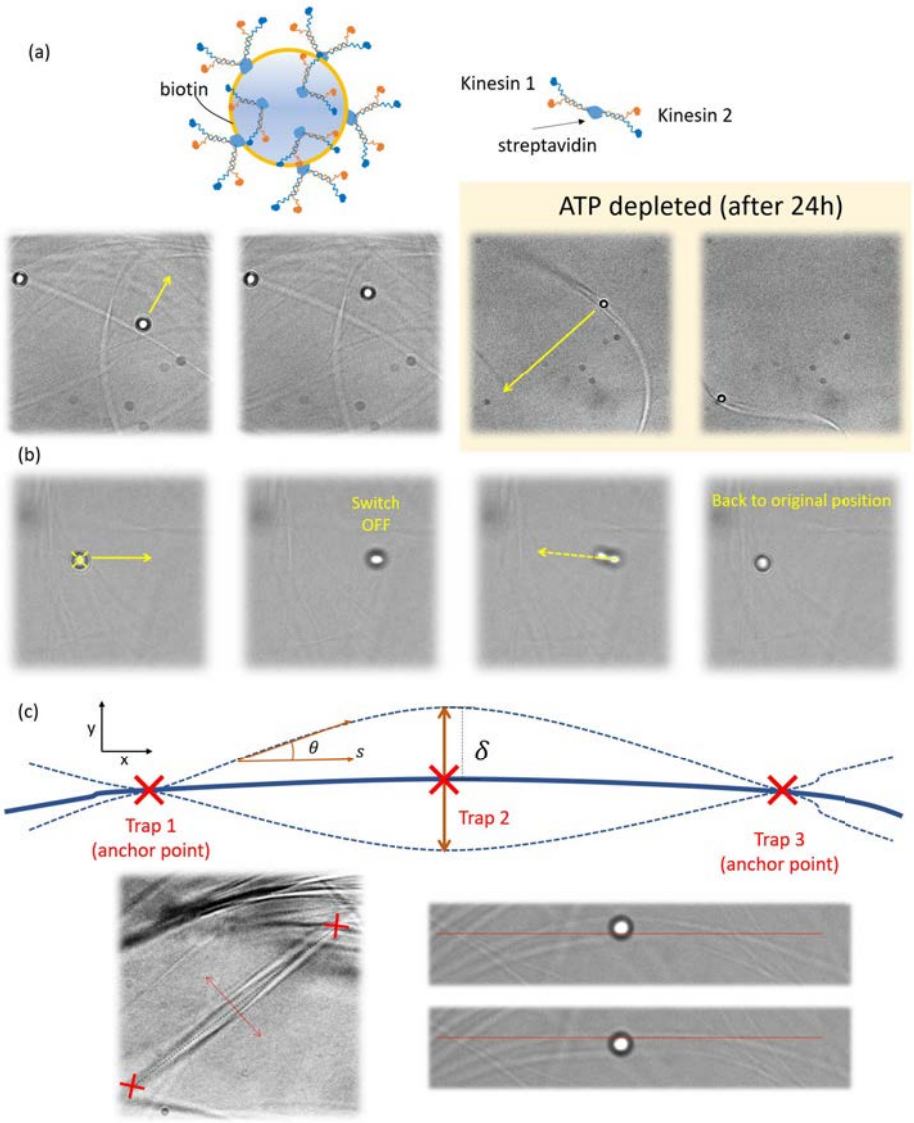


**Figure 3.16:** (a) Injection of kinesin-covered 3-$\mu m$ polystyrene microspheres. While bundles are active, all kinesins are randomly attaching and detaching from the microtubules, resulting in no gluing force. However, once ATP is depleted, all kinesins attach to the bundle. (b) Demonstration of the elastic behavior of the bundle network. (c) Scheme and experimental examples of the bundle bending experiment using three time-shared optical traps.

In the experiment from figure 3.15(e) the trapping power was set to the maximum value around 950mW, for this particular scenario different neutral density filters were used to avoid PSD saturation in the force measurement system (which had to be re-calibrated for the new sensitivity). In this case, the trapped bundle could not escape from the optical. The bundle bends until it either breaks into two new bundles, or until the direction of movement is parallel to the bundle, and it slides. During the time bundles are trapped, the measured force curves show a high activity which we attribute to all kinesins acting on the bundle in a cooperative way.

In the second stage, once all ATP is depleted, all biological activity ceases completely and bundles can be manipulated more easily. The goal of the experiments is to extract the mechanical properties of such tubulin bundles, especially the elastic propperties. By looking at the passive power spectrum of a trapped non-active bundle, we note the same viscoelastic behavior as when trapping a protein body inside the cell cytoplasm (figure 3.4). In this particular case, the elastic component is directly attributed to the bundle structure, whereas the viscous part comes from the hydrodynamic drag forces of the buffer (water).

In order to extert high optical forces, different 3-$\mu m$ polystyrene microspheres are added into the system. The polystyrene mirospheres have been biotin covered and immersed in a solution with kinesin complexes, in this way all the microsphere surface is covered with kinesins. When ATP is depleted all kinesins will attach to the bundles and the microspheres can be used as handles to deform the bundle structure, as seen in figure 3.16(a). The elastic behavior of tubulin bundles is demonstrated in figure 3.16(b), when moving the microsphere from its original position we are deforming all the surrounding bundle network, instead of remaining on the new position, the particle jumps back to the original equilibrium position when the optical trap is switched off.

Assuming that tubulin bundles behave as pure solid materials, the bundle's Youngs modulus (E) and flexural rigidity (EI) can be extracted by measuring the force required to deform the bundle structure up to certain extent, i. e. by measuring the resistance offered by the bundles while undergoing bending. The proposed experiment is schemed in figure 3.16(c), in which the bundle is grabbed and aligned in a straight line using three equally distributed time-shared optical traps. Traps 1 and 3 act as anchoring points, preventing the bundle to be translated vertically, while trap number 2 at the center is responsible for the bundle deformation by applying different load forces. Considering the bundle deformation to be described as the linear elastic bending of a cylindrical rod, the flexural rigidity (EI) of the bundle can be calculated by solving the following equation: $EI\frac{d^2\theta(s)}{ds^2} - \kappa_s\theta(s) = q$. Where $\theta(s)$ describes the shape of the bent tubulin bundle, with the coordinate $s$ along the bent bundle, $q$ being the applied load force and $\kappa_s$ the bundle's shear resistance which is neglected in our case to simplify calculations.

Since optical forces of all three traps ($F_1$, $F_2$ and $F_3$) are perfectly known by means of the direct force measurement apparatus, the flexural rigidity of the system can be directly calculated by assuming that $q = F_2$ and imposing the boundary conditions $\theta(L/2) = 0$, $\theta'(0) = 0$ and $\theta'(L) = 0$, being L the distance between the two anchoring positions. With all this:

$$\delta = \frac{FL^3}{48EI} \tag{3.12}$$

$$E = \frac{FL^3}{\pi a^4 12\delta} \tag{3.13}$$

Where $\delta$ is the vertical position of the center of the bundle, which in our case corresponds to $x_L - \beta Sx$, being $x_L$ the position of trap number 2 and $\beta Sx$ the relative position of the bundle with respect the optical trap and $\beta$ calculated from a previous force profile. The Young's modulus can be decoupled from the flexural rigidity by means of the momentum of inertia, which is $I = \frac{\pi a^4}{4}$ for a rigid and homogeneous rod.

In figure 3.16(c) we show two examples of this bending experiments. At first, the idea was to use the previously injected microspheres as handles to exert high forces. However, due to all the biological activity previous to the experiment, is was impossible to find a single bundle with three attached microspheres. All this limited most experiments to trap the bundles themselves, for which in the vast majority of attempts it was impossible to apply enough force to perceive an appreciable deformation. Moreover, even though the experiment is designed with three different traps, in most cases traps 1 and 3 were switched off to increase the power, and thereby maximum force, of the central trap. Then, the measured bundle was selected to be already anchored to other high-density bundle aggregates, preventing the bundle from moving.

The results for three different bending experiments are shown in figure 3.17. In all three bundles the applied load force seems proportional with the bundle deformation $\delta$, with the exception of bundle 3 showing the end of the elastic zone at forces higher than 70pN, attributed to excessive bundle elongation or sliding. The reported Young's modulus values from figure 3.17(c) fall within the GPa range, which surprisingly coincides with previous studies stating that if tubulin were homogeneous and isotropic its Youngs modulus would be $\sim$1.2Gpa [65]. Regarding flexural rigidity of the bundles, there is a huge variety since this magnitude depends on the bundle cross section. Thus, in order to be able to compare the EI of our tubulin bundles with corresponding studies for individual microtubules, the obtained values have to be scaled by $(d_{mt}/d_{bundle})^4$. Where $d_{mt}$ is the diameter of a single microtubule, around 20-25nm, and $d_{bundle}$ is the thickness of our measured bundles, which for all three cases were between 0.5-0.7$\mu m$. By doing this, our measured flexural rigidity values are between $4.4 \times 10^{-26}$ and $1.25 \times 10^{-24} Nm^2$, which are somehow consistent with single microtubule bending studies [66, 67, 68].

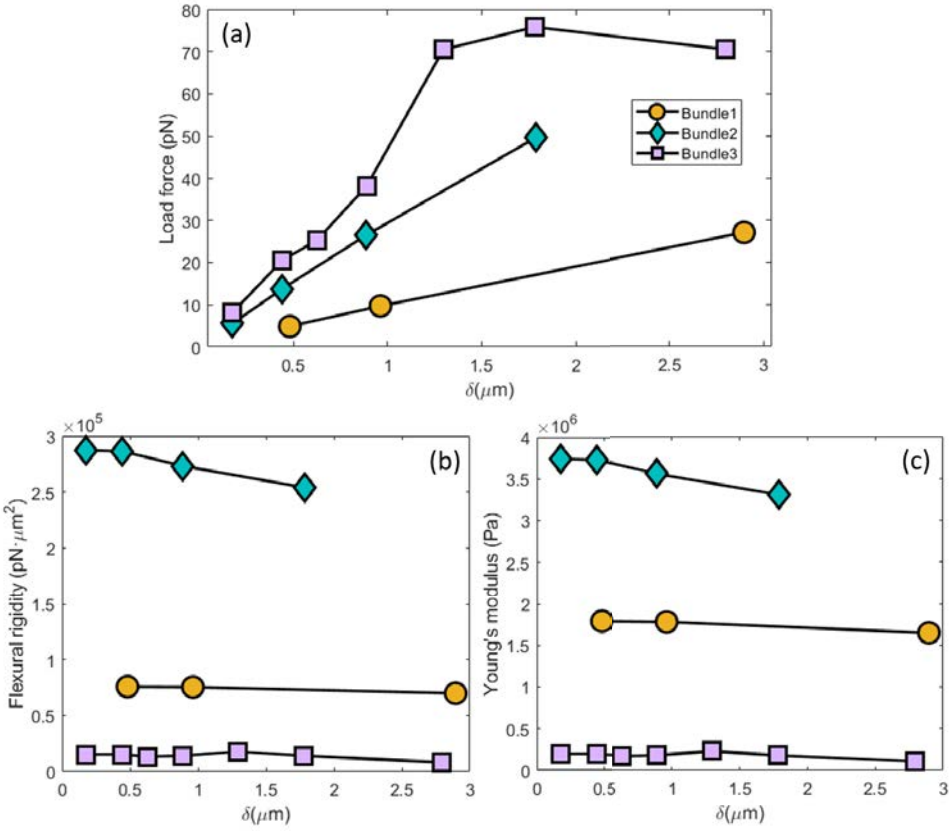


**Figure 3.17:** Results from bundle bending experiments for three different bundles.

# Chapter 4

# Enhanced acousto-optic modulation: acousto-holographic optical tweezers

In the previous two chapters, the two orthogonally arranged acousto-optic devices have been used to fast steer the optical trap allover the field of view of the microscope. As its own name indicates, AODs are designed and engineered as pure beam deflectors. However, by doing some modifications to the driving radio-frequency electronics, the same pair of AODs can be used as a full complex wavefront shaping device capable of generating arbitrary intensity patterns. Providing the system with great flexibility, being able to project static and stable intensity patterns when temporal resolution is a concern.

Even though time-sharing optical traps allow independent control over multiple targets, some problems may arise when lots of objects are involved. Traps are not permanent, and while the laser is off (visiting the other positions), the particle diffuses away from the trap location. Thus affecting the accuracy to which the particle can be positioned, or its force measured. Fluctuations in the position or trap stiffness can be significant, especially in single-molecule experiments [69]. Even though hundreds of time-multiplexed optical traps have been generated with rapid AODs [70], there is considerable limitation on the number of traps when measuring with laser-based detection methods and accuracy is a concern [47]. Apart from spatial resolution, temporal resolution is also compromised. Since the laser is visiting one trap each time, the effective sampling frequency of each of the N-trapped objects is reduced by a factor of N, which can lead to a loss of information at high frequencies due to aliasing effects [40].

To overcome this issue, since many experiments do not require simultaneous measurements in all positions, we propose an alternative technique where we combine the benefits of both holographic and time-shared optical traps, without any further

modifications to the optical system. In this chapter, we successfully demonstrate the creation of multiple and permanent holographic intensity patterns by means of AODs driven by specially encoded radio frequency signals. The generation of complex acoustic signals allows us to treat such devices as super-fast spatial light modulators. Using this technique, it is possible to generate several static optical trap arrays and switch them at kilohertz (kHz) rates, allowing independent control of each trap group. Everything is done using the same pair of AODs used in the previous chapters, with the exception of the driving electronics. Finally, we discuss the compatibility of this method with precise force and position measurements, and the improvement in their frequency bandwidth compared to time-sharing optical tweezers, especially when many objects are trapped.

## 4.1 Acousto-optic deflectors as full complex spatial light modulators

This section explains the differences between the time-sharing regime, explained in chapters 2 and 3, and the holographic regime. From this moment on, the time-sharing regime is put aside and the thesis focuses on the development of holography with AODs. Especially in its experimental implementation, and its use for optical tweezers applications at first. And later on, in the following chapters, on the development of a flexible and programmable confocal microscopy unit.

One way to understand the concept of holography with AODs, is to analyze how the acousto-optic cell behaves when increasing the time-sharing frequency $f_{TS}$. Assuming an infinitely large crystal in the direction of propagation of the acoustic wave, one can assign a specific signal lenght to each of the individual frequencies that are being displayed, one after the other ($f_1$,$f_2$,$f_3$,...). For a fixed $f_{TS}$, the piezoelectric transducer oscillates at each frequency $f_i$ for an specific time duration equivalent to $1/f_{TS}$. This means that from $t = 0$ to $t = 1/f_{TS}$ the acoustic wavefront has propagated $d = v_A/f_{TS}$, which corresponds to the physical signal size, in distance units. As an example, for $TeO_2$ $v_A = 650m/s$, a time-sharing of 10kHz means that each pure sinusoidal signal extends for 6.5cm. From the point of view of the incident light, given that the AOD window and therefore the beam size, is around $D = 5mm$, the laser beam is only experiencing the effect of a single frequency at each time. However, it is easy to see that when $f_{TS} \uparrow$ the signal size diminishes, until the point where several frequencies fall within the AOD window.

This is what we call the holographic regime, if $f_{TS} >> 1/\tau = v_A/D$, the laser beam is no longer switching between the different positions, but all the light intensity is distributed between the different locations. The frequencies are being sent sequentially, so fast that multiple sinusoids are displayed within the illuminated area of the AOD, in such a way that each of them creates one optical trap (pure tones of different frequency). The implementation of this holographic approach does not require any additional electronics or optical setup modification, by simply increasing $f_{TS}$ the optical traps transition from blinking to be almost static over time. However, the

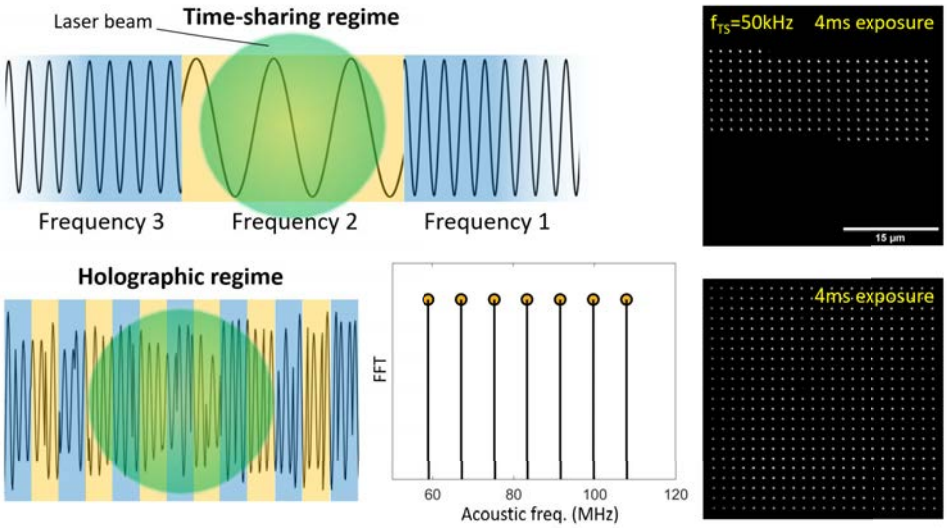


**Figure 4.1:** Difference between the time-sharing and holographic regime. The images correspond to a 4ms camera exposure of a 529 (23x23) traps arranged in a square grid, and demonstrate higher trap stability that on the time-sharing case.

running wave corresponding to each point runs through the laser beam, and different pure sines see different intensities as they cross the Gaussian intensity distribution.

Note that under this approach, the frequency information, i. e. the spatial intensity distribution of the desired pattern, is spatially distributed throughout the AOD window, causing that the individual spot intensities slightly fluctuate in time. So, for the traps to be totally static and stable, it is necessary that the frequency content of the driving signal is distributed homogeneously. Figure 4.1 shows the difference between the time-sharing and holographic regimes. As can be seen in the holographic case, the intensity distribution information is encoded directly in the frequency domain rather than in the real space. In that particular example the desired intensity pattern is a 23x23 square grid of points, whose frequency content corresponds to 23 equally distributed frequencies for both the AODx and AODy driving signals.

Instead of introducing the pure sinusoidal signal that produces a deflection, we compute and encode the amplitude and phase information of a desired diffractive optical element (DOE) within a more complex RF signal. In such a way that, after crossing the AOD cell, light would diffract in the same manner just as a physical diffraction pattern would [71, 72, 73]. We call this approach acousto-optic holography (AOH).

Considered carefully, this is not too different from the way certain SLMs modulate the amplitude or phase of the laser wavefront. That is also achieved by inducing changes in the refractive index of the material filling the pixels of the device. AOH allows the generation of permanent holographic traps, but also changes of the desired

configuration at super-fast rates, much higher than the typical refreshing times of SLMs, limited to hundreds of Hz at the most. Moreover, since the amplitude and phase information is encoded into the driving RF signal, which in turn causes an equivalent modulation of the refractive index, AOH allows to freely and independently modulate both the amplitude and phase of the incident laser wavefront. Which current SLMs do not, because they are subject to characteristic amplitude-phase curves with almost null amplitude modulation depth.

Acousto-optic holograms that spatially modulate the amplitude and phase of a passing beam of light can be synthesized by driving each AOD cell with a modulated sinusoidal signal of the form:

$$s(t) = A(t)\sin(2\pi f_d t + \phi(t)) \tag{4.1}$$

With time-varying amplitude $A(t)$ and phase modulation $\phi(t)$. The frequency $f_d$ is the carrying driving frequency of the generated RF signal, which normally is chosen to be equal to the central frequency $f_c$, around which the diffraction efficiency is optimal. Once the piezoelectric transducer actuates, the spatial index perturbation (diffraction grating) along the acoustic path $n(x,t)$ takes a similar form to that of the driving signal, albeit with a material-specific factor $\gamma$ [71]:

$$n(x,t) = \gamma s(t + \frac{x}{v_A}) = \gamma A(t + \frac{x}{v_A})\sin\left[2\pi f_d(t + \frac{x}{v_A}) + \phi(t + \frac{x}{v_A})\right] \tag{4.2}$$

Note that the propagative acoustic wave causes the refractive index modulation to be time-dependent, since the whole distribution moves at a constant speed $v_A$ in the acoustic wave direction, as indicated by the propagative term $t + \frac{x}{v_A}$. Then, assuming a collimated beam crossing a single AOD cell of thickness $L$, light experiences a spatial phase modulation due to the optical path difference induced by $n(x,t)$. When the incoming beam electric field $U_0(x,t)$ incides perpendicular to the AOD entrance surface, the resulted modulated beam $U(x,t)$ can be written as:

$$U(x,t) = U_0(x,t)e^{i\frac{2\pi L}{\lambda_0}n(x,t)} \tag{4.3}$$

Since the incident beam is entering fulfilling the Bragg condition, almost all of the diffracted energy is concentrated in the first diffraction order. This allows us to simplify equation 4.3. The exponential term can be easily decomposed into the different diffraction orders with the Jacobi-Anger identity $\big(\exp(i\alpha\sin\beta) = \sum_{n=-\infty}^{\infty} J_n(\alpha)\exp(in\beta)\big)$, with $\alpha = \frac{2\pi L\gamma}{\lambda_0}A(t + \frac{x}{v_A})$ and $\beta = \sin\left[2\pi f_d(t + \frac{x}{v_A}) + \phi(t + \frac{x}{v_A})\right]$. Assuming that the phase modulation is rather small ($\alpha \sim 0 \rightarrow exp(i\alpha\sin\beta) = \frac{\alpha}{2}\exp(i\beta)$) and neglecting all orders but the first diffracted order (Bragg condition), the modulated field distribution after crossing the AOD cell can be approximated by:

$$U(x,t) \approx U_0(x,t)\frac{\pi L\gamma}{\lambda_0}A(t + \frac{x}{v_A})e^{i2\pi f_d(t+\frac{x}{v_A}))}e^{i\phi(t+\frac{x}{v_A})} \tag{4.4}$$

That is to say, the amplitude and phase modulation of the electronic RF driving signal is directly translated into an identical amplitude and phase modulation of the first diffracted order wavefront. By looking at the optical design of figure 2.18, the back-focal-plane stationary beam steering system directly images the AODs pivot plane into the microscope objective's BFP, through telesope T3. Under this configuration, the relation between the displayed acousto-optic hologram and the electric field distribution at the sample plane (microscope objective focal plane) is an Optical Fourier Transform (OFT) performed by the objective lens. The intensity distribution corresponds to the modulus squared of the resulting electric field.

Thus, for a given intensity pattern, the corresponding amplitude and phase distribution with which to encode the discrete acousto-optic hologram $H(x, y)$ is simply given by the Inverse Fourier Transform (IFT) of $\sqrt{I(x, y)}$, being $I(x, y)$ the desired intensity distribution at the sample plane. Note that for propper scaling, the intensity distribution has to be computed taking into account the characteristic $\lambda_0 f_{obj}$ scale factor of the OFT and magnification due to T3 telescope ($M_3 = \frac{f_6}{f_5}$). In such a way that $I(x, y) = \left|\tilde{H}\left(\frac{M_3}{\lambda_0 f_{obj}}x, \frac{M_3}{\lambda_0 f_{obj}}y\right)\right|^2$ where $\tilde{H}(u, v)$ is the Fourier Transform of the acousto-optic hologram $H(x, y)$.

### 4.1.1 Acousto-optic holography constrains

Even though AOH seems a powerful and useful technique for very fast generation of patterns, the method suffers from two inherent drawbacks that do not arise with traditional SLMs. The first limitation of this acousto-optic holography is that each AOD only modulates the laser wavefront in the corresponding axis. In the same way as in the 2D laser scanner, a bi-dimensional acousto-optic spatial light modulator (AOSLM) is composed of two individual one-dimensional AODs. In this way, through the telescope T2 of figure 2.18 both acousto-optic holograms are optically multiplied. The hologram displayed at the BFP of the objective lens corresponds to $H(x, y) = Hx(y)Hy(x)$, being $Hy(y)$ and $Hx(x)$ the acousto-optic holograms displayed at AODy and AODx respectively. This limits the number of degrees of freedom that the AOSLM can encode to 2N different values, instead of $N^2$ for regular LCOS-SLMs, being N the number of pixels. Taking as reference any digital hologram displayed at the BFP, AODx can only modulate the amplitude and phase of the rows, whereas changes on $Hx(y)$ (AODy) only affect $H(x, y)$ columns. It is impossible to modify the amplitude or phase of a single point without modifying the entire row and column.

This restriction limits the intensity configurations to those that are mathematically separable in x and y. Therefore, the desired intensity distribution at the sample plane, needs to be expressed in terms of two functions $F(x)$ and $G(y)$ such that $I(x, y) = F(x)G(y)$. In practical terms, this means that the precalculated digital image must be product of two matrices $F(x_i)$ and $G(y_i)$ of dimensions Nx1 and 1xN each, being N the number of pixels of the AOSLM, as shown in figure 4.3(a). A barcode is separable, whereas a QR code is not. If the desired distribution requires a more general light field $I(x, y)$, it should be decomposed as an incoherent superposition of

products of separable functions of the form:

$$I(x,y) = \sum_{i=1}^{N} F_i(x) G_i(y) \tag{4.5}$$

which would then be displayed and integrated over time at the cost of reconstruction speed. Any function can be synthesized by means of separable functions through singular value decomposition, but imposing only non-negative values to account for the incoherent superposition (Non-Negative Single Value Decomposition (NNSVD)) [74]. Once $F_i(x)$ and $G_i(y)$ are obtained, one can make a compromise between reconstruction fidelity and speed, deciding whether to use all the terms or choose those with more information and go faster. Regarding the number of terms, for an arbitrary image of NxN pixels, the NNSVD algorithm provides N different separable patterns. However, for the applications discussed in this thesis, optical tweezers or confocal microscopy, the desired intensity distributions are typically sparse, consisting of discrete focused spots arranged in different configurations, such as forming a 2D array. In practice, the vast majority of patterns are already x-y separable, and if not, the few required terms are *a priori* known and directly synthesized.

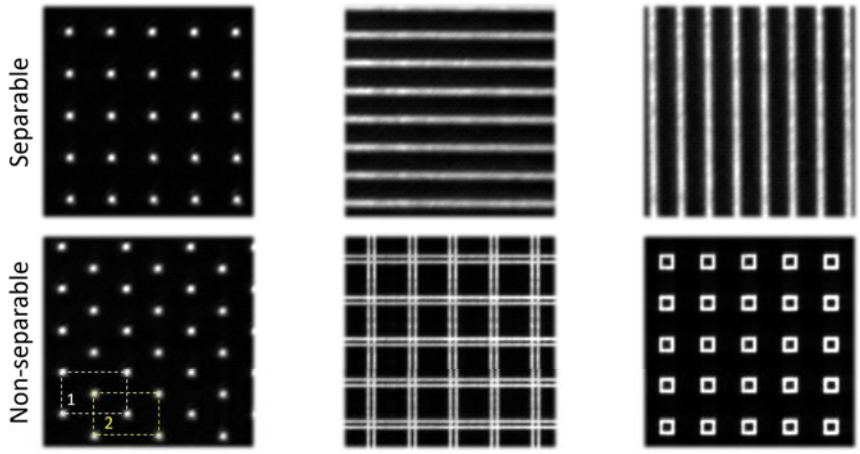


**Figure 4.2:** Experimental examples of x-y separable and non-separable patterns. For the non-separable case, the number of terms is always 2. All images are obtained by placing a mirror at the focal plane of the microscope objective.

Figure 4.2 shows different examples of separable and non-separable patterns used through this thesis. Especially for optical tweezers applications, only the point arrays are used and the most common case is the rectangular grid. Note that the honeycomb-like point array can be understood as time-sharing between two rectangular grids, where the corners of the first are centered into the second's rectangle.

The second important limitation of AOH is that, in principle, AOH do not permit three-dimensional manipulation, as the information is encoded in a traveling sound

wave. AODs only produce a stable intensity pattern at a Fourier conjugate, since the motion of the hologram appears as a pure phase term due to the shifting property of Fourier transforms:

$$I(x,y,t) = \left| FT_{\lambda_0 f_{obj}} \left[ H(x \pm v_A t, y \pm v_A t) \right] \right|^2 \tag{4.6}$$

$$\left| e^{\pm i \frac{2\pi v_A}{\lambda_0 f_{obj}} xt} e^{\pm i \frac{2\pi v_A}{\lambda_0 f_{obj}} yt} \tilde{H}\left( \frac{x}{\lambda_0 f_{obj}}, \frac{y}{\lambda_0 f_{obj}} \right) \right|^2 = I(x,y,0) \tag{4.7}$$

Where $v_A t$ is the distance propagated by both acoustic waves after a time $t$. As can be seen in equations 4.6 and 4.7, the sound wave propagation appears as a time-varying linear phase term that, does not affect the final intensity distribution. Note that, since the two AODs are indentical, both acousto-optic holograms propagate at the same acoustic speed $v_A$, resulting in an effective linear phase along the $45^{\text{o}}$ degree direction. Even though the intensity distribution remains static at the focal plane, where the laser wavefront is flat, the out-of-focus intensity distribution is constantly moving at $45^{\text{o}}$. Outside of the focal plane, the relation between the BFP and the sample plane is no longer a $\lambda_0 f_{obj}$ scaled Fourier Transform. An spherical wavefront appears ($\exp\left\{ i\pi \frac{x^2+y^2}{\lambda_0 f_{obj}} \left( 1 - \frac{z}{f_{obj}} \right) \right\}$), causing a constantly moving intensity distribution when the acosutic wave propagates.

There are different ways to "freeze" or "stop" the effect of the propagative acoustic wave, but all of them represent a more expensive and complex experimental system. On the one hand, by using femtosecond laser pulses it is possible to minimize the effect, during the laser pulse duration the acoustic wave is considered static. However, the incorporation of pulsed lasers involve the addition extra AOMs to compensate for the spatial dispersion of the pulse in the AODs (due to the high refractive index and thickness of the AO medium) [75, 76]. The other solution is to double the number of AODs, two AODx and two AODy, in such a way that acoustic wave propagation is the same but with opposed direction. This way, the linear phase introduced by each pair is of opposed sign, canceling the movement of the pattern in out-of-focus planes.

### 4.1.2 Generation of complex acoustic RF signals

To dynamically control the desired intensity patterns we have developed a set of Matlab and Labview routines that synthesize and display the acousto-optic holograms at each of the AODs. The algorithm is described in figure 4.3(a), and basically codifies the amplitude and phase information of any intensity pattern into two complex sinusoidal RF signals, that once displayed into the AOD crystal, creates the corresponding refractive index distribution $n(x,y)$ for which the first diffracted order generates the desired pattern in the sample plane.

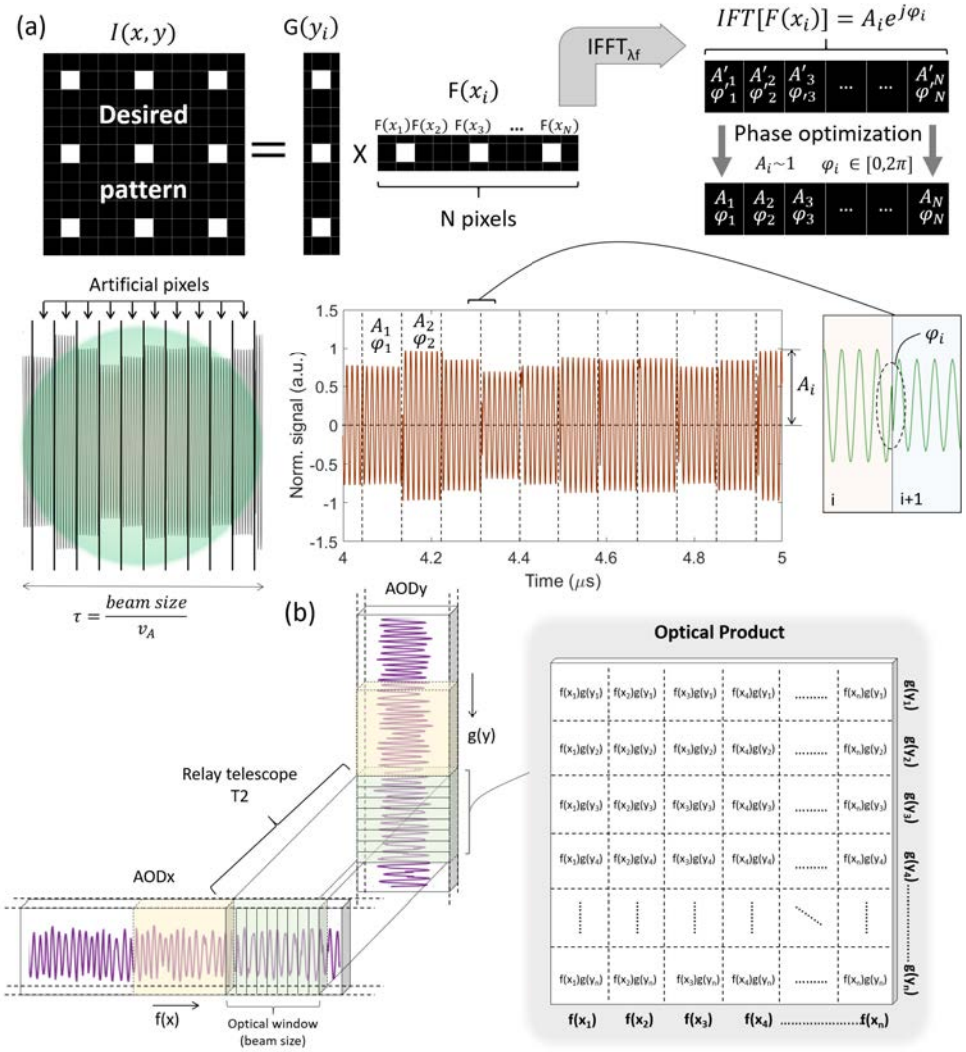


**Figure 4.3:** (a) Scheme of the algorithm we used to calculate the complex RF signals. (b) Schematic drawing of the optical product between both acousto-optic holograms. Note that for propper multiplication the delay between the AODx and AODy acoustic waves has to be precisely controlled.

The intensity pattern is codified first on a digital image $I(x_i, y_i)$ of NxN pixels, and decomposed into two one-dimensional (1D) digital vectors of N elements each, $F(xi)$ and $G(y_i)$. After an Inverse Fourier Transform to each of the intensity vectors, we obtain the corresponding amplitude and phase values ($A_i$ and $\phi_i$) for each acousto-optic hologram.

As opposed to an SLM, AODs are considered analog devices, in the sense that the AO crystal is not quantized or divided into different chunks or pixels, the created acoustic wave is continuous. So, in order to work with discrete images and its corresponding discrete amplitude and phase values, the whole beam size is divided into N artificially created segments or pixels. Being N only limited by the sampling rate of the waveform generator, much larger than the number of resolvable spots that the AODs can produce, which for our set of AODs is $\tau\Delta f = 231$points ($7.7\mu s$ and 30MHz).

Once the amplitude and phase values of the hologram are known, the signal corresponding to the $i^{th}$ pixel consists of a pure sinusoid of the same RF driving frequency $f_d$, with amplitude $A_i$ and phase $\phi_i$. Finally sinusoids from all pixels are concatenated creating the final complex RF signal, $Sx(t)$ and $Sy(t)$ respectively. As can be seen in figure 4.3(a), in this way of synthesizing the signal, the calculated phase is encoded in the abrupt voltage jumps between neighboring pixels, while the amplitude is simply encoded as the amplitude of each sinusoid separately. From equation 4.4 we can deduce that the reconstruction center, i.e. the digital image center, corresponds to $f_d$. By just codifying the same amplitude and phase distribution with a different driving frequency $f_d$ the generated pattern will be the same as before, but shifted according to the acoustic frequency.

Alternatively, the complex RF signal can be calculated using the fact that AODs satisfy the superposition principle (inter-modulation effects are negligible). The complex RF signal is simply the sum of sinusoidal functions, each with its own frequency and amplitudes:

$$s(t) = \sum_{i=1}^{N} A_i \sin(2\pi f_i t + \phi_i) \tag{4.8}$$

Considering that each position in the sample plane corresponds to a fixed acoustic frequency within the AO bandwidth $\Delta f$ (equation 2.31), we can map each intensity value of $I(x_i, y_i)$ with its corresponding position $(fx_i, fy_i)$ and intensity $A_i^2$. For optical tweezers applications, where the patterns are very sparse, the number of added terms is commonly small, one for each trap position. However, note that if we take as many frequencies as number of pixels, this method is equivalent to the previous one, but taking the amplitude and phase of the image plane, i.e. the Fourier Transform of $A_i e^{i\phi_i}$. Since $I(x_i, y_i)$ is *a priori* a real-valued distribution, all $\phi_i = 0$. This second way of encoding information does not show sudden phase and amplitude jumps due to pixelation, which results in the absence of discretization effects, such as reconstruction replicas at the boundaries of the field of view.

It is worth mentioning that the size of the acousto-optic hologram $D_h$, that is the

signal duration, must be equal or smaller than the incident beam size $D$, which exactly corresponds to $\tau$. Using a bigger hologram would affect the final reconstruction quality. If the signal duration $t_h$ is longer than $D/v_A$, the outer parts of the hologram, that is the high frequency information, will not be illuminated by the Gaussian laser beam. Therefore the intensity reconstruction would be filtered in the same way as an abrupt low pass filter. Once $t_h$ is set, both the hologram size $D_h$ and the pixel pitch $d_p = D_h/N$ are already defined. Note that one of the benefits of this AOSLM is that we have a modulator with variable size, number of pixels and pixel pitch. Parameters that can be changed in a continuous way.

Regarding the acoustic wave propagation, even though equation 4.7 tells us that the final intensity reconstruction is invariant to the constantly moving hologram, the complex RF signal must be repeated cyclically. Interestingly, if the signal is just sent once, the desired pattern will only be projected when the center of the hologram coincides with the center of the AOD window. This will only happen for an instant of time $t = 0$. After some time $\Delta t = \tau/2$ the hologram would have moved $D/2$, implying that half of the laser would illuminate pixels from 1 to $N/2$, contributing to the sample reconstruction, while the other half of the laser would not see any modulation and would go to the zero order. By cyclically repeating $S(t)$, the same information lost at the window's leading edge is reappearing at the trailing edge. Resulting in no information lost due to acoustic wave propagation. Moreover, the reconstructed trap configuration would not be altered, due to the Fourier Transform already assumes that our signals are repeated indefinitely. With all this, the mathematical formulation of the physical holograms $Hx(x)$ and $Hy(y)$ is as follows:

$$H(x,t) = \left( \left[ \left( \sum_{k=1}^{N} A_k e^{i\phi_k} \cdot \delta(x - kd_p + v_A t) \right) * \Pi\left(\frac{x}{d_p}\right) \right] * III_{D_h}(x) \right) \cdot \Pi\left(\frac{x}{D}\right) \tag{4.9}$$

Where $*$ is the convolution operator and $H_k = A_k e^{i\phi_k}$ corresponds to the hologram value of each pixel. The function $III_{D_h} = \sum_{n=-\infty}^{\infty} \delta(x - nD_h)$ is a Dirac's delta comb accounting for the infinitely periodic hologram, and $\Pi(x/D)$ and $\Pi(x/d_p)$ are both the AOD (or the laser beam) and the individual pixel windows. From equation 4.9 we can see that, either when $D_h >> D$ or $D_h << D$, different parts of the hologram will be seen by the laser's window, resulting in different partial reconstructions that will overlap incoherently as the acoustic wave runs through the laser beam.

### 4.1.3

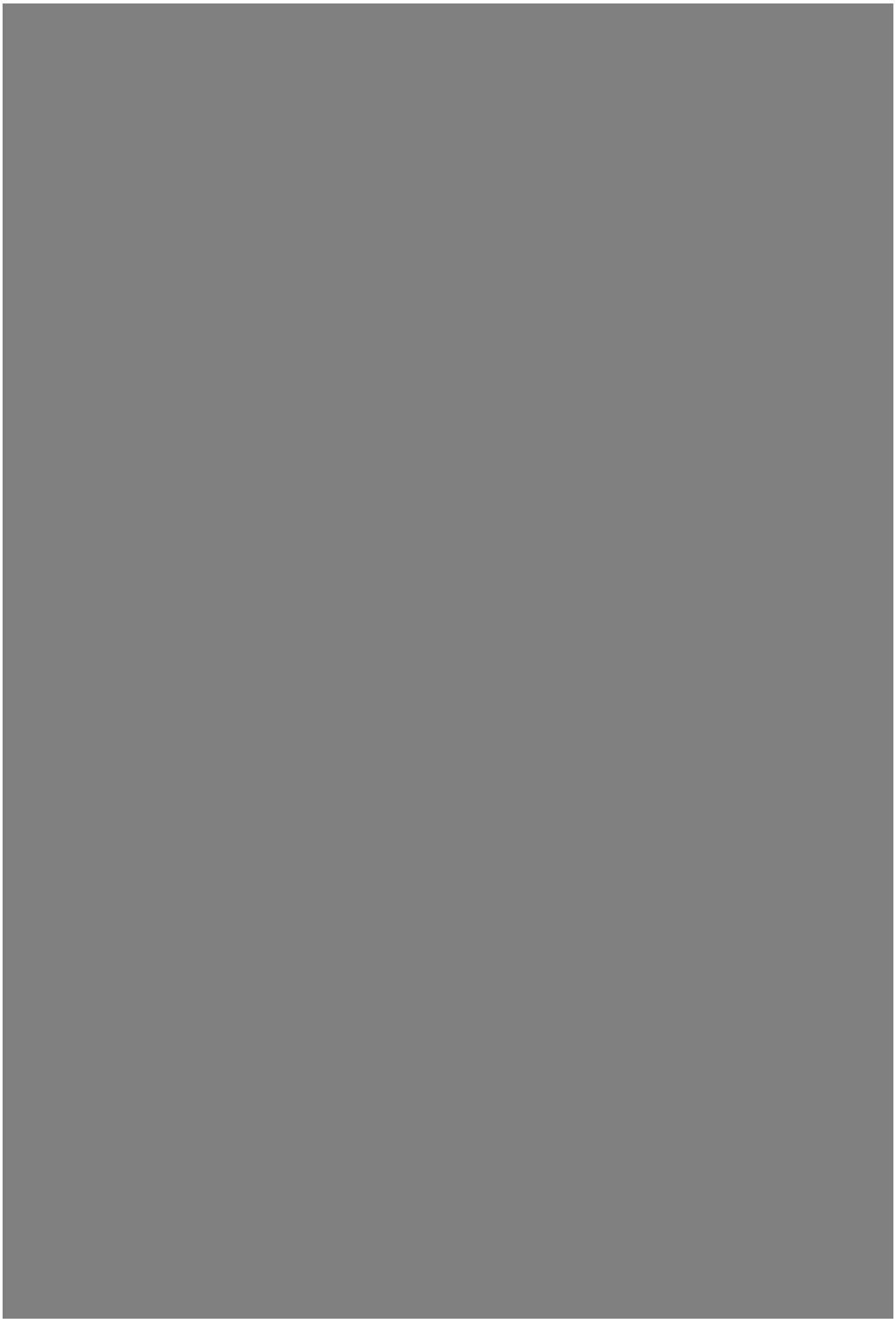

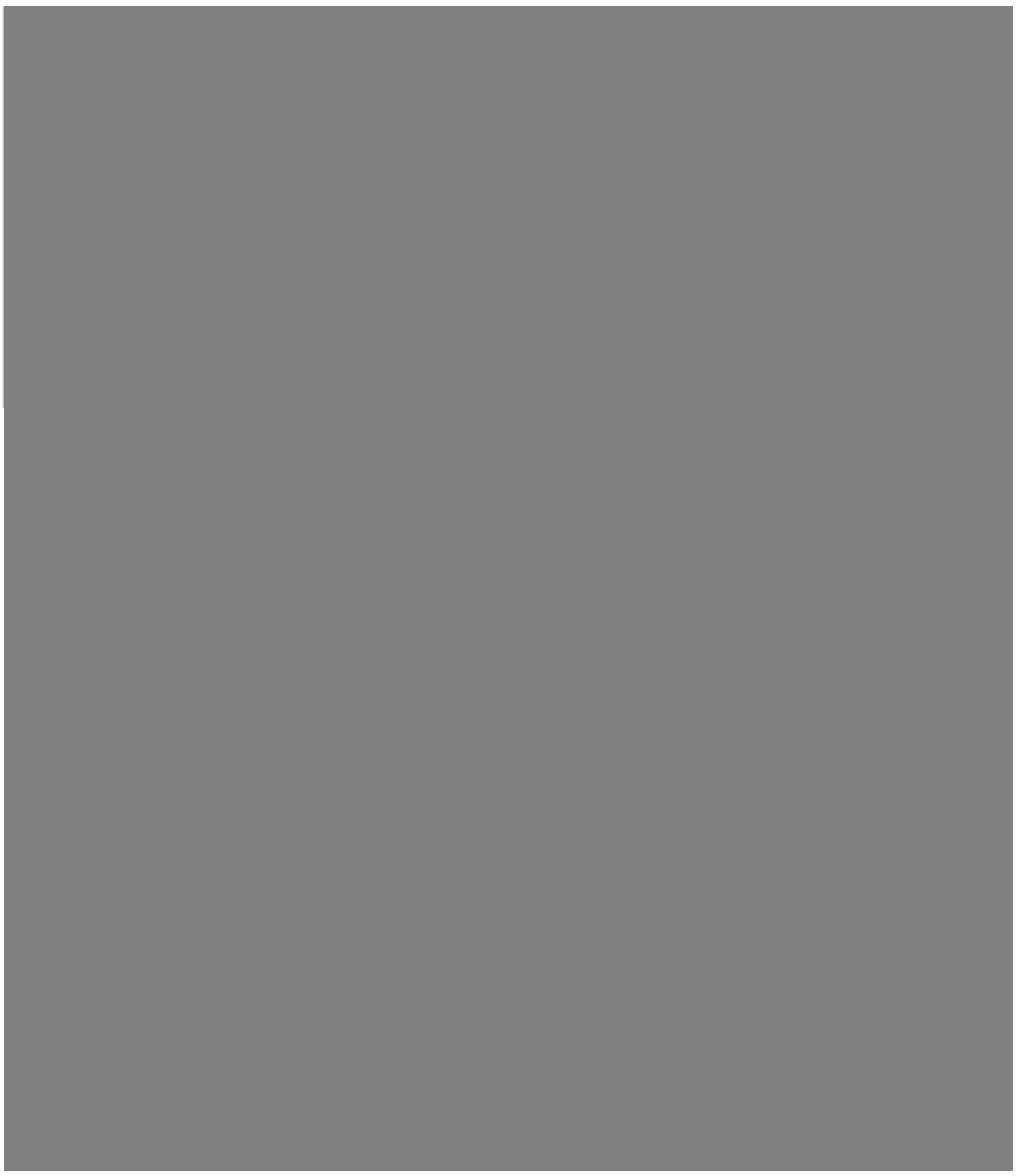

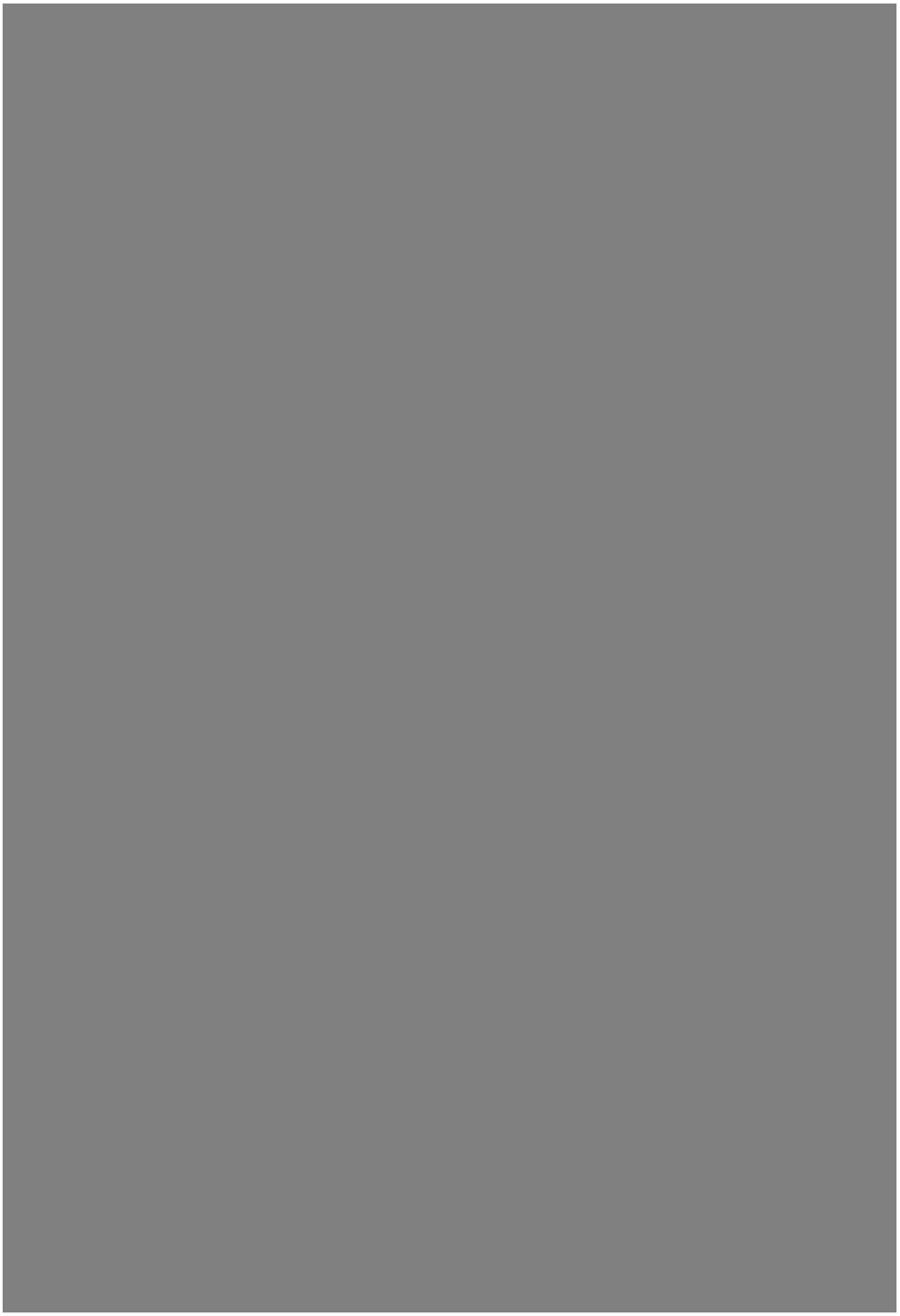

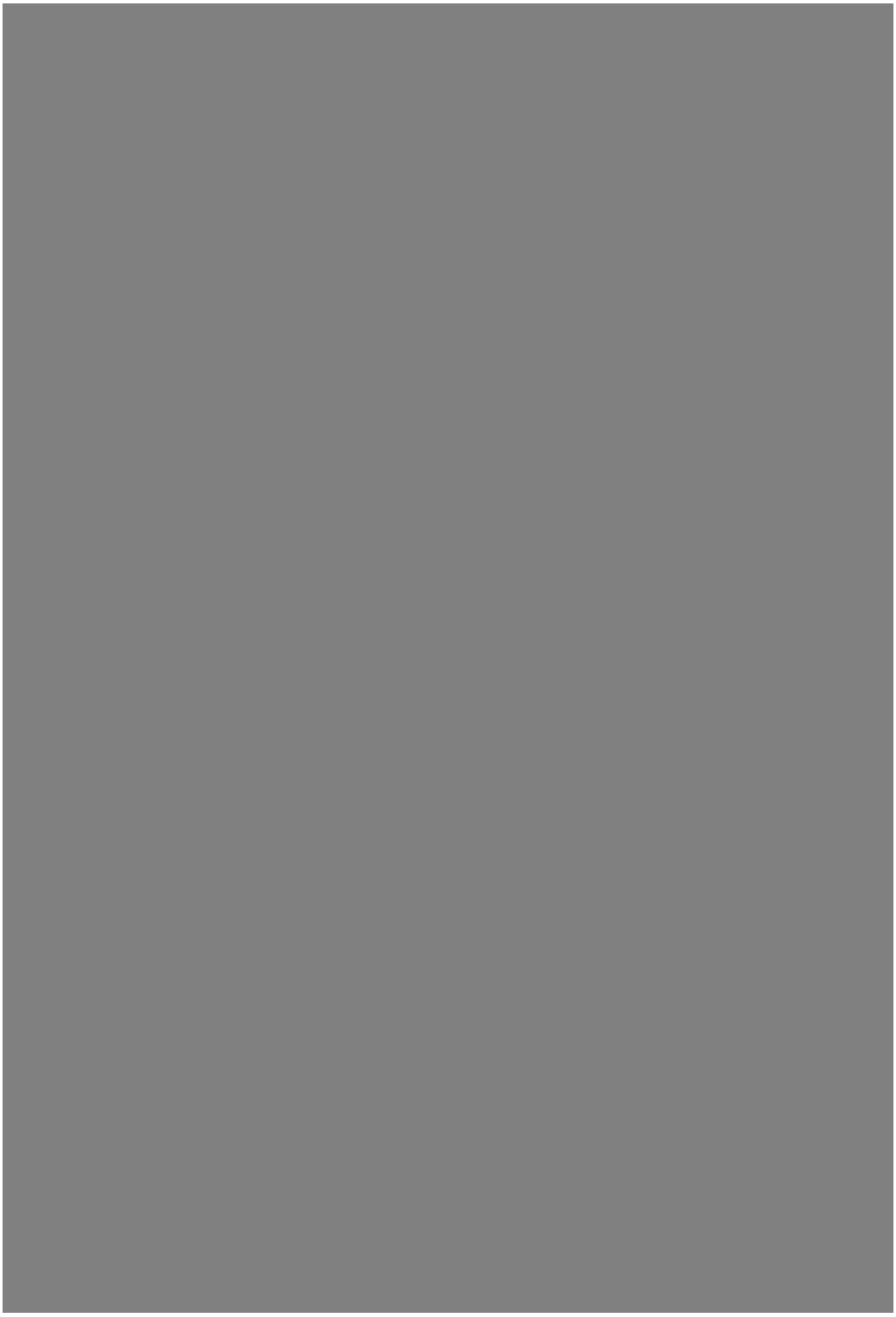

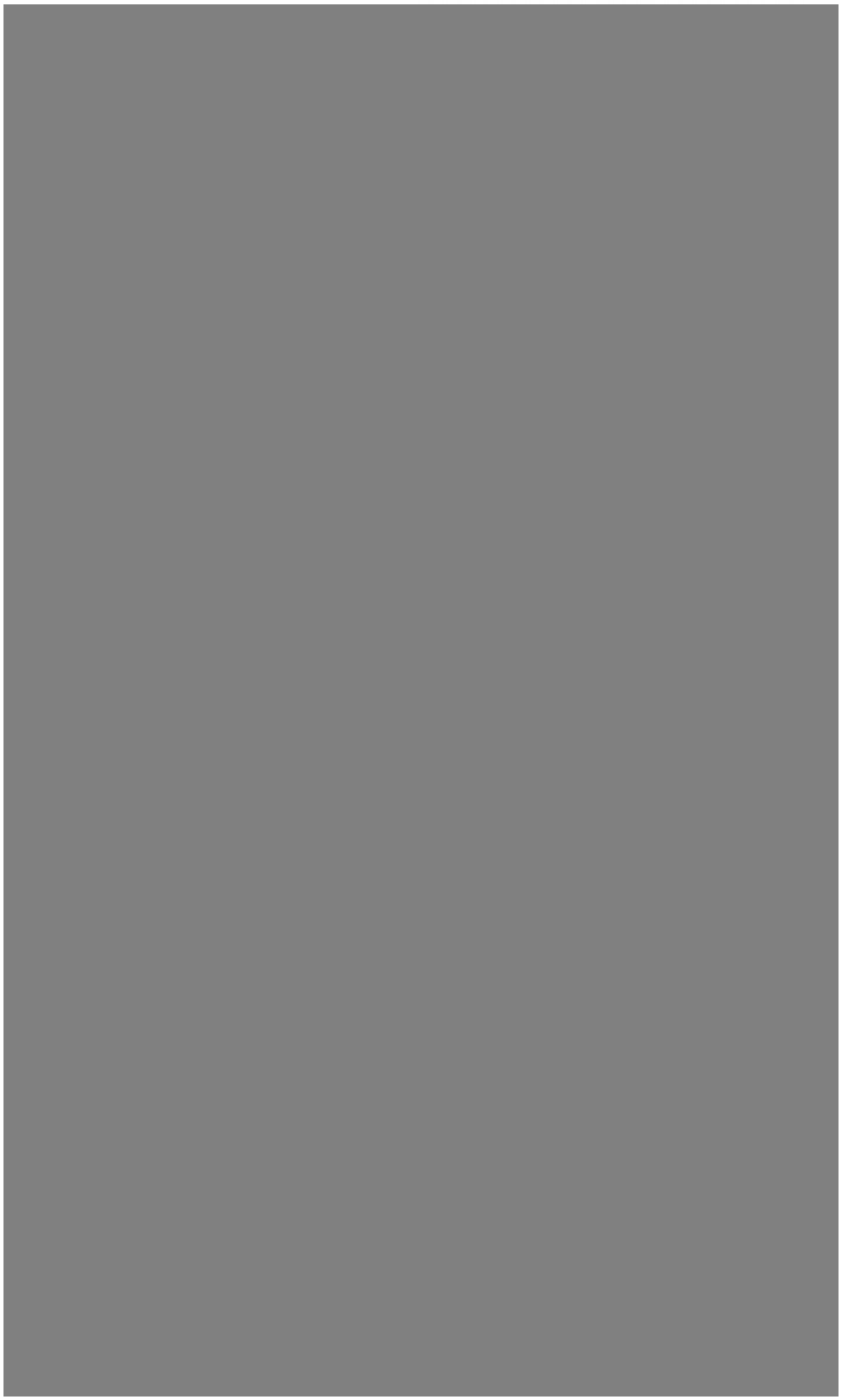

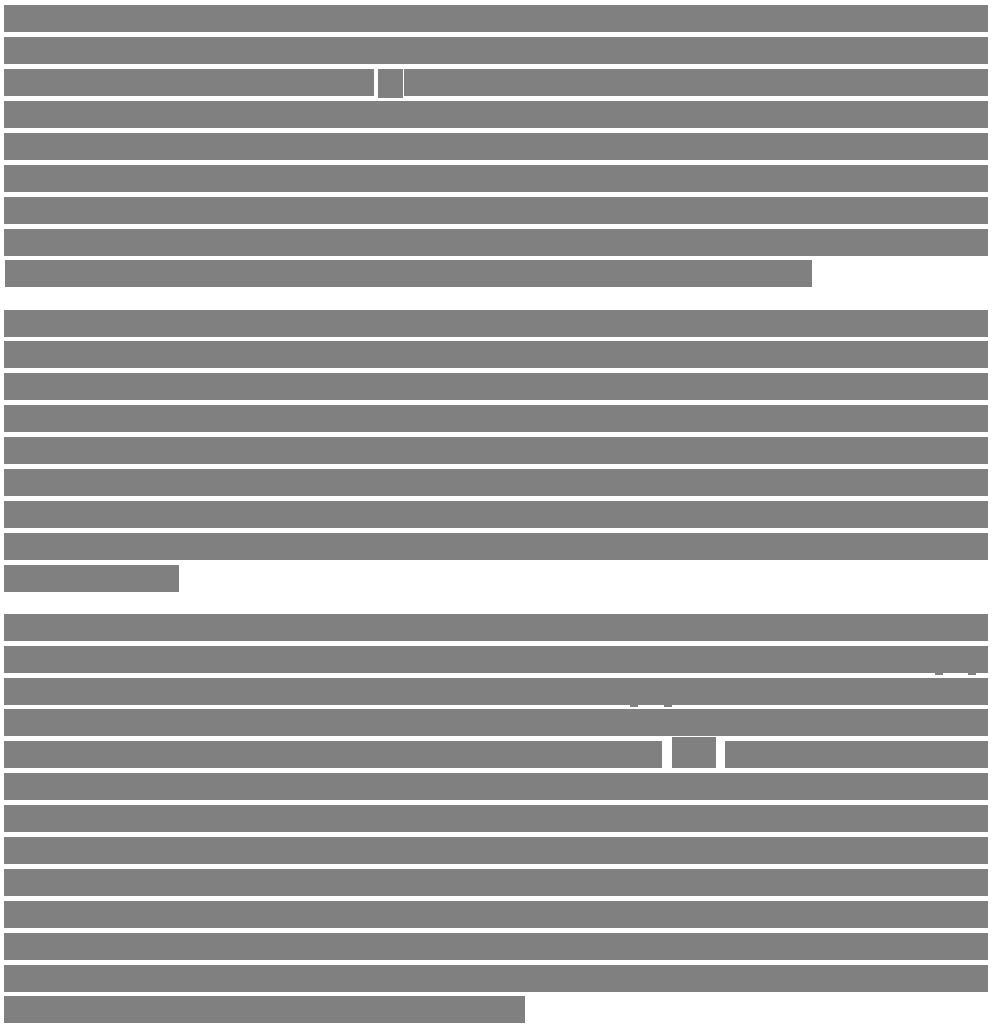

### 4.1.4 Experimental implementation of acousto-optic holography

The experimental setup for the implementation of this new holography with AODs is exactly the same optical micro-manipulation unit described and analyzed in chapters 2 and 3. However, the direct digital synthesizer and power amplifier unit (DDSPA) is not able to generate such complex RF signals described in the previous sections. The DDSPA only allows us to change the amplitude and frequency of the acoustic wave, not the phase, which is crucial for holography. Additionally, even though it has a response time of 40ns, meaning that 225 different pixels can be created within the AOD window, the control PCI NI-DAQ only permits modulations up to 250kHz, i.e. 2 pixels.

In any case, the DDSPA only outputs pure sinusoidal signals, making it impossible to implement the kind of acoustic signals described by equation 4.8 (superposition of sinus). Due to this, the DDSPA is substituted by an arbitrary waveform generator (AWG). Driving the AODs by means of an AWG gives us the freedom to codify any kind of acoustic signal. For optical trapping applications, the AWG used was a RIGOL dual-channel DG5102 with 100MHz of bandwidth, a sampling rate of 1GSa/s and 14-bits of voltage resolution. The AWG has an internal memory of 128 million points and can be controlled through USB3.0 via either Matlab or Labview.

The number of data points of the acoustic signal, that is the physical size of the hologram displayed at the AODs, is given by the AWG's sampling rate, fixed at 1GSa/s. For our particular beam size of 5mm, the number of sample points with which to define the holographic acoustic signal is between $N_s = 7500-8000$. Resulting in around 15 points per individual hologram pixel, depending on the chosen number of pixels. Taking $N_s = 7700$ and $N = 512$, the pixel size is $d_p = 9.78\mu m$ and the pixel duration $d_p v_A = 15ns$. This means that for a central frequency of $f_d = 75MHz$, only 1.127 cycles fall inside each pixel. All the desired intensity patterns, holograms and corresponding signals are calculated using custom Matlab programs and Labview routines.

For optical tweezers applications multiple patterns are time-shared to have independent control over different optical trap configurations. Once calculated, all the different holographic RF signals ($Sx_1(t)$, $Sx_2(t)$, $Sx_3(t)$, ..., $Sx_n(t)$) and ($Sy_1(t)$, $Sy_2(t)$, $Sy_3(t)$, ..., $Sy_n(t)$) are sent to the AWG internal memory by means of USB-3.0. Due to limited bandwidth of USB-3.0, trap configurations can not be controlled in real time. Instead, all the different holograms for each channel are concatenated into a much bigger signal. Which later on, replayed in continuous loop. This way the different holograms $S_i(t)$ are sequentially displayed in the same way as pure frequencies in time-sharing mode, section 2.4.4.

The maximum time-sharing frequency is $1/\tau_h$, being $\tau_h$ the signal duration, which for our laser beam of 5mm is 130kHz. Lower time-sharing frequency values are reached by repeating each signal $S_i(t)$ M times until $f_{TS} = \frac{1}{Mt_h}$, allowing M to be a real number. To put an example, for $f_{TS} = 15kHz$ (M=8.66) each signal $S_i(t)$ is repeated 8 full times, and 2/3 at the end of the sequence. Remember that time-sharing frequency values lower than 25kHz are needed for precise synchronization with the force sensing device (PSD bandwidth limitations, section 2.3.3).

Before being sent to the AODs, the X and Y channels are time-delayed in order to compensate different acoustic-wave transition time from the transducer to the laser beam, $\tau_{0x}$ and $\tau_{0y}$ as discussed in section 2.3.2. In AOH, the acoustic-wave delay has a much bigger impact than in the pure time-sharing approach. Not propperly compensating these acoustic path differences result in a wrong alignment between $Sx_i(t)$ and $Sy_i(t)$, that is a different encoded hologram and therefore a totally different reconstruction. For a good reconstruction quality, the pixel rows from the AODx hologram must be aligned with pixel columns from the AODy.

The maximum output voltage of the AWG is $V_{pp} = 10$V, corresponding to an RF

power of $P_a$=250mW for an AOD impedance of 50Ω. If we take a look at figure 2.5(b), for such $P_a$ the difraction efficiency is around 3.5%, which results on less than 50mW of maximum trapping power. To increase diffraction efficiency, the AWG was connected to a custom made and custom designed amplifier box, consisting of a 12V DC power supply and two high-power RF amplifiers, one for each channel (Mini-Circuits ZHL-1010+ Gain Block). Comment that the amplifier box has been designed for the other set of AODs used in this thesis, for which less RF power is needed (see figure 2.5). The maximum input RF power for each gain block was 158mW (22dBm) and the maximum output power 790mW (29dBm), corresponding to $\sim$ 25% diffraction efficiency for the AODs and 390mW of maximum trapping power (assuming the full 5W output power of the trapping laser).

## 4.2 Generation of multiple static traps with AODs

Acousto-optic holography can be applied into many different fields, this section summarizes the results of the implementation of AOH for optical tweezers applications. The presented technique called Acousto-Holographic Optical Tweezers (AHOTs), combines the trapping stability of HOTs with the compatiblity of TSOTs with precise and fast laser-based position and force measurements.

The motivation for the creation of AHOTs is to be able to trap, manipulate and measure external forces in multiple objects, without being limited by the PSD sensor bandwidth, as explained in section 2.3.3. The idea of AHOTs is that, since most experiments do not require simultaneous measurements in all positions, acousto-optic holograms are used to generate static and stable optical traps for handling and manipulation, while time-sharing between different positions of interest allow selective and accurate measurements at the desired locations.

This idea of time-multiplexing different trap configurations has already been implemented by using a combination of two devices such as galvanometric-mirrors and SLMs [78] to increase the field-of-view of a single SLM, or with SLMs and AODs [79, 80] to correct aberrations in a multiplexed array of optical traps. In AHOTs, the same pair of AODs take care of both the holographic and multiplexing parts. AHOTs can be easily incorporated in a regular TSOTs setup just by driving the AODs with an AWG, adding this new trap generation capability to the regular time-sharing mode, the user being able to choose the method that best suits the conditions of the experiment.

The AHOTs principle is illustrated in figure 4.8(b), where five objects are trapped, but measurements are only necessary in one of the sites. This can be the case, for example, of the experiment performed by Turlier *et. al.* on the study of the mechanical properties of red blood cells [15]. In that particular case, instead of different objects they used multiple time-shared traps to hold and manipulate the cells. Then, controlled cell membrane deformations were applied by moving one trap, while all the other traps were kept at the same position, to prevent red blood cells from moving during the experiment.

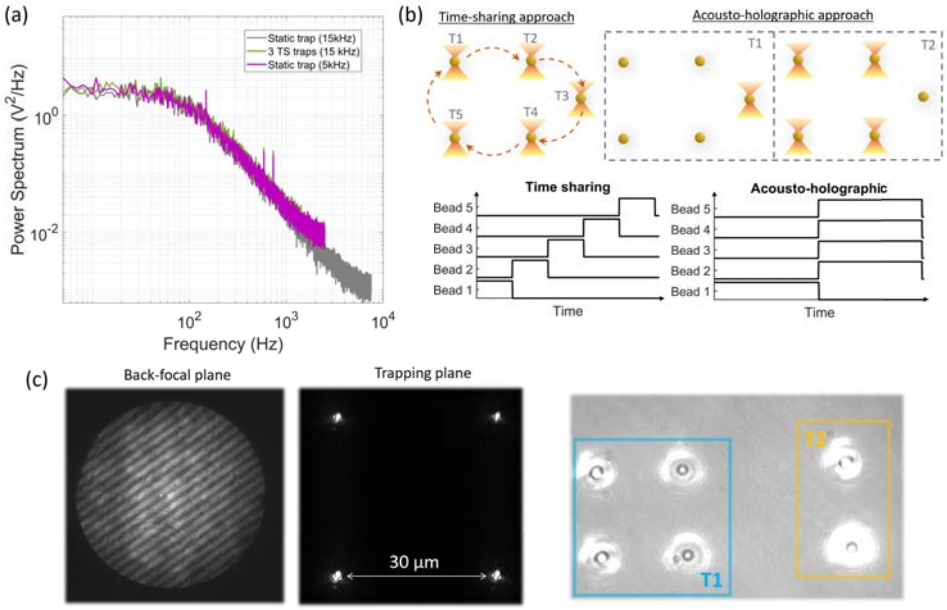


**Figure 4.8:** (a) Power spectrum of a 3-$\mu m$ polystyrene microsphere. Comparison between continous wave trapping, AHOTs and TSOTs. Showing aliasing effects at high frequencies. (b) Comparative scheme between TSOTs and AHOTs. Note that for AHOTs, the duty cyle is always 1:2 and $f_{SW} = f_{TS}/2$, no matter the number of trapped elements. (c) On the left, BFP and trapping plane images of a single trap configuration generated with out AHOT approach. The interference fringes at the microscope objective BFP demonstrate that spots are permanent and stable. On the right, microscope image of 6 different microspheres trapped by time-sharing two trap groups (4+2).

In the time-sharing approach the laser beam is visiting sequentially all positions, with the consequent reduction in the sampling rate. In the AHOTs approach, the five traps are divided in two different sets: a group of 4 static holographic traps and a single trap. Note that for the single trap, the acoustic signal is just a pure sine wave, whereas the 4-trap group is generated by means of an acousto-optic hologram, calculated with the algorithm explained in the previous section. When time-sharing both sets of traps at $f_{TS}$ faster than the system's response time, all five objects are trapped simultaneously. The difference is that here, independently on the number of generated traps, the switching frequency is always $f_{SW} = f_{TS}/2$ and the duty cycle is 1:2. Resulting in a substantial improvement in both the trapping stability and force measurement frequency bandwidth, especially when increasing the number of objects.

As explained in section 2.3.3, in TSOTs the effective sampling frequency of the detector is reduced by a factor on N (being N the number of trapped objects). This effect is shown 4.8(a), where we compare the power spectrum of the same 3-$\mu m$ polystyrene

microsphere trapped with both a continuous wave (CW) trap, and one of three time-shared traps. Since the laser switching is much faster than the response time of the bead, the trapped object cannot respond to such flickering, consequently averaging the laser power. This is the reason why, in order to compare with the CW case, the laser power was incremented a factor 3. In the TSOTs case, even though the laser power is set to 30mW, the trapped object behaves as being trapped by a 10-mW trap.

Both power spectra are identical, showing the same corner frequency, demonstrating that the trapped particle dynamics is the same for both cases. However, even though the PSD's sampling rate is set to 15kHz in all cases, in the time-sharing mode each object is just sampled 1/3rd of the time, resulting in an effective sampling rate of 5kHz. Additionally, the power spectrum in the time-sharing case exactly matches to that of a continuous-wave trap sampled at 5kHz (instead of 15kHz). This simple experiment tell us that, if $f_{TS}$ is high-enough, the effect of the laser flickering is the same as reducing the sensor bandwidth. This reduction on the effective sampling rate causes, a part of high-frequency information loss, aliasing effects visible near the Nyquist frequency of the power spectrum. Such increase of the PS values at high-frequencies can affect the Lorentzian fitting quality, therefore resulting in an erroneous estimate of the trap stiffness $\kappa$.

It is worth mentioning that all these sampling effects get worse as the number of elements increase. Putting the example of just 10 optical traps and using the force sensing apparatus, which has to work at a sampling rate ¡25kHz for accurate force signals (typically 15kHz), each trap would be sampled at 1.5kHz. This frequency range starts to overlap with camera-based techniques. On top of that, trapping stability can be compromised for cases where the corner frequency sits within this range, which occurs just by increasing the trapping laser power, see figure 2.10(c).

Regarding the intensity fluctuations of AHOTs, we confirm their stability by the presence of an interference pattern at the back-focal plane of the condenser lens, figure 4.8(c). It is worth mentioning that, due to the propagative nature of the hologram, the intensity distribution at the BFP is constantly moving at the same speed $v_A$ as the acoustic wave. For this reason, all intensity distributions observed at the BFP are averaged by the camera-limited integration time. Even though the FT of the sample plane distribution is also a spot array, we observe fringes at $45^{\text{o}}$, that correspond to the effective propagation direction of the hologram.

The presence of an interference pattern confirms coherence between the traps, if there is any fluctuation, it must be global and/or very fast, faster than the PSD response time. Some minor fluctuations can appear when the hologram crosses the Gaussian laser distribution. Even though the circular symmetry of the hologram, the when hologram runs across the AOD window, pixels are being weighted differently. To quantify such effect, we performed a numerical calculation, that simulates the temporal evolution of a 5x5 trap array, within one hologram transition (around $\tau_h = 7\mu s$). Showing a global fluctuation of around 1% (STD = 1% and Peak-to-peak = 2%). Comment that this fluctuations increase when making the beam size smaller, so in order to minimize the effect is better to overfill the AOD window. The best scenario would be to illuminate the AODs with a flat-top beam. All this leads us to

The results from the drag force measurement analysis are shown in figure 4.10. Since the force measurement system is perfectly synchronized with the trap generation, that is the AWG, two different force signals can be clearly distinguished, one for each group of traps. In the same way as direct force measurements using HOTs [19], the force signals obatined with AHOTs correspond to the sum of all traps created by each acousto-optic hologram, due to the force measurement instrument collects light scattered by all the particles.

With out AHOTs approach, the force from two different groups of traps can be measured at the same time, without a drastic reduction of the sampling frequency. Both sets of traps were time-shared at 15 kHz by repeating each corresponding hologram $\sim 8$ times, so each trap configuration is sampled at 7.5 kHz respectively. If instead we use a pure TS approach, the sampling frequency would be 2.5 kHz, losing high frequency information and compromising trapping quality (since the trap stiffness would be reduced a factor of 1/6, and the switching frequency would be very close to the PS corner).

In figure 4.10(c) we can see all the measurements performed, several combinations of micro-spheres of two different sizes were analyzed, including also cases where one or both trap groups were empty, where null force was measured. All force values fall within $\pm 7\%$ of the theoretical value, which can be calculated by knowing the particle size, the buffer viscosity and the velocity of the piezo-stage. This result demonstrates that, with this new AHOTs technique, it is possible to generate multiple stable and static optical traps, while being fully compatible with laser-based position of force measurement methods, being able to address single object information.

Both grups of traps can de distinguished due to the laser flickering. However, is it worth pointing out that traps within the same group are not completely indistinguishable. The AOD cell increases the electric field frequency by an amount equal to the acoustic carrier frequency $f_d$ (acousto-optic Doppler shift, see equation 2.5). This change in wavelength can be either positive or negative, depending on the propagation direction of the acoustic wave. Due to this effect, each trap is of a slightly different wavelength thus carrying a distinct label that makes it distinguishable from the others, in contrast to regular HOTs. So, it may be possible to arrange some type of heterodyne detection at the PSD in order to deduce single trap information in continuous mode. This new idea has not been tested in this thesis and can be implemented in future experiments.

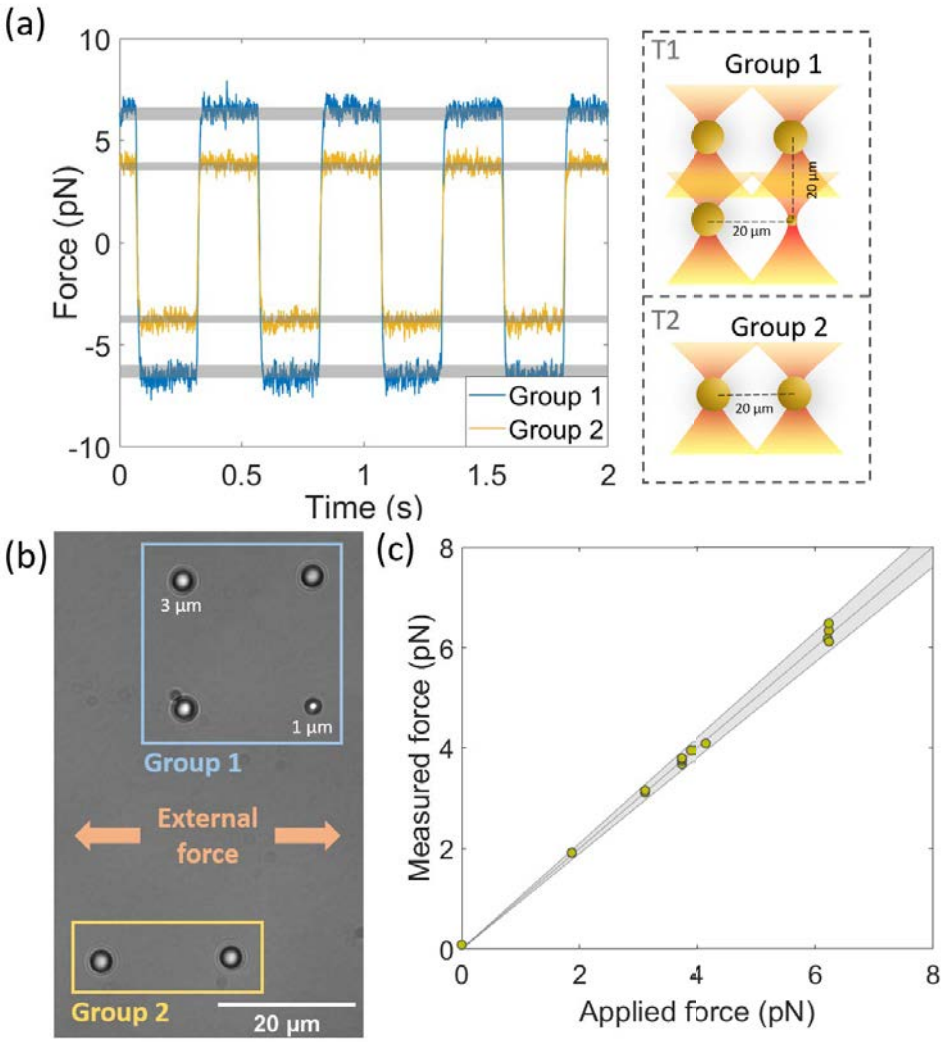


**Figure 4.10:** (a) (Left) Force signals corresponding to each trap group generated with the AODs. Negative values correspond to the stage traveling in the opposite direction. The theoretical force given by Stokes' law is displayed in gray (±7%). (Right) Schematic representation of the trap configurations; the two trap groups were separated by $30\mu m$ to avoid hydrodynamic interaction between them. (b) Snapshot of the six trapped microspheres, indicating the two different trap groups. (c) Comparison of measured and applied force for all drag force measurements. The shaded area corresponds to a ±5% error.

# Chapter 5

# Design and development of a fully programmable array microscope

Although the implementation of acousto-optic holography for optical tweezers applications is very interesting, allowing to generate multiple static optical traps, while being compatible with single object direct force measurements. The reality is that, in experiments with living specimens, where the trapping efficiency is quite low, only a few traps are useful. So, in the practical case the speed improvement compared to regular TSOTs is only marginal. On top of that, the limitations on the generated patterns considerably reduces the manipulation possibilities. Thus, apart from purely academic experiments, or exceptional cases requiring a huge number of elements (such as in the study of colloidal systems), the applicability of AHOTs is quite limited. Even though TSOTs and AHOTs are totally compatible techniques, in the sense that both use the same optical setup, an end user would only use such feature in sporadic situations.

While the benefits of AOH in the field of optical tweezers may not be very attractive. The same ideas and concepts that led us to the development of the AHOTs system, can be applied in other fields, such as image projection or fluorescence microscopy. Which we believe can unleash the full potential of the developed AOSLM unit, constituted by two AODs, a relay 4f system and a complex signal generator system (AWG + amplifiers). In the field of image projection, the AOSLM unit may suppose the appearance of new laser video-projectors, providing higher-than-average quality and speckle-free images. The development of this part is not object of study of this thesis.

Is in fluorescence confocal microscopy where we believe that the enormous modulation speed of AOSLMs can help to push forward the development of more capable devices. Either in image projection or optical tweezers, the complexity of intensity patterns one can encounter directly affects the modulation speed. In the sense that, in order to be displayed, the desired patterns have to be decomposed into different sub-patterns, at the expense of reconstruction speed. So, for a typical AOD in the vis-

ible spectrum capable of producing patterns of 450x450 points, the aimed $\sim$ 100kHz modulation speed is translated into an effective rate of 230Hz. However, for illumination purposes, such as multi-point confocal microscopy, the geometry of the intensity patterns can be chosen to match the mathematical constrains (X-Y separable) of the AODs. Therefore, taking advantage of the full modulation speed of AODs. 3D object scanning systems or even LIDAR devices can also be added to the application list, practically any situation where precise scanning with multiple beams is beneficial.

From now on, optical tweezers are put apart and the rest of this thesis is fully dedicated to the experimental implementation of AOH in fluorescence microscopy. In the following 3 chapters we show the whole development process of a new fully flexible confocal microscope, using two novel technologies for both sample excitation and confocal filtering. On the one hand, we designed a fully programmable illuminator using the AOSLM as key modulation element. By using the same algorithms described in chapter 4, the illumination system can generate and project on the sample a huge variety of excitation patterns and shift them following any scanning protocol at very high speeds, with high optical efficiency. Then for the final image reconstruction, i.e. out-of-focus light filtering, we propose both a software and a hardware solution. For the software part we developed and implemented different image processing algorithms that combine all images from sample scanning into a single high-contrasted final reconstruction. Then, for the hardware approach we custom designed and co-developed a CMOS camera whose pixels can be selectively read following the same excitation patterns. Sensor partial readout significantly increases the effective framerate (over 20 kHz) and directly provides high-contrasted images, since the selected pixels themselves act as virtual pinholes.

With these two key ingredients, our prototype offers the user a versatile instrument. It eliminates all moving parts that can introduce vibrations or mechanical drifts, such as motorized mirrors or rotating disks, and physical elements that lead to misalignment over time, as is the case of physical pinholes. The prototype combines the benefits and capabilities of many existing confocal microscopes into the same device, so the user can decide the best operating mode depending on the sample or experimental requirements. But also, due to the programmable nature of the AOSLM, allows the implementation of future excitation patterns, smart scanning approaches or new emerging super-resolution techniques.

This chapter focuses on the development process of the illumination system, making special emphasis on both the optical and mechanical design of the prototype. We first describe the concept of fluorescence microscopy, the importance of confocal microscopy to visualize thick samples and a brief review of the most popular confocal microscopy techniques. Then the optical design of the prototype is described in detail, showing its performance for two different wavelengths. After this, the different excitation patterns generated with the illuminator are described in terms of speed and sectioning capabilities, showing how different patterns can be used to best suit the user or sample needs. Once the patterns are described, we explain how a fluorescent sample is scanned, describing both the algorithm to shift the pattern and the scanning protocol. Finally, some ideas for new excitation patterns and scanning protocols are

presented.

## 5.1 Introduction. Fluorescence confocal microscopy and the programmable array microscope concept

When dealing with biological samples, one encounter that most of the structures are transparent. The refractive index of biological structures is very similar to that of the environment or the buffer they are embedded into. Apart from a loss on optical trapping efficiency (as seen in chapter 3), such low relative refractive index results in a lack of contrast, rendering these specimens nearly invisible under bright-field illumination. Although microscope objectives are constantly improving, in terms of numerical aperture and optical quality, capable of offering high-resolution and highly-magnificated images, such features become worthless if the contrast is almost null.

As in any imaging technique, the two aspects that define the image quality are: resolution, both lateral and axial, and contrast. Being both aspects equally important. While the spatial resolution depends exclusively on the optical quality of the system, concretely on the numerical aperture (NA) of the objective lens, contrast depends upon interaction between the illumination light and the sample itself. The image contrast defines the ability of the optical system to record information coming from the sample. So, it depends on many parameters such as: the type of specimen, the light efficiency of the system, the sensitivity of the detector and the illumination light characteristics.

Being almost transparent, specimens still induce phase shifts to the light's wavefront, described in terms of scattering and diffraction. The problem is that light detectors, such as cameras, photo-diodes or even the human eye, are only sensitive to intensity changes, not phase differences. Several microscopy techniques exist to improve image contrast, designed to convert phase differences induced by the sample into detectable intensity changes. This is the case of phase contrast, dark field, differential interference contrast (DIC) or polarization microscopy. In all of them, the information about the optical path length of the sample is codified and detected in the form of intensity, interferometric pattern or polarization changes. Although the above-mentioned methods are used to enhance the image quality in unstained, transparent samples, there are several reasons that make staining the specimen with fluorescent molecules a better choice.

In fluorescence microscopy different biological structures are labeled with fluorescent molecules called fluorophores, that emit light of a different wavelength as a response to an excitation light source. In order to target specific biological structures, i. e. specific proteins, the fluorescent molecules are combined with antibodies that, once penetrate into the cell, they attach to their antigen. This process is called immunofluorescence. Another approach is to genetically modify the DNA sequence of the specimen in such a way that fluorescent molecules are expressed by the cell itself. Allowing to

perform in vivo imaging, as opposed to immunostaining. Depending on the size of the fluorophor+antibody, the cell membrane becomes not permeable to it, so in most cases the specimen has to be killed and fixed.

This way, by splitting the excitation and emission light through a dichroic micrror, only light coming from the target molecules reaches the detector. The fluorophor signal stands out on an almost black background, providing extremely high-contrast. Moreover, fluorescence microscopy offer high specificity, the fact that different structures can be labeled with different flourophores, allows the user to see at different cellular components just by changing the excitation color. Finally, fluorescence is quantitative, if the system is calibrated correctly, areas with higher fluorescence signal correspond to areas with higher molecule density.

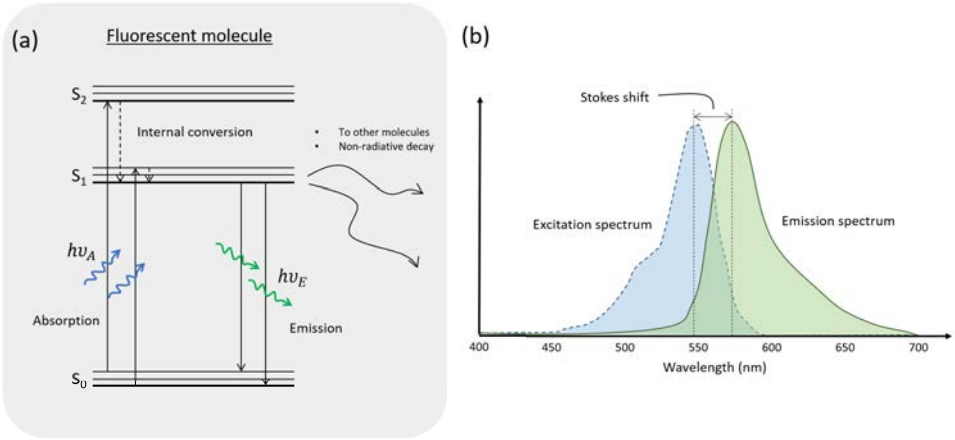


**Figure 5.1:** Fluorescence. (a) Jablonski diagram of a regular fluorescent molecule. (b) Example of the excitation (absorption) and emission bands for Alexa 488.

This last fluorescence feature has huge consequences, since it allows to extract important information about the biological system. Apart from indicating the specimen's shape and geometry, flourophores can be used as biomarkers or biosensors, indicating when a particular biological process takes place or the presence of a certain protein [81]. The vast majority of assays in drug-development are based on the cellular responses to different compounds or light stimuli. Such cellular responses are usually captured in the form of a fluorescence image and subsequently analyzed to obtain relevant information. In many cases, it is a brute force process based on trial and error, where small compound libraries are screened for selecting potential candidates. By means of fluorescence image analysis, one can more easily count cells, measure its size, shape, texture, localize certain structures, etc.

To better understand the fluorescence principle, figure 5.1(a) shows an scheme of the electronic levels of a fluorophore. When shining the molecule with high-energy energy photons $h\nu_A$, electrons from the ground state $S_0$ are excited to $S_2$ band, which then loose energy by means of thermal dissipation (internal conversion) up to $S_1$, finally

electrons in $S_1$ band fall down to the ground state again emitting a photon of a lower energy $h\nu_E$. For regular molecules, the whole process between excitation and emission is in the order of nanoseconds.

As shown in figure 5.1(b) fluorophores are mainly characterized by their excitation (absorption) and emission spectrum and the corresponding Stokes shift. For proper imaging, i. e. an efficient excitation, is preferable to choose the laser light source close to the excitation maximum. Regarding the dichroic mirrors and filters, this one is chosen to discriminate between both excitation and emission spectra. In addition, it is common to add excitation and emission filters; the first one ensures only the required wavelengths are transmitted (usually a band-pass filter), however the appearance of high-power and cheaper single-wavelength LED light sources, may obviate the need for filter wheels. Then the emission filter is used to block any spurious excitation light, or when exciting several fluorophores at the same time, selecting just the desired channel [82]. However, note that for fluorophores with very small Stokes shift, almost half of the excitation spectrum is lost. Other fluorophore properties worth mentioning are the quantum efficiency (QE), as the ratio between absorbed and emitted photons and the fluorophore brightness, defined by the absorption coefficient at the specific excitation wavelength and the QE.

One practical aspect to be aware of, and the main enemy of fluorescence, is photobleaching. Fluorescent dyes do not last forever, they have some limited number of cycles the can go through, and over time, the fluorescence signal tends to bleach out. Once on the excited state, electrons can transition to another excited triplet state, relatively long-lived with respect the single state. During this time, they may interact with other molecules (typically $O_2$) to produce irreversible changes to the fluorophore, causing it to no longer emit light. The maximum number of excitation/emission cycles a fluorescent dye can do depends on its molecular structure and specially on the local environment. As a rule of thumb, a regular fluorophore can emit between $3\text{-}4\cdot10^4$ photons before becoming permanently switched off. Additionally, comment that this number of cycles is constant and intrinsic of each molecule, it does not depend on how the excitation light is delivered, either continously of through very short pulses.

To avoid or minimize photobleaching, several recommended strategies involve: select fade-resistant dyes, increase the fluorophor density, decrease bleaching by anti-fade compounds (remove oxigen from the environment by, for example, using glycerol), expose excitation light only when observing, and minimize exposure time/excitation power.

### 5.1.1 Optical sectioning: confocal microscopy

The most simple fluorescence imaging technique is called wide-field fluorescence microscopy or epifluorescence. The basic fluorescence microscope is a common tool of modern cell biologists. In epifluorescence microscopy, the light coming from the source is reflected upwards by the dichroic mirror towards the microscope objective, where its focused at its back-focal plane. This causes a parallel beam of excitation

light to simultaneously and homogeneously illuminate the whole sample volume. As a response, each individual excited fluorophore emits light of a longer wavelength in return. Since the size of fluorescent molecules is about 2-10nm, they are considered point sources, emitting light in all directions. Then, the microscope objective collects all the emitted light that falls within the light cone defined by the NA. Which then, passes through the dichroic mirror reaching either the camera sensor or the eyepiece. The higher the NA, more photons will hit the camera, and the brighter will be the final image.

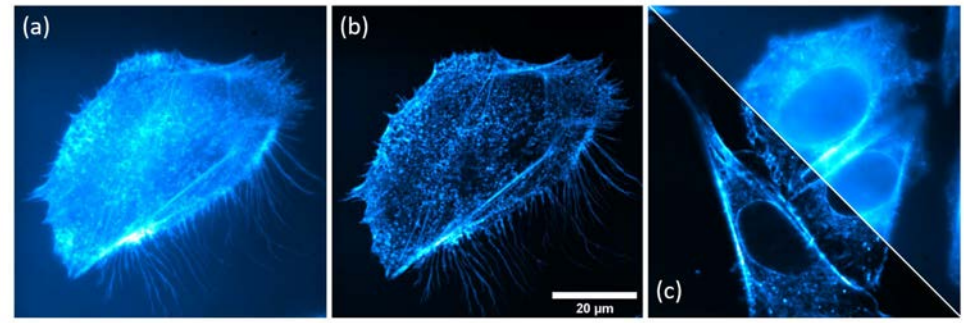


**Figure 5.2:** Fluorescence images of the actin network of CHO cells immunolabeled with Palloidin+TRITC. (a) Epifluorescence, (b) Confocal image and (c) Comparison between filtered and non-filtered. All images are obtained with the prototype developed in this thesis.

The advantages of epifluorescence microscopy are clear, all parts of the sample are observed at the same time and a complete 2D reconstruction is obtained for each camera exposure. However, even though all fluorophores are excited equally, i. e. with the same light intensity, the camera plane is only focused at the objective lens focal plane. So, light emitted from out-of-focus fluorophores appears onto the camera plane in the form of a blurred background, degrading the final image. Resulting in poorly contrasted images, that affect the lateral resolution, and above all, the axial resolution or sectioning capabilities. Despite this drawbacks, epifluorescence is one of the most used techniques because of the ease of use (very simple optical setup) and imaging speed (technically speed is only limited by the sensor's frame-rate).

Especially in thick specimens, epifluorescence produces very nice images, but that they have both in-focus and out-of-focus light. By looking at images of figure 5.2(a) we can see some structures that appear clear and sharp, but then there is a lot of blurr that shows up on top of the in-focus parts, which is produced by parts of the sample that are not in focus. This out-of focus blurr increases with the sample thickness, in 5.2(c) we observe out-of-focus light in the nuclei of the cells. Which have not been marked, only the surrounding actin network.

In most cases, this out of focus light makes it impossible to obtain 3D reconstructions of the sample. One way to get around that is by means of confocal microscopy, whose purpose is to eliminate all the out-of-focus blurr from the image, leaving only visible

the focused parts [83]. By doing that, the confocal microscope is characterized by a very good optical sectioning, which is defined as the capability of a microscope to reject light from other planes, thereby enhancing the axial resolution [84, 7]. Comparing figures 5.2(a) and (b) we can see that the confocal image presents less blurred background and much higher contrast (deeper blacks), both contributing to an improved optical sectioning. Then, by moving the sample along the axial direction, one can record an image for each position, combining all of them into a final 3D reconstruction of the cell.

Ideally, the axial and lateral resolution that an optical microscope can achieve, is only limited by the finite size of its exit pupil, i. e. the finite NA, and the excitation and emission wavelengths (diffraction limit). Resolution is also referred as resolving power, or the ability of a given microscope to distinguish different features of the observed specimen. Under some approximations and criteria, the resolving power of a microscope is given by the size of the point spread function (PSF) of the microscope objective, given by:

$$d_z = \frac{1.78\lambda_0 n}{NA^2} \tag{5.1}$$

$$d_{xy} = \frac{0.61\lambda_0}{NA} \tag{5.2}$$

Being $d_z$ and $d_{xy}$ the axial and lateral resolution, and $n$ the refractive index of microscope objective immersion medium. It is worth mentioning that the definition of $d_z$ and $d_{xy}$ is based on a criteria, Rayleigh's criterion in this case, other resolution criteria are Sparrow's ($d_{xy} = \frac{0.47\lambda_0}{NA}$) or Abbe's ($d_{xy} = \frac{\lambda_0}{2NA}$). In practice, we say that the microscope is able to distinguish or resolve point emitters separated $> d_{xy}$ laterally or $> d_z$ axially. Objects or structures closer than this magnitudes are considered to be the same. Even though resolving power is defined for two different emitters, the same concept can be interpreted for fine structures. The typical example is when observing individual filaments, the minimum filament thickness a microscope can see is $d_z$ (or $d_{xy}$). All filaments thinner than $d_z$ will be considered point emitters, and its size will always be $d_z$. To put some numbers, for a central wavelength of $\lambda_0 = 550nm$ and an oil-immersion NA=1.3 objective ($n = 1.516$), an optical microscope can achieve $d_{xy} \sim 260nm$ and $d_z \sim 870nm$. Remember that these values are calculated as the spot size of a single point emitter, the background haze and other aspects such as light source coherence or optical aberrations can drastically degrade the image, preventing the optical system to reach such theoretical values $d_{xy}$ and $d_z$.

In principle, the resolution can be always improved by using a higher NA, specially on the axial direction. However this is not a good strategy, the NA can take a maximum value of $n_{medium}$, which for the vast majority of specimens is very close to $n_{water} = 1.33$. Using objective lenses with $NA > 1.33$ does not make any sense, specially for volumetric imaging, i. ee. when imaging deeper into the specimen. As an example, assuming that we are using a NA=1.45, all light rays from NA=1.33 to NA=1.45 will be totally internally reflected at the coverslip-water interface, creating

non-propagative evanescent waves. Then, the effective PSF would be the same as using $NA = n_{medium} = 1.33$, apart from being less light efficient since part of the energy would be filtered out.

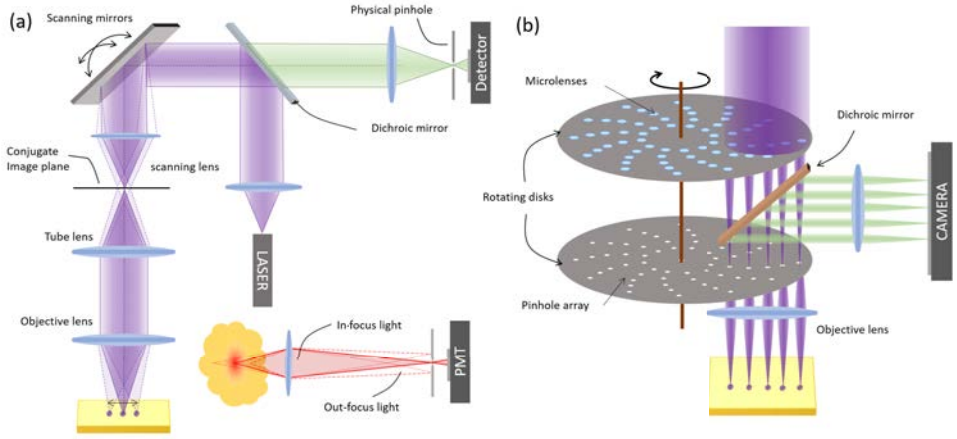


**Figure 5.3:** Schematics of the two most used confocal microscopy systems, showing its principle of operation. (a) Confocal Laser Scaning Microscope (CLSM) and (b) Spinning disk confocal.

The confocal microscope, an optical technique invented more than sixty years ago by M. Minsky [85], has become the cornerstone for sample visualization and is considered the standard for optical sectioning. Here, as opposed to parallel illumination used in wide-field microscopy, the light source (usually a laser) is focused on a diffraction-limited spot that is scanned on a point-by-point basis over the whole specimen. Before detection, a small aperture –the pinhole–, which is placed at a conjugate image to that of the excitation spot, filters the fluorescent emission from out-of-focus planes canceling the background flare. The pinhole is the key element in the confocal design that allows the observation of thick specimens with excellent contrast, and specially, optical sectioning.

Regarding the experimental implementation of confocal microscopes, in the early days the laser was kept stationary and the scanning was achieved by moving the sample [86], simplifying the setup due to allowed the use of a stationary pinhole. Unfortunately, a moving stage has the disadvantage of being slow and vibration-sensitive, which finally makes it inconvenient for biological observations. Although more technically challenging, scanning the beam is a superior alternative that is almost universally adopted today. However, with a "flying" laser spot comes the necessity of moving the pinhole in synchrony. For example, Nipkow-type multipoint confocals use small apertures perforated on a rotating disk for both creating $\sim 1000$ light foci as well as filtering out background flare. In this arrangement, the pinholes naturally track the excitation spots over the sample [83, 86]. Then, the final image is being composed as the disc rotates (at around $\sim 5000$rpm) and the camera sensor is exposed.

However, for the single-beam scanning case, the necessity of a "moving pinhole" is

very complicated to implement. Fortunately, a very smart solution is to "descan" the laser beam before it gets filtered. Descanning is rather straightforward when the scanning device is based on mirrors. Figure 5.3(a) shows the schematic design of a Confocal Laser Scanning Microscope (CLSM). Here, a tilting mirror deflects the excitation laser beam off to the desired location on the sample plane, exciting the fluorescence emission. Fluorescent light then travels back down the same optical train used for excitation, being reflected by the same mirror as before and is directed to the pinhole, which can be fixed in space regardless of the tilt angle of the scanner. Otherwise, the beam would only pass through the pinhole in one position, requiring one pinhole for each position. However, when the scanner is not a reflective device (for example, is based on diffraction (such as with AODs) or the confocal microscope operates in transmission descanning the beam becomes much more difficult.

The final element in a confocal microscope is the detector. Several types of optical sectioning microscopes use a camera as the image-capturing device, such as re-scan [87], light-sheet [88] and multi-point confocals [89, 90]. In all these cases, the image is being composed as the excitation light, either a single laser point (re-scan), multiple-foci or a light sheet, moves with respect stationary camera. In a regular CLSM, pixels the same context as in a camera do not exist. Due to the laser beam is "descanned", the intensity information is always at the same position, reason why a high-bandwidth single-pixel detector is used. The light non-blocked by the physical pinhole, by definition in focus, reaches a photo-multiplier tube (PMT) which amplifies the incoming signal and provides an intensity value for each laser position. Final reconstructions are obtained by plotting the recorded intensity values on the laser position map. While PMTs are extremely fast and can detect very few emitted photons, they suffer from a low quantum efficiency (QE) of around $25 - 30\%$, compared to $> 95\%$ achieved by modern sCMOS cameras.

It is also worth mentioning that, in all the described microscopy techniques fluorophores are considered to respond linearly with the excitation light power. Another type of optical sectioning microscopy is two-photon or multi-photon microscopy [91, 92], where optical sectioning is not achieved by blocking the out-of-focus light with a physical pinhole, but by localized excitation. Two-photon microscopy rely on non-linear processes were two photons of longer wavelength can excite fluorescence. This process is less probable to occur, so two-photon (or multi-photon) excitation, and the consequent fluorescence emission, only takes place near the focusing area. This way, all the collected photons come from the focal plane, so the need for a pinhole disappears.

### 5.1.2 The PAM concept

When imaging speed is a concern, it is obvious to say that any scanning procedure is detrimental. The single-beam laser scanning approach is a very time consuming process, that however provides extraordinary imaging quality. Although being slow, at 1-5fps, the simplicity of the optical setup provides CLSMs huge flexilibity in terms of being compatible with other techniques. As an example, super-resolution

Stimulated Emission Depletion Microscopy (STED) can be implemented on a regular CLSM just by adding a vortex phase plate. Moreover, the possibility to steer the laser at almost any region of interest (ROI) allows FRAP (Fluorescence Recovery After Photobleaching) essays. On the other hand, to speed up the imaging process, spinning-disk confocals or any multi-point confocal rely on the parallelization principle to sample many ($\sim$ 1000) positions at once, reducing the number of total scanning positions. Offering much better temporal resolution and less phototoxicity than single-point scanning systems, since the total laser energy is distributed among all positions. Spinning disk confocals can easily achieve video-rates, the limitation mainly being the camera sensitivity (specially at such high-rates) and the specimen's fluorescence efficiency.

On the down side, dividing the laser beam into multiple "beamlets" imply especially designed fixed optical components such as perforated discs and microlens arrays, resulting in very rigid (non-flexible) optical setups that only serve for one particular purpose, going fast. This rigidity in the optical assembly also results in limitations in terms of compatibility with multiple objective lenses, magnification and pinhole size. While in CLSMs, an adjustable pinhole size allows the user to reject more or less background flare, (depending on the objective's PSF) spinning-disk confocals offer two sets of pinhole discs at most, limiting the possibilities.

On top of that, the high-speeds that spinning-disk microscopes can achieve, comes at the price of lower optical sectioning. Multi-point scanners, typically exhibit lower sectioning capabilities due to crosstalk between neighboring foci. Regarding the design of the perforated disk, there is an inherent trade-off between speed, optical sectioning and light efficiency. If the pinholes, and thereby the excitation foci, are very close, the imaging frame-rate and disk transmittance increases but compromising confocality. Whereas if foci are very far apart, the disk is a wasteful of laser light as only 1-3% of the laser beam is used. The light efficiency of an spinning disk can be calculated as $\propto \frac{d^2}{D^2}$, where $d$ is the hole size and $D$ the distance between holes. For the most advanced systems, microlens arrays are introduced in the disk to collect more light, allowing to reach $\sim 50-60\%$, however 100% is never reached due to mirolenses limited size and packing factor. Although in a multi-point confocal the different features can be slightly tuned, the decision has to be done at the optical design stage. Once the setup is built, the user can no longer improve the sectioning capabilities or light efficiency of the system.

In an effort to make single-point scanners faster, recent CLSMs use resonant scanning mirrors that can reach up to 30 frames per second. However, as a consequence of the resonant mode, the laser position follows a sinusoidal function which results in an image deformation, that has to be compensated off-line. So, even though CLSMs are becoming faster and less phototoxic, and multi-point confocals better in terms of optical resolution, both approaches clearly target two different needs. The high phototoxicity of CLSMs forces the need to fix the specimen, which not only limits life cell imaging, but also the fixation process can alter the behaviour and structure of the specimens [93]. However the optical sectioning they offer make them shine at imaging thick samples. Whereas for live cell imaging multi-point scanners are the choice due

to higher imaging speed, better sample health and more sensitive detectors (with also higher dynamic range).

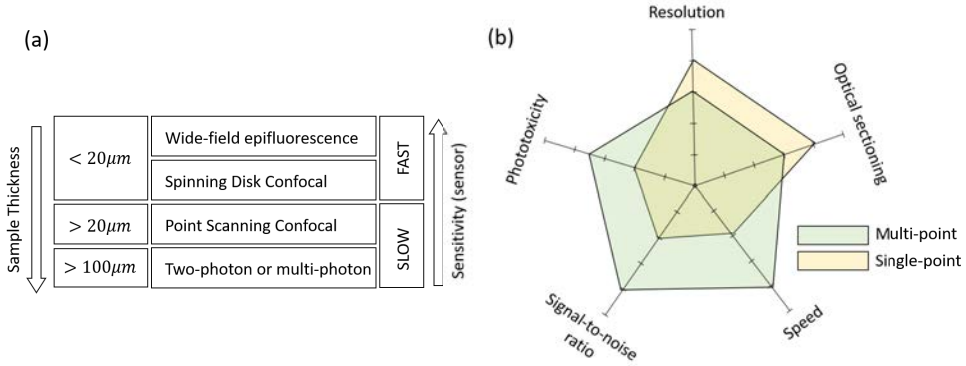


**Figure 5.4:** Comparison between different optical sectioning microscopes.

Figure 5.4 compares the most common and established optical sectioning microscopes for life science applications. There is a clear distinction between different microscopes, each one optimizing one particular image quality indicator to the detriment of the others. This trade-off between the different features, is inherent to the technology used to generate the excitation light patters, and results in an over-specification in the microscopes catalog [94]. Forcing the final user or the imaging facility to purchase the system that best suits their specific application, closing to future experiments that may arise. Or as in most cases, have both types of systems to cover all possible needs.

As a consequence of this trade-off, the idea of combining the capabilities of nearly all optical sectioning microscopes into a single unit is very appealing and has been pursued since 1993, when IBM defined the Programmable Array Microscope (PAM) concept. The key element of a PAM is a light modulation device capable of generating different illumination patterns in order to choose the imaging mode that best suits the needs of the specimen/experiment. For a successful implementation, the arbitrary illumination system needs has to go hand in hand with a filtering system that adapts to these patterns. Unlike CLSMs and spinning diks confocals, the programmable light modulation device of PAMs removes all moving parts and physical pinholes from the optical design, allowing full software control over both the sample illumination and confocal filtering (detection), with all the benefits that this entails. For example, the pinhole size can be dynamically changed or the laser and the filtering aperture can be made to automatically realign when needed.

However, the PAM concept is not only based on imitating the virtues of already existing microscopes. The implementation of a fully working PAM would allow the user to freely move along the multidimensional property space of figure 5.4(b) and therefore investigate optimized excitation patterns and scanning schemes that extract the information in a more efficient and fast manner. Taking as an example speed-vs-sectioning trade-off, the PAM concept allows testing all the intermediate positions

of the curve where CLSMs and spinning discs are opposite extremes. T. Wilson demonstrates that the illumination patterns of a regular CLSMs are not optimal for best optical sectioning [7]. The same applies for the detection system, the flexibility of the camera-based detection system, permits the use of image processing techniques for a more general removal of out-of-focus light than what is possible by a physical pinhole.

The lack of a light modulator element capable of generating all light patterns efficiently and at high speed results in the fact that there is not a single commercially available PAM unit. The designs that have come closest to the PAM objective use a DMD for pattern generation [8, 9, 95, 96, 10] and a regular CMOS camera for detection. In all designs, the DMD is placed at a conjugate sample plane and, usually a grid of points, is generated by tilting the corresponding micro-mirrors (one for each laser position). Then, sample is scanned by shifting the pattern in both directions, and the corresponding camera usually takes an image for each of the scanning positions. The background-flare removal is typically done by means of an algorithm that combines the whole stack of frames into a single high-contrasted reconstruction. An interesting aspect of using a DMD for pattern generation is that the emission light can be "descanned" and the micro-mirrors themselves act as physical pinholes removing the out-of-focus light. This way, the pinhole shape automatically adapts to the excitation pattern. However, the pinhole size can not be changed (by definition is fixed to 1 DMD pixel) it has been demonstrated to not work properly due to very low contrast and pixelation artifacts, reason why a post processing algorithm is always needed. This can be seen on the prototype in [96], where both descanned image and complementary image are subtracted for better optical sectioning. Moreover, the fact that DMDs work by reflection imply a pattern-depending light effiency, extremely low for sparse reconstructions. Finally, pixelization effects limit both the point separation and the pattern shift to be a multiple of the pixel size. Most of the improvements in current PAMs are based on simply using faster and more pixelated DMD devices, offering a higher resolution and arbitrariness of the generated patterns.

## 5.2 The SCREAM microscope: optical setup

The PAM prototype presented in this thesis, takes a completely different approach. Instead of using the same DMD technology as other PAM attempts, our PAM unit is designed using the AOSLM described in chapter 4. In summary, by means of the AOH algorithm described in section 4.1.2 different Fourier holograms, in the form of complex RF signals, are calculated, synthesized and injected into each AOD cell. Producing, in turn, a complex acoustic wave that modulates the refractive index and therefore the laser wavefront. Which is diffracted taking the desired shape.

### 5.2.1 Custom designed AOD for multiple wavelengths

The advantages of using an AOSLM with respect of a DMD are several. The fact that AO devices are diffractive elements result in a better light diffraction efficiency. The efficiency of an AOD does not depend on the reconstruction, the Bragg condition defines the ratio between the modulated and non-modulated orders, but in all cases the number of photons exciting the specimen is the same. Whereas for a pixelated DMD, the overall reflectance of its display depends on the ratio between the number of pixels in the "ON state" and the "OFF state". As an example, if one laser beam is desired (to imitate the performance of a CLSM) only 1 pixel is switched on at each time. The resulting efficiency would then be $\frac{1}{NxNy}$, being $Nx \cdot Ny$ the DMD screen resolution. Assuming 1Mpix DMD (1024x1024) and an homogeneous laser illumination the efficiency becomes $9.5 \cdot 10^{-5}$%, whereas for the AOD almost 60%. On the opposite part, for a wide-field illumination the DMD efficiency would be almost 100% and 60% for the AOD. A more realistic case is to imitate the spinning disk confocal microscope, in which the sample is illuminated with $\sim 1000$ beams, here the DMD efficiency is 9.5%, but still 6-times less efficient. In practical terms, this low and pattern-depending efficiency results on the need of more powerful and expensive lasers.

In terms of light modulation capabilities, both AODs and DMDs are extremely fast devices, DMDs can reach up to 20kHz whereas, as seen in previous chapters, AODs can go up to 130kHz (or even more by reducing the beam size). However, either of them have to compromise modulation speed to benefit from purely arbitrary intensity patterns. For the case of DMDs, by definition they can only project binary patterns. Gray levels are achieved by means of non-coherent superposition of different patterns and camera integration, at the expense of reconstruction speed. Intensity depth modulation is quite important to, for example, compensate for the non-homogeneous illumination (Gaussian laser distribution) resulting on dimmer intensity values at the image boundaries.

On the other side, by means of AOH, AODs can project almost any intensity pattern, its modulation depth depends exclusively on the voltage resolution of the AWG (16-bit). However, in order to benefit from the full speed modulation, intensity patterns are mathematically constrained to be XY separable patterns (section 4.2). In any case, we believe that for microscopy applications, the balance is opting for AODs. The number of separable patterns needed is lower than the ones needed to modulate $2^{16}$ gray levels with a DMD. On top of that, the modulation speed of AODs is still 6-times greater.

Is in multi-wavelength operation where DMDs, and also LCOS-SLMs, work better than AODs. The multi-wavelength performance of a DMD typically depends on the micro-mirror coating, so for metallic coatings the reflectance becomes constant over the visible spectrum (400-700nm). For an LCOS-SLM, although the manufacturers specify the operation wavelength, one always can use it for a shorter wavelength just by re-calibrating the LCD lookup table, at the expense of bit-depth. For example, using a 1064nm display with 532nm results in a reduction from 256 to 128 phase

values.

The ability to work with different wavelengths is essential, multiple laser lines allow exciting several structures at the same time, marked with different fluorophores. The number of channels a confocal device supports is as important as image quality or field of view. Handling multiple wavelengths with the same AOD is rather difficult. By looking at the Bragg condition in equation 2.6 and momentum-space diagrams of figure 2.4, it can be deduced that when the AOD is aligned for maximum diffraction efficiency at $\lambda_1$, i. e. the incidence angle $\theta_1$ fulfills Bragg condition, the read-out at a shifted wavelength $\lambda_2$ produces a drastic loss on diffraction efficiency. The reason to that is because, at $\lambda_2$ the new incident vector $\vec{k_2}$ has the same direction but slightly different length (assuming a constant refractive index), introducing an axial offset of $\sin\theta(|\vec{k_2}| - |\vec{k_1}|)$ causing a momentum mismatch $\Delta k_z = 4\pi\frac{\sin^2(\theta)}{\cos(\theta)}\left(\frac{1}{\lambda_2} - \frac{1}{\lambda_2}\right)$ that affects the diffraction efficiency following equation 2.14. In practical terms, the use of a different $\lambda$ has the same effect as changing the incidence angle $\theta$.

For a new $\lambda_2$, equation 2.6 tell us that we can realign the new laser in such a way maximum diffraction efficiency is recovered. This is not a possible solution for microscopy applications, since would imply a realignment of the laser beam for every channel. In a commercial confocal unit, all the lasers are combined into a single mode optical fiber, which plugs into the main element, the confocal scan head. One possible solution would be to separate all different laser lines with multiple dichroic mirrors (inside the confocal head), and then introduce a slight angle to each of them in such a way each line fulfills Bragg. However, different incidence angle means also different diffraction angles, the deflection area would be different for each line. Different specimen regions would be excited with only one particular wavelength, and the common area would be very small.

Most of the AODs on the market are designed to maximize diffractive efficiency and deflection angle for one particular wavelength. The AOD used in our PAM prototype has been specially designed to work efficiently with two wavelengths at the same time. This means that, when entering the AO cell with the same incidence angle, both lasers are diffracted efficiently while sharing almost the same deflection area. This device simplifies a lot the optical design, between the fiber tip and AODs all wavelengths are collinear. Allowing us to use less optical components and shrinking down the prototype's footprint.

The design of a custom AOD is an engineering process very similar to lens design, where the desired performance parameters are introduced into a merit function, that is minimized by varying different construction parameters, such as the cutting angle of the AO crystal and the geometry of the piezoelectric transducer (controlling the size and divergence of the acoustic wave). In practical terms, during the design process, what is sought is to increase the frequency range for which the Bragg condition remains valid. Depending on the AO cell constitution, increasing the bandwidth of the AOD can result in: either increasing the maximum deflection angle for a single wavelength, or as in our case, keeping a reasonable field of view for two simultaneous wavelengths.

This multi-wavelength AOD customization has been made in collaboration with AA

Optoelectronics where the initial requirements were:

- It has to work with 4 different laser lines, 405, 488, 561 and 633nm, the most used in confocal microscopy, covering the excitation spectra of most of the fluorophores on the market.
- The diffraction efficiency has to be higher than 50%.
- The deflection areas for all wavelengths have to overlap as much as possible, more than 50%.

Meeting all the requirements is almost impossible, one parameter can be optimized but to the detriment of the others. For example, one can cover the whole visible spectrum at the expense of reducing the deflection angle. Actually this is the reason why AOTFs and AODs are different devices, and the ideal device for fluorescence microscopy applications is something in between".

The resulting prototype is a custom AOD modulator that works efficiently for 488 and 561nm. It was not possible to include the extremes of the visible spectrum (405 and 633nm), where the Bragg condition mismatch $\Delta k$ is too high. However, in chapter 7 we show experiments with a 405nm UV laser, demonstrating that the AOD still diffracts in UV, although in a less efficient way. The specification of the custom AOD are listed in the table below:

| | 488nm | 561nm | 1064nm |
|---|---|---|---|
| Central frequency $f_c$ | 83.5MHz | 80MHz | 75MHz |
| Bandwidth $\Delta f$ | 53MHz | 50MHz | 30MHz |
| Scan angle $\Delta\theta$ | 40mrad | 43mrad | 49mrad |
| Common angle | 33mrad | | |
| Apperture | 7.5mm | | |
| Material | $TeO_2$ | | |
| Laser beam diameter $D$ | 0.5-6mm | | 1.2-6mm |
| Max. accepted RF power | 1.1W | | 2.2W |

**Table 5.1:** Specifications of the custom modified AOD. The 1064nm AOD from the optical tweezers setup is also described for comparison.

As can be seen in table 5.1, the specifications of this custom AOD for the visible spectrum are very similar to the one used in the the previous chapters for optical tweezers applications. However, the fact that is designed for shorter wavelengths results on a less power demanding device, as can be deduced from equation 2.10. For the near-IR AOD $\sim$ 75% maximum efficiency is achieved with 2.2W, whereas here $\sim$ 60% with less than 1.1W (see figure 2.5).

Regarding the RF bandwidth, the custom AOD accepts approximately 50MHz for both laser lines, which corresponds to a bandwidth $\sim$ 60% higher than the near-IR, single-wavelength version. Moreover, it has been designed in such a way the scan

range for both colors fall within the same 50-115MHz range, since they share the same impedance matching circuit. For 488nm the frequency range is 57-110MHz and for 561nm is 55-105MHz. However, even though the bandwidth is almost twice than the near-IR device, the scanning range is quite smaller (40 and 43mrad compared to 49mrad). AODs obey the laws of diffraction, so it is intuitive to see that all diffracted angles are proportional to the incident laser wavelength. This is the reason why for the same material $TeO_2$ and same frequency range, the 561nm laser is deflected at slightly higher angles than the blue 488nm laser. In terms of AOH, this means that for the same RF induced refractive index modulation $n(x, y)$, i.e. the same acousto-optic hologram, the reconstruction will be larger for the green laser.

Apart from a different Optical Fourier Transform $\lambda_0 \cdot f_{obj}$ scaling factor, both modulated areas are slightly offset due to custom AOD design limitations. There is a 3.5MHz difference between each central frequency $f_c$. Even though the scan angle for each individual wavelength is 40 and 43mrad respectively, the common area is just 33mrad, which corresponds to a 76% overlapping. Translated to the sample plane, this means that a higher field of view (FOV) can be observed with just one color. Two color images can be obtained, but at the price of a reduced FOV, see figure 5.5. However, it is possible to achieve 100% FOV overlapping by introducing a custom dichroic mirror system, as we will show in the next sections.

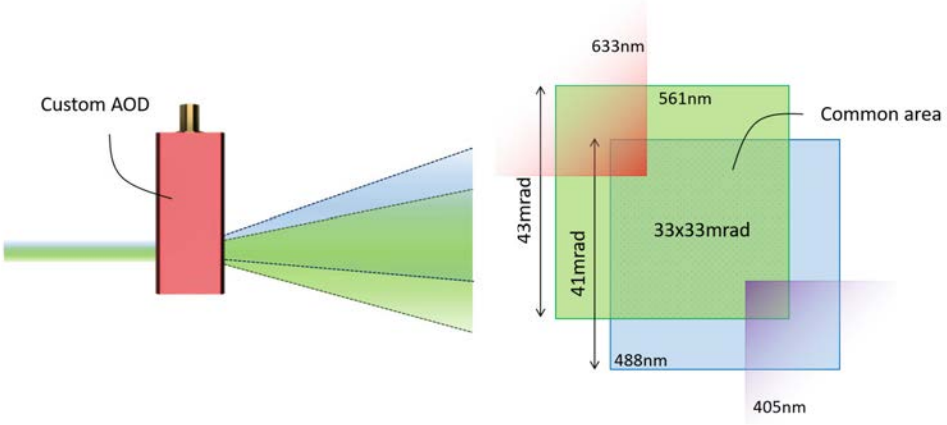


**Figure 5.5:** Custom designed AOD for multiple-wavelengths.

### 5.2.2

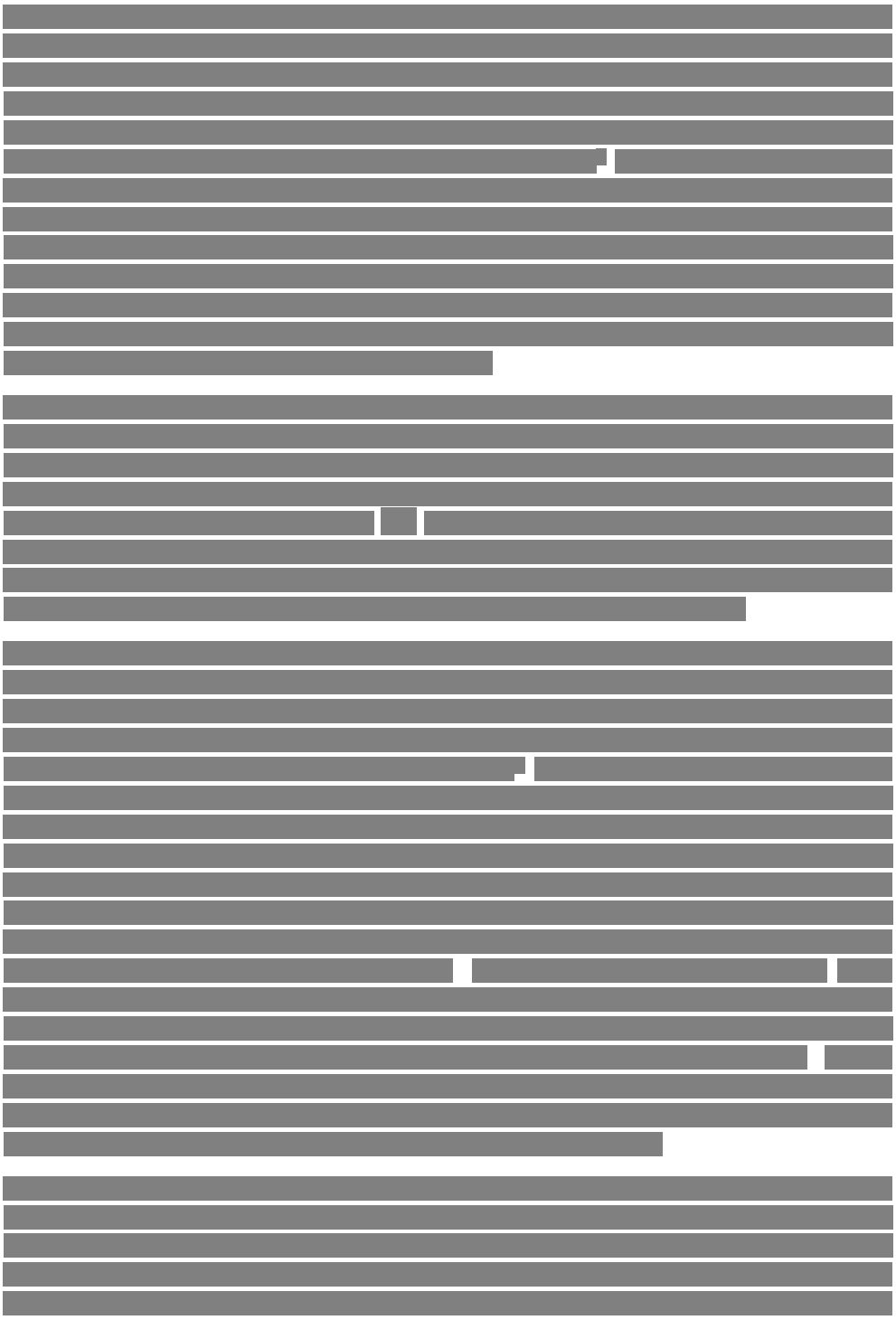

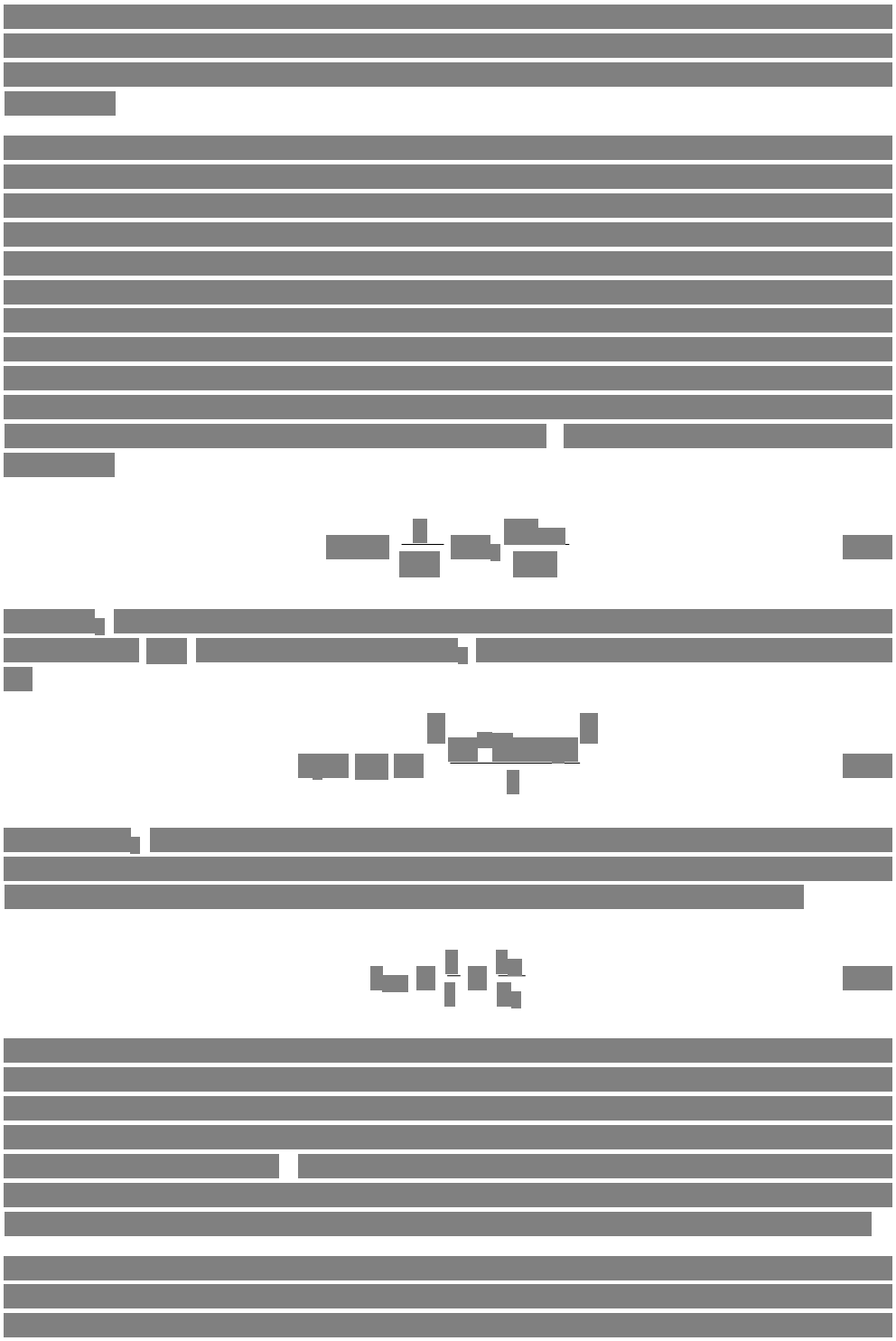

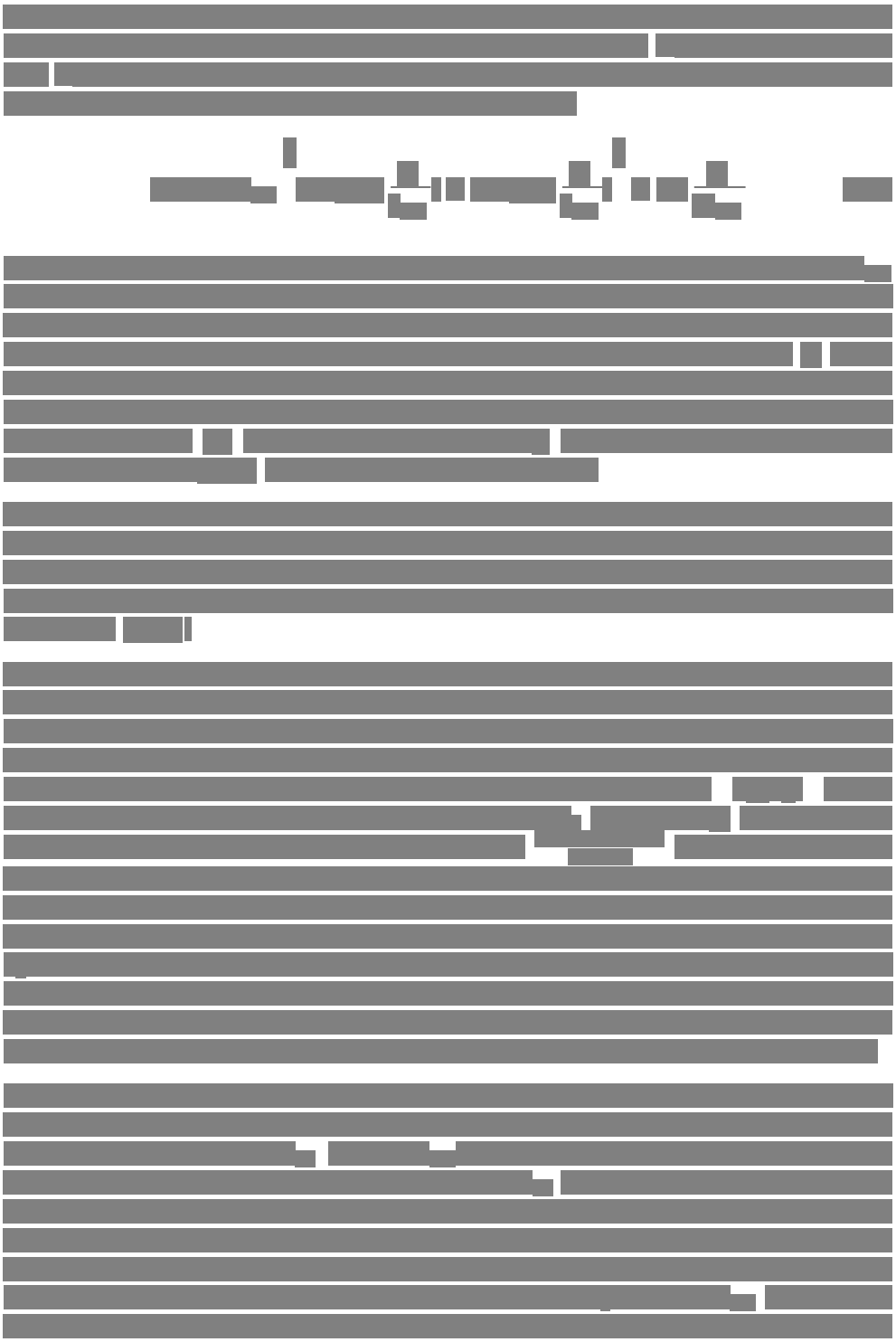

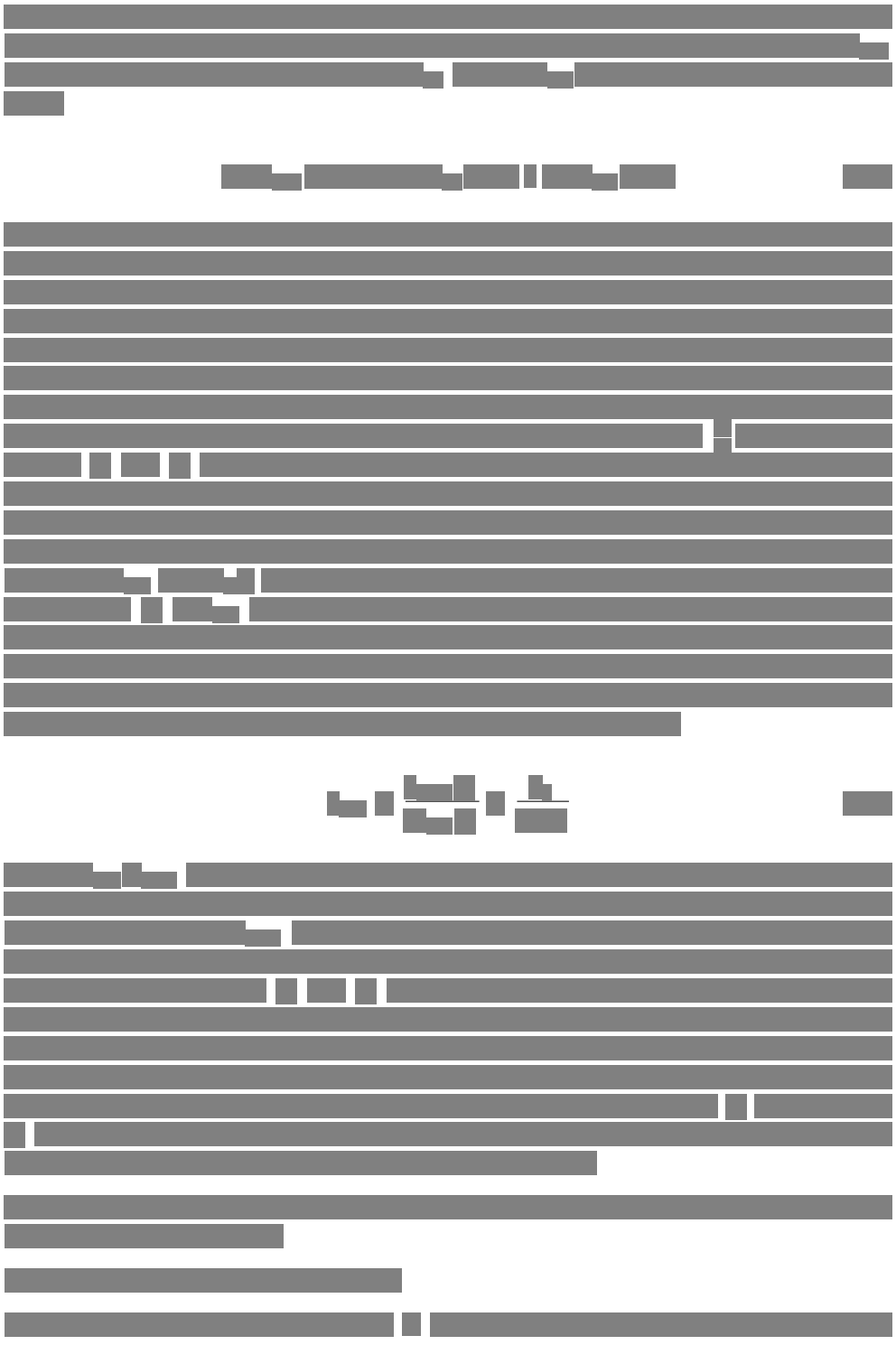

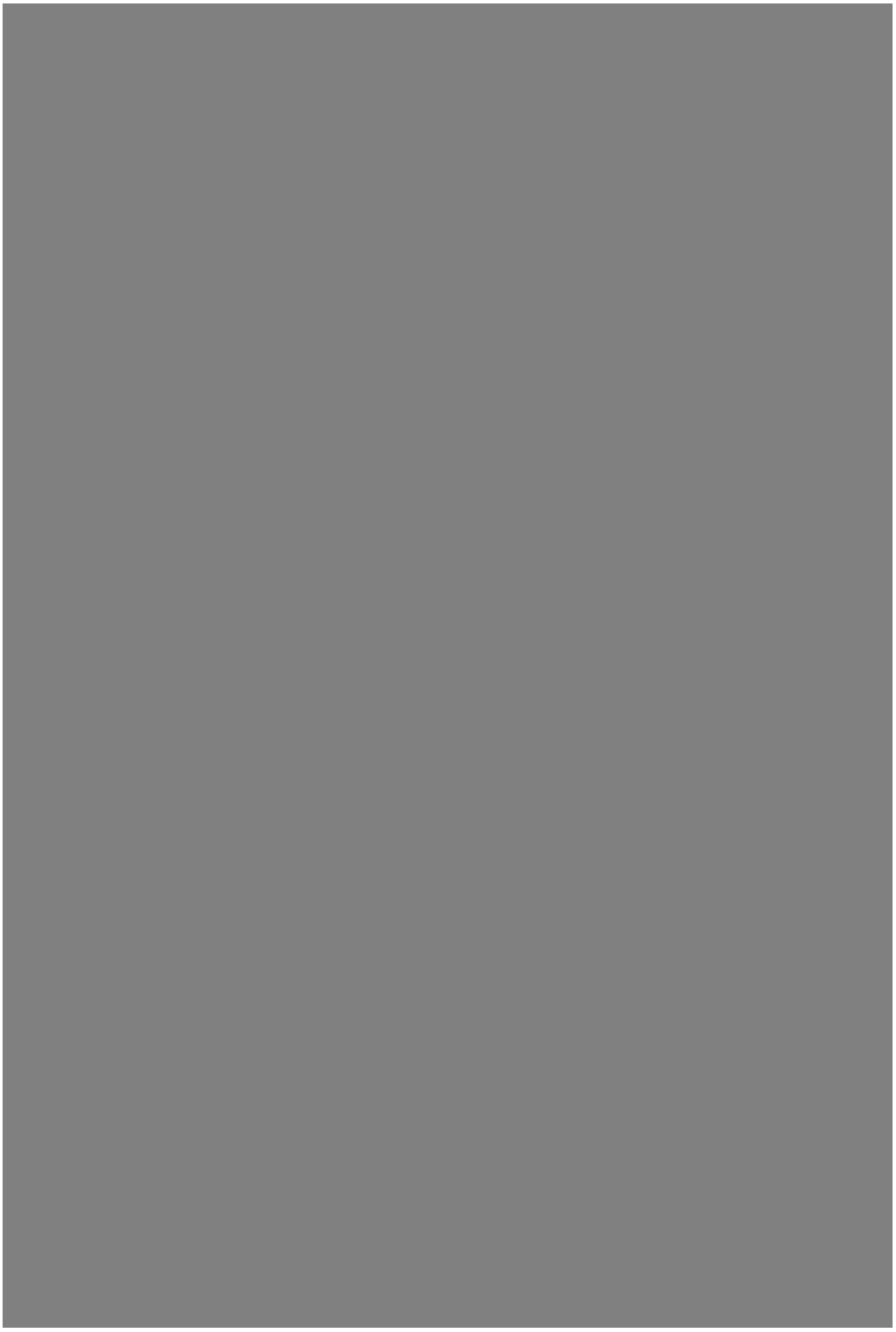

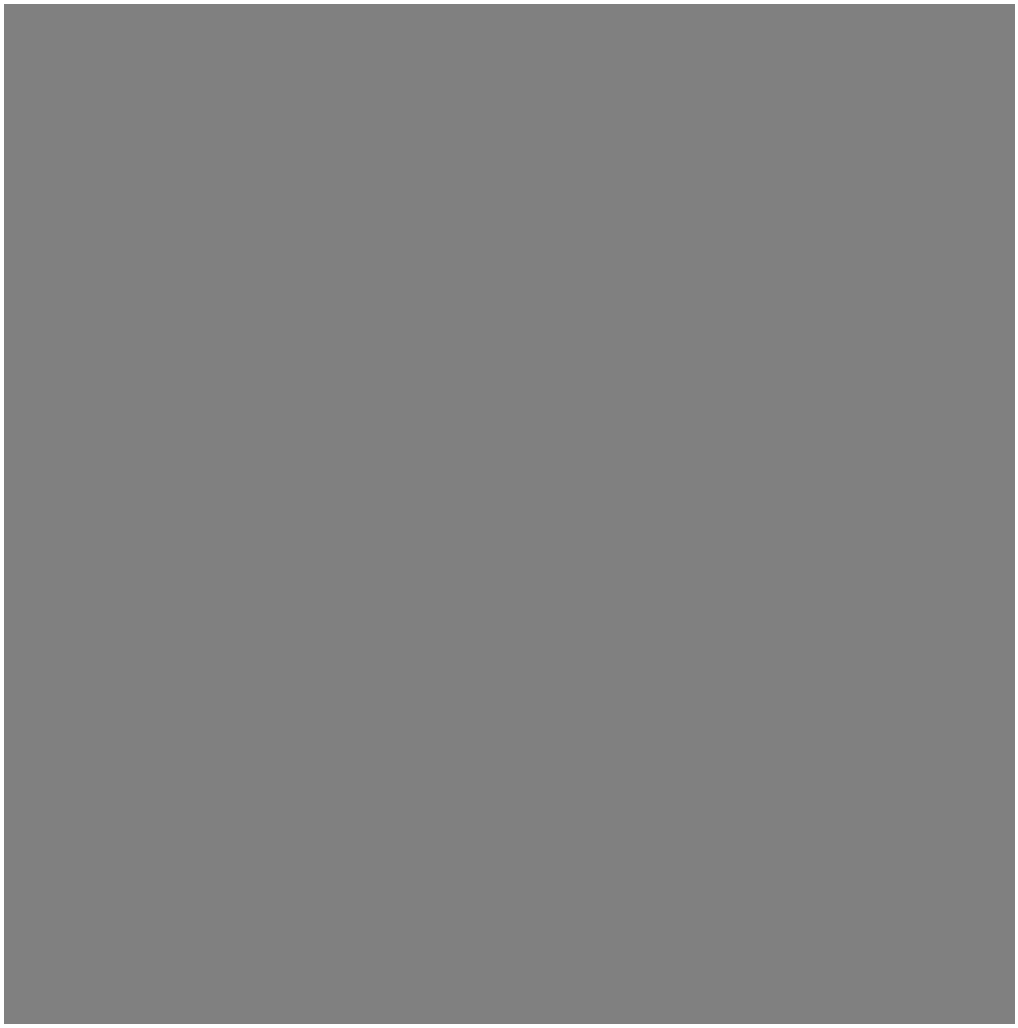

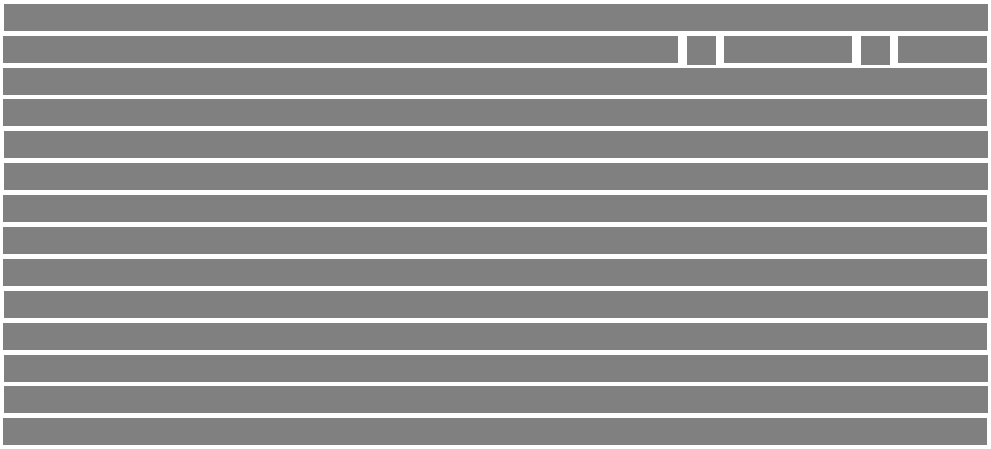

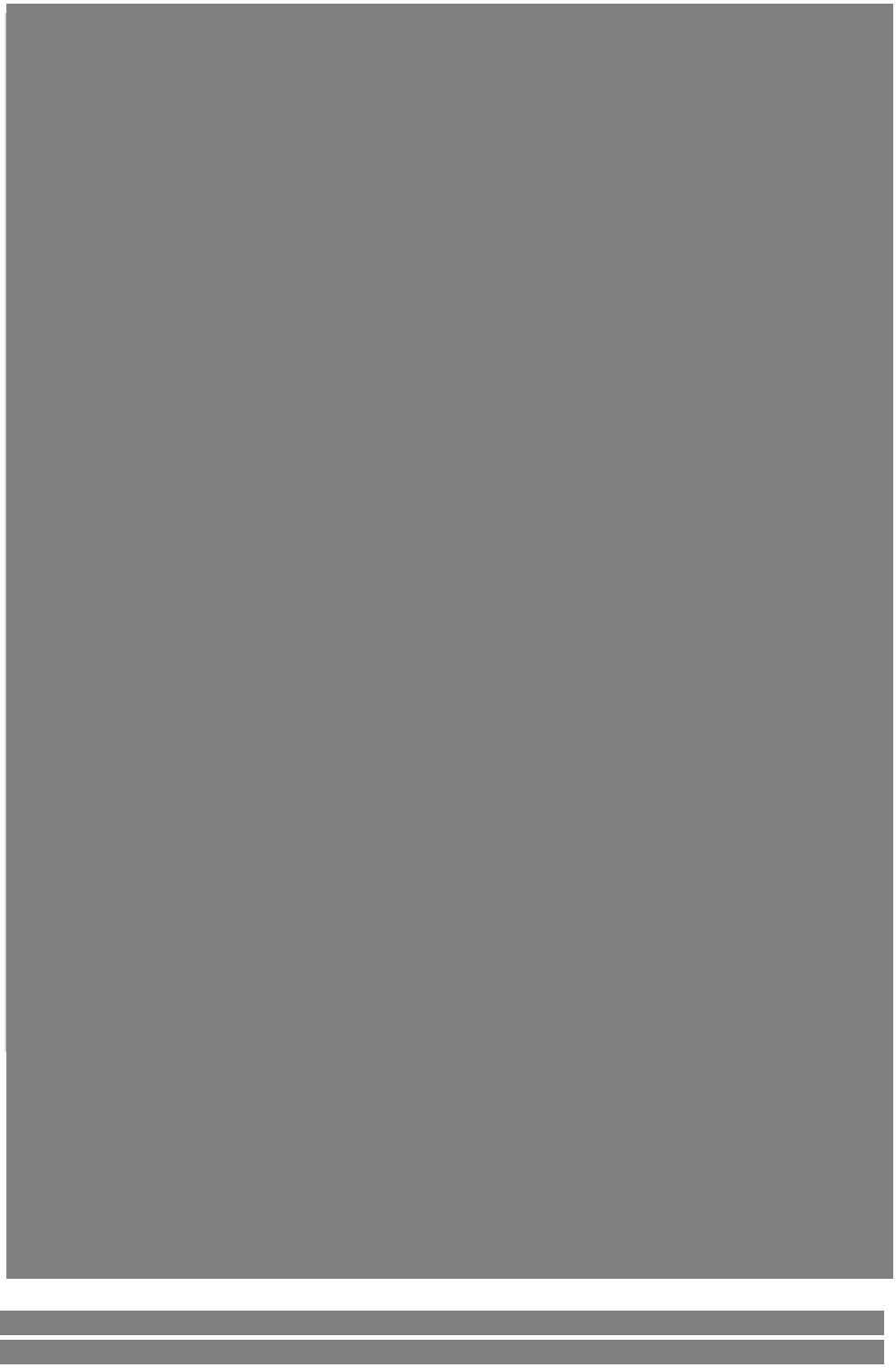

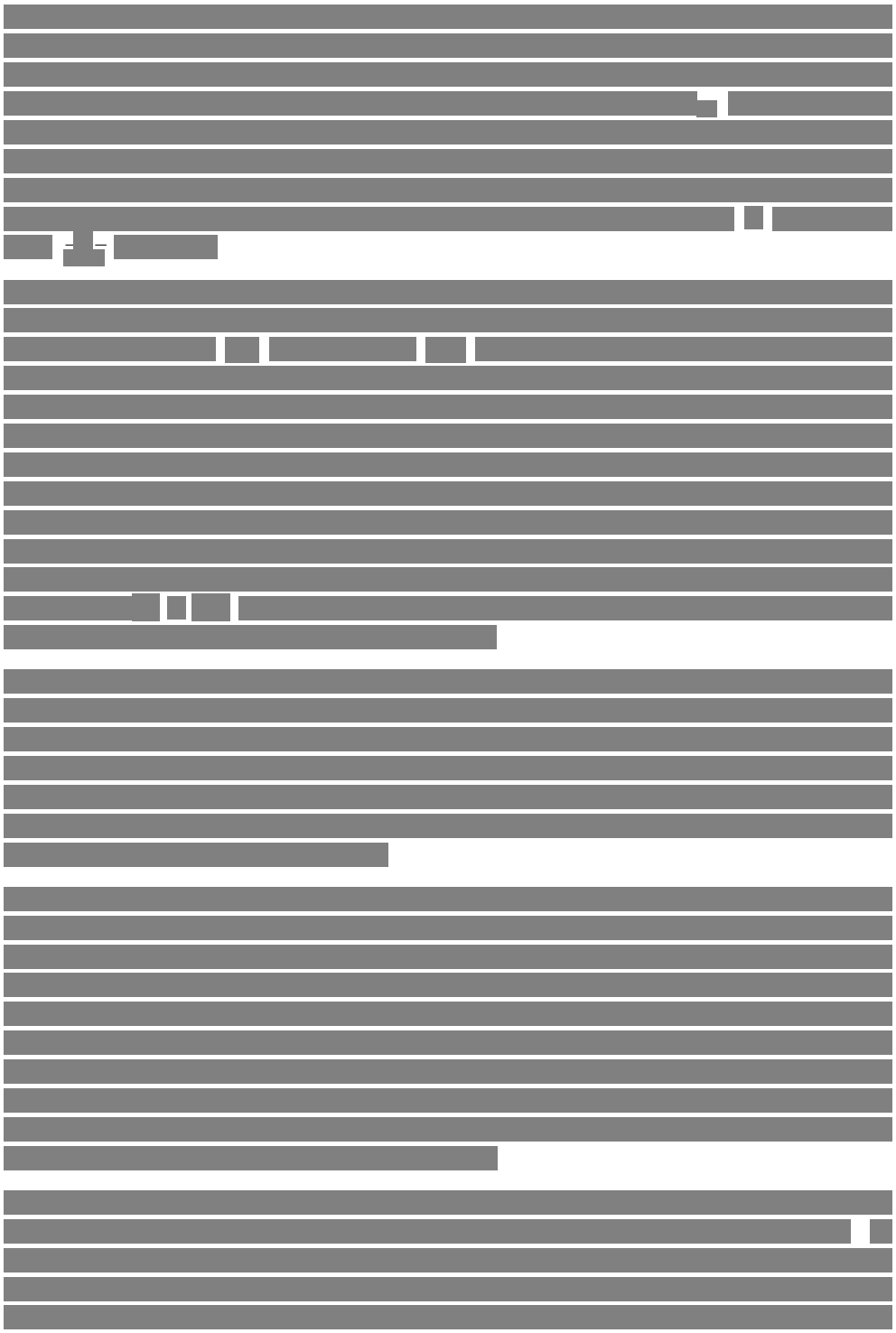

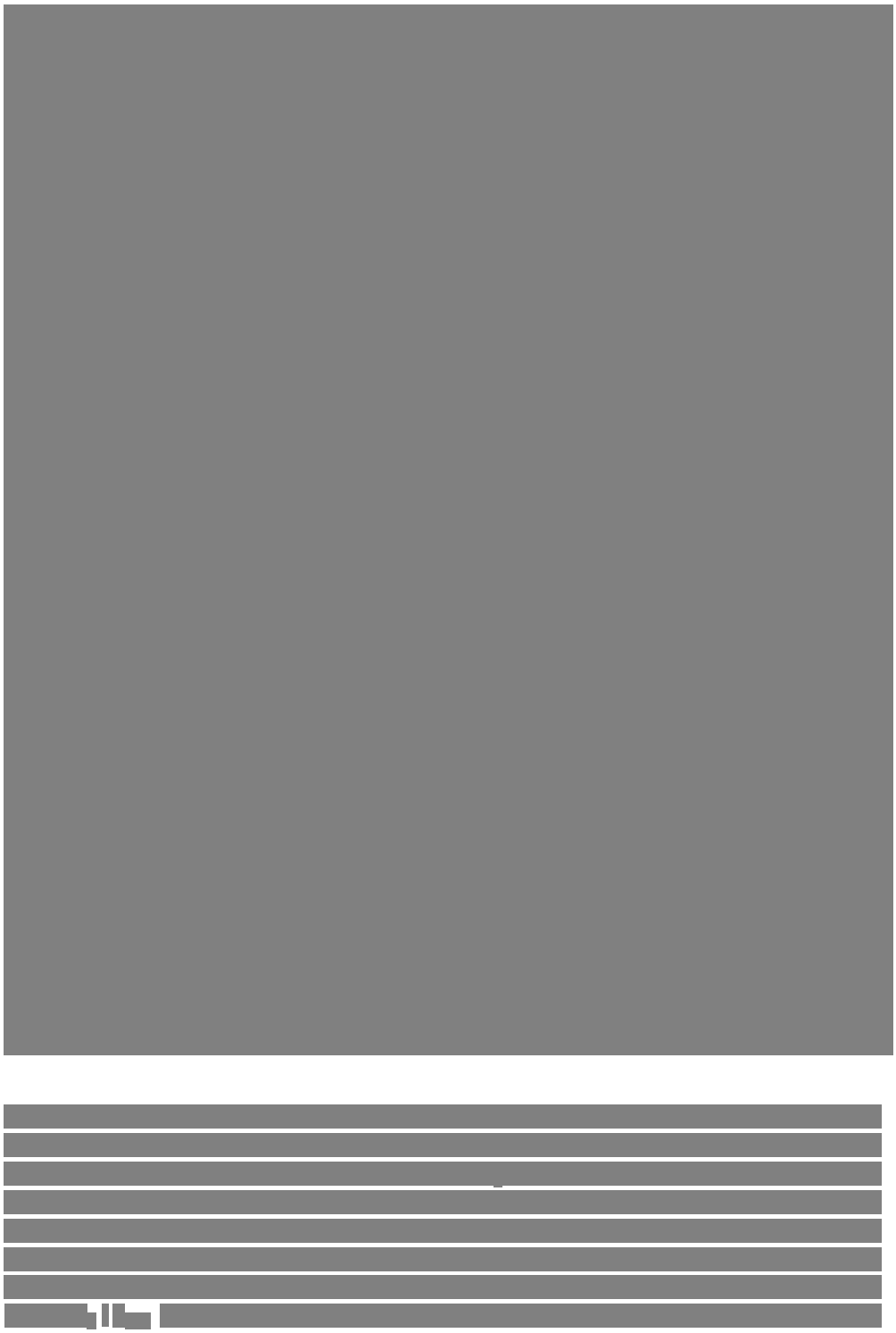

## 5.3

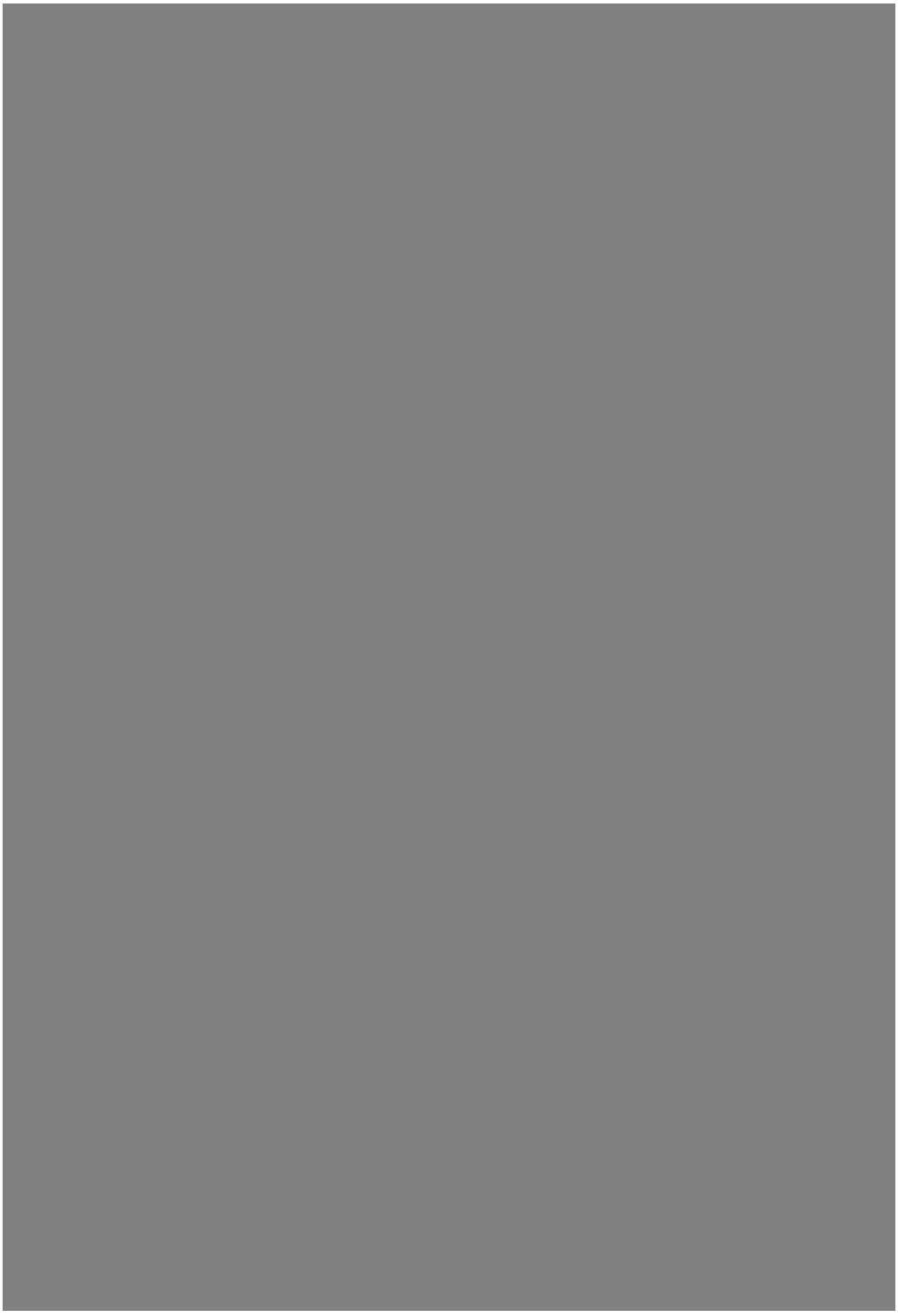

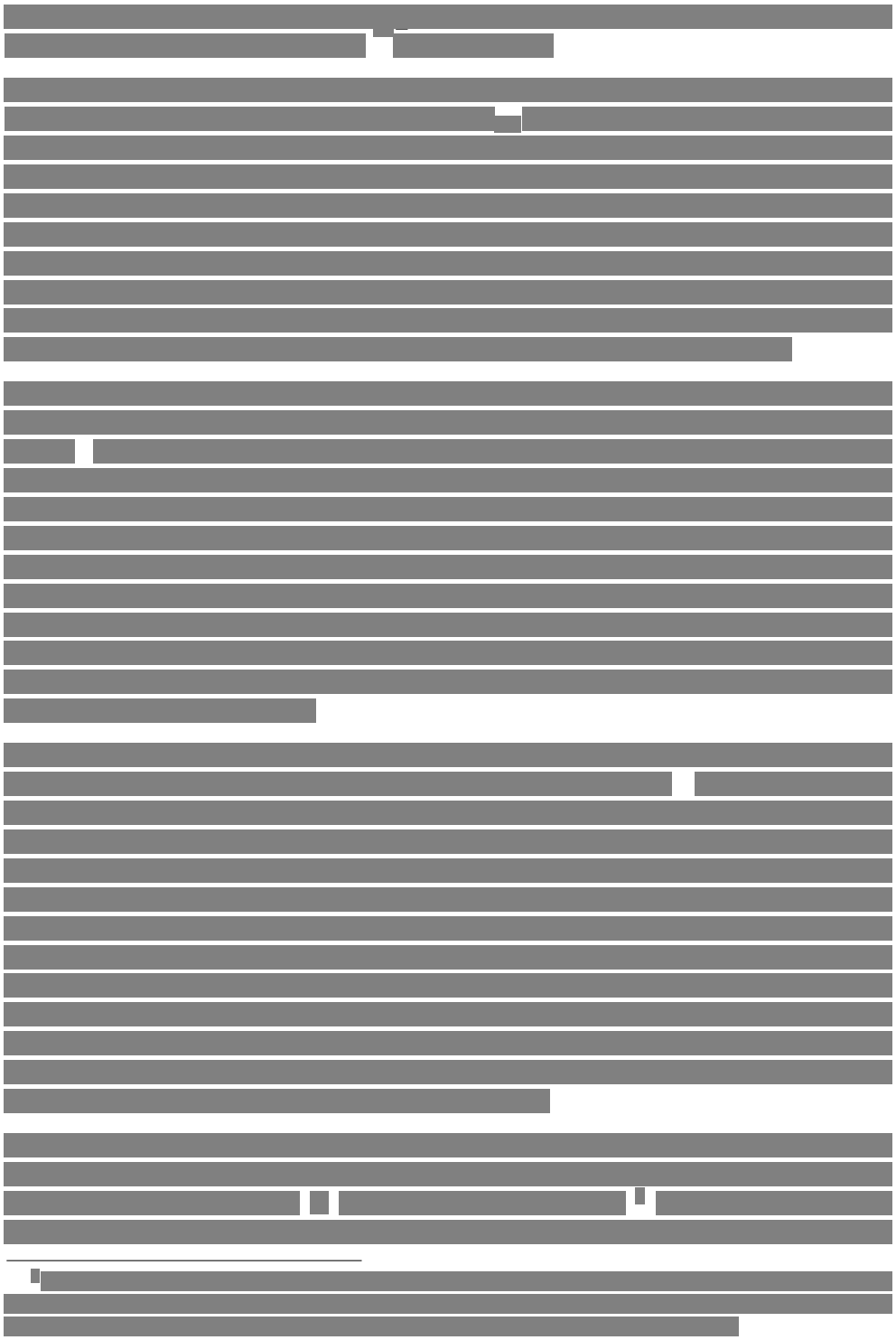

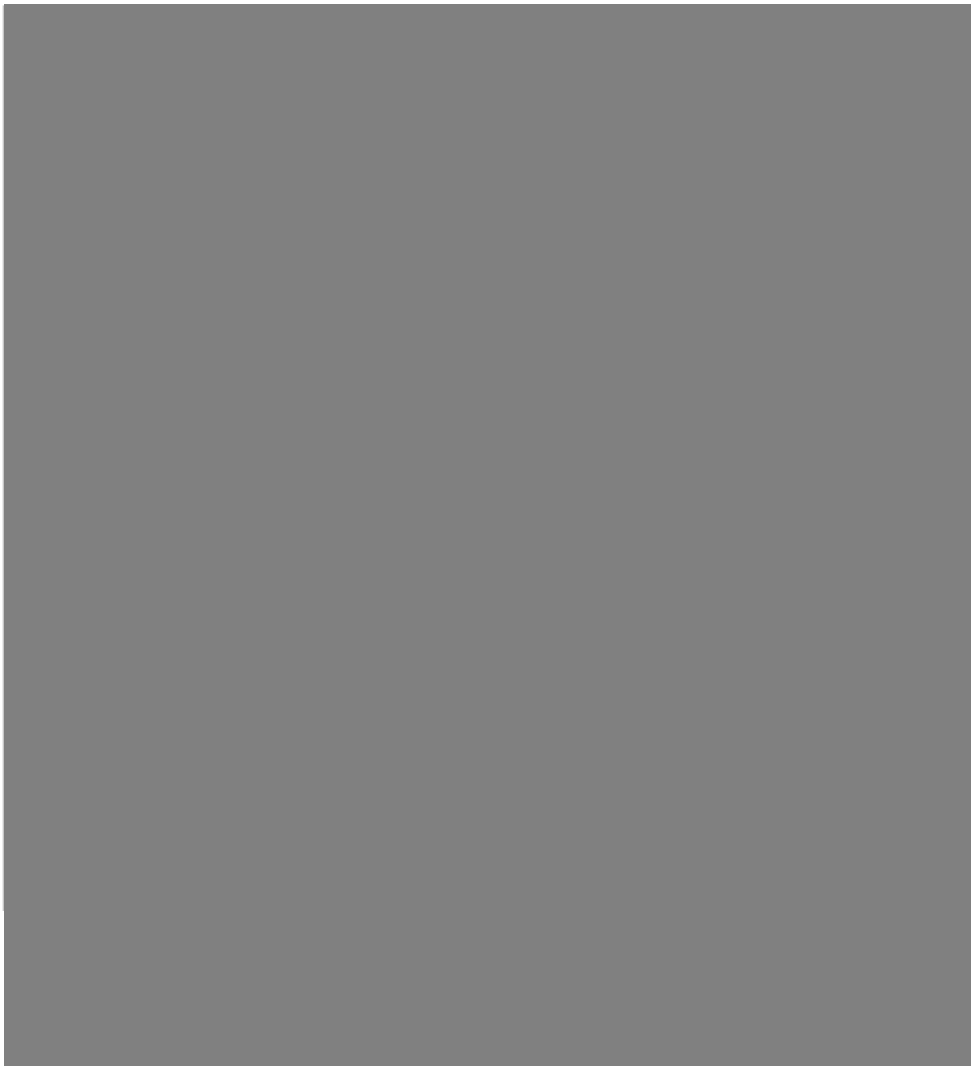

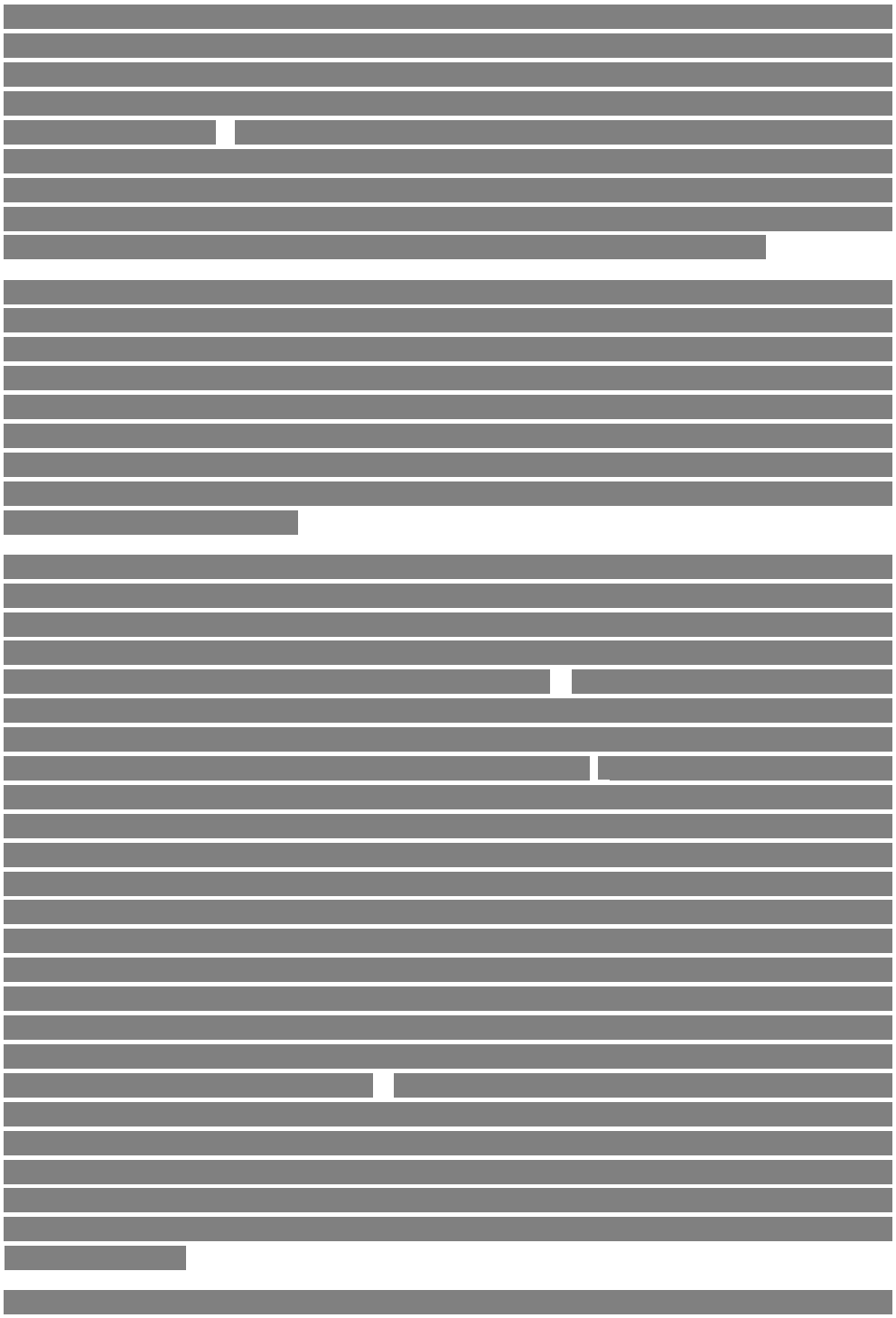

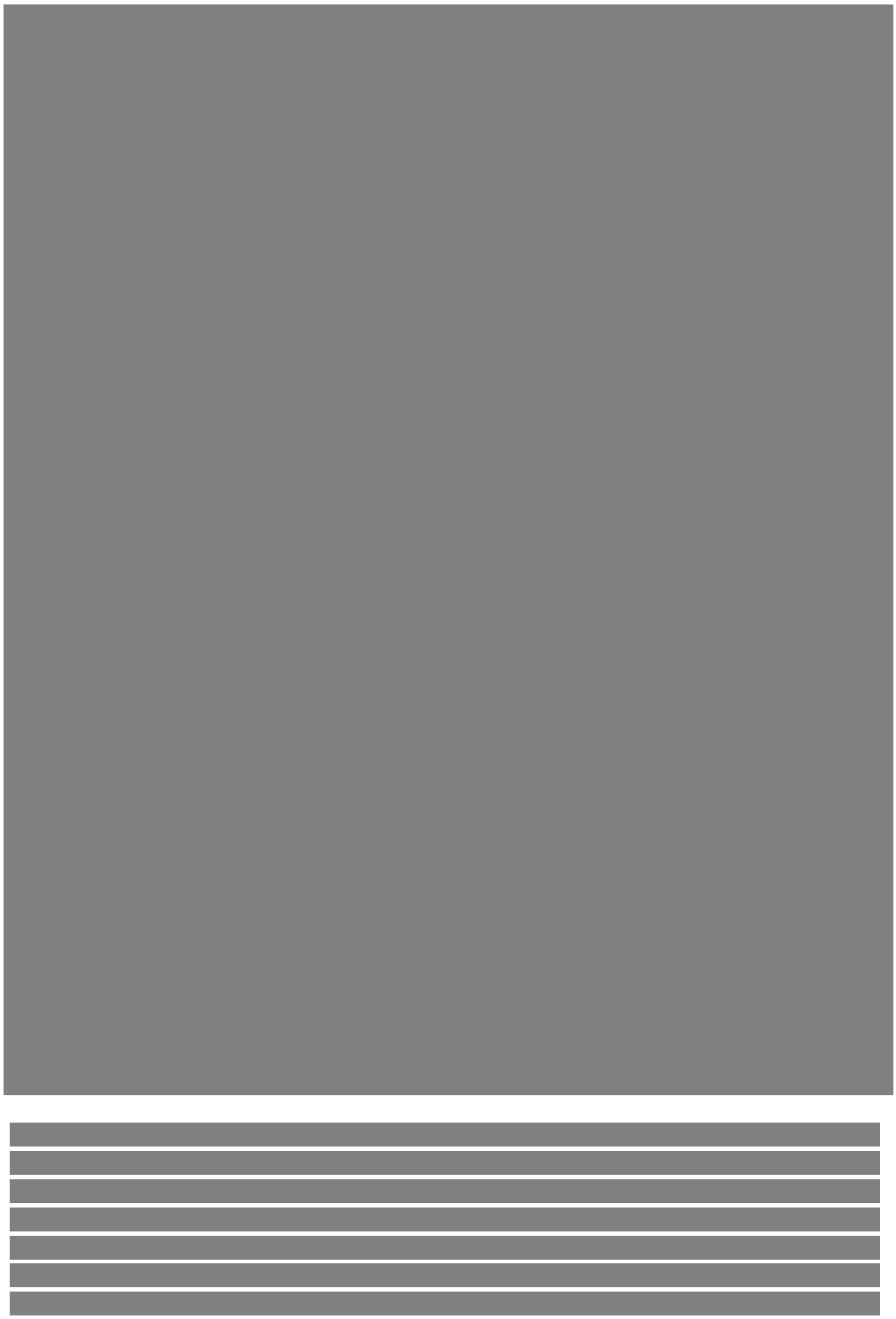

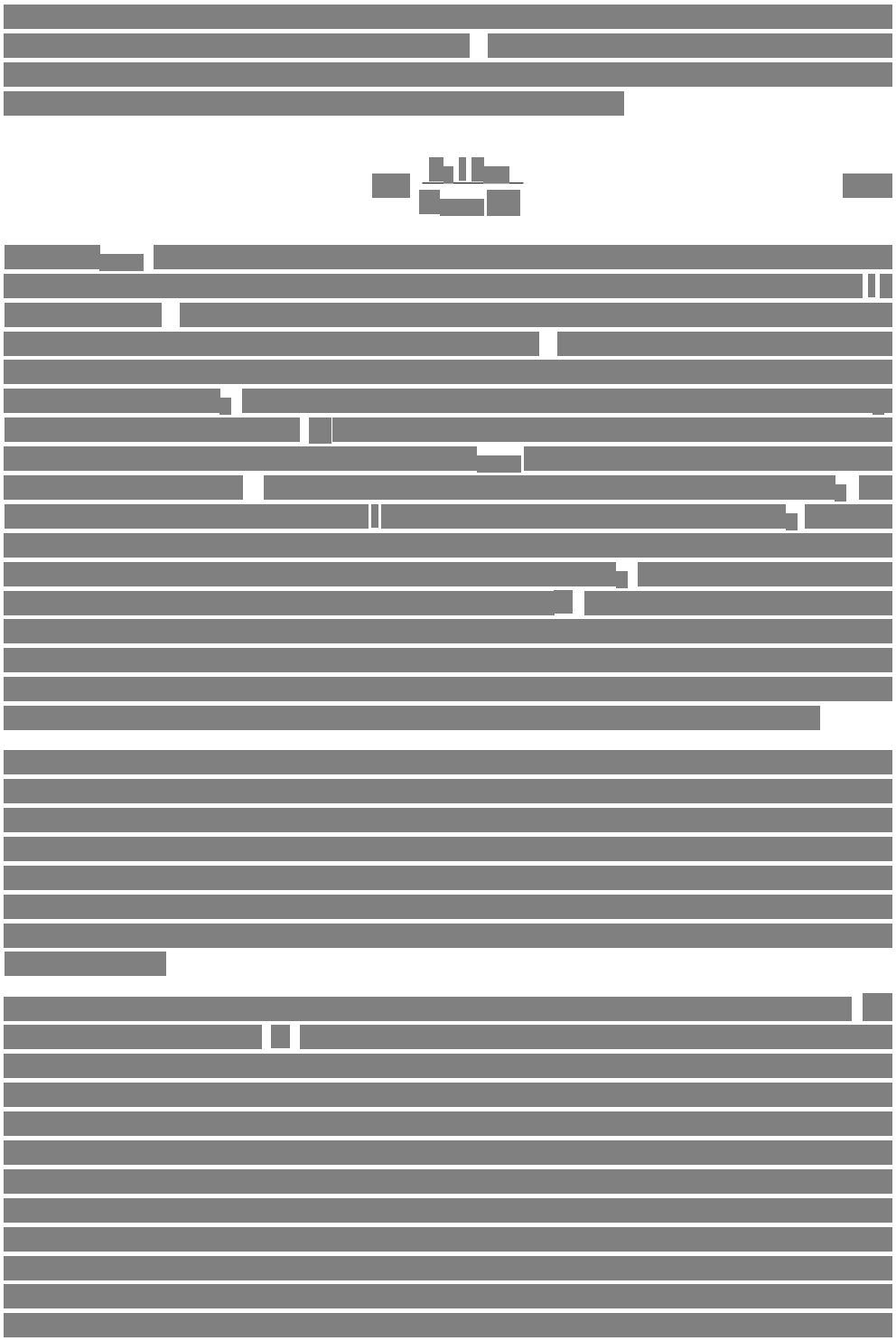

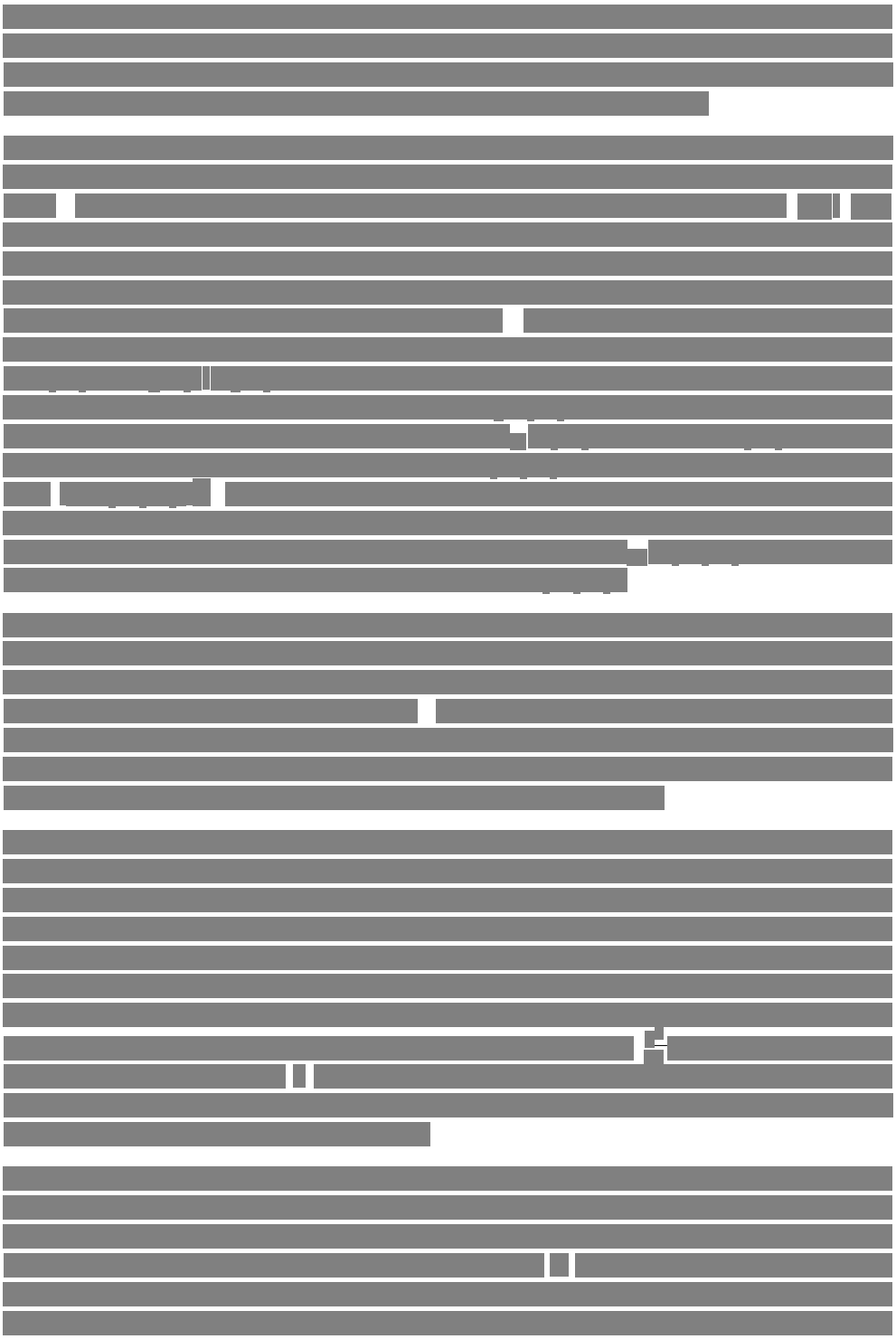

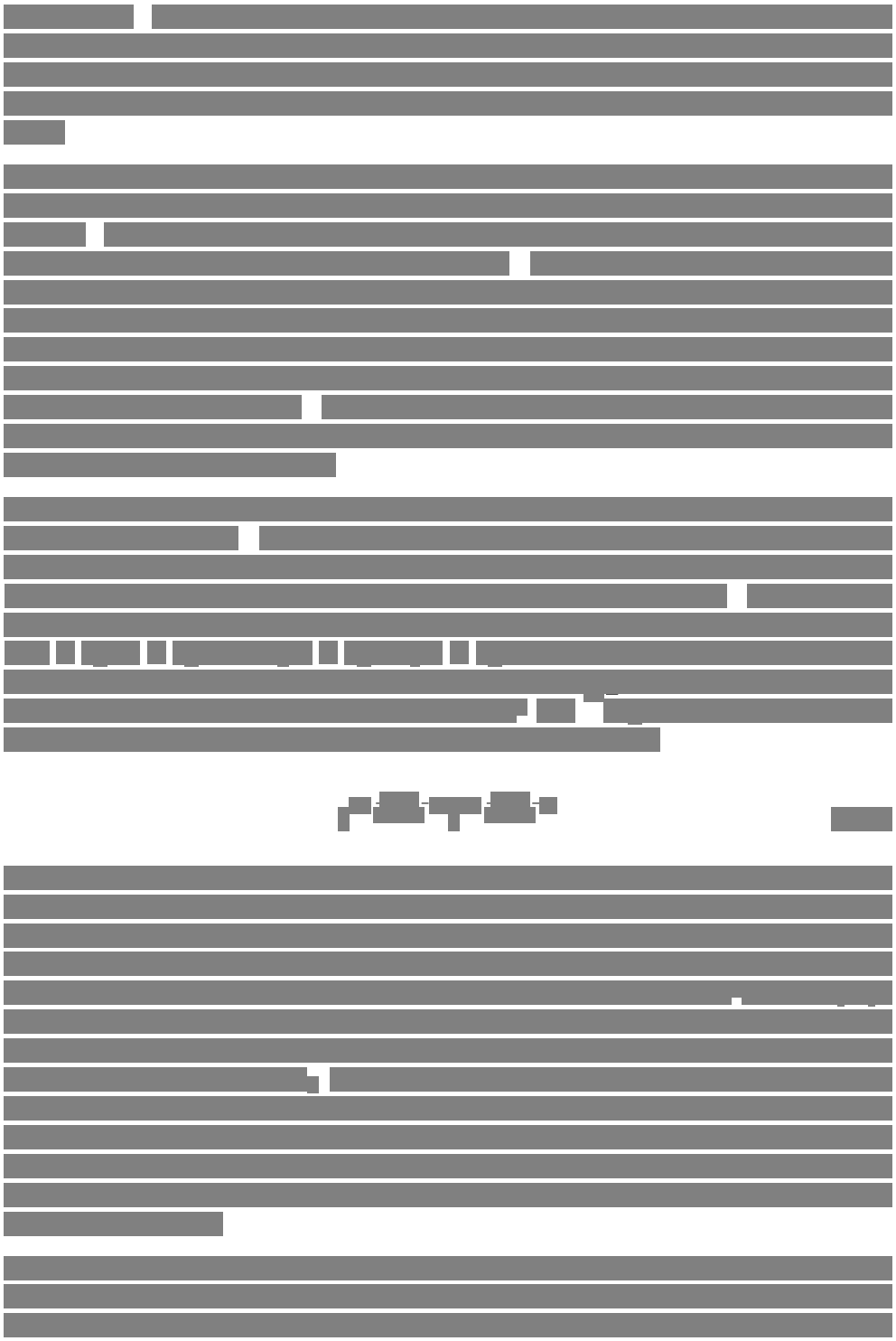

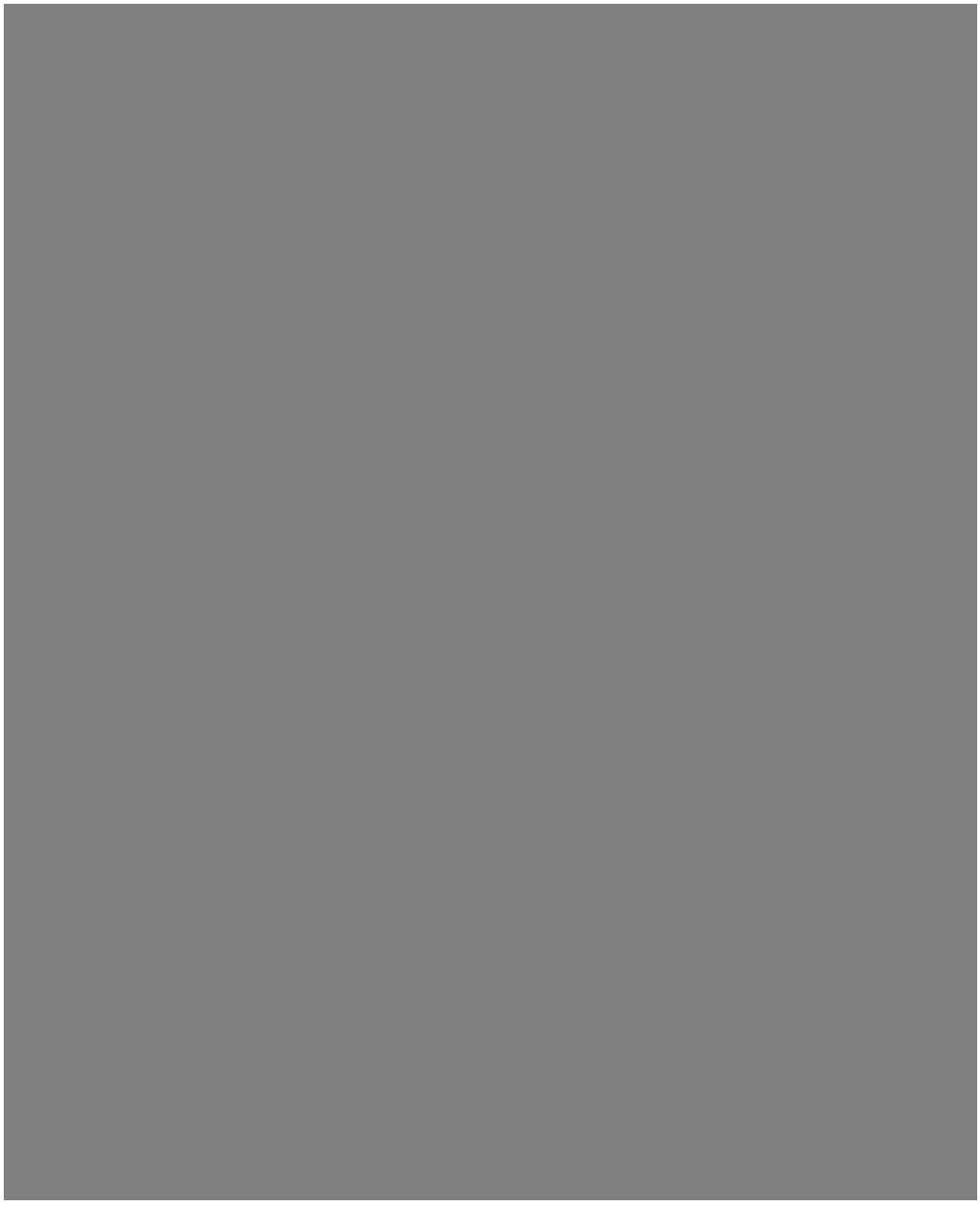

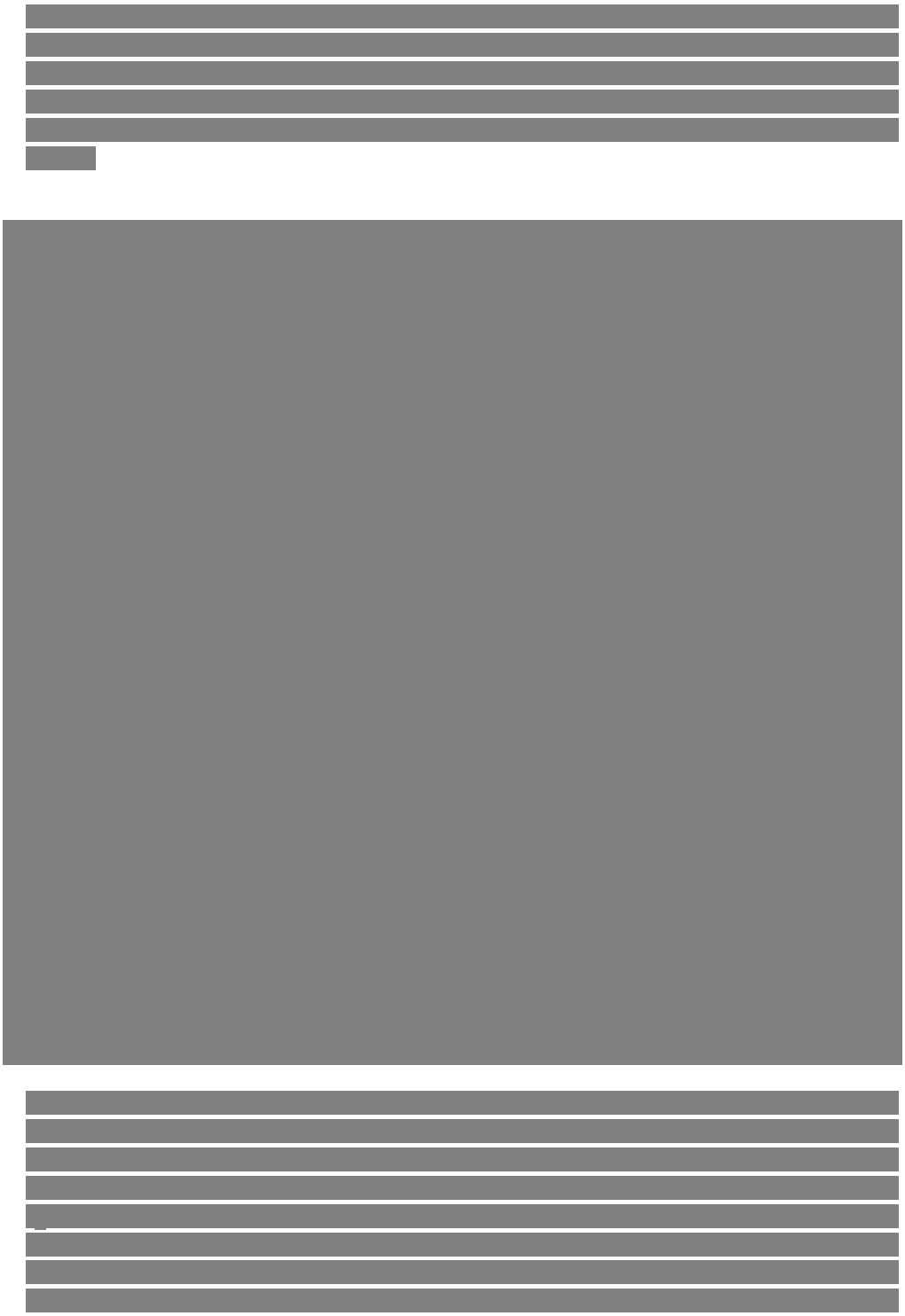

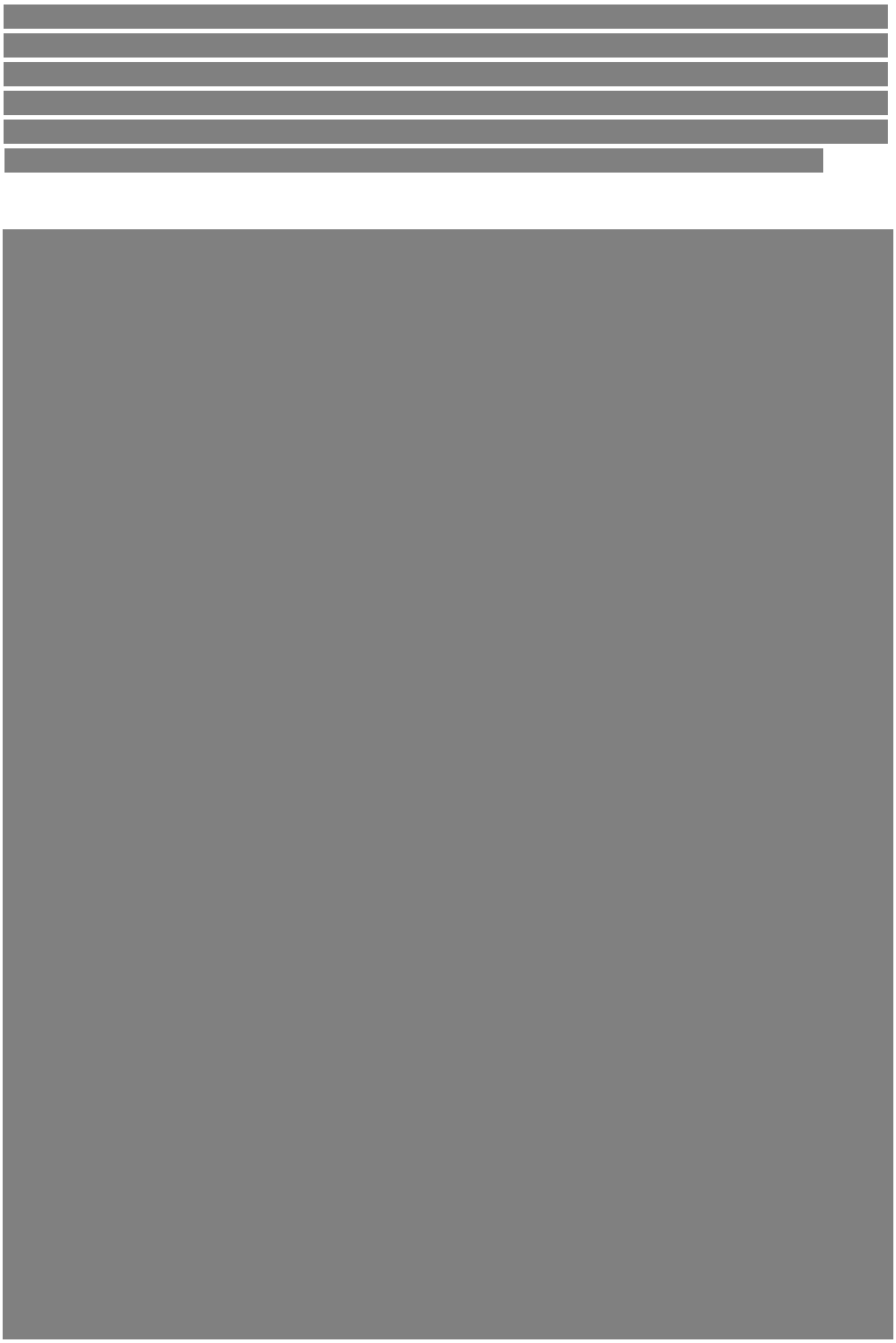

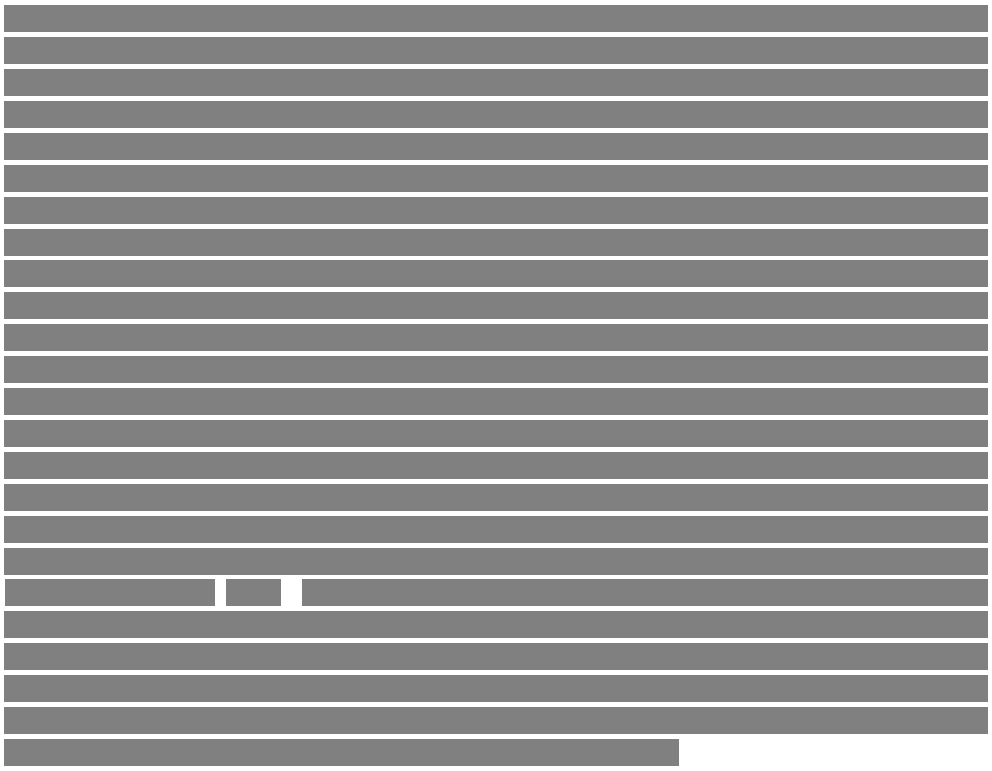

## 5.4

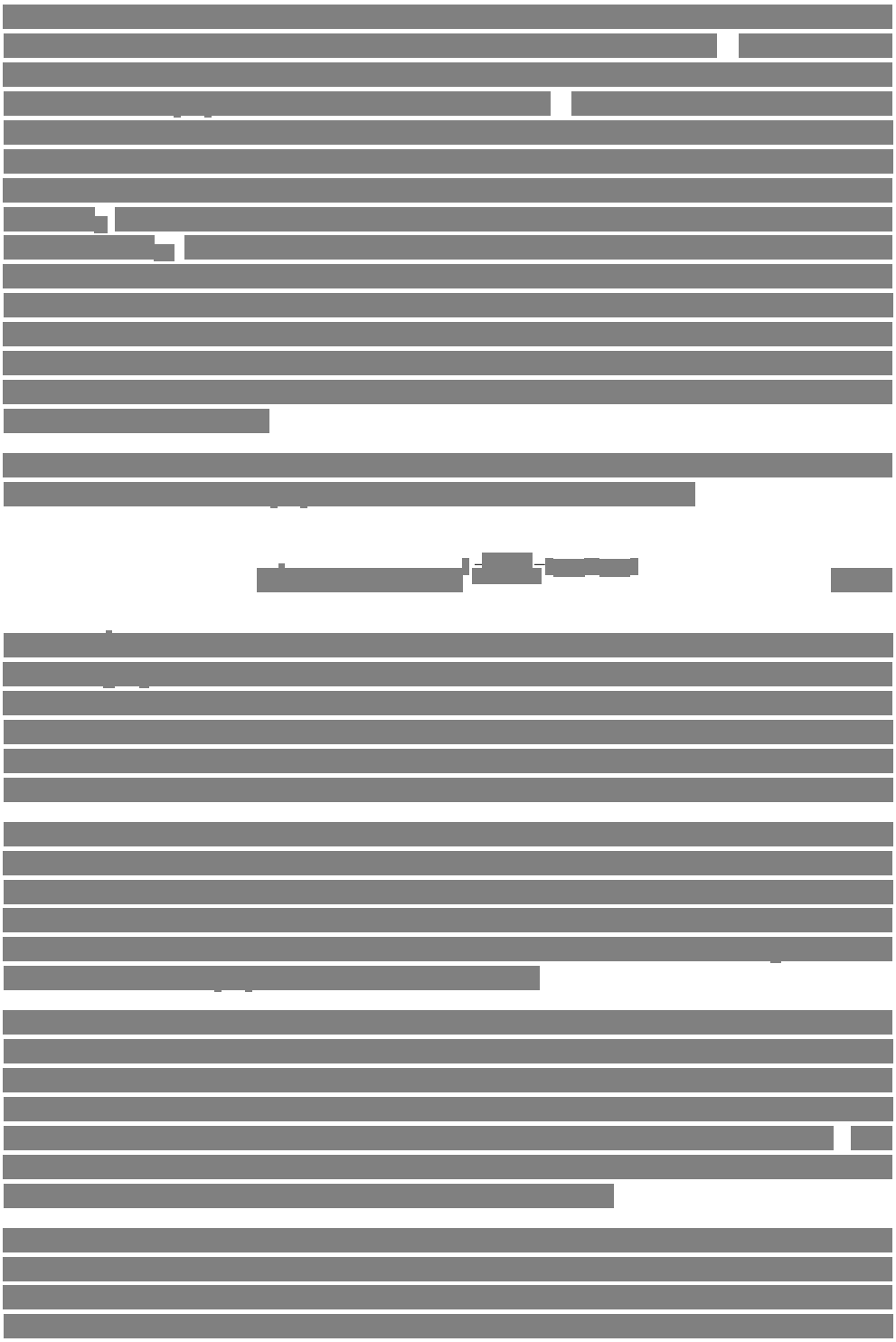

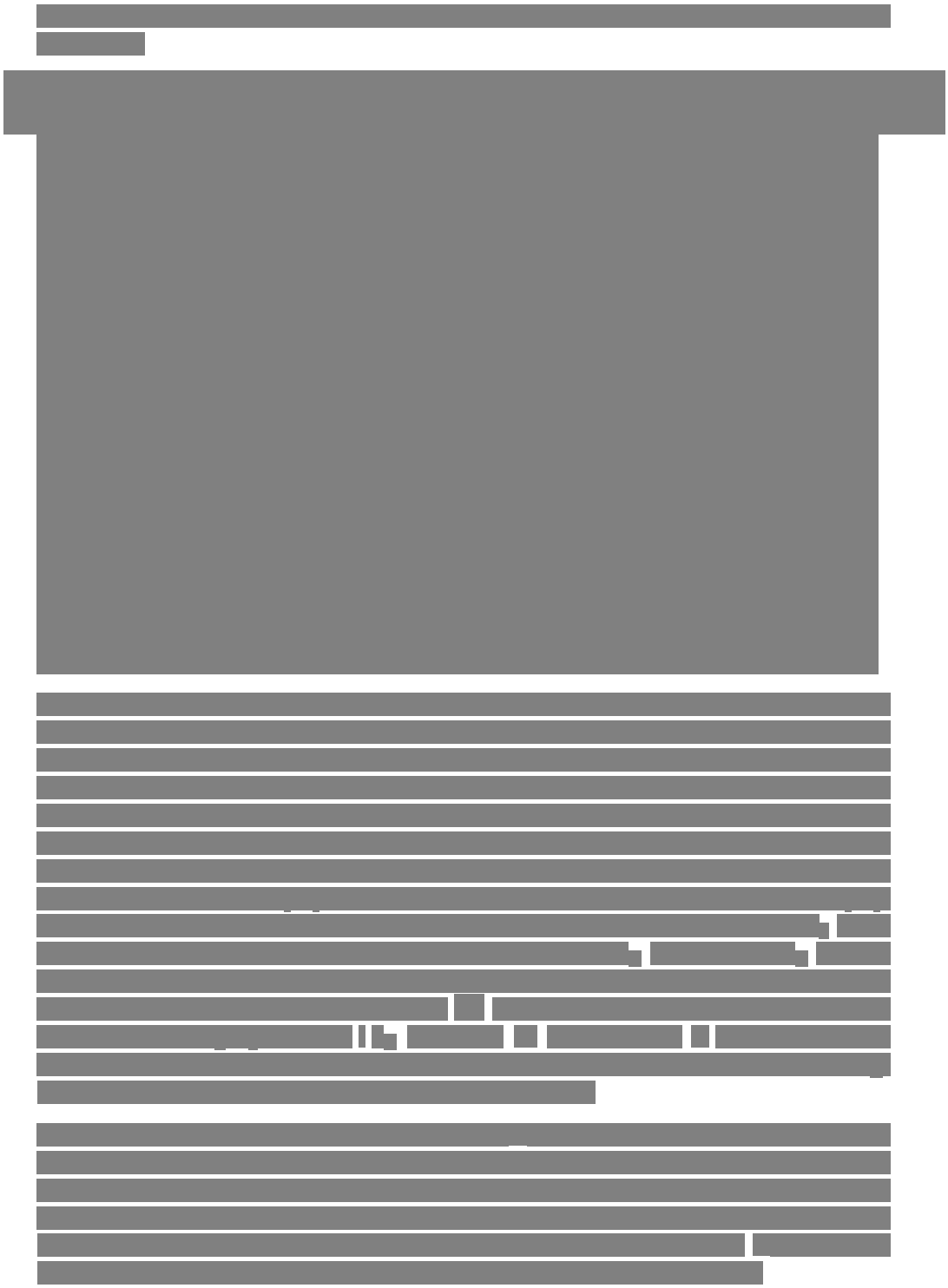

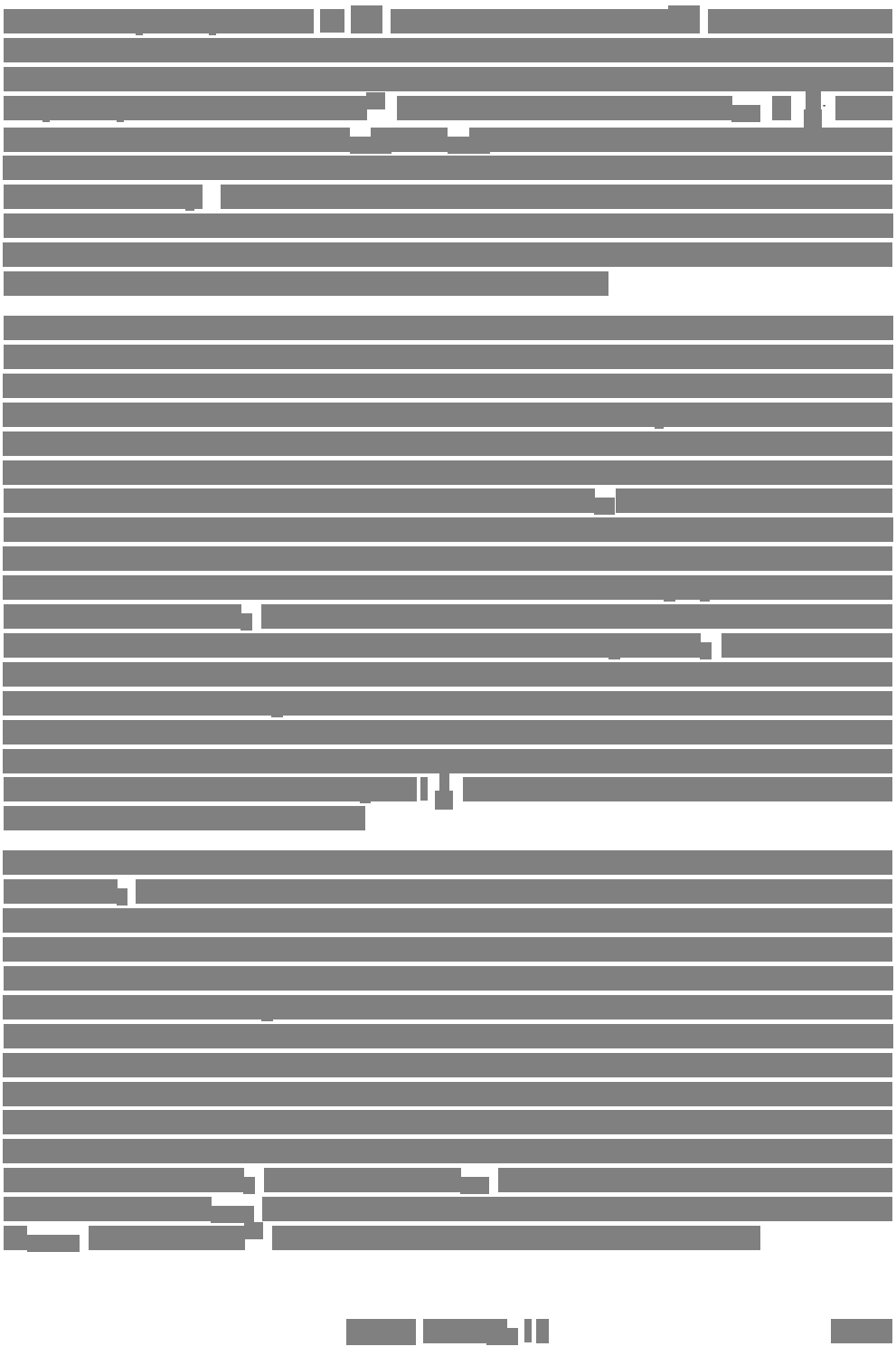

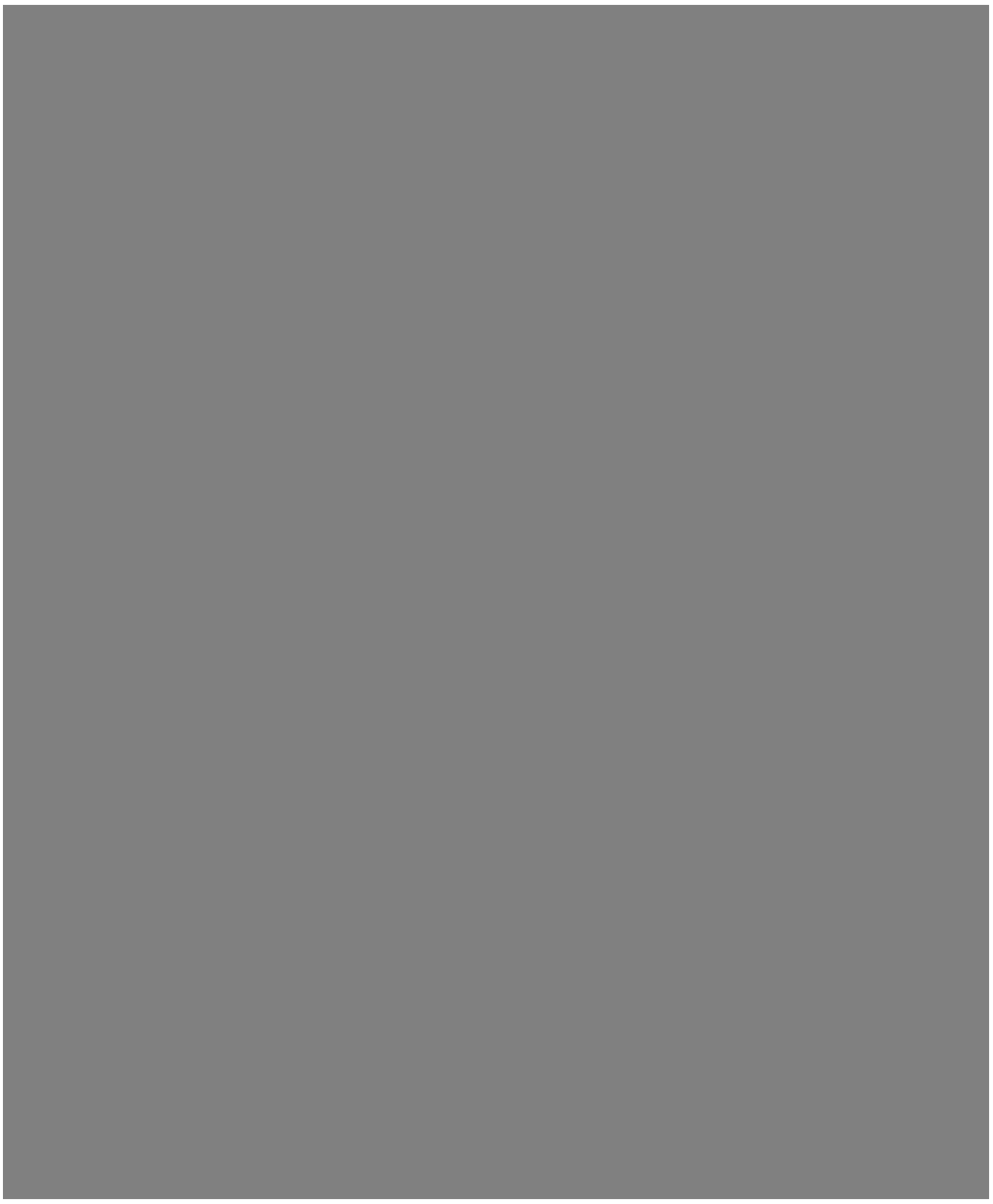

### 5.4.1

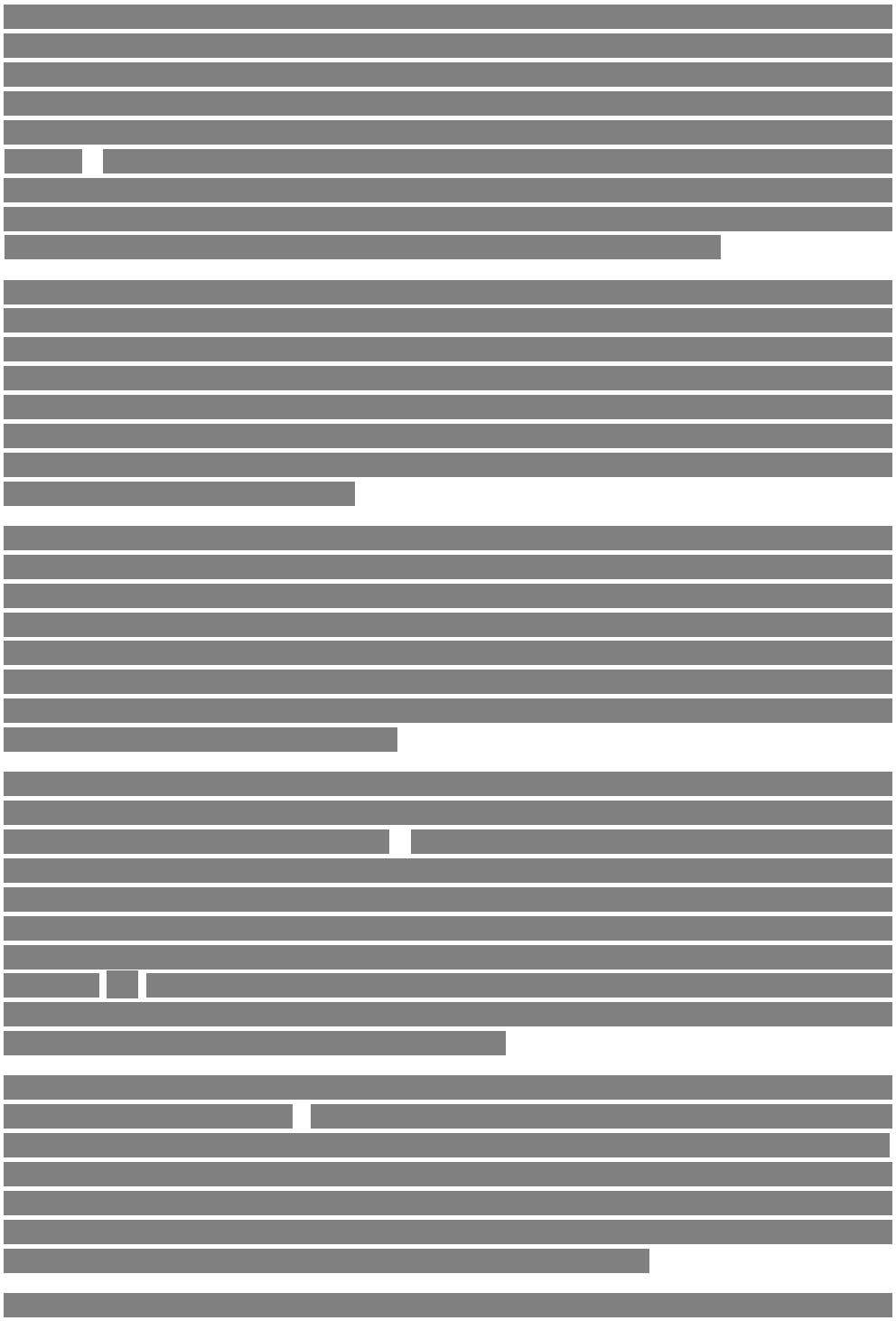

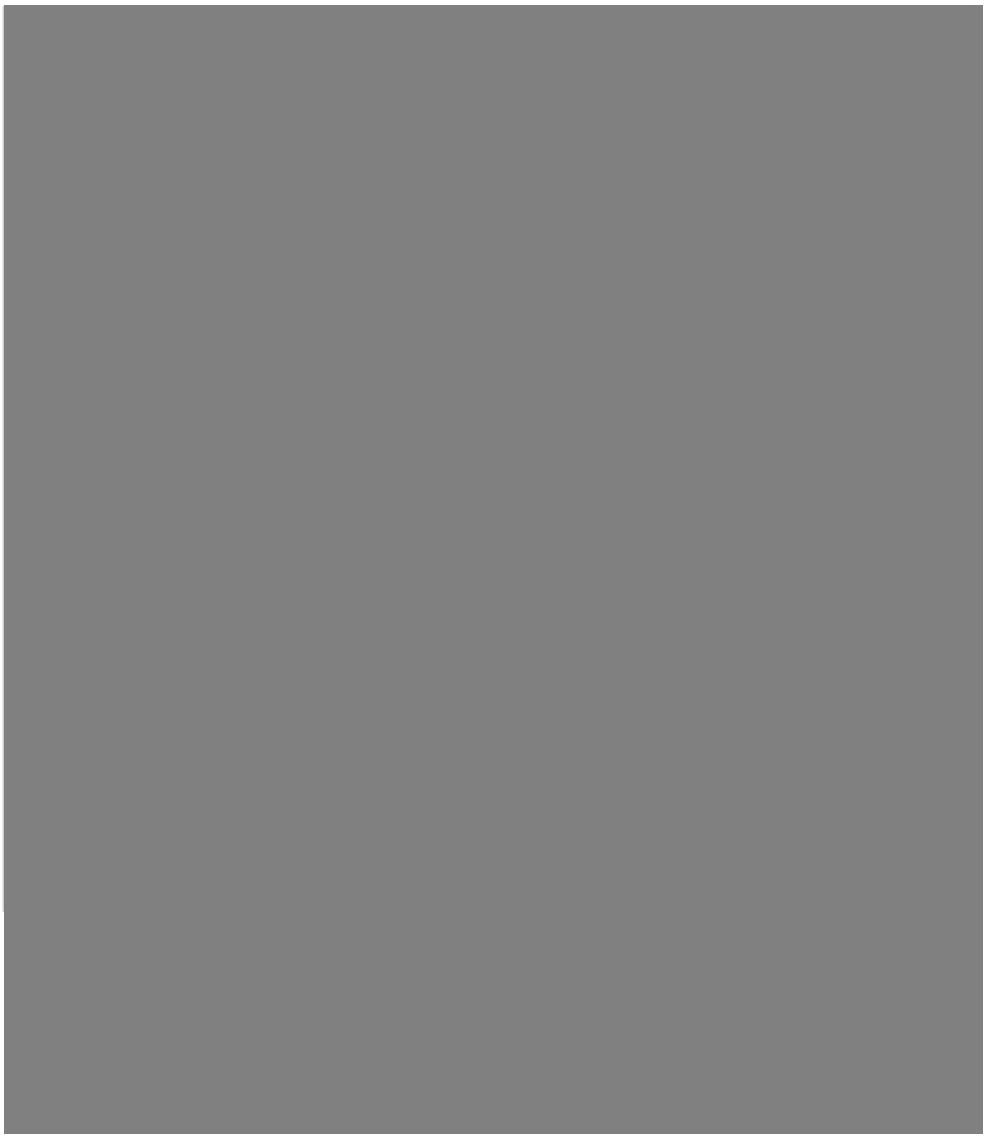

# Chapter 6

# Hardware and software filterings solutions

The main reason why the sample is scanned with a sparse excitation pattern, is to be able to remove the out of focus light, responsible for the image quality degradation due to a strong background, affecting the optical sectioning. In a CLSM or spinning-disk confocal, the focused excitation beam (or multiple beamlets in spinning-disk) is combined with a set of physical apertures (pinholes) where out-of-focus light is filtered-out, letting only the central part of each emission focus to pass through. On the final digital image, the pinhole is the element that discriminates what pixels are in focus and which ones correspond to background light.

However, the use of a physical aperture with a scanning laser comes the necessity of moving the pinhole in synchrony. In other words, both the laser spot and pinhole centers must coincide at all times. On a spinning-disk unit, this is done by means of a pinhole disk, that rotates in synchrony with the excitation disk, using the same common rotation axis. This way, when the motor spins, both disks are aligned at any time during scanning (figure 5.3). The final image is then reconstructed on a static camera, in focus light is transmitted by the disk, covering the sensor area as disk rotates.

Although spinning disk solve the synchronism problem between pinhole and laser by moving the pinhole, a more elegant and general solution is to "descan" the beam before it gets filtered. Descanning is rather straightforward when the scanning device is based on mirrors. Here, fluorescence emission light travels back down the same optical train used for excitation, reaches the mirror and is directed to the pinhole, which can be fixed in space regardless of the tilt angle of the scanner (see figure 5.3).

However, when the scanner is not a reflective device, for example, is based on diffraction or the confocal microscope operates in transmission, descanning the beam becomes much more difficult. In our particular case, descanning the excitation pattern is not an option, due to AODs work by diffraction. Our pair of AODs only work as

expected in one particular direction, from left-to-right in figure 5.6. On the left side of the AOSLM unit (formed by AODx, AODy and telescope T1) the laser beam is collimated, and on the right side, the beam is divided into many different beamlets traveling at different angles (one angle for each foci). This means that, if we were to pass the emission light (also with a multi-point structure) through the AOSLM in reverse, we would obtain a collimated beam again, losing all the spatial information of the sample. The light emitted from each excitation foci would be recombined into one beam. On top of that, the diffraction efficiency would depend on the fluorophore Stokes shift and the temporal coherence of emitted light, which due to the nature of fluorophores correspond to a wide-band.

The huge flexibility in both excitation pattern geometries (multi-point, multi-line, or any arbitrary excitation) and scanning protocols (sequential scan, random scan,...) our SCREAM unit offers, cries out for a filtering system capable of adapting to this infinity of patterns and modes. For example, the benefits of changing the pattern periodicity in terms of optical sectioning, will become limited if we use physical filtering element, where periodicity and scanning step are fixed.

The solution then, is to filter the out-of-focus light at the camera level. The filtering process can be carried out either using the pixels themselves as pinholes or process the fluorescence image to remove the background noise by digital methods, a procedure known as "virtual pinholing" or "CMOS descanning" [105, 106]. Pinholing at the camera has many advantages. For example, the pinhole size can be dynamically changed to adapt to different objectives lenses (each one with its own $PSF_{ex}$ FWHM), or the laser and the filtering aperture can be made to automatically realign when needed. Whereas in a CLSM, pinhole misalignment is one of the most common issues, and although it does not affect lateral resolution results on dimmer images, due to in-focus light is partially blocked.

The idea of implementing a virtual pinhole approach is to bring flexibility also to the filtering stage, in such a way that both the illumination arm (through the AOSLM and AOH) and the detection arm (filtering part) are fully programmable. Both illumination and detection parts can adapt to the specimen or experiment requirements. As can be seen in figure 5.25 and 5.23 each excitation pattern and scanning protocol is characterized by a particular image quality indicator, such as speed, lateral resolution or confocality. As an example, we show that line-based excitation offers remarkable optical sectioning performance, so having a camera/processing that automatically adapts to the change from multi-point to multi-line scanning, without the need of changing any additional element, is highly valued.

Moreover, several image processing techniques can be applied to the camera image for a more general removal of out-of-focus light than what is possible by a physical pinhole [107, 108, 109, 110, 111]. Finally, in Image Scanning Microscopy (ISM), the camera pixels act as tiny filtering apertures (as their effective size is reduced by the objective's magnification) of $\sim 50-80nm$, way below one Airy unit, which leads to an enhanced resolution by a 2 factor after the image is processed by proper algorithms [100, 10].

This chapter describes all processing algorithms we implemented in our PAM unit to filter out-of-focus light, which are divided into two main categories: software and hardware solutions. On the software side, a complete fluorescence frame is obtained for each EP pattern position, we describe a set of algorithms we developed that combine all frames from the image stack and provide a highly-contrasted reconstruction as output. The implemented algorithms are divided into: regular focus tracking and digital masking, and simple pixel-based operations, those latter being faster in terms of computation resources. Then, we explore some super-resolution capabilities of the previously developed methods.

For the software solutions, the maximum recording speed is always limited by the camera fame-rate and number of acquired frames. Moreover, real time visualization needs for high-performance computing. Then, in order to visualize the final reconstruction in real time, we present two hardware-based solutions, where no image stack is acquired, but the final image is reconstructed as the camera sensor is digitized. First, we demonstrate how background flare can be removed by simply synchronizing a line-scan with a cheap rolling shutter camera. Then, we explain all the development process of a custom-designed camera sensor that allows partial and arbitrary reading, in order to adapt to multi-point and multi-line scanning, as well as different periodicity values. The camera is designed in such a way that the sensor pixels are read following the same geometry and scanning procedure as the sample is being scanned. Since at each frame only few rows are digitized (only those with in-focus information), the new camera sensor allows us to reach very high frame-rates, much higher than regular full-frame mode, without losing information (at each frame, the important information is distributed at precise locations).

## 6.1 Virtual pinhole. Description of the digital processing techniques

This section is devoted to all the image processing algorithms whose purpose is to remove out-of-focus light and increase contrast, allowing us to see new features and structures of the sample, that otherwise are covered under the background noise. Mention that all the algorithms are applied in a post-processing stage. Which means that, depending on how computer demanding the algorithms are, the refresh rate may be affected. In any case, this only affects to real-time visualization, where some reconstruction frames may be lost. In other words, the frame-rate at which our SCREAM prototype can record videos is just limited by the camera properties, not by the algorithm. One can always record a whole sequence first, then process and replay it afterwards. However, optimized algorithm implementations, either by means of a GPU or FPGA, or less demanding calculations, are always welcome because they help to improve display rate. It is worth mentioning that the SCREAM microscope is still in a development stage, especially on the camera side we are still working towards high-speed imaging. Real time reconstructions have only been successfully implemented for a line-scan and rolling shutter (60fps), that will be explained in the

next section. For all the other cases, that is multi-point and multi-line scanning, the presented results are single snapshots.

Regarding the software image processing algorithms, this section presents two different approaches. In the first solution, each frame is processed independently, leaving only in-focus light, and then all processed frames are added in the final reconstruction. For the second approach, the image is reconstructed all at once using the information of the whole image stack. The idea behind is that, by looking at the pixel value evolution, we perform a set of simple operations that allow us to discriminate whether a certain pixel (i,j) corresponds to in-focus or out-of-focus light. Each pixel is processed independently from the others, allowing for parallel computing by means of a GPU.

### 6.1.1 Virtual pinhole processing

The first stack processing algorithm we implemented is the virtual pinholing. For the explanation of this processing we assume that the sample is scanned using multi-point excitation pattern and sequential scanning. In this imaging mode, a full-frame fluorescence image is taken for each excitation pattern position, which is shifted N-times in one direction (the X direction for example) and then in the perpendicular one. Each excitation foci scans a very small area of $p_x \cdot p_y$, ending up with $N^2$ different frames after the scanning process.

The physical principle behind virtual pinholing is to create the same effect as a physical pinhole, but digitally. In figure 6.1(a) we show an example of fluorescence frames upon multi-point scanning. By zooming in on any of the emission spots, we can distinguish the in-focus light, corresponding to the central part of the blob, whereas the rest of the pixels correspond to light from outer planes. Taking a square centered on the emission focus nominal position, we can make a correspondence between the radial position and the plane where light comes from. Only the central pixels, such that they cover $PSF_{eff}$ area (being $PSF_{eff} = PSF_{ex} * PSF_{em}$) correspond to in-focus light, providing information of the focal plane. Then, due to light is focused at sample plane, as we move away from the center of the focus, the captured light comes from deeper and deeper planes.

In a regular CLSM, the pinhole is placed at a sample conjugate plane, and the pinhole aperture diameter is chosen to approximately match the objective lens PSF. This way only in-focus light reaches the detector, placed just after the aperture. The digital version of the pinhole is just a mask of the same size as $PSF_{eff}$, in such a way that background pixels are multiplied by zero, and not taken into account for the final reconstruction.

Regarding the digital mask, since is a pure computational process, it can be chosen of any desired size and geometry. The possibility to change the pinhole size becomes very useful to adapt to different objective lenses. Low magnification objectives allow bigger FOV, however the longer focal length implies, in general, lower NA values, and thereby the $PSF_{ex}$ becomes wider. For the pinhole geometry, the digital mask can be either a binary square or circle, or as in our case a Gaussian distribution with zero

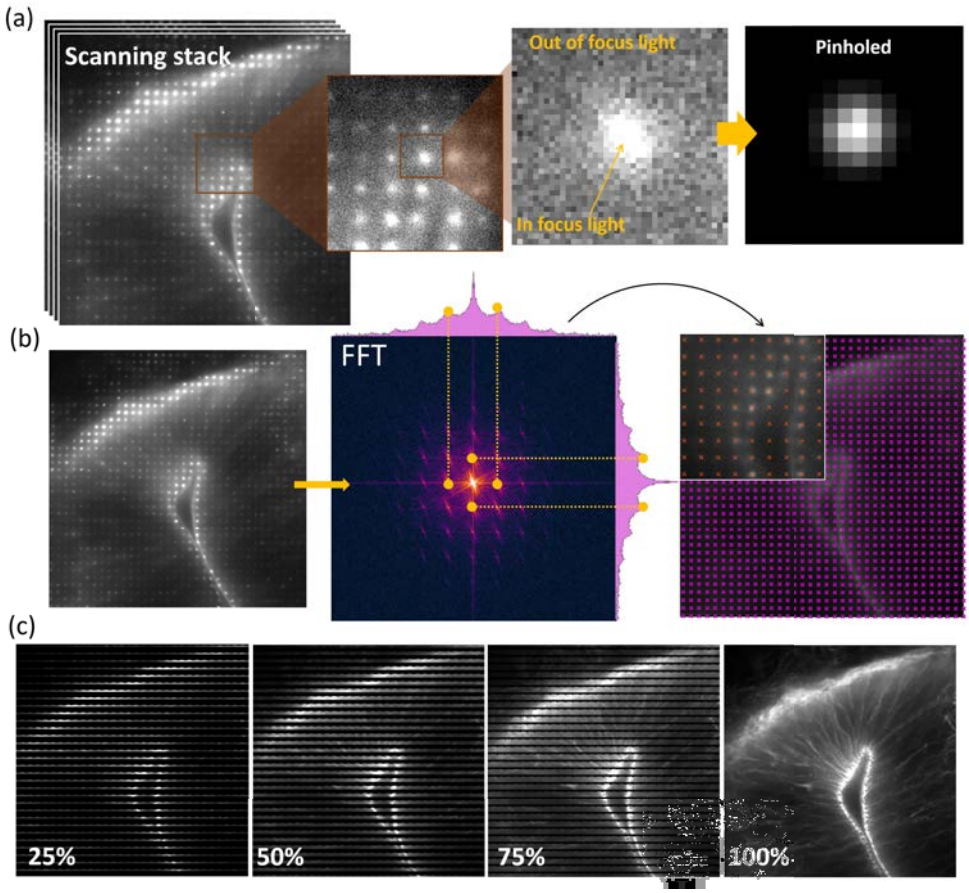


**Figure 6.1:** Explanation of the virtual pinhole processing. (a) Explanatory scheme of the virtual pinhole. Showing the removal of out-of-focus light by applying a digital Gaussian mask around each foci. (b) Identification of all excitation foci by finding the first peak in Fourier space, and then fitting a synthetic pinhole array. The pattern accuracy decreases for sparse/low labeling density samples. Point calibration can be done on the image stack itself, or using a calibration slide (lake sample). (c) Sequence showing how the image is being composed as more frames are added.

offset. Additionally, the mask can also adapt to line or multi-line scanning, where the ideal aperture is not a round pinhole, but a rectangular slit. From the virtual pinhole point of view, the analogy of a physical rectangular slit is to directly select the corresponding pixel rows, discarding all the others.

It is easy to see that for the multi-point excitation pattern used, the corresponding virtual pinhole mask is also a "pinhole grid". For each image stack, a corresponding pinhole-grid stack is created, such that all Gaussian filters from the $i^{th}$ pinhole-grid stack are centered within the excitation pattern foci. Each image stack frame is then

multiplied by its corresponding mask, and all resulting frames are added together in the final reconstruction. Figure 6.1(c) shows the evolution of the reconstruction as "pinholed" frames are added.

The most critical aspect for the implementation of the virtual pinhole algorithm is obtaining all the EP centers. It is very important that the digital mask is centered with the excitation pattern. If the corresponding virtual pinhole is not centered with the emission laser, we would be applying the analogy to a misaligned pinhole. Apart from out-of-focus light, part of the in-focus information would be filtered too, resulting on a decrease of the signal at that specific region. Using non-centered masks result on the appearance of square artifacts, due to each virtual pinhole is offset a different amount, hence the scanned square by each spot will be weighted a different amount. This effect is exemplified in figure 6.2.

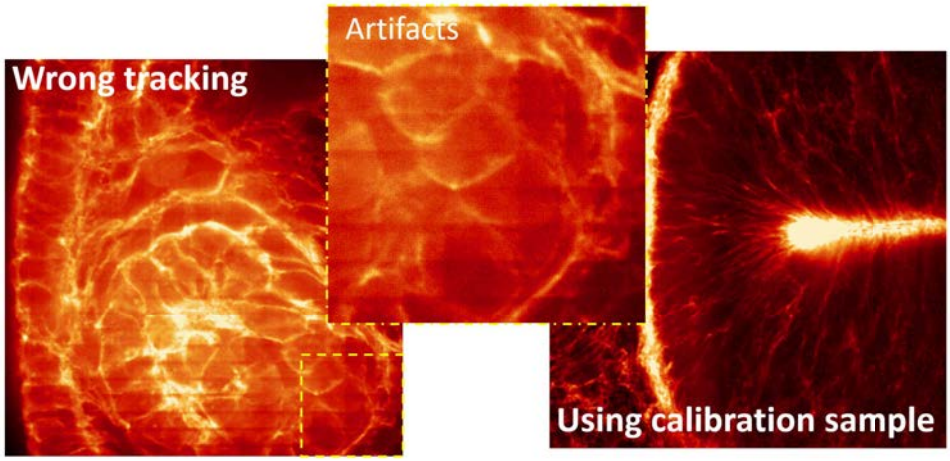


**Figure 6.2:** Experimental example of artifacts due to wrong pattern tracking, the excitation pattern has been fitted only on the first frame. Although for the first frames the error is minimum, it accumulates and grows as the excitation pattern is shifted. Reason why at the last frames signal decreases, black lines appear.

The center identification accuracy is crucial for high-quality reconstructions. Ideally one would use the nominal values, which can be obtained from the hologram information. However we observed that tracking the points *in situ* improves image quality, since any field distortion introduced by a non-perfectly aligned setup, or the sample itself, can cause points to be slightly shifted from its nominal position. It is worth mentioning that even though the tracking can be done on the image stack, the best accuracy is always obtained using a calibration sample. Which consists on a highly dense fluorophore solution sandwiched between two nr.1 coverslips. Another and easiest option is to use the same mirror sample used in chapter 5 to characterize the EP. This way, we ensure that the tracked center corresponds to the actual excitation laser spot. Which is no longer true for very sparse samples, where the tracked position, i. e. the center of the emission blob, is very close to the excitation position, but it does

not coincide.

For our SCREAM unit we developed a custom tracking software, where the EP pattern is tracked just using the first image stack frame. Thanks to the huge scanning linearity and positioning accuracy that AOSLM offers, all positions for the rest of the frames are obtained using the nominal laser step $d_L$. Making the algorithm faster, since only 1 image is needed to obtain the whole set of coordinates.

When it comes to the tracking procedure, the EP pattern point grid is modeled using four parameters: $p_x$, $p_y$, $off_x$ and $off_y$. Corresponding to the pattern periodicity and pattern offset for the X and Y directions respectively. For the pattern periodicity $p_{x,y}$, this one is obtained from the image power spectrum, invariant to any pattern shift. Figure 6.1(b) shows and scheme of the pattern tracking process. In Fourier space, $p_{x,y}$ is obtained from a Gaussian fitting to the first peak, corresponding to the first harmonic. Both positive and negative first harmonic spatial frequencies are obtained for both X and Y, and averaged for better accuracy.

The pattern offset $off_{x,y}$ can be obtained from the phase in Fourier space, however we obtained it from an optimization process in the real space. Where we sweep $off_{x,y}$ from 0 to $p_{x,y}$ and choose the values such that maximize the following merit function:

$$M(x_0, y_0) = I(x, y) \cdot \left[ \cos^4 \left( \frac{\pi(x - x_0)}{p_x} \right) \cdot \cos^4 \left( \frac{\pi(y - y_0)}{p_y} \right) \right] \tag{6.1}$$

Where $(x_0, y_0) = (off_x, off_y)$, and $I(x, y)$ is the fluorescence image. Basically $M(x_0, y_0)$ is the amount of light crossing the virtual pinhole array (maximized when pinholes and EP centers coincide). Where, as can be seen in equation 6.1, is modeled as two perpendicular cosine functions, very similar to the desired pinhole grid (computed as the superposition of multiple Gaussian distributions). Once all four parameters are known, we create a stack of $N^2$ virtual pinhole grids, such that each one is offset $p_{x,y}/N$ according to each scanning direction.

Mention that for the periodicity $p_{x,y}$, the algorithm also accounts for a pitch varying pattern of the form $p_x = p_0 + p_1 x + p_2 x^2$. This is implemented as an approximation to field distortion aberration, which we observed to appear when AODx and AODy are not properly conjugated with the BFP of the microscope objective. This distortion also can appear when using F-theta or scanning specific lenses (especially L4 in figure 5.6), most used in scanning systems, which do not satisfy the Abbe sine condition, essential for a correct holographic reconstruction.

This virtual pinholing procedure also allows for the implementation of ISM methods, also known as photon reassignment or pixel reassignment, whether is an optical [112, 90] or digital implementation [100, 10]. Photon reassignment is a procedure where, by replacing the photo-multiplier tube in any point-scanning microscope by a multi-pixel detector, i.e. a digital camera, the lateral resolution can be improved by a factor of $\sqrt{2}$, which becomes a factor of 2 after proper deconvolution by means of an inverse filter.

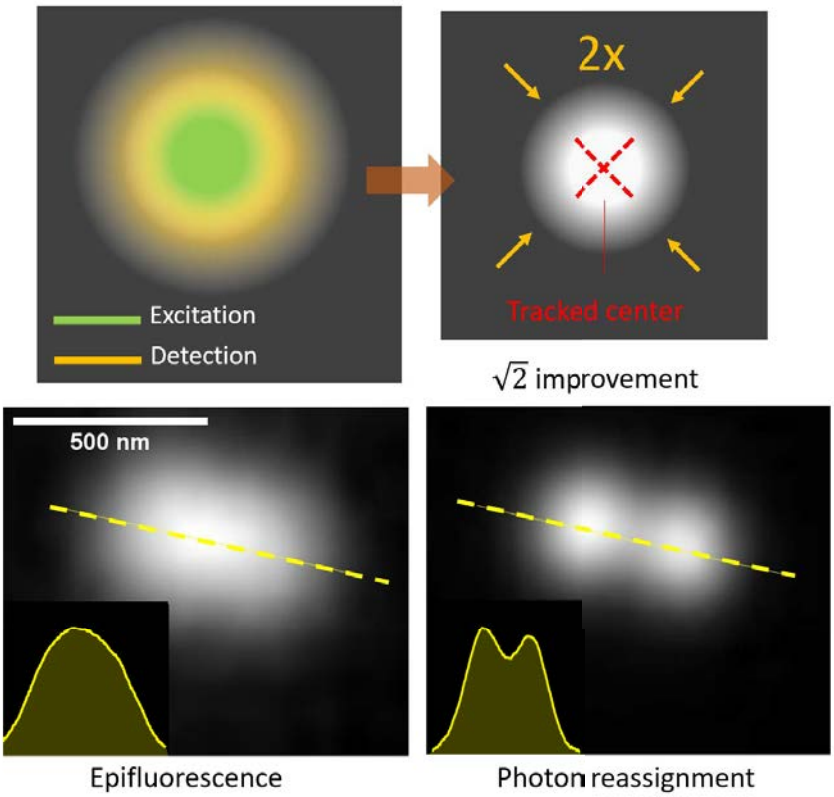


**Figure 6.3:** Explanatory scheme and experimental implementation of ISM for our multi-point excitation pattern, also known as photon reassignment. The 2x local contraction around each focus offers a $\sqrt{2}$ improvement in lateral resolution over regular epifluorescence (obtained just by averaging all frames). The images shown correspond to experimental images of 170nm fluorescent beads.

As explained in the previous chapter 5, if we assume an homogeneous fluorescent sample which is scanned with a focused laser, we see that the emission spot size at each laser position, depends on both the excitation and emission PSFs ($PSF_{eff} = PSF_{ex} * PSF_{em}$, as shown in figure 6.3). In a CLSM with a wide-open pinhole, all photons from this convoluted area are directly assigned to the nominal excitation laser position. However, if instead we repeat the same procedure but with a closed pinhole, now only the central photons are assigned to the nominal position. In theory, by closing the pinhole the transverse resolution can be enhanced by a factor of $sqrt2$ with respect the wide-open pinhole image or any wide-field epifluorescence microscope.

The intuitive reason to this improvement is because, all photons from the outer parts of the emission spot, are actually not emitted from this region. Or at least, the probability that the photons outside the excitation spot actually come from the center (where are assigned) is very low, whereas the probability that the central photons

have been emitted from the center is very high. Thus, by closing the pinhole, we are capturing only those photons most likely to have been emitted in $PSF_{ex}$ area. Which can indeed be assigned to the nominal position. In practice, working with such closed pinhole gives unacceptable SRN, requiring increasing the laser power, which can be harmful for the cells.

Photon reassignment allows us to benefit from the increased resolution offered by a closed pinhole, but without losing light. By replacing the single pixel detector, which integrates all light from the spot region, with a multi-pixel detector, we now obtain information about the emission spot spatial distribution. If the microscope magnification is such that each camera pixel is much smaller than $PSF_{ex}$, each individual pixel can be understood as a tiny closed pinhole, offset from the central position depending on the corresponding pixel. However, here not a single photon is lost due to the small size of the pinholes, since lost photons from pixel (i,j) will be captured by all the neighbors.

By acquiring a full frame image for each scanning position, instead of a single reconstruction, given by the single pixel PMT, we can reconstruct a complete image for each of the sensor pixels. Each of these images are characterized by being very faint (due to the small pixel area) and that they are displaced from each other. However, due to pixels themselves act as "tiny pinholes" lateral resolution increases $\sqrt{2}$. Each pixel "sees" the same sample, but from a different point of view, given by their relative position, only the central pixel provides a centered reconstruction. Concretely, each image is displaced half the distance between the position of the pixel and the camera center. The reason to that displacement is because is where the probability for a photon of being detected $P_{det}$ is maximized, being $P_{det} = P_{em} \cdot P_{ex}$ given by $PSF_{ex}$ and $PSF_{em}$ respectively.

All this "pixel images" can be re-centered and combined (summed up) into a high-resolution reconstruction. Even though all this procedure is explained for a single-point scanner, it can be also applied to multi-point or multi-line scanning. The transition to multi-point photon reassignment relies on replicating the same process at each of excitation focus. For the correct implementation, in our SCREAM unit, once all excitation spot centers are determined, the image stack is divided into multiple chunks, as many as excitation foci. Each sub-stack corresponds to the square area covered by each excitation focus when scanning. Which is then processed by means of photon reassignment, and then the final image is obtained by assembling the puzzle again.

In a confocal unit based on descanning, the excitation spots remain always at the same position, making the whole photon reassignment process easier, photons have to be reassigned to half the distance between the corresponding pixel and the image center. Mention that in our unit, this is not possible, and we have to account for the moving laser. During photon reassignment, each pixel value is assigned to half the distance between the pixel and the center of the laser, which is previously known thanks to the precise tracking algorithm. As can be seen in figure 6.3, after the virtual pinholing and photon reassignment, we obtain an image with better lateral resolution. The two spherical 170nm fluorescent beads, become distinguishable after

photon reassignment. Whereas if we just sum up all frames, equivalent to wide-field epifluorescence, both emitters fall within the same emission blob.

### 6.1.2

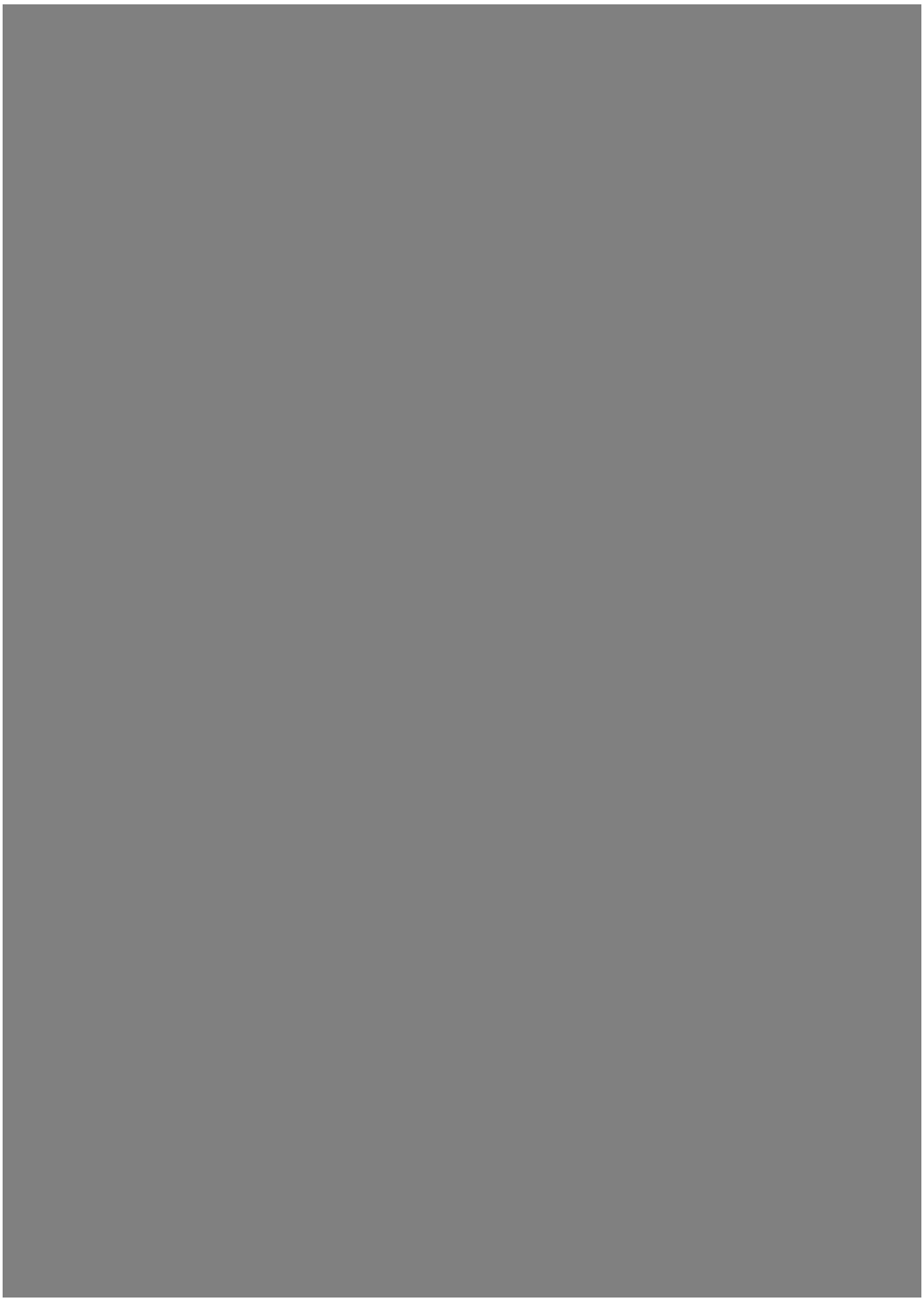

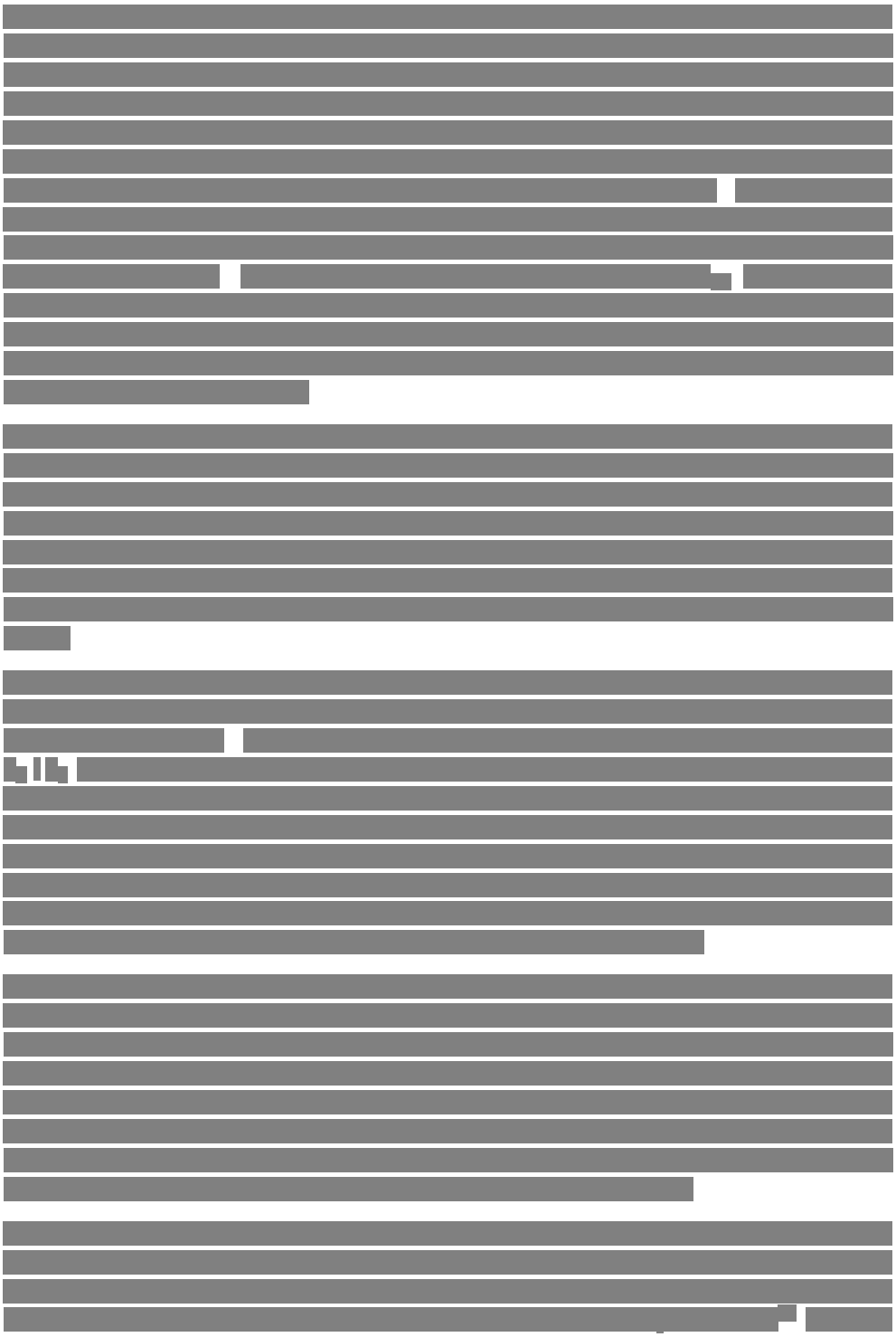

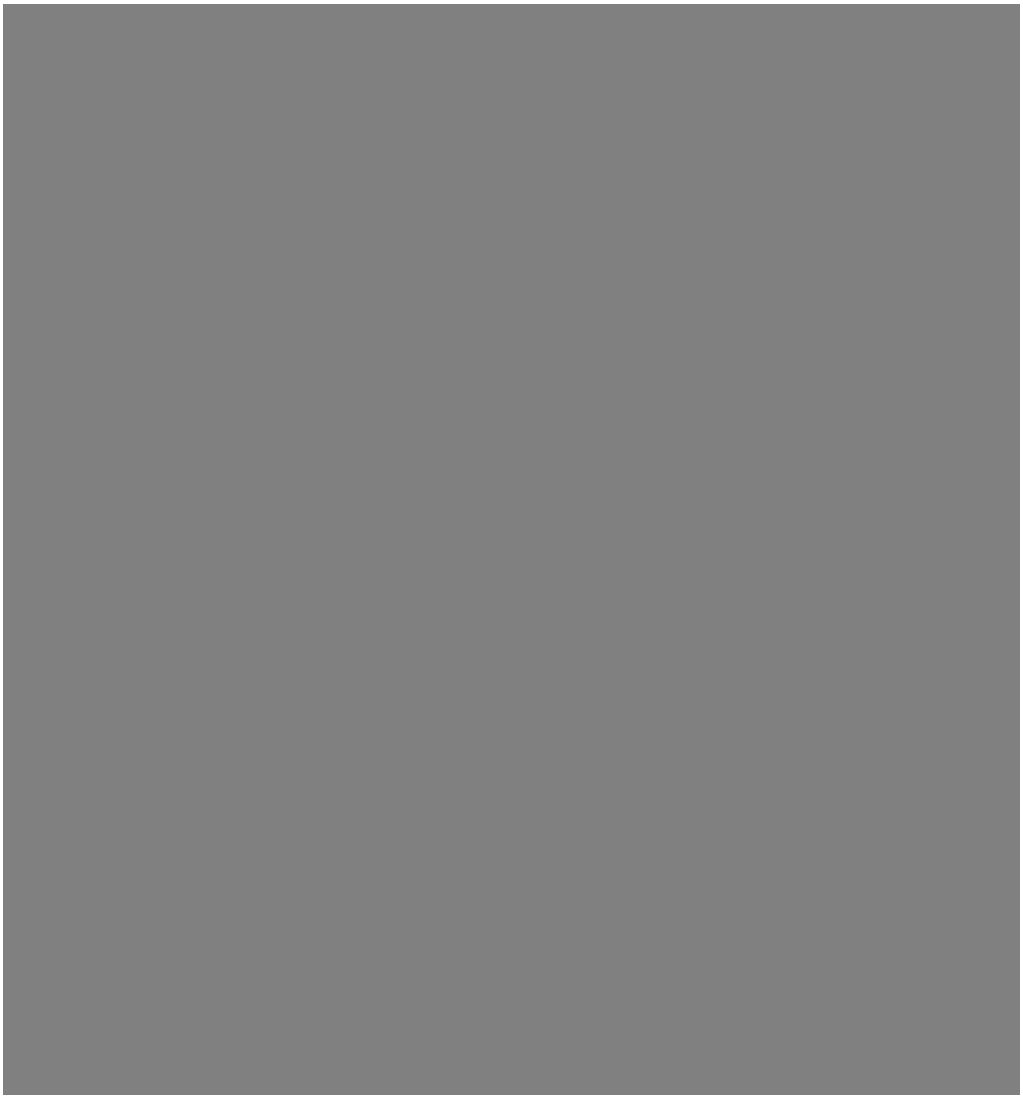

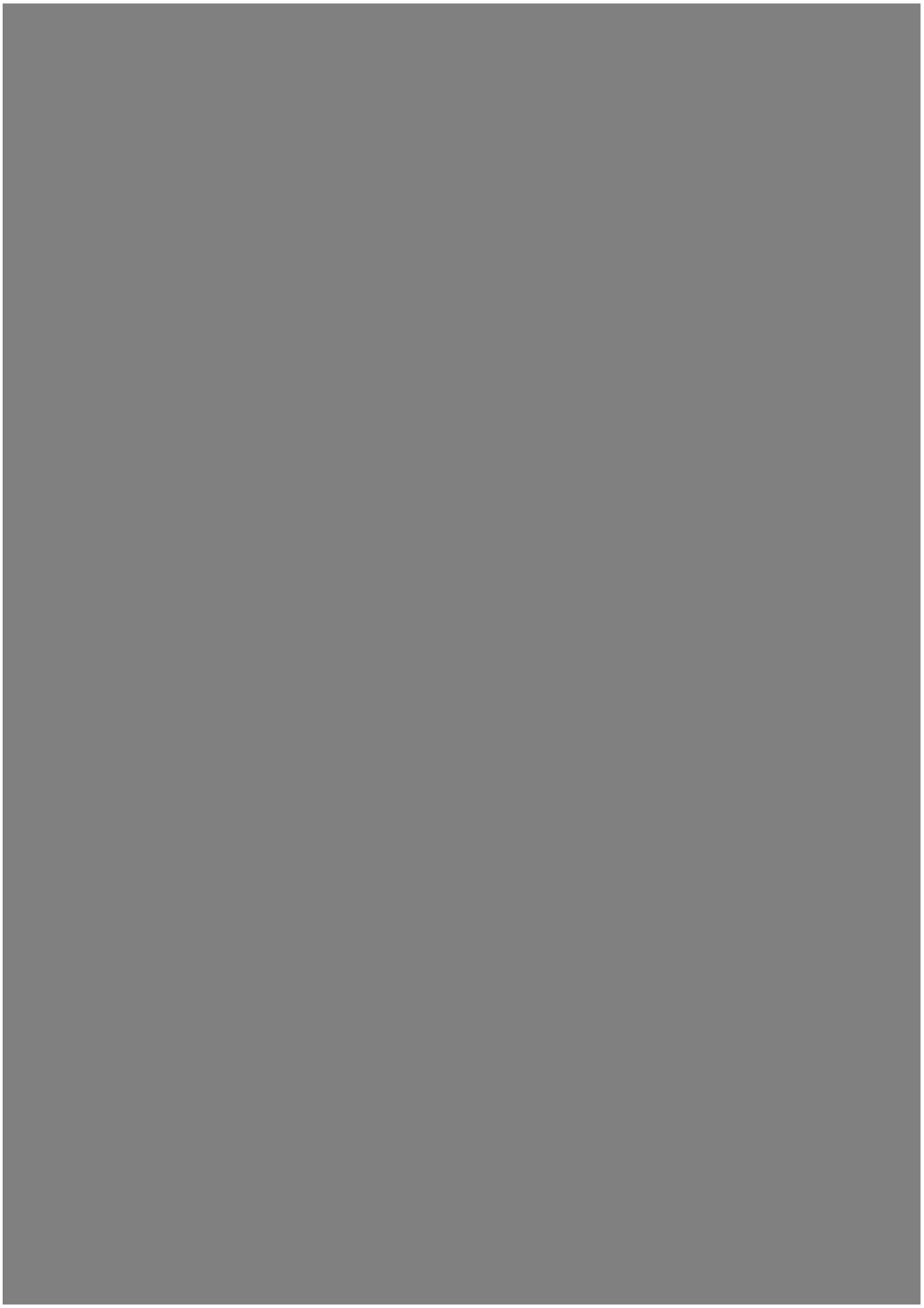

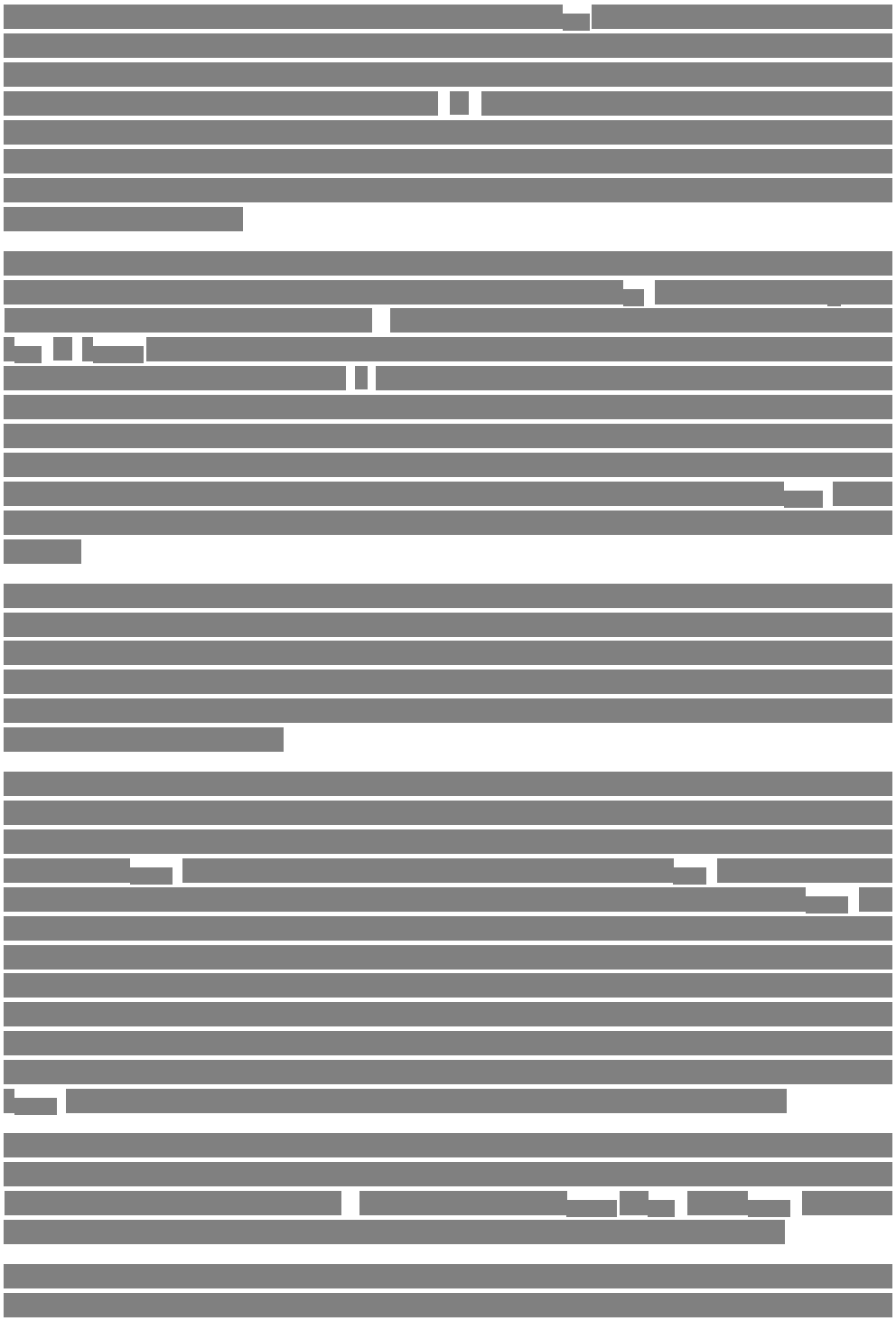

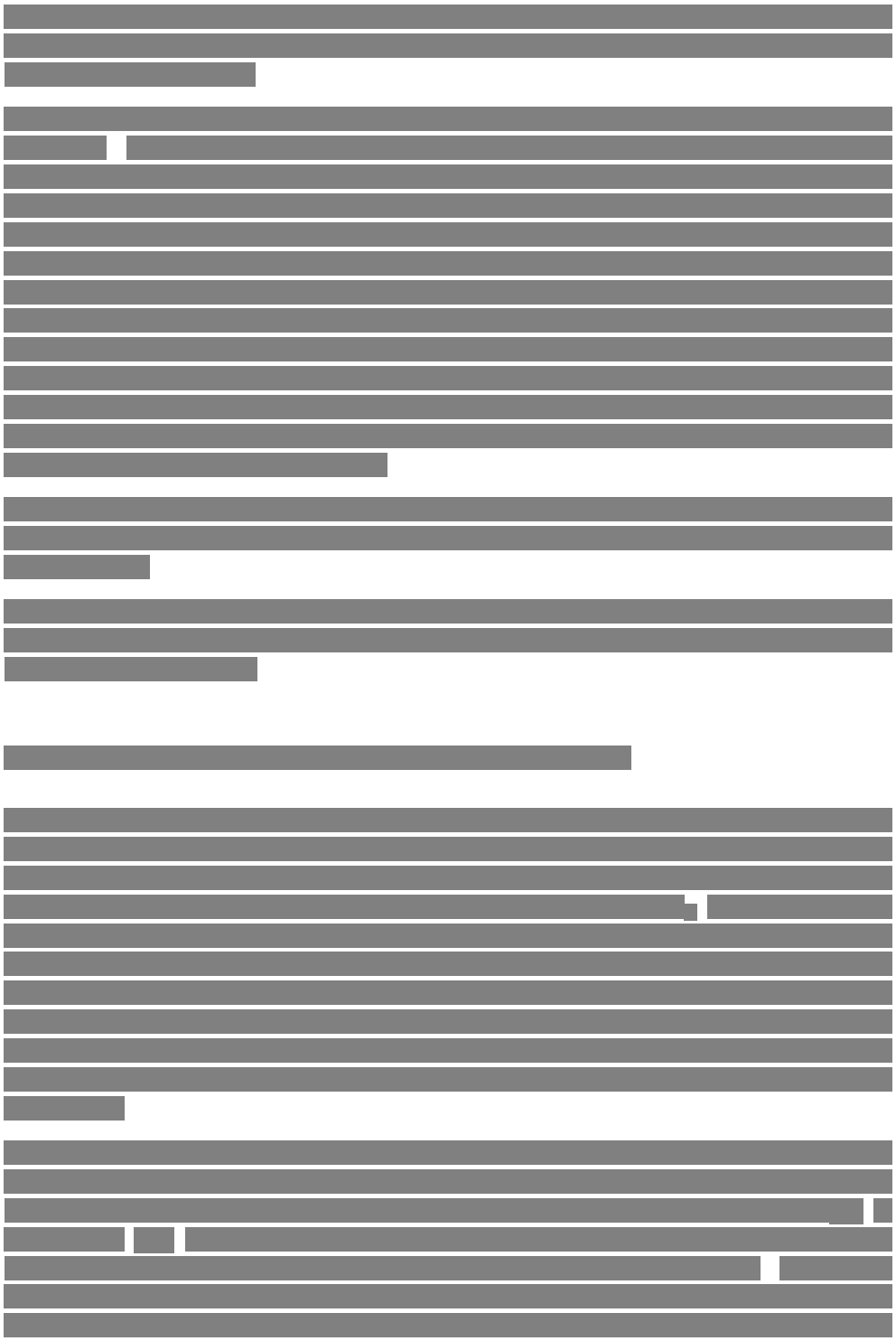

| | | |
|---|---|---|
| | | |
| | | |
| | | |
| | | |
| | | |
| | | |

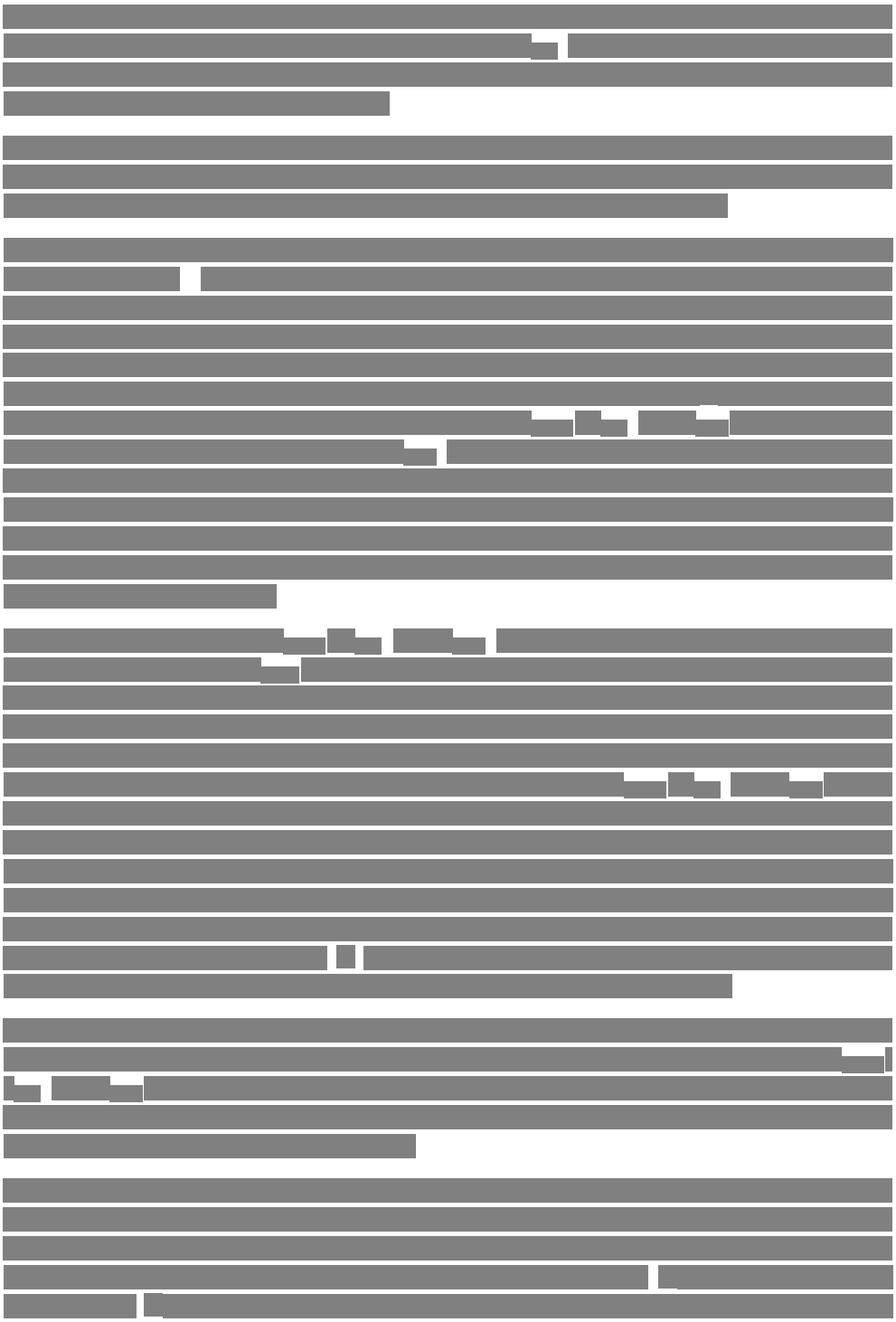

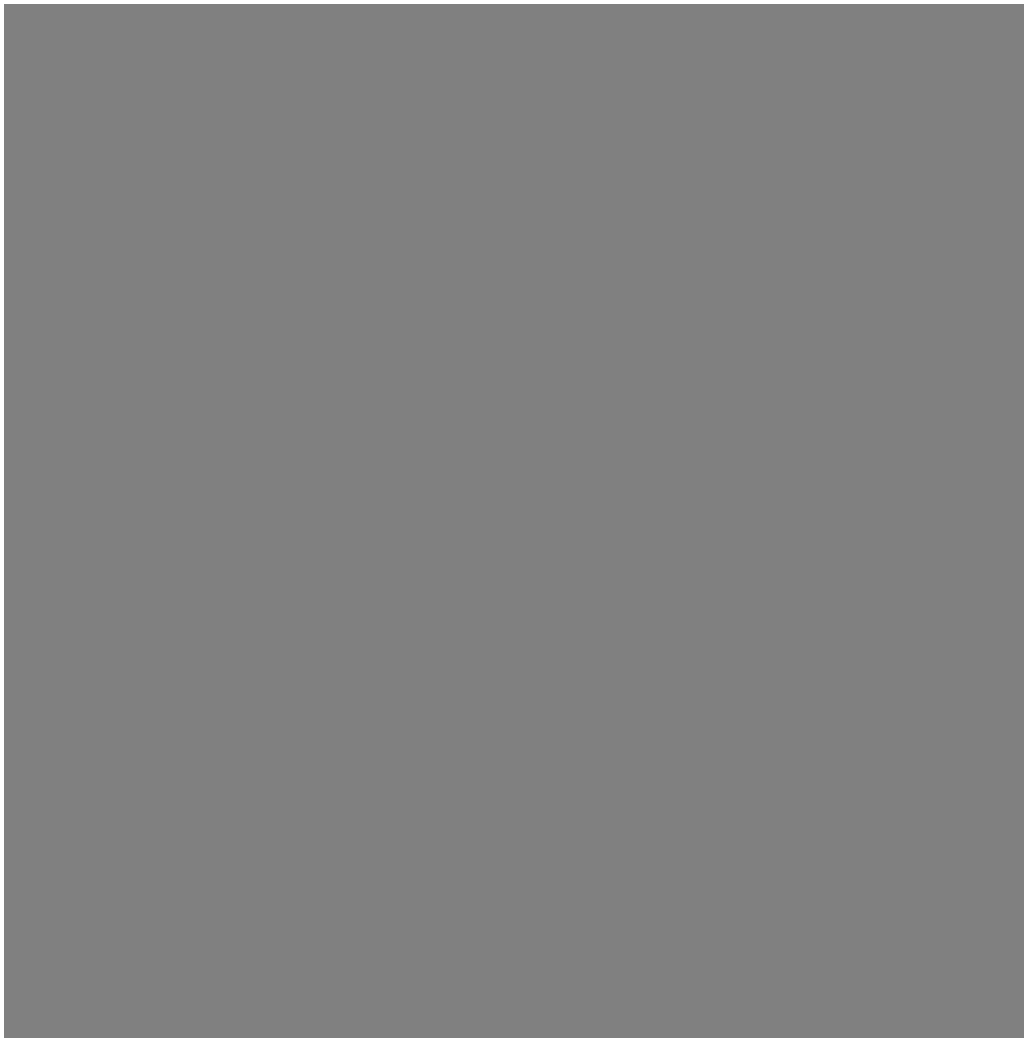

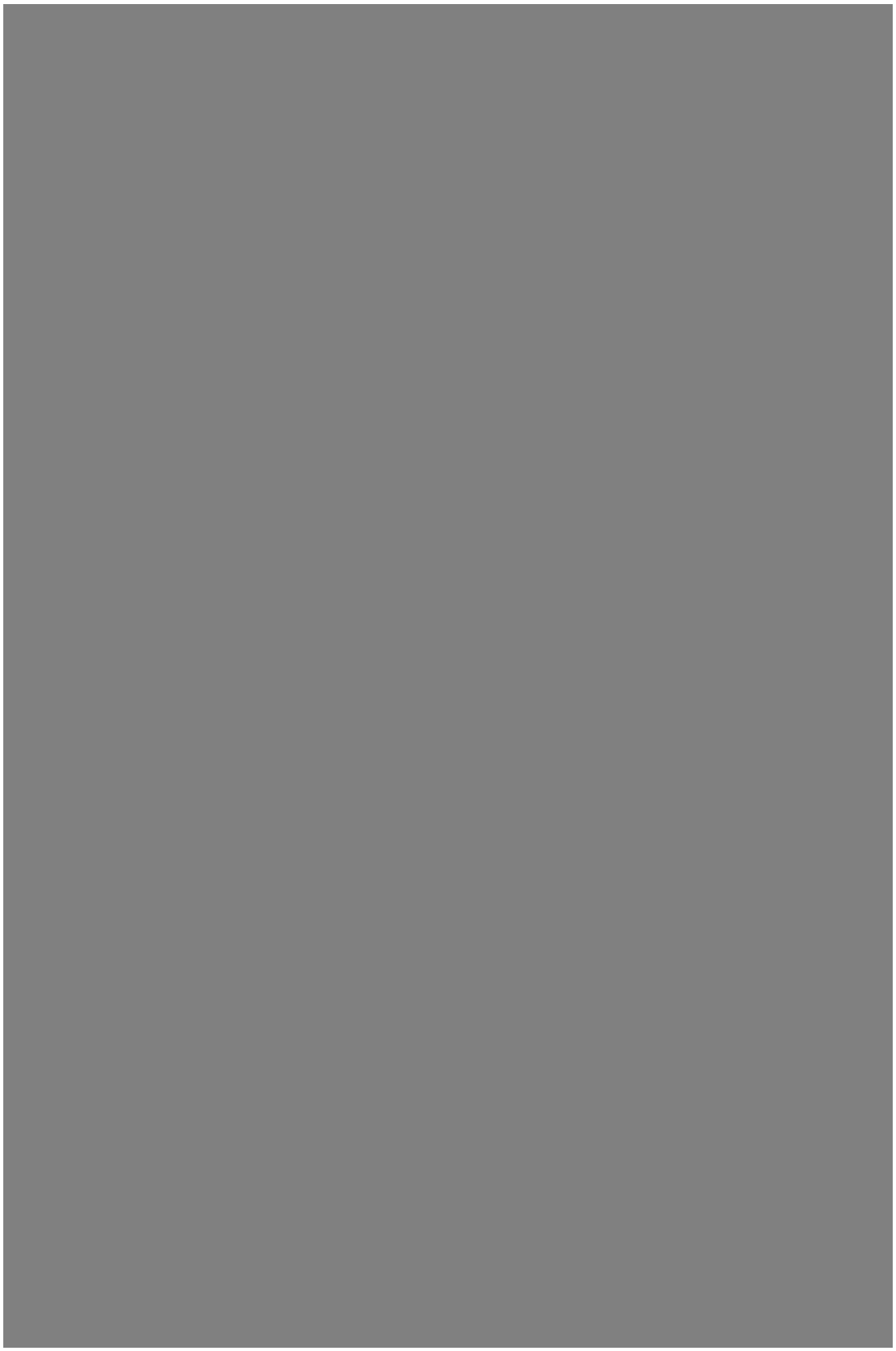

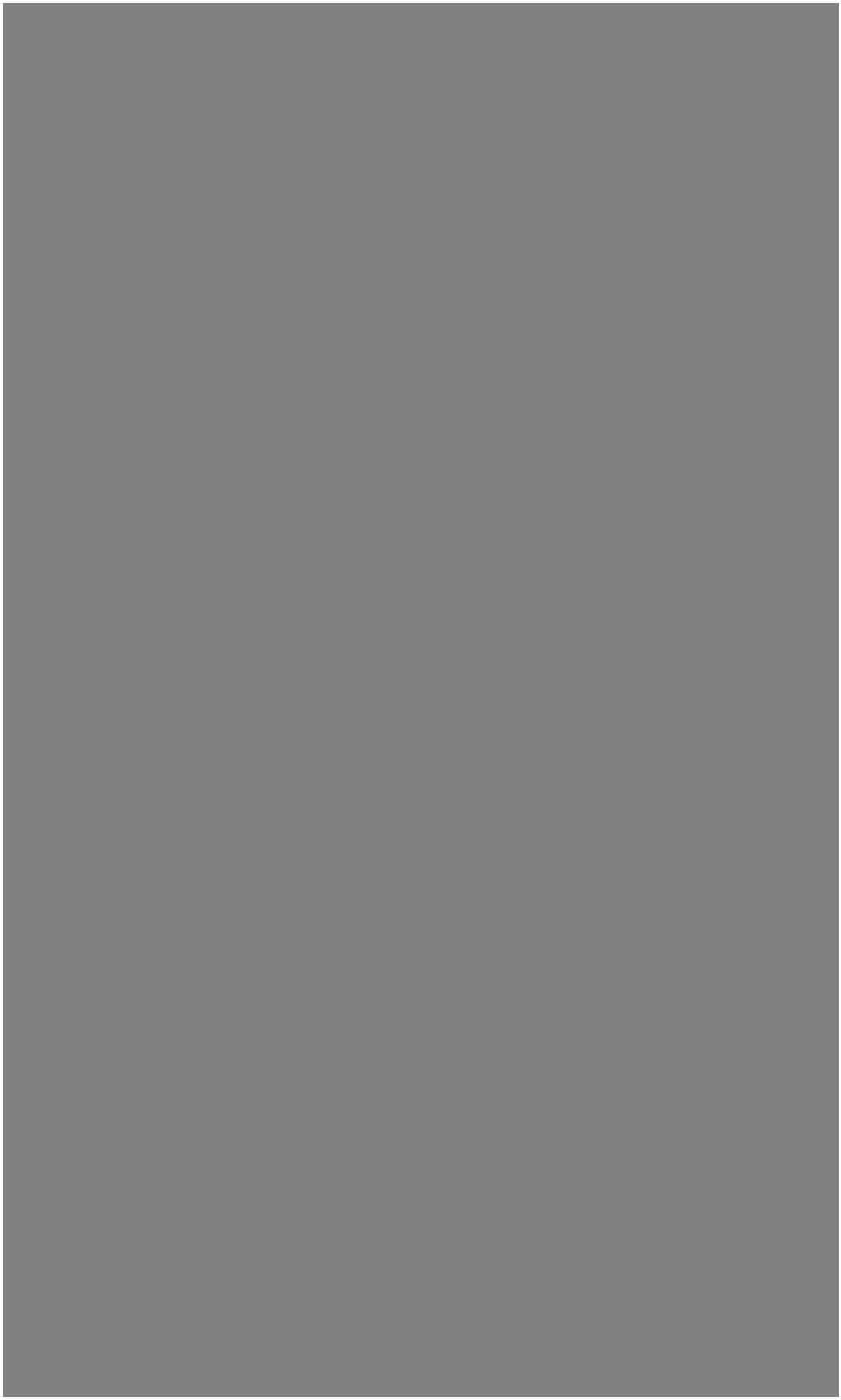

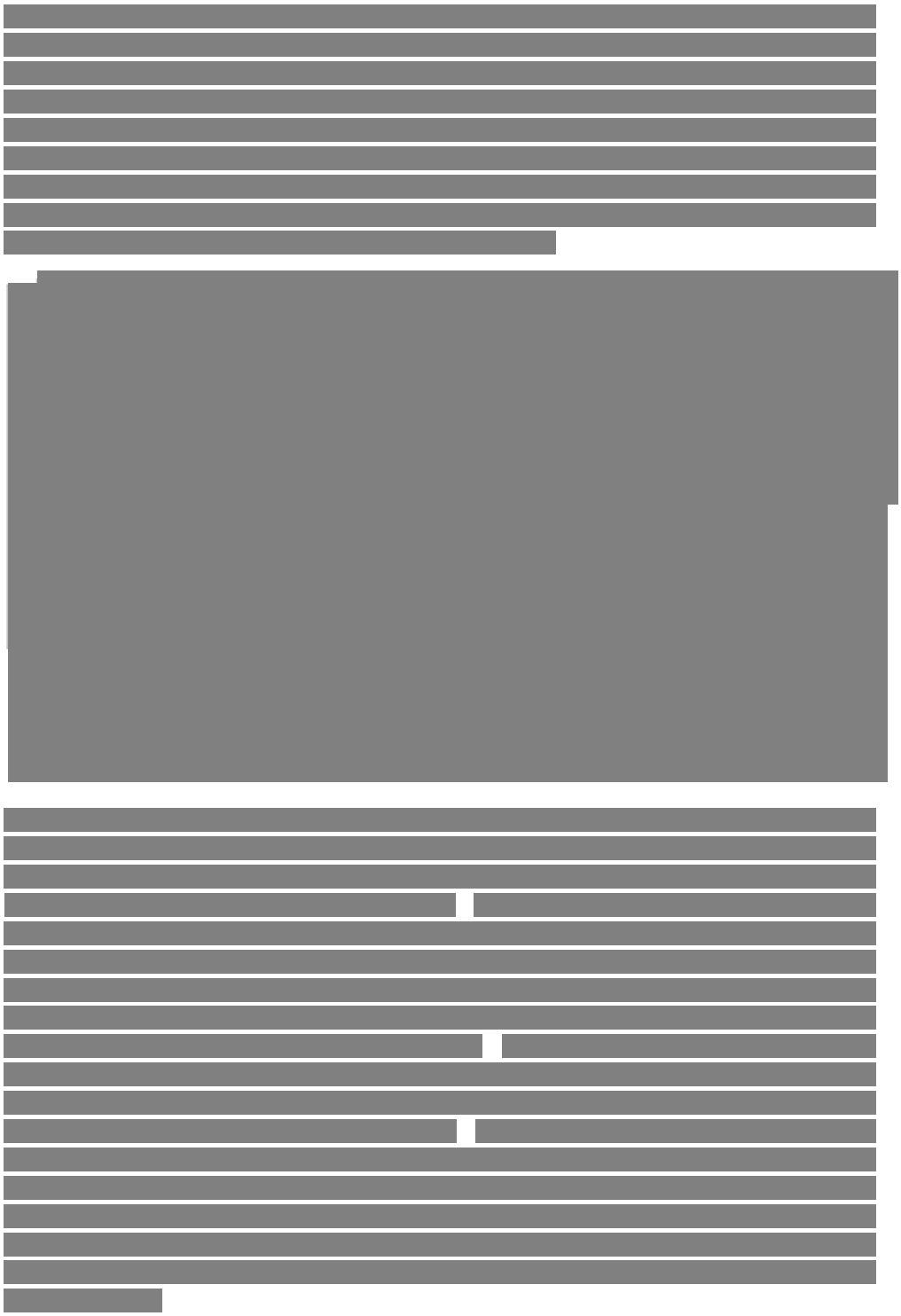

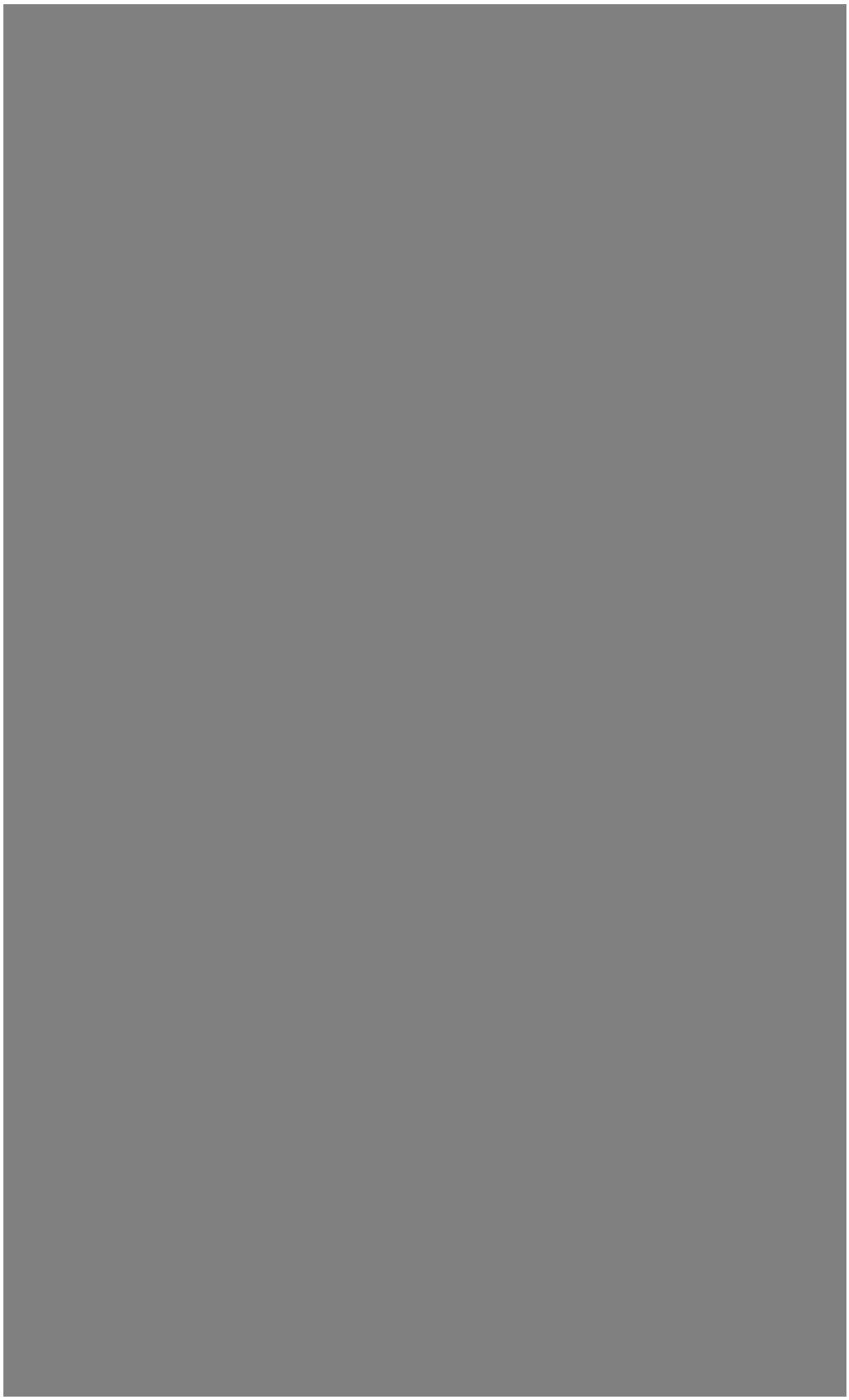

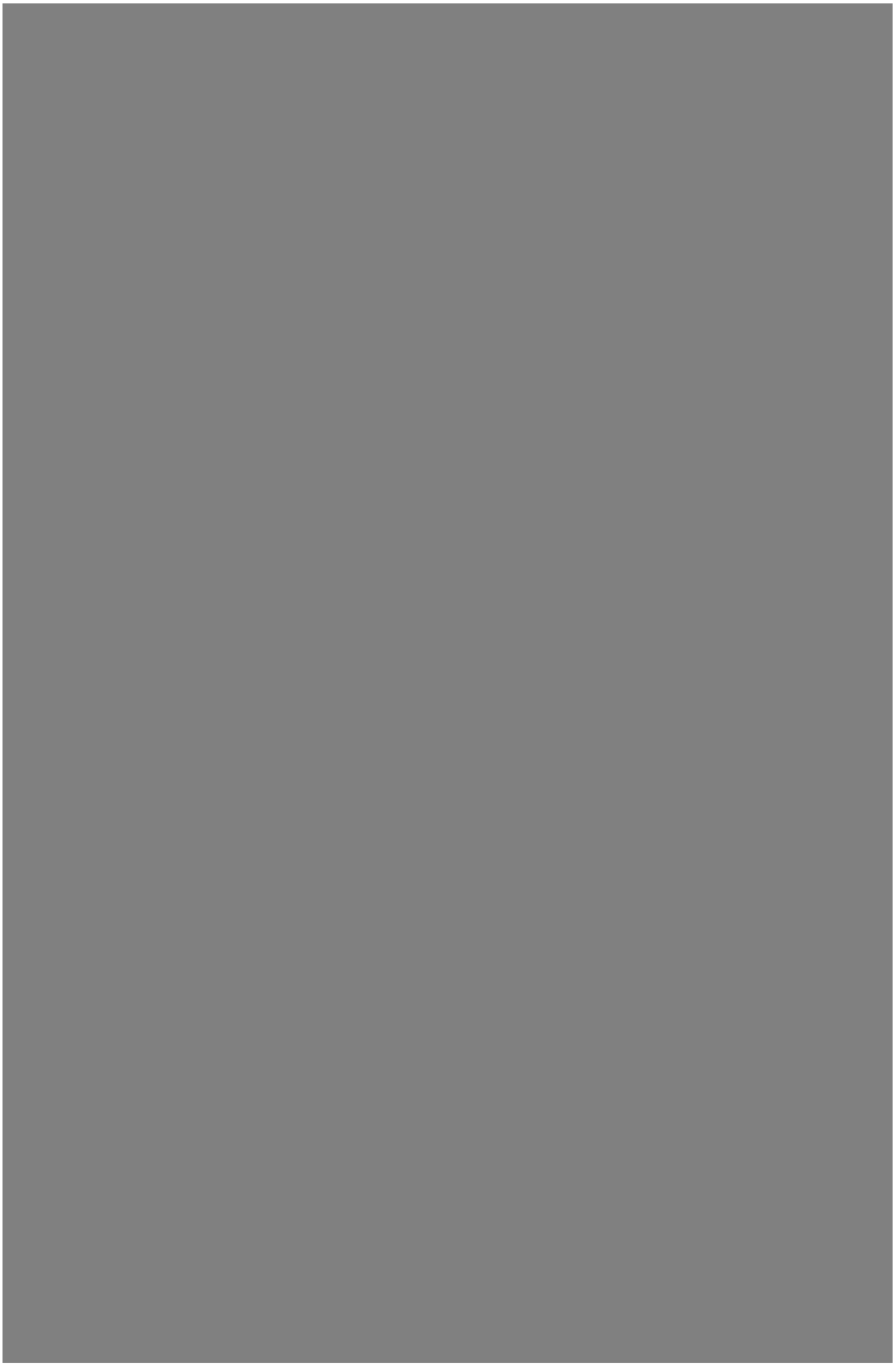

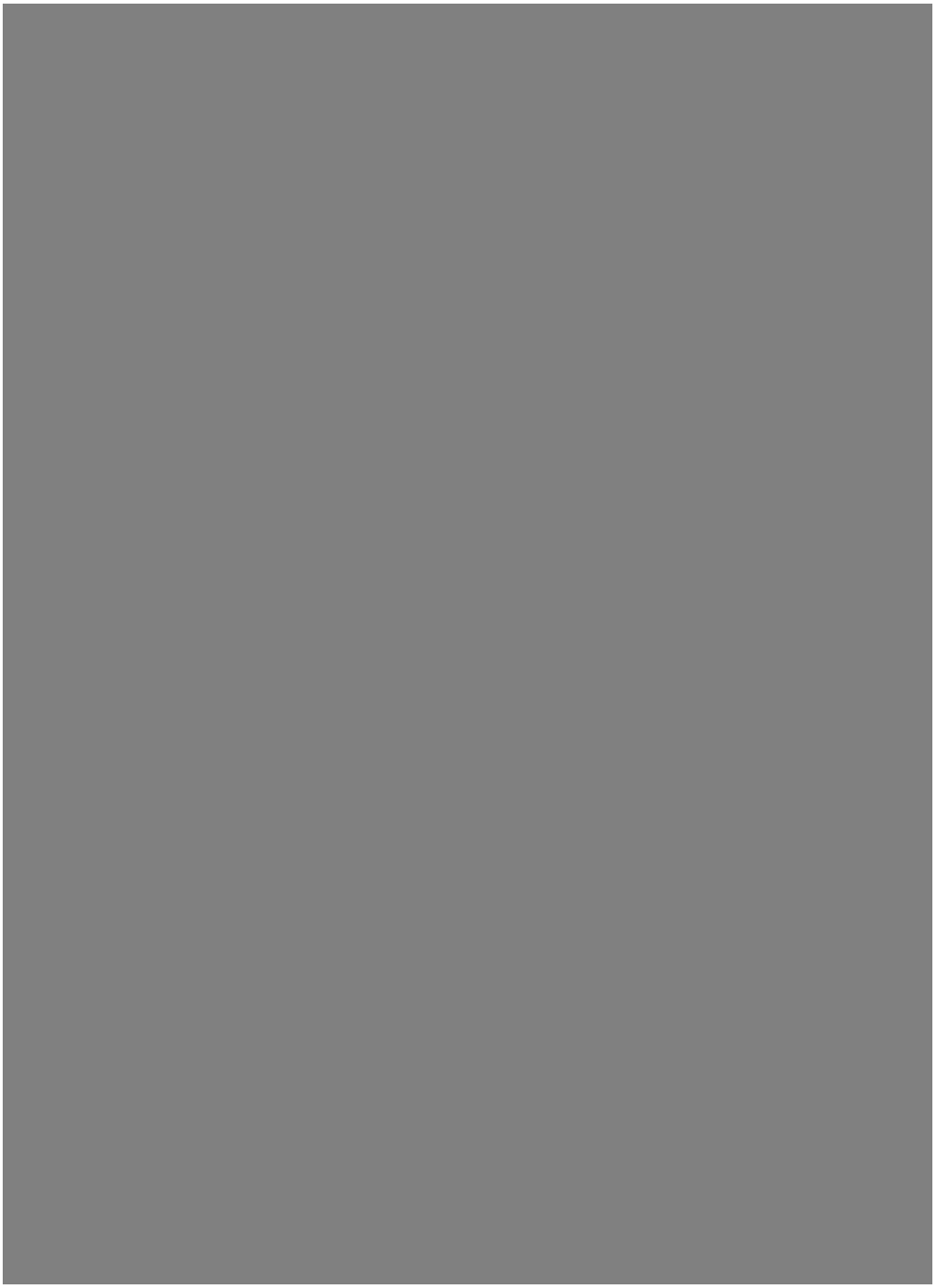

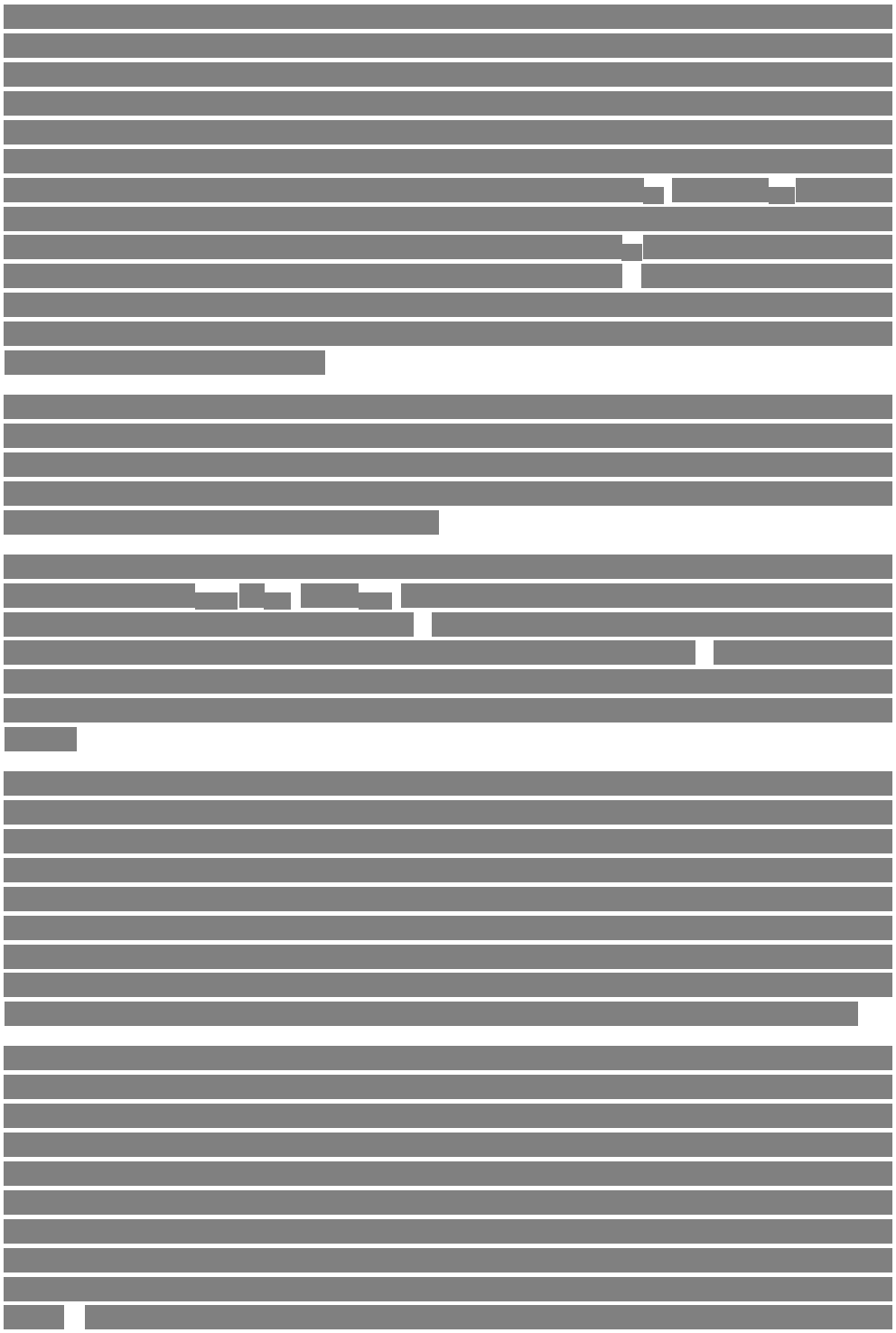

### 6.1.3 Super-resolution capabilities of the stack processing algorithms

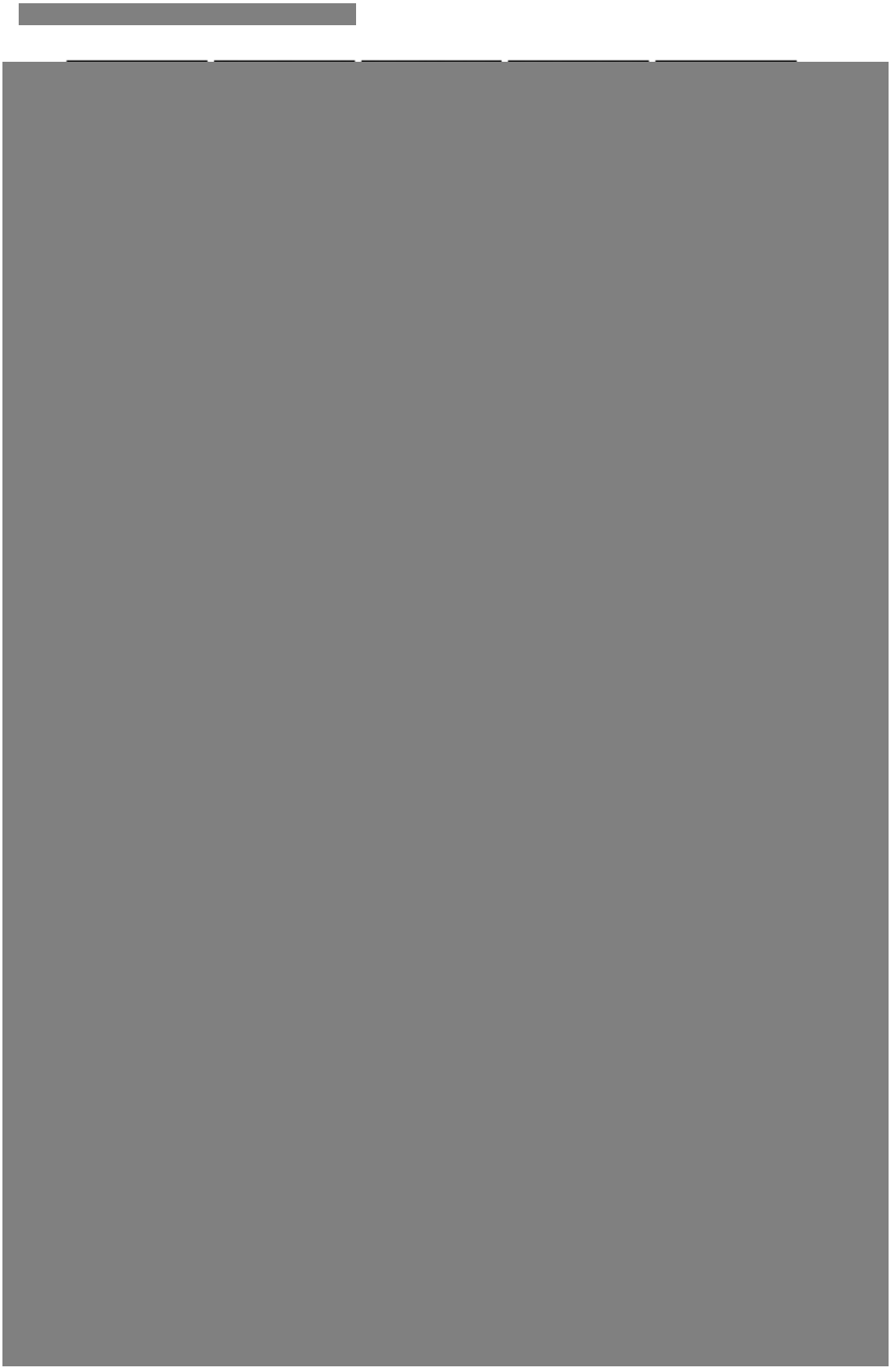

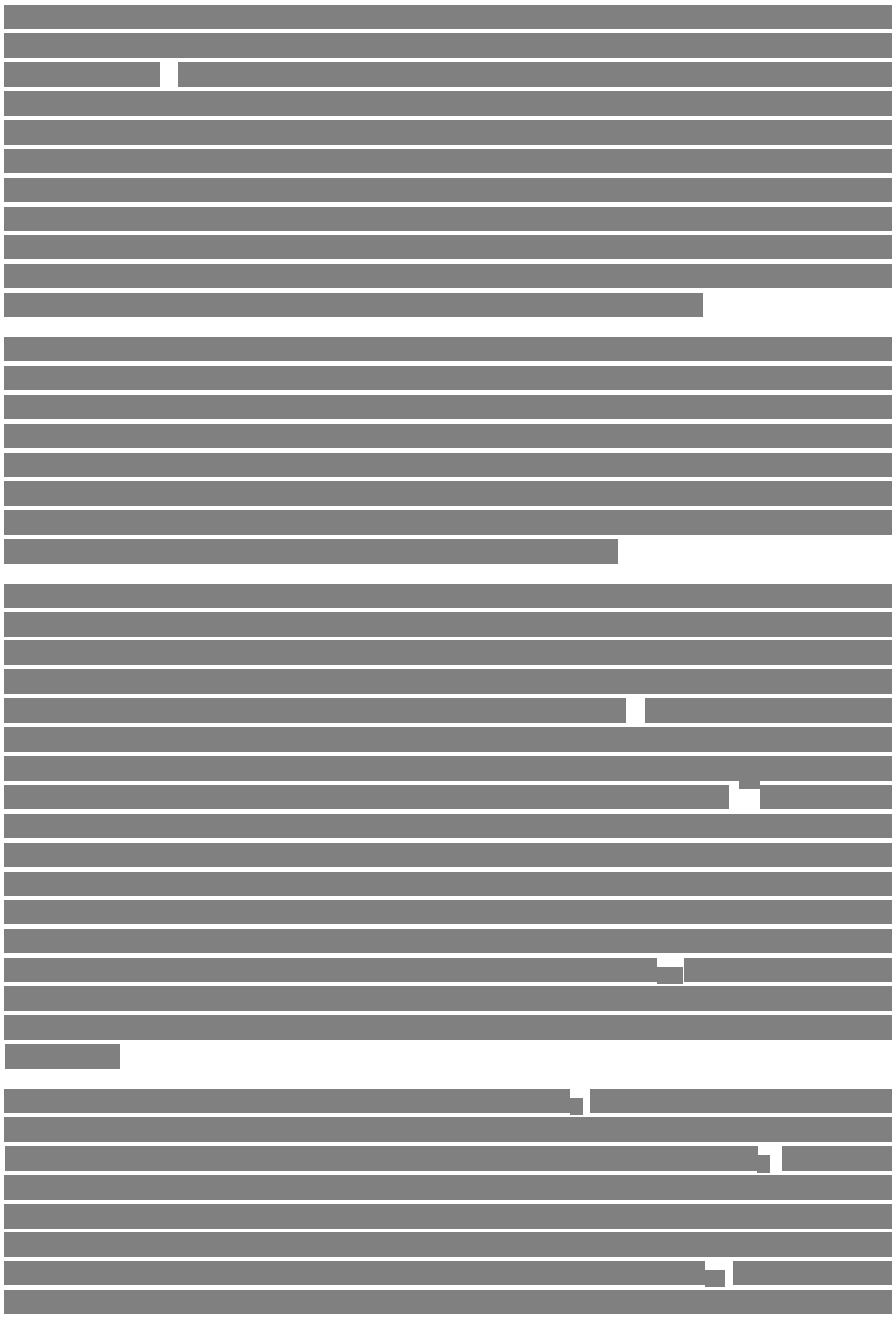

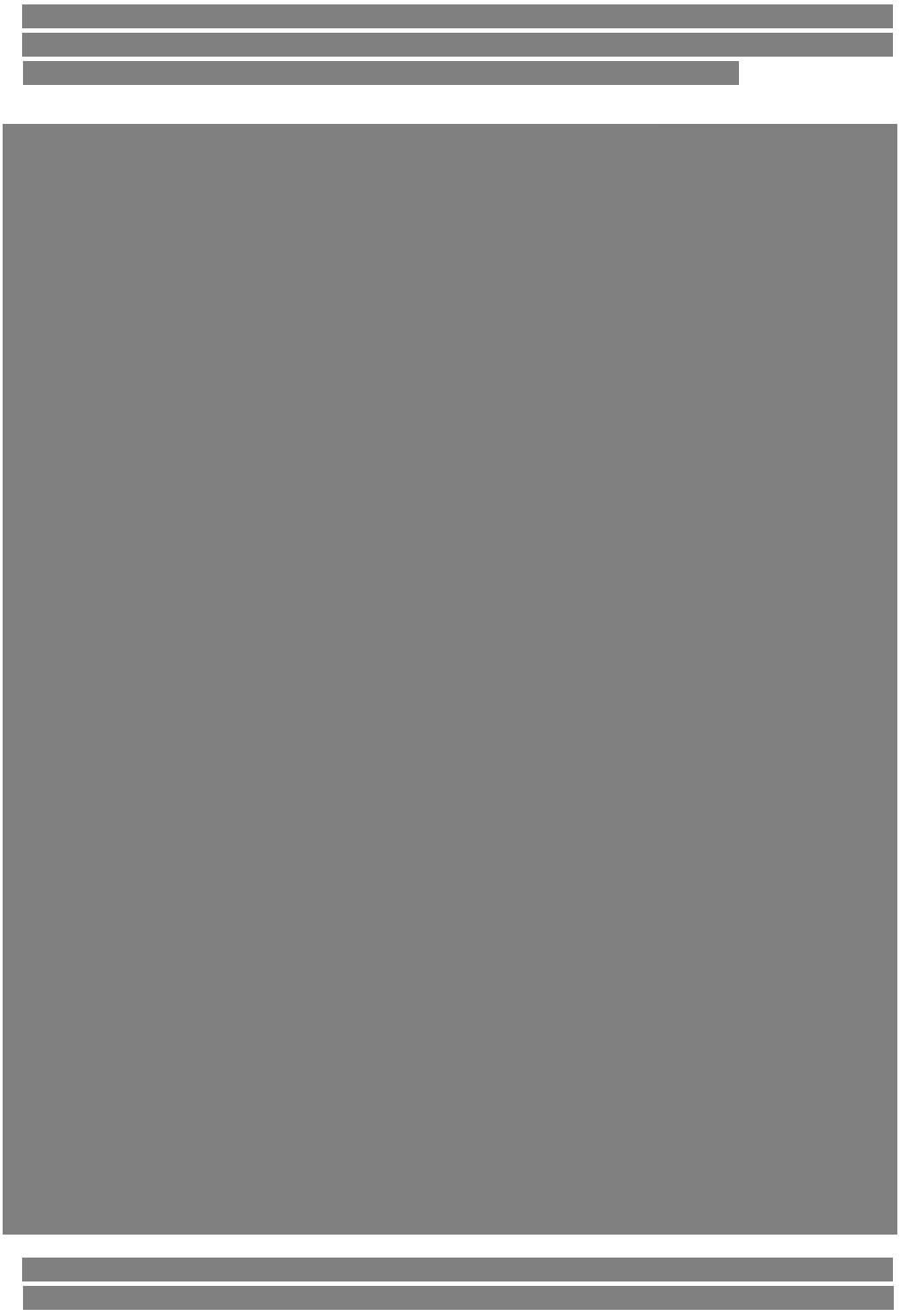

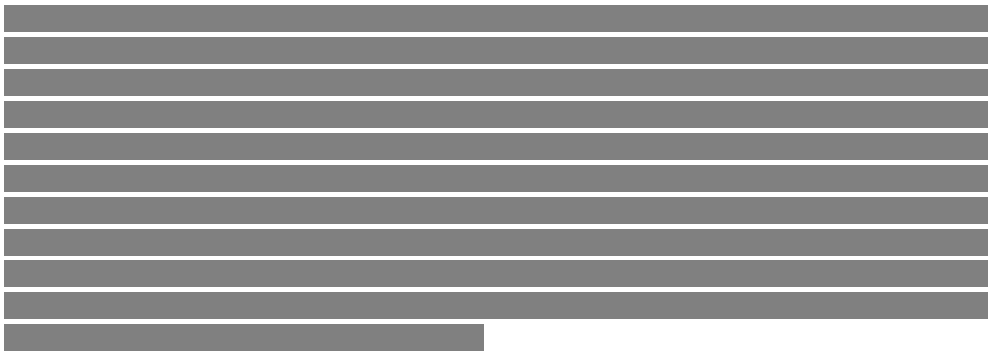

## 6.2 Virtual pinhole. Hardware implementation

Regarding the acquisition speed or imaging frame-rate of the SCREAM microscope, thanks to the extreme modulation frequency of the AOD, this one is limited exclusively by the camera sensor. The developed AOSLM unit, formed by AODx, AODy, telescope T1 and the AWG, is able to change the excitation pattern in just $8.8\mu s$, which means a modulation speed of 115kHz. Or even faster if we reduce the beam and hologram sizes ($D$, $D_h$). However, driving the AOSLM at such maximum speed is extremely inefficient since the available integration time will be almost zero. At 115kHz, the hologram corresponding to each excitation pattern position will only be centered with the laser beam once. At any other time the AOSLM will be in a transition state between two contiguous positions, something we want to avoid. In practice, each hologram has to be repeated at least 2-times in order to have an integration time of 1 hologram transition ($1t_h$). Reducing the available repetition time to 57.5kHz. Obviously, the more times each hologram is repeated, the higher the integration time, and therefore the image-stack acquisition speed will be reduced. Moreover, the hologram repetition allows us to avoid frequency leakage, improving the reconstruction quality, as wee explained in section 4.2 (figure 4.6). Integration times lower than $1t_h$ can be achieved, for example by repeating 1.2-times each hologram, but at the expense of lower pattern quality, and ghost-artifacts due to transition effects, as explained in the implementation of AHOTs (see figure 4.9).

This modulation frequency only corresponds to the transition between two consecutive holograms, a complete confocal image is obtained by exposing the camera sensor $N$, $2N$ or $N^2$ times, depending if we use multi-line, double-line or multi-point scanning. Reducing the effective frame-rate by the same amount. Although the illumination module of our SCREAM unit is surprisingly fast, the camera is always the speed bottleneck. This is the main drawback of the SCREAM unit. The sensor has to be exposed multiple times to obtain a reconstruction, in the same way as in SIM. While for example, on a spinnning-disk confocal, the imaging frame-rate matches the sensor maximum speed, the confocal image is being composed at the same time sensor is exposed (only 1 exposure is needed). An interesting factor from the spinning-disk is that, even though the sensor is exposed throughout the entire scanning process, each

pixel only captures light for a much smaller time-window. In other words, although the camera's exposure time is in the order of milliseconds, each pixel only receives photons for a few microseconds. This is completely equivalent to use a high-speed camera in our SCREAM prototype.

In order to achieve video-rates, apart from the need of multiple exposures, which can be achieved by using a high-speed camera, the obtention of a confocal image also involves real-time processing of the image stack by the algorithms described in section 6.1. To put some numbers, for 30fps or 30 confocal images per second, assuming multi-point scanning where the pattern is moved 256 times, we would need a high-speed camera going at ∼7500fps. However, if we use 100 scanning positions (N=10 instead of N=16), we would need a 3000fps camera. All the casuistry is detailed in figure 5.22.

Even though the stack processing algorithms we developed are simple mathematical operations, its implementation at such thousands of frames per second is a huge challenge. Involving high performance computing and a good management of the memory buffers. For example, assuming a typical ROI of 1024x1024 pixels at 3000fps and 10bits, the reconstruction program would have to deal with 31Gbit/s. Such volume of data is not supported by any USB protocol, nor by the PCI bus of a conventional computer. So frame-grabber cards and GPUs, using high-bandwidth protocols such as CoaxPress (CXP), are needed for storing and processing all the data coming from the SCREAM unit.

If we take a look at one emission frame from the image stack (obtained after scanning) and the virtual pinhole algorithm (section 6.1.1), is quite obvious to see that each individual frame does not contain the full sample information. From each frame, only few pixels are useful for image reconstruction. We only need pixels close to each emission focus, the rest of the pixels are not used at any time. This way, it is easy to see that acquiring the complete full-frame image is a waste of data, extremely inefficient in terms of computation. Assuming a multi-point excitation spaced $1.5\mu m$, we calculate that only 0.95% of the sensor is used for the final reconstruction, the rest of the pixels are filtered out by either virtual pinholing or the other processing algorithms.

Taking all this into account, this section is devoted to the development and implementation of two smart hardware solutions that aim to improve the display frame-rate. By reading only pixels with emission information, the square pixel area acts as a physical pinhole, directly blocking the out-of-focus components. Additionally, since at each frame only few pixels are read, the amount of data to process is drastically reduced. Thereby, the camera frame-rate can be increased by a factor close to 10. Allowing the SCREAM unit to display (in a near future) dual channel (473nm+532nm lasers) and full-frame (100x100$\mu m$ of FOV) confocal images at $\sim$ 196fps in multi-point mode and 2166fps in multi-line scanning mode.

In this section, first we demonstrate how the synchronization and alignment of the EP with the sequential reading (rolling shutter) of a low-cost camera sensor, already improves optical sectioning. Providing confocal images at 60fps, the maximum sen-

sor offered by the sensor itself. Then, in order to improve optical sectioning in the perpendicular direction, we present a hybrid confocal mode that combines hardware filtering, with on-the-fly image processing offering real-time confocal imaging (6fps). The second part of this section is devoted to the whole development process of a custom and flexible high-speed camera that allows arbitrary row reading. We demonstrate the implementation of a custom shutter mode, where the sensor can be read following the same scanning protocol for the EP.

### 6.2.1 Rolling shutter confocal and hybrid filtering

In any confocal unit using physical pinholes, the single aperture (CLSM) or array of pinholes (spinning-disk) is placed at a conjugate plane of the sample. In our SCREAM unit, instead of a physical aperture we have the camera sensor. In section 6.1.1 we presented the concept of virtual pinhole where, by applying a Gaussian mask around each excitation spot, the out-of-focus light is filtered-out, providing the final image with better contrast.

Intuitively, by applying a digital mask to each full-frame image, we are only selecting certain regions of pixels (the region around each excitation focus), while the rest of the pixels are multiplied by zero, that is, discarded. This process is repeated for all frames of the image stack. At the end, $< 1\%$ of the pixels are used for the final reconstruction. For virtual pinholing, capturing a stack of full-frame images is a very inefficient process in terms of data stream. Is is easy to think that, if only 1% of pixels are used, it is possible to increase the frame-rate a factor $\sim 100$, while keeping the same data bandwidth. The only thing to do, is just reading this 1% of pixels from the sensor, and not the full-frame.

On top of that, by reading the individual pixels, we would be already filtering the out-of-focus light. This way, a post-processing stage would not be needed. The sensor would be read in the same way that the sample is scanned, that is with multiple points (or lines) and shifting those positions every time. Once the entire sensor is read, the image will be already confocal.

However, this ideal camera still does not exist. Partial sensor reading is possible in most commercial cameras, where by selecting a very small region of interest (ROI), the framerate can be drastically increased. However, due to CMOS sensor architecture, where the sensor reads the whole pixel row every time, the maximum frame-rate scales with the number of rows and not the number of pixels. So, instead of a 100-fold increase in framerate, we would achieve a 10-fold increase. On top of that, and the most important limitation, is that commercial CMOS sensors do not allow random access to pixel rows. Regarding the ROI geometry, typical cameras only allow the user to select one continuous ROI. In an ideal world, we would need a whole set of tiny ROIs (1x1 or 2x2 pixels), as many as excitation focus.

Even though a random access camera is almost impossible to achieve, in the next section we present a custom modified high-speed sensor, allowing arbitrary row reading and per-frame ROI change. In which we implemented a sensor scan mode based on

multiple lines.

Previous to the development of this custom high-speed camera, in this section we present two different imaging modes using a cheap CMOS camera sensor, characterized by having a rolling shutter mode. In a rolling-shutter camera, pixel rows are being exposed and read (digitized) sequentially, one after the other. Every time we send an external TTL pulse, after some programmed delay, the camera starts exposing row 1, once exposure of row 1 is finished, row 2 is exposed while row 1 is being read. This process is repeated until the whole set of pixel rows are transferred to the PC.

In the first mode, we call "rolling confocal", the sequential rolling shutter is synchronized with the excitation pattern, generated by the AOSLM. Figure 6.20 shows an scheme describing this mode. Instead of using a multi-point or multi-line pattern, here the sample is excited and scanned with a constant intensity line, of the same width as the camera sensor. This way, all the light diffracted in the 1-1 order of the AODs goes to that position, increasing the photon density, and therefore, the fluorescence signal. For the generation of this horizontal line excitation pattern, only AODx is working in holographic mode. Whereas AODy is just used as a deflector, which moves the line diffracted by AODx from row 1 to row 1024 of the camera sensor, and thereby scanning the specimen from top to bottom. The complex RF signal (acousto-optic hologram) for the AODx is always the same, whereas for the AODy the frequency of the pure sinusoidal signal is changed discretely from $f_1$ to $f_2$ in 1024 steps. This way each pixel row position corresponds to a fixed frequency. When AODy is driven by $f_1$ the excitation line is aligned with row 1, the same applies for row 1024 and $f_2$.

The camera used for these modes is a IDS UI-3242LE board level camera, with a resolution of 1280x1024 pixels ($5.3\mu m$), 12-bits of dynamic range, 60% of quantum efficiency (QE) and 60fps of maximum frame-rate. The camera is connected to the computer by means of USB3.0 and controlled using MicroManager software.

In order to filter the out-of-focus light, is very important for the excitation line to be moved at the same speed as the rolling shutter. In other words, we need the excitation line perfectly centered with the rolling shutter line, at all times. This is done by changing 3 parameters: $f_1$, $f_2$ and $t_s$, where $t_s$ (or sweeping time) is the time it takes for AODy to go from $f_1$ to $f_2$. Note that AODx is treated independently, all the synchronization and alignment process is done just modifying AODy signal. $f_1$ and $f_2$ are calibrated experimentally using an homogeneous fluorescent sample, and an iterative process where the intensity in rows 1 and 1024 is maximized.

Once $f_1$ and $f_2$ are calibrated, $t_s$ is given by the camera frame-rate $f_{cam}$. If $t_s < 1/f_{cam}$, the excitation line is moving faster than the rolling shutter. If $t_s > 1/f_{cam}$, the sensor is read faster than the sample. In both cases, optical sectioning will be degraded as the distance between both the rolling shutter and excitation lines increases. Since the sensor is read from top to bottom, a wrong synchronization is observed as a contrast gradient along Y direction (as shown in figure 6.20(b)). Moreover, apart from perfect timing between line generation and row readout, is very important to match the sensor X-Y axis to the same AODx and AODy axis. Otherwise the generated line

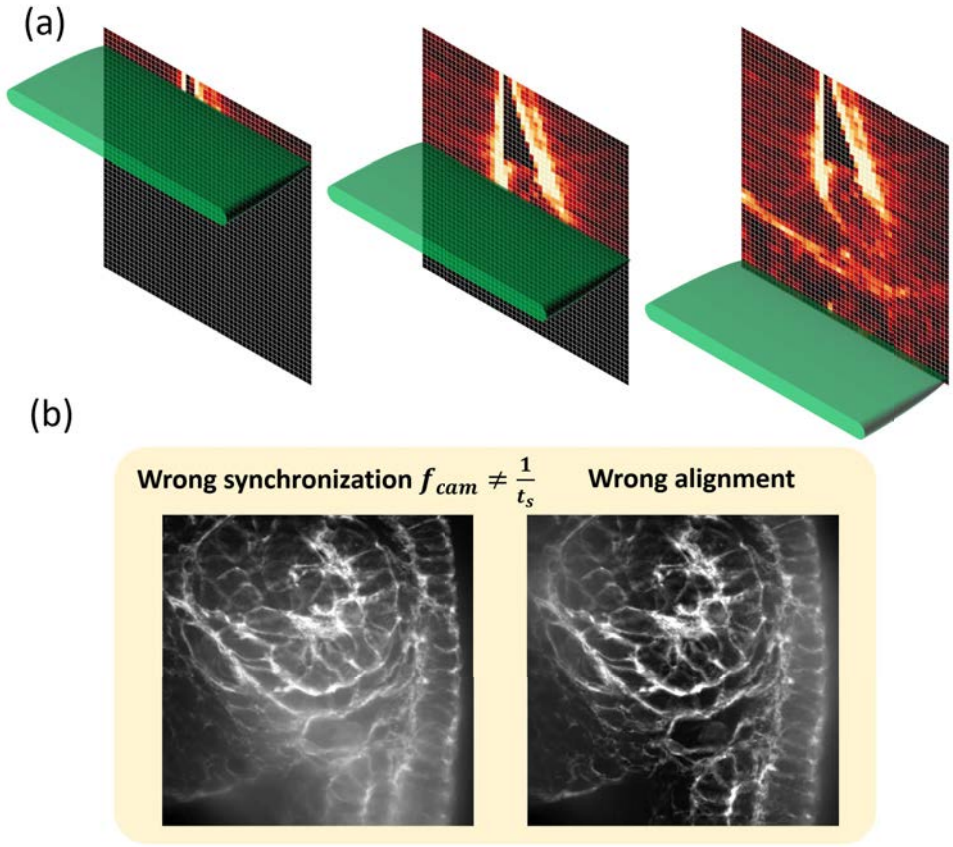


**Figure 6.20:** (a) Scheme of the rolling shutter filtering mode (rolling confocal). By properly synchronizing the excitation line with the rolling shutter of a CMOS sensor, no post-processing is needed to remove the out-of-focus light. The rolling shutter itself acts as a physical pinhole (rectangular slit), filtering light from outer planes. With this method, the image provided by the sensor is already confocal. (b) Synthetic images describing the effect of wrong timing and wrong alignment between the excitation line and rolling shutter row.

will be tilted with respect the rolling shutter row, and only the matching region will be filtered. In the laboratory, a tilted excitation line is observed as a high-contrast in the central part of the image, whereas optical sectioning decreases at the boundaries of the FOV, see also figure 6.20(b).

When both lines, i.e. the rolling shutter the excitation, are perfectly aligned, the rolling shutter readout acts as a rectangular slit of 1280x1 pixels. So, the out-of-focus light is filtered out only in the Y direction. The effective pinhole size is the pixel size at the sample plane, 88.3nm. Such a small pinhole improves resolution but affects the final signal, since most of the PSF area is blocked. To solve that, we change the

exposure time of each row, which in our case is completely equivalent to change the pinhole size. This way, the excitation line remains static at the same position during $k$ consecutive row readouts, having the same effect as a pinhole of size $k \cdot 88.3nm$.

Rolling confocal mode allows us to display images at the maximum frame-rate given by the camera, without the need of multiple full-frame exposures and post-processing algorithm. With this particular cheap sensor, which can be found in most webcams, we are able to achieve 60fps in full-frame mode, which corresponds to a FOV of $\sim 100\mu m$ for the 60x NA 1.2 objective. Regarding the optical sectioning capabilities, the use of a constant intensity line offers a complete removal of out-of-focus light in the Y direction, but none in the direction along the line.

The second mode we implemented is a new concept for confocal filtering we developed and named "hybrid confocal". The basis of this mode is to combine both hardware filtering in the sensor scanning direction, in the same way as in rolling confocal mode, with the real-time implementation of the stack processing algorithms, taking care of filtering the out-of-focus light in the perpendicular direction (columns). The aim of this mode is to improve the optical sectioning capabilities of the single-line-scanning mode, without the drastic reduction in frame-rate that multi-point scanning supposes. In single-line-scanning mode the X direction can not be filtered due to infinite excitation crosstalk along the line direction. In this hybrid confocal mode, the sample is excited with a set of focused spots distributed equally along the X direction. Instead of an array of 40x40 spots (muti-point scanning mode), here we only project a 1D array of 40x1. Figure 6.21 shows an schematic description of this hybrid mode.

As in the multi-point scanning mode, the point spacing can be changed to adapt to the sample thickness or imaging depth, separating the excitation foci for thicker specimens, allowing to preserve the same optical sectioning and SNR for all z-slices. For the generation of this dotted line, AODx is driven by exactly the same RF signals as in the multi-point scanning mode, while AODy deflects the diffracted distribution generated by AODx. For the AOSLM part, both rolling confocal and this hybrid mode, are very similar. The only difference is that here the excitation line is substituted by an array of points, allowing a post-processing algorithm to filter the out-of-focus light in the X axis.

This dotted line provides even more SNR than a constant line, due to all the excitation laser power is distributed in less positions. Compared to single-line excitation the dotted line EP provides a $\sim$ 11 fold increase in excitation density, and a 40-times increase when compared to the equivalent multi-point excitation pattern. This values assume the full FOV and a periodicity of $2.5\mu m$. Obviously the excitation energy scales with the number of foci, the more sparse is the EP, more excitation photons are available at each spot. Such 40-fold increase in SNR that dotted-line excitation offers, allows the use of lower power, and hence less expensive, diode lasers. In addition to this, we experimentally found that fluorescence emission frames using this mode, suffer from less point-to-point crosstalk, than an equivalent 2D array of points. For the same periodicity value and considering just the first neighboring spots, 8 different focus contribute to crosstalk for the multi-point approach, whereas only 2 in this dotted line. This means that, for the same periodicity value, hybrid confocal

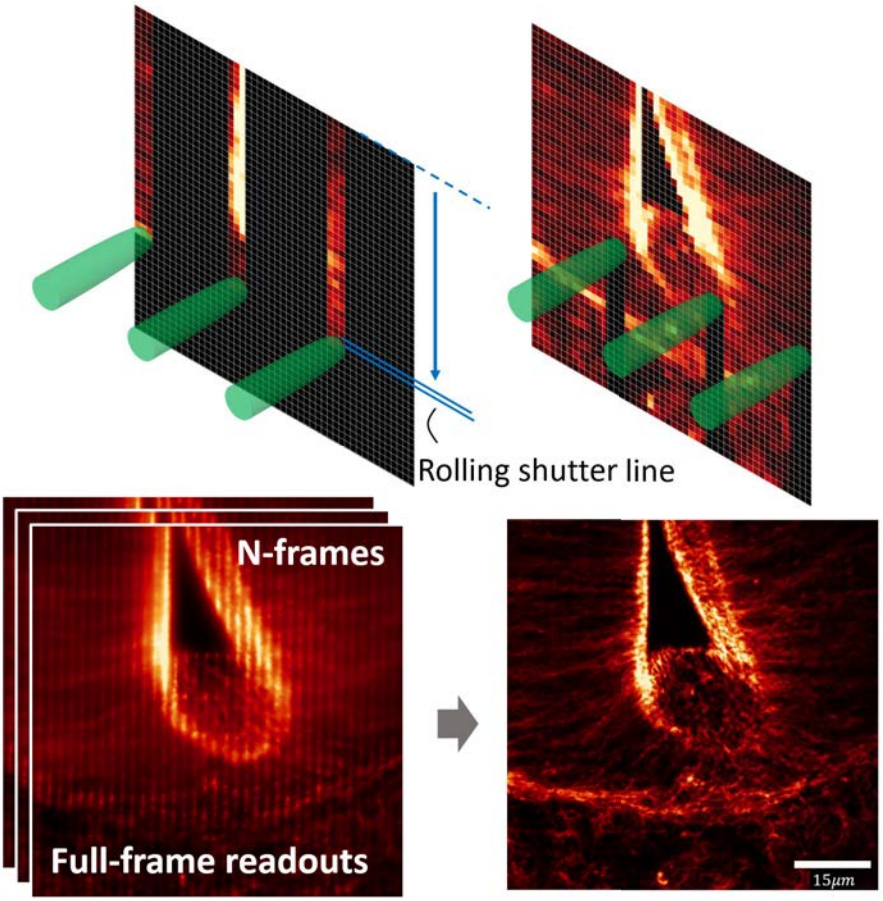


**Figure 6.21:** Scheme of the hybrid rolling shutter mode. In order to filter out-of-focus light in all directions, the rolling shutter is synchronized with a set of horizontally arranged focus, then the dotted-line excitation pattern is shifted to the right N-times until the scan is completed. Then, the image stack is collapsed by means of superconfocal or homodyne detection algorithms. In this hybrid mode, the out-of-focus light is physically filtered in Y direction (by the rolling shutter itself) and in the X direction the remaining background flare is removed by software. In this mode, the effective frame rate is reduced by a factor of N, instead of $N^2$ for the regular multi-point mode.

offers slightly better optical sectioning than the multi-point case. Or as in our case, the excitation spots can be brought closer, for which less scanning steps are needed, increasing the effective frame-rate.

The rolling shutter alignment and synchronization procedure is exactly the same as for the previously explained rolling confocal mode. The dotted line is synchronized with the rolling shutter, in such a way that every time the full-sensor is read, the multiple

points scan the sample from row 1 to row 1024. As before, the rolling shutter line readout acts as a 1 pixel (or several, depending on the line exposure time) pinhole in the Y direction, filtering the background flare.

As can be seen in figure 6.21, after each full-sensor readout, the excitation points are moved to the right N-times, until the whole sample is scanned. Under this scheme, only N full-frame exposures are needed to obtain a final reconstruction, as opposed to the multi-point scanning where we need to exposure the full sensor for each scanning position ($N^2$). As a consequence of the rolling shutter synchronization, that already filters out most of out-of-focus light, hybrid confocal mode just needs 1 exposure for each X position.

In each full frame exposure, the dotted line, followed by the rolling shutter, is swiped from top to bottom, resulting in a fluorescence frame with vertical lines. Note that, along the vertical line the out-of-focus light is already blocked. From the rolling shutter line point of view, the laser remains static for the whole sensor readout, we name this filtering method "CMOS descanning". Once all frames are captured, the N images are then combined into a final confocal reconstruction. One option is to apply a vertical slit virtual pinhole, which is basically selecting only those pixel columns visited by the laser at each frame. by means of the stack processing algorithms described in section 6.1.

In figure 6.22 we show the experimental results of this hybrid confocal mode for two different specimens, with different thicknesses: a flat sample of Chinese Hamster Ovary (CHO) cells ($\sim$5-10$\mu m$ in thickness) and a $\sim$40$\mu m$ chicken embryo slice. In both samples the actin network is labeled with phalloidin+TRITC. In this particular case, the periodicity is 1.5$\mu m$ and the number of scanning steps is N=10, which means that complete confocal images were displayed in real-time at 6fps. The epifluorescence image is obtained afterwards (for comparison) by projecting a constant intensity pattern and capturing a full-frame image, everything with the same SCREAM unit.

In hybrid confocal mode, the final frame-rate is given by $\frac{f_{cam}}{N}$, which represents an N-fold increase over the multi-point excitation and full-frame exposure case ($\frac{f_{cam}}{N^2}$). For the camera control part, we implemented all the stack processing algorithms in Java, as part of a MicroManager plugin. Concretely, the stack processing has been implemented using the On-The-Fly processor pipeline. This way, a flat-field correction can be also implemented to remove the fixed pattern noise of the low-cost camera sensor.

### 6.2.2 Custom camera development with arbitrary partial reading

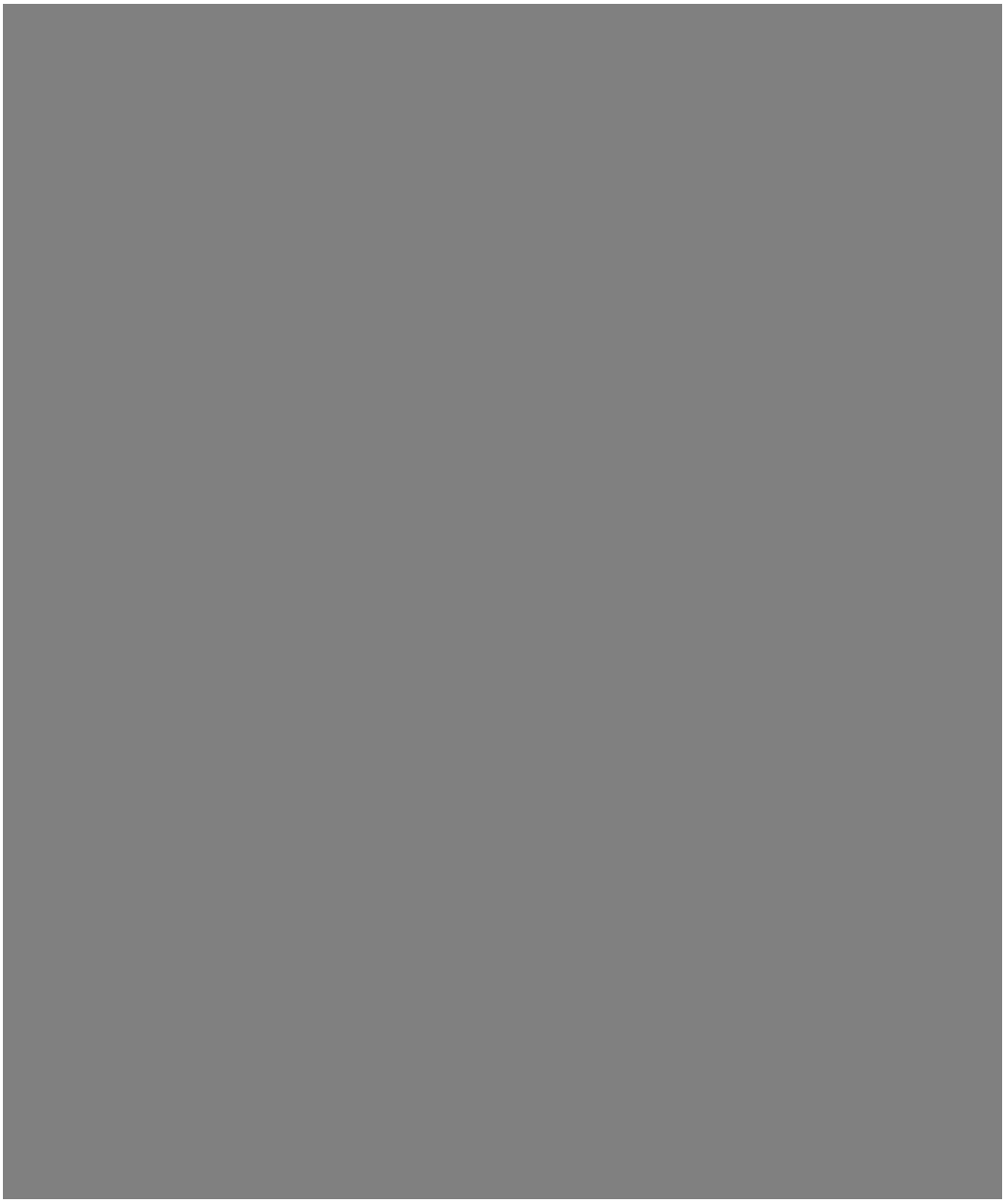

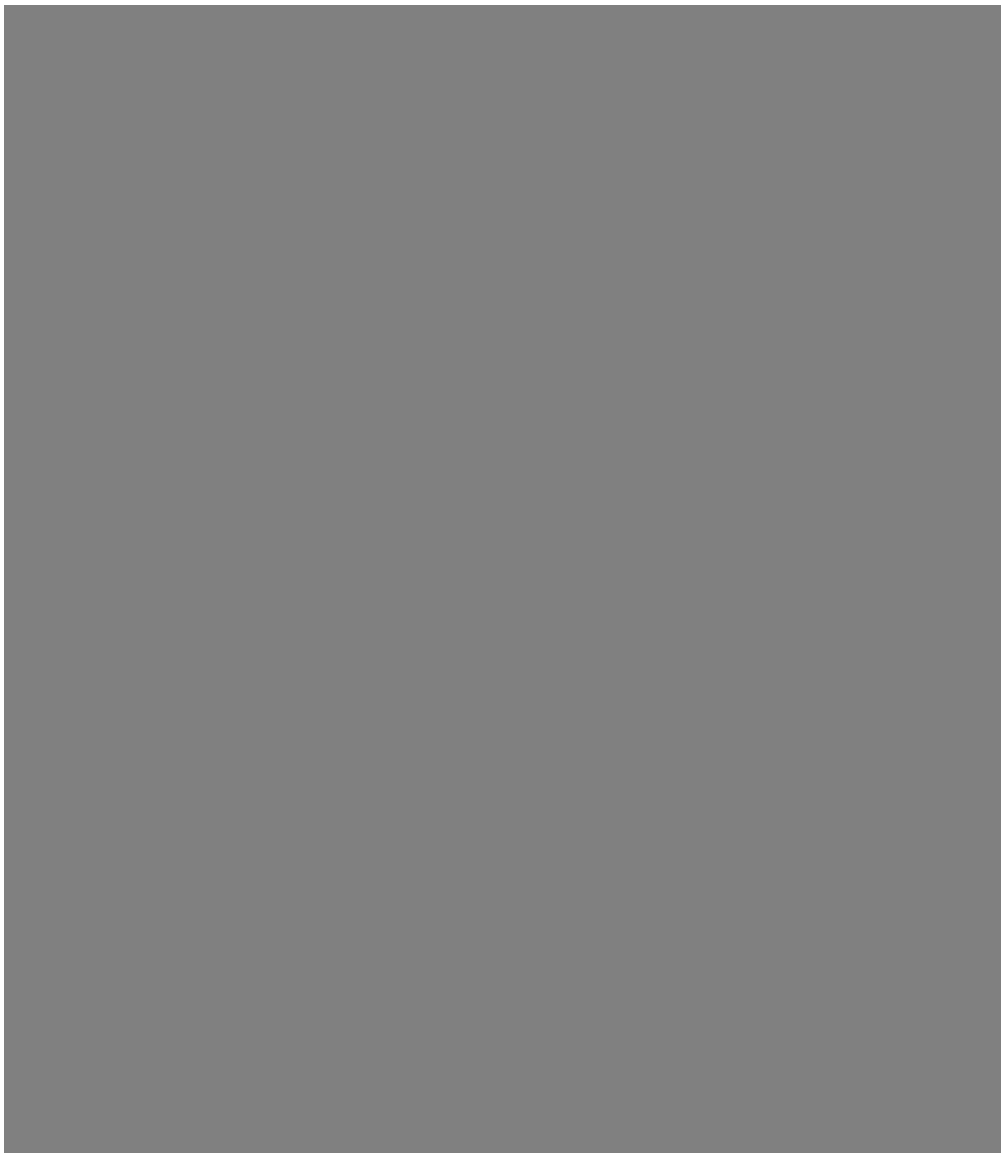

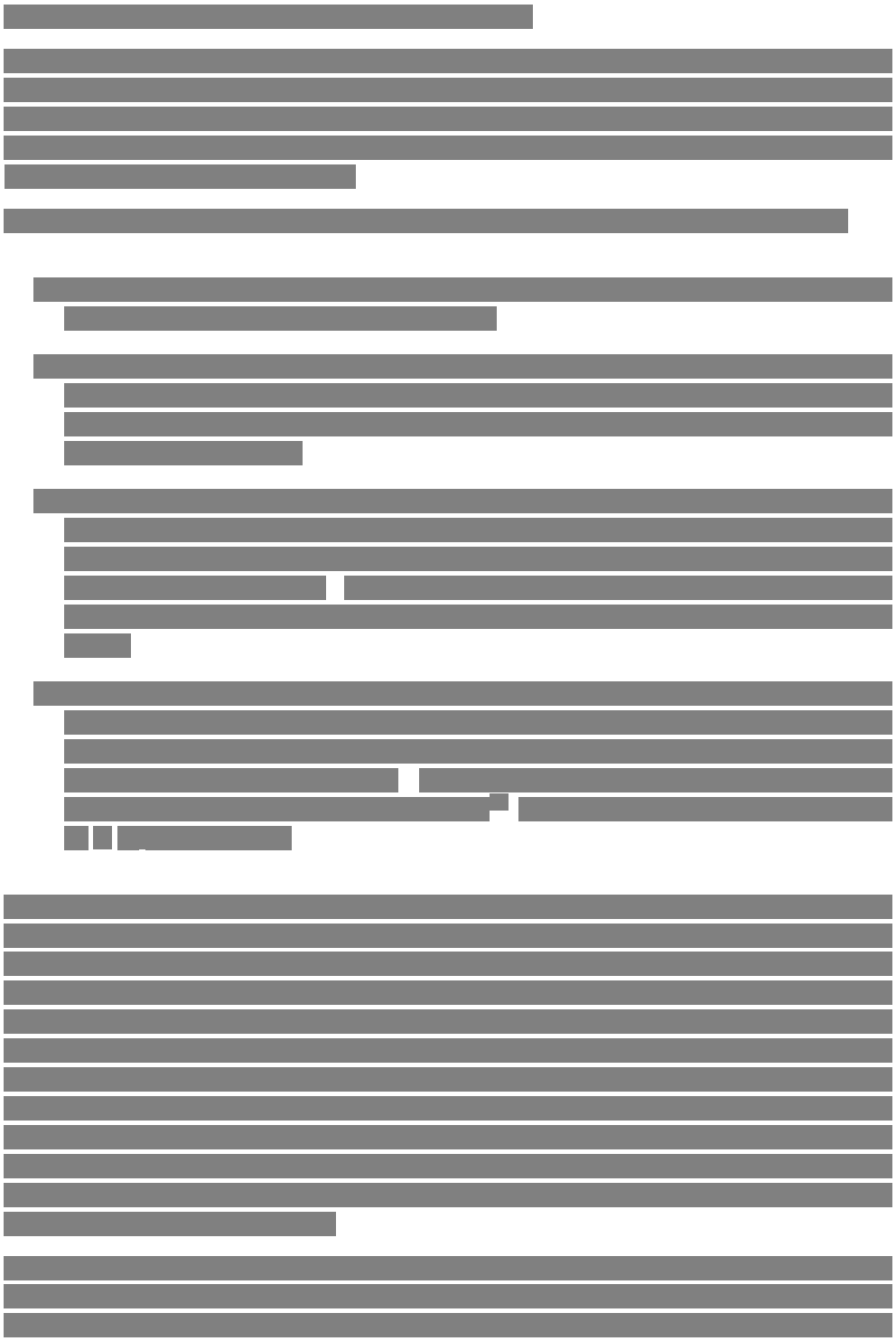

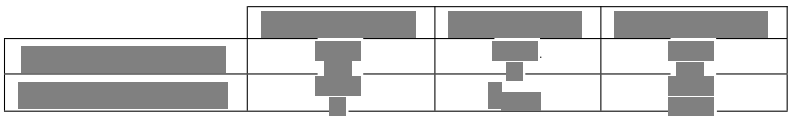

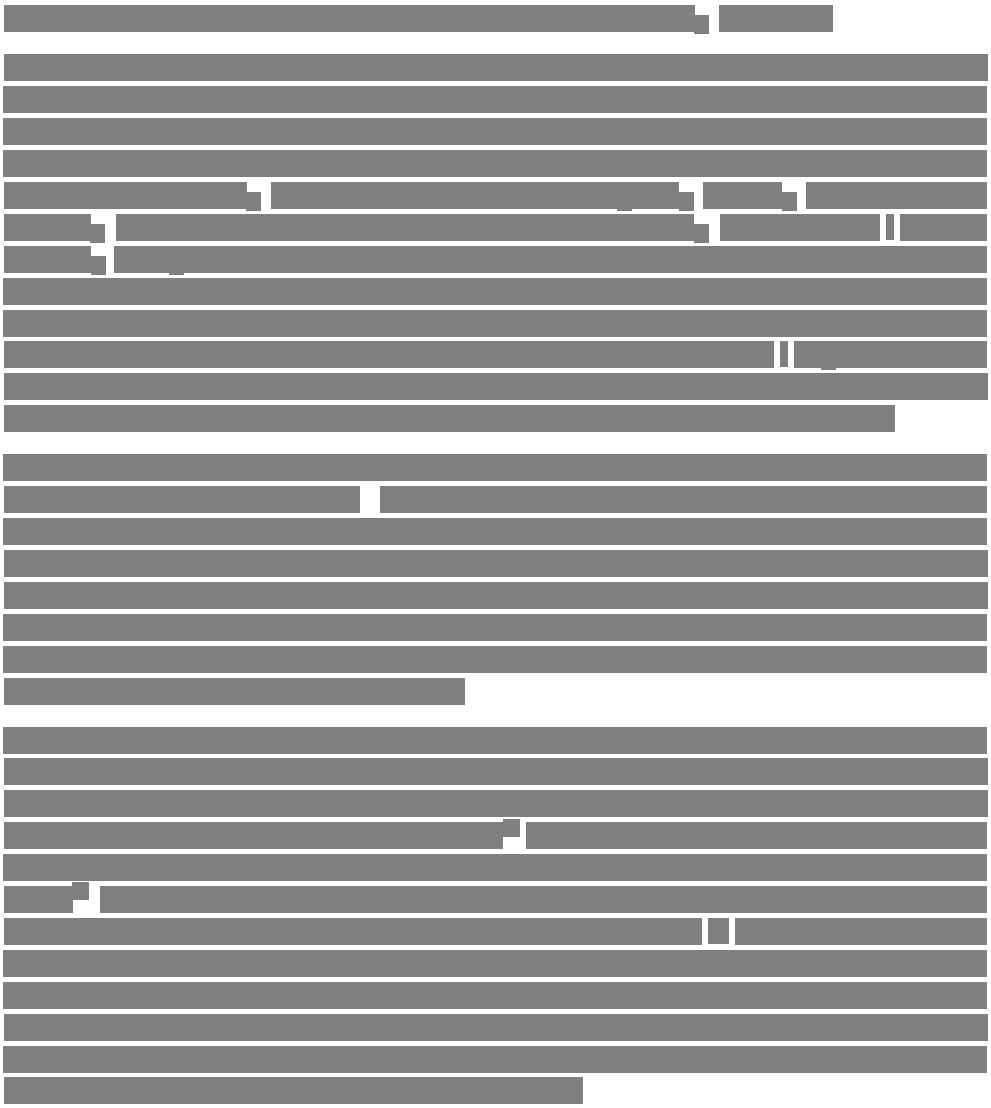

# Chapter 7

# Enhanced acousto-optic modulation for super-resolution microscopy

As demonstrated in previous chapters 5 and 6, the PAM unit developed in this thesis provides images with extraordinary high-contrast. Moreover, the extreme speed and full-complex modulation capacity that characterizes the AOSLM (key component of the SCREAM setup), combined with a completely digital confocal filtering part, opens a wide range of possibilities. Such flexibility in the generation of high-quality (artifact-free) illumination patterns, and the extreme positioning accuracy and modulation speed, permits the use of the SCREAM unit in complementary techniques.

More than just a confocal microscope, the SCREAM unit can be interpreted as a programmable module. Where future developers can implement new techniques and illumination schemes. The same optical setup described in chapter 5, without any extra modification, can be used to project arbitrary patterns for optogenetics applications, or in FRAP, to perform experiments in multiple sites in parallel. Additionally, the high control over the laser-wavefront, offers the possibility to implement different wavefront shaping methods to compensate scattering in very thick samples and turbid media [114]. This would allow imaging deep inside biological tissues with high-contrast.

Although offering high-contrast, confocal images straight from the SCREAM microscope are limited in resolution due to light is a wave, and diffraction through the microscope objective establishes the minimum spot size it can be concentrated. To surpass this barrier, different solutions and techniques have been appearing during the last years under the concept of super-resolution optical microscopy. In the same way the invention and development of confocal fluorescence microscopy supposed a revolution for most of biological studies, the field of super-resolution microscopy nowadays is growing at a vertiginous level. While confocal microscopy allowed the observation in 3D of whole specimens, with super-resolution microscopy biologists now can observe and study cellular structures at the molecular level. With all the benefits that

this entails. Allowing, for example, to observe individual cytoskeleton filaments or co-localize specific bio-markers.

Regarding super-resolution techniques, multiple brilliant solutions exist to break the diffraction barrier, based on completely different principles. The two most popular approaches are: optical methods (patterned light) or the use of specifically designed emitters. Moreover, most recently a set of computational super-resolution techniques appeared, thanks to advances in parallel computation and digital image processing.

This chapter is fully devoted to study the super-resolution capabilities of the SCREAM platform. First implementing an already developed concept using photoswitchable probes, and then presenting a new concept of super-resolution, based on a trained convolutional neural network. The successful implementation of both methods demonstrate the flexibility of the SCREAM unit to adapt to different situations, either implementing existing techniques, or new ideas.

On the first part, we show how the same SCREAM unit is able to generate and parallelize the illumination pattern sequence needed for RESOLFT microscopy (REversible Saturable OpticaL Fluorescence Transitions). Showing experimental results using a custom designed exotic depletion pattern. The generation of all illumination patterns with the same AOSLM device, simplifies a lot the optical setup, and above all, the alignment process. It supposes an step forward in the parallelization of such technique, and the first demonstration of RESOLFT microscopy using a totally programmable device. Allowing the user: faster imaging (transition from stage scanning to laser scanning) and to change the pattern periodicity. Something that, up to date, has been done with fixed optical components.

On the second part, we present the preliminary results for a new super-resolution technique. In this method, the sample is scanned in the same way as when obtaining a confocal image, using the same excitation patterns and scanning protocols. But instead of processing the image stack with the pixel-based calculations of chapter 6, here the stack is collapsed by a convolutional neural network, entirely trained with synthetic data from the simulator tool developed in this thesis. Finally, experimental results are shown in a sample of fluorescent beads.

## 7.1 Introduction to super resolution

The main problem regarding the optical resolution is that the area to which light can be concentrated is limited by the laws of diffraction. As explained in section 5.1.1, both the excitation and emission PSF's ($PSF_{ex}$ and $PSF_{em}$) can be approximated by a Bessel function with a FWHM given by equation 5.2. Since light can not be focused more than $d_{xy} = 0.61 \cdot \lambda_0/NA$, all fluorophores that fall within this round spot are excited simultaneously, which in turn also emit all at the same time. The consequence of this is that, at the camera plane, these individual emitters are not distinguishable. Due to diffraction, the minimum resolvable distance is given by $d_{xy}$, so all emitters inside this region are considered the same.

The scale of $d_{xy}$ commonly does not affect imaging at the tissue or whole specimen level. The $\sim 250nm$ size of the $PSF_{ex}$ is more than enough to observe embryos, tissues or small organs. But when we start zooming in into cells, sub-diffraction structures such as cytoskeleton filaments, small vesicles or mitochondria, the diffraction barrier becomes an obstacle for studying such fine structures in detail.

By looking at the $d_{xy}$ expression we see that one option is to use high-NA objective lenses. However, this value is limited by the specimen's refractive index. Under some approximations, the cellular cytoplasm can be understood as a mixture of an aqueous solution with many different components, so the effective refractive index does not differ much from $n_{water} = 1.33$. Although NA=1.5 and NA=1.6 lenses exist, it is easy to observe that when used to image structures inside cells, the effective NA is always the specimen's refractive index. Note that for light rays traveling at angles such that $nsin(\alpha) > NA_{obj}$ (being $n$ the medium's refractive index), total internal reflection occurs and light is not propagated inside the specimen. In other words, using a NA=1.5 objective lens in water has the same effect as using an equivalent, and less expensive, NA=1.33 lens.

The main goal of optical super-resolution microscopy is to come up with new methods to be able to distinguish structures inside the big 250nm light blob, captured by any wide-field microscope. Different smart strategies exist to surpass this barrier and they can be distinguished by the type of fluorophores used in the imaging process. Basically whether they use the linear emission region of fluorophores, where emitted light is proportional to excitation light, or if instead they take advantage of non-linear processes that occur near saturation (or specially modifies molecules).

On the first part, several optical methods or "optical tricks" exist to overcome the diffraction limit barrier. On one side, as explained through chapters 5 and 6, a regular CLSM working with a closed pinhole, already improves lateral resolution a factor of $\sqrt{2}$ with respect the open pinhole (wide-field) case. The same improvement is achieved by means of photon/pixel reassignment (ISM theory), where similar to what a closed pinhole does, all photons are re-organized an assigned to a smaller area, reducing the effective spot size. $\sqrt{2}$ improvement is also provided by two/multi-photon microscopy, where the two-step (non-linear) absorption results on an effective $PSF_{ex}$ which is $\sim PSF_{ex}(x,y)^2$, also extending the lateral barrier $\sqrt{2}$. All this techniques are fully compatible with iterative deconvolution algorithms, able to improve lateral resolution another factor of $\sqrt{2}$, ending up with a total improvement of $\sim 2$, depending on the SNR.

An identical improvement, is also achieved using a different approach. It is possible to enhance the spatial resolution by exciting the sample by means of a patterned illumination. In this technique called Structured Illumination Microscopy (SIM) a sinusoidal pattern, by definition with a single spatial frequency, is projected into the sample and its fluorescence image captured with a camera. The same pattern is then shifted and rotated several times, and a post-processing algorithm combines all images into a super-resolved reconstruction with 2-times better resolution [115]. The basis behind this principle is that, the illumination pattern frequencies are mixed with those of the sample itself, producing an interference (Moire fringes) that brings the high-

frequency components of the sample (which, in principle, are filtered out by the limited NA) towards the detection range of the objective lens. SIM has been demonstrated to improve lateral resolution a factor of 2 in all three dimensions [116, 117, 118]. To achieve isotropic resolution improvement, sinusoidal patterns need to be generated also in the axial direction.

The advantages of this methods is that they work with almost any fluorescent sample, however the resolution improvement is marginal, reducing the minimum resolvable feature to half.

On the second part, there is a set of techniques that combine working on the non-linear emission zone of fluorophores, with the introduction of sub-diffraction limit features in the illumination pattern. The first technique in this category is STED microscopy (Stimulated Emission Depletion), which is based on the stimulated emission phenomenon [119, 120, 121]. Once on the excited state, it is possible to "force" electrons to go back to the ground state by using photons of the same energy as emission photons, that is using an additional laser that matches the energy difference between both excited and ground state. This way, by depleting all fluorophores that reside at the periphery of the Airy disk, only the central part will still emit. The depletion of the surrounding region allows to assign all the emission photons collected by a single-pixel detector (PMT) to the nominal laser position, improving the lateral resolution up to 30-40nm.

STED microscopy can be easily implemented in a regular CLSM, just by adding this additional "depletion" laser. Apart from the excitation laser, in a STED microscope a longer wavelength laser is aligned into the same optical axis. It is easy to see that, for a good improvement of the effective PSF's FWHM, the depletion laser has to shaped like a "doughnut", such that the intensity at the center is exactly zero, whereas different than zero at the periphery. In other words, we want to deplete just the periphery, not the center. The solution to this, is to use a Laguerre-Gaussian or "vortex" beam, generated by means of a physical phase plate, or an SLM. Then the imaging procedure for an STED image is exactly the same as for a CLSM, the sample is scanned point-by-point by means of motorized mirrors. STED microscopy can also be implemented in all 3 dimensions by generating more complex depletion beams. In [122], a regular vortex beam, responsible for the lateral improvement, is combined incoherently with a "top-hat" beam (radial 0-$\pi$ phase mask), confining the detected fluorescence emission into a volume of $\sim$30x30x30nm.

The main problem of STED microscopy is that, using the stimulated emission principle for depletion is a very inefficient process. In practice, to achieve proper depletion, and thereby remarkable resolution improvement, an enormous laser power is needed. Commonly of the order of $10^9 W/cm^2$. Apart from being quite harmful for the specimen (since all the light is concentrated into one single, and high-power, spot), this implies the need for very powerful lasers, or short pulses to concentrate such huge number of photons. Additionally, such high demand of depletion photons makes the parallelization of STED, an impossible task. Forcing to follow a point-scanning approach, limiting the imaging speed. Although the generation of illumination patterns for the parallelization of STED is possible [123], the need of laser $\sim$ 100000-times

more powerful makes it impossible.

A solution to this problem, is found in a more generalized concept, under the name of RESOFLT microscopy (Reversible Saturable Optical Fluorescence Transitions) [124]. The basis behind the resolution improvement is exactly the same as in STED, a depletion laser is used to "swith-off" fluorophores at the undesired periphery. However, instead of switching off molecules using stimulated emission, RESOLFT microscopy uses a more efficient process by means of changing the photo-physical and chemical properties of the fluorescent molecules. RESOLFT uses specially modified fluorophores that can be photoswitched between two different stable electronic states: an "ON state" or fluorescent state, and an "OFF state" or non-fluorescent state (dark state), much long lived than the first. The transition between both involves a conformational change of the fluorescent protein, which is controlled with light of a particular wavelength. This way, by shaping the illumination pattern responsible for such transition, we can control whether molecules will emit or not. A fluorophore in the dark state simply does not absorb excitation light, it becomes completely transparent to excitation, hence not emitting afterwards. The saturation of the OFF-state allows the fluorescence readout of the remaining molecules at the ON-state.

The main benefit of using this kind of probes, is that the transition between theses two stable states needs much lower light doses, aroung $\sim 600W/cm^2$, compared to $10^9W/cm^2$) needed in regular STED. This allows much faster imaging, less photobleaching, longer imaging time and the possibility to parallelize the whole process. In RESOLFT microscopy, as in STED, the achieved resolution is a function of the depletion laser intensity, as follows:

$$d'_{xyz} \propto \frac{d_{xyz}}{\sqrt{1 + \frac{I}{I_S}}} \tag{7.1}$$

Where $d_{xyz}$ is the size of the diffraction-limited spot, $I$ the depletion laser's intensity and $I_S$ the saturation threshold, which depends on the fluorescent protein itself. In the laboratory, the achieved lateral resolution depends on the intensity value at the center of the depletion beam. Note that, if the center is not zero, molecules in that region will be also switched to the OFF-state, although to a lesser extent. Then, the resolution will find an upper limit that cannot be improved, the resolution will no longer improve as depletion intensity increases.

For this reason is important to properly align the system and take care of polarization states, very important to achieve good vortex quality, especially for very high NA, where the Z-component of the electric field starts to play an important role. Any aberration results in "filling" the central region, limiting the maximum achievable lateral resolution.

The same kind of reversible fluorophores used for RESOLFT, can also be used in non-linear SIM to be able to effectively encode higher frequencies into the illumination patterns [125]. Another family of super-resolution techniques are englobed under the name of single-molecule localization microscopy, PALM (Photoactivated local-

ization microscopy) and STORM (STochastic Optical Reconstruction Microscopy) being the two most popular and most successful implementations [126, 127, 128]. This techniques rely on different algorithms to localize the emission centers of individual fluorophores. Although the emission spot size ($PSF_{em}$) of each molecule is limited by diffraction, producing a "big blob", its center can be localized with much higher precision than the Airy disk itself. The center localization precision of a single isolated emitter depends on the SNR, affected by the camera noise and the fluorophore emission (i.e. number of collected photons $N$) as $d'_{xyz} = d_{xyz}/\sqrt{N}$. The problem in regular wide-field epifluorescence microscopy is that all molecules emit at the same time, so what we observe is the superposition of thousands, or even millions, of individual emissions.

Even though individual molecules can not be distinguished spatially, the use of switchable probes breaks the diffraction-limit barrier in the temporal domain. PALM/ STORM uses switchable probes that randomly transition from dark to bright states upon applying light of a very specific wavelength (different than the excitation one). This way, the acquisition of thousands of frames in a simple wide-field or TIRF setup, allows parallel localization of individual emitter coordinates. Such coordinates are then mapped into a final digital image whose resolution improves with the number of processed frames.

This simple method of time-splitting the emission of individual molecules within the diffraction spot, allows the observation of biological structures up to $\sim 10 - 20nm$. Mention that the achievable resolution depends on the sample density. Single fluorophores are easier to localize in sparse samples than in dense aggregates. Regarding reconstruction speed, live cell imaging is almost impossible due to the need of thousands of frames for a single high-resolution reconstruction. Using high-speed cameras and high-performance computing (for localization), PALM/STORM has demonstrated 30-60 seconds per image at most. Typical reconstruction times are in the order of tens of minutes. Although being extremely slow, PALM/STORM has become very popular due to it can be implemented on any wide-field setup.

Finally, it is worth mentioning the recent appearance of several super resolution techniques based on the same PALM/STORM localization principle, but without the need of complex switchable probes. New complex algorithms are able to localize and extract super-resolution information from multiple frames, without the need of complex optical assemblies (STED/RESOLFT) or specially designed probes (STED, RESOLFT, PALM, STORM). Two examples are SRRF [129] and SOFI microscopy [130]. Here, the spontaneous intensity fluctuations are used to identify different emitters. The basis of this principle is to analyze the spatio-temporal correlation between neighboring pixels and consecutive frames, to discriminate whether the collected photons have been emitted by the same molecule, or if instead photons have been generated from different sites. Taking a look at the emission of a single emitter, it can be observed that all pixel values within the diffraction-limited spot fluctuate in synchrony, following the same temporal evolution. Whereas if more than one fluorophore is emitting, such fluctuation become uncorrelated.

Such new super-resolution computational methods, benefit from being extremely easy

to implement, especially in terms of optical setup and sample preparation (staining protocol). The main drawback is that these spontaneous fluctuations in fluorescence are of extremely low amplitude, as opposed to a switchable protein that offers infinite contrast between the OFF and ON states. Resulting in the need for higher number of frames in order to achieve comparable resolution. Another complication emerges from the camera noise, since sometimes this fluctuations are of the same order, reason why noise models have to be implemented in order to discriminate both contributions.

To solve that, to increase the amplitude of fluctuations or reducing the acquisition time in SRRF or SOFI, it is possible to actively modulate the excitation light in a random manner. This way, time-varying speckle patterns can increase the fluctuation amplitude, and thereby the performance of such algorithms [131].

Similar to this, fluorescence fluctuations can be also introduced by moving the sample with sub-nanometer resolution, which is the case of Translational Microscopy (TRAM) [132]. Here, a full-frame image (either using a CLSM or wide-field setup) is acquired for many coordinates of a piezoelectric stage. In such a way that, after the complete stage scan, the sample fluorescence has been tested and sampled at a much finer level, similar to over-sampling it. After the scan, an image stack is obtained, which can be understood as multiple views of the same specimen. Then, the stack is passed through an iterative optimization process (similar to a multi-input deconvolution) able to extract super-resolution information from the stack of images. This latter TRAM concept, has been the inspiration for the development of a new super-resolution technique with our SCREAM unit. That uses the extreme positioning accuracy, and random access nature, of AODs, to extract super-resolution information from a very fine scanning of the sample.

## 7.2 Parallelization of RESOLFT microscopy with AODs

This section summarizes the work done during a four months stay at the Testalab in Stockholm. The aim of the stay was to contribute to the parallelization of the RESOLFT concept [1]. And test the modulation capabilities of the SCREAM unit, for the generation of exotic illumination patterns needed for depletion. For this reason, the AOSLM part of the SCREAM unit was incorporated into one of the excitation branches of a MoNaLISA (Molecular Nanoscale Live Imaging with Sectioning Ability) optical setup [133, 134].

In figure 7.1 we show pictures of the incorporation of the AOSLM into a MoNaLISA optical setup. For the illumination arm, the setup is exactly the same as the original SCREAM unit. In principle, thanks to the flexibility and extreme modulation speed of AODs, the AOSLM has the potential to project all three illumination patterns needed

[1] I greatly thank Professor Ilaria Testa and all the members of the TestaLab group for their great reception. For introducing me to the field of super resolution and letting me adapt one of their MoNaLISA systems

for the parallelization of RESOLFT microscopy. Either the excitation or ON-switch, the OFF-switch (depletion) and the final fluorescence readout. Moreover, although not implemented yet, it allows the implementation of a laser scanning approach, instead of the stage-driving sample scanning used until the moment. Finally, as can be seen in figure 7.1, the incorporation of a programmable element (as is the AOSLM) allows miniaturization of the optical setup. All fixed optical components from figure 7.1 are replaced by the highlighted AOSLM.

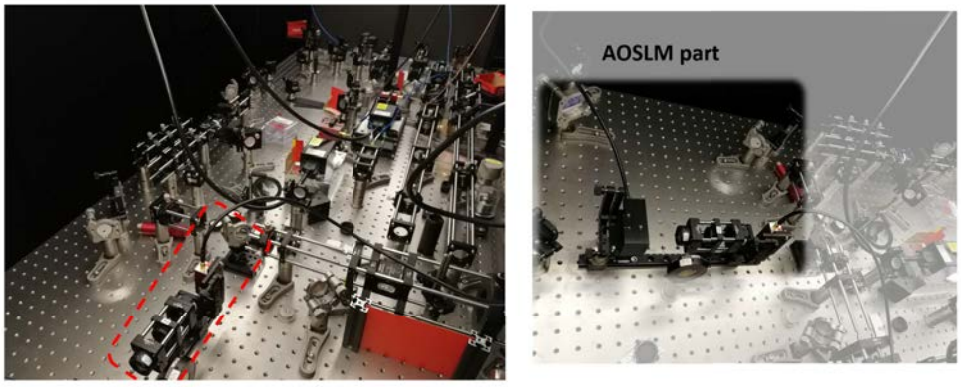


**Figure 7.1:** Picture of the AOSLM unit incorporated into one of the multiple branches of the MoNaLISA setup. The idea is that the AOSLM aims to replace all the optical components visible in the image. Demonstrating how, the programmability of the AOSLM, can reduce the complexity of an equivalent setup based on fixed optical components.

In order to parallelize RESOLFT, MoNaLISA uses three different patterns, each one responsible for one specific electronic transition: the ON-switch, the OFF-switch, responsible for the lateral resolution improvement, and finally the fluorescence readout. This three illumination patterns are displayed sequentially, one after the other in the following sequence: first the ON-pattern is switching all the molecules to the ON-state, and thereby they become fluorescent. Note that now, all molecules shined with the ON-switch light can emit upon excitation. After this, the OFF-pattern is displayed at a much higher power than the rest, to saturate the OFF-state and bring molecules at very specific regions to the non-radiative state again. Finally, the remaining "ON" molecules are excited by means of the readout pattern and the corresponding emission (at a longer wavelength) is captured by a high-sensitivity camera (Hamamatsu ORCA Flash 4.0 v2, 100fps, 2048x2048 pixels and QE=82%).

Regarding the wavelength selection, it depends on the photo-switchable protein of choice. For the case studied in this thesis we use the rsEGFP2 photo-switchable green fluorescent protein. Where the transition from OFF to ON state finds its absorption maximum at 408nm and from ON to OFF at 503nm respectively. Once on the ON state, rsEGFP2 behaves as a regular fluorophore with an excitation band at 478nm and the corresponding emission peaking at 510nm. In the laboratory all three steps

are performed using two different diode lasers, a 405nm for the ON-switch (Cobolt 06-MLD 405nm), and two 488nm (Cobolt 06-MLD 488nm) for both the OFF-switch and fluorescence readout.

Figure 7.2 explains how each of this patterns are generated. In principle, the most important illumination pattern is the OFF-pattern, since is the one taking care of saturating the OFF (or dark/non-fluorescent state) state, and therefore confining the emission into a much smaller area. The quality of the zero in the OFF pattern determines the achievable lateral resolution. In a regular point-scanning RESOLFT setup the OFF pattern is a single doughnut beam.

In order to parellelize the process, MonaLISA uses the incoherent superposition of two orthogonal sinusoidal patterns, similar to the ones used in SIM. Each sinusoidal pattern is generated by focusing two symmetric spots at the periphery of the microscope objective back aperture. Both spots are the $+1$ and $-1$ diffraction orders of a phase grating, custom modified to enhance the diffraction efficiency for $\pm 1$ orders. This way, each focused spot at the BFP corresponds to a plane wave travelling at a very steep angle (TIRF angle) at the sample plane. Since both spots are generated with the same laser, an $\propto sin^2$ interference pattern appears in the region where both waves overlap.

One interference pattern confines the molecules in only one dimension, so for an isotropic depletion the same procedure is repeated in the perpendicular direction. It is very important that the two orthogonal interference patterns are added incoherently, as shown in figure 7.2. This means that each pattern needs to be generated with either an additional laser, or as in this case, dividing the laser in two and working with perpendicular polarization states. With all this, the resulting pattern is a modulated sinusoidal grid with infinite contrast, since the minimum of intensity corresponds to a complete destructive interference. Regarding the destructive interference, it is very important for the polarization to be tangential to the back aperture border, as indicated in figure 7.2. The reason to that is because with such high-NA objective lenses (Zeiss Plan Apo 100x NA 1.45 Oil), the axial component of the electric field $E_z$ starts to play an important role, it can not be neglected, as in the scalar approximation. It is easy to see that only when polarization is tangential, $E_z$ is zero by symmetry. Whereas if polarization is parallel to the radius, a strong z-component appears, resulting in a loss of contrast of the interference fringes, hence affecting lateral resolution.

For the ON and readout steps, this can be done using a collimated light, i.e. a constant illumination (as in any wide-field epifluorescence setup). Technically, the resolution improvement only depends on the "zero" quality of the OFF-pattern. However, in MoNaLISA both the ON and readout patterns corresponds to arrays of multiple foci arranged in a square grid with constant periodicity. Both patterns are generated by means of two physical microlens-arrays. Regarding the foci periodicity, this one is chosen and changed manually by changing the magnification of a 4f relay system.

The use of multi-foci patterns for the ON-switch and readout provides better optical sectioning than wide-field RESOLFT. Even though the OFF-pattern does not confine

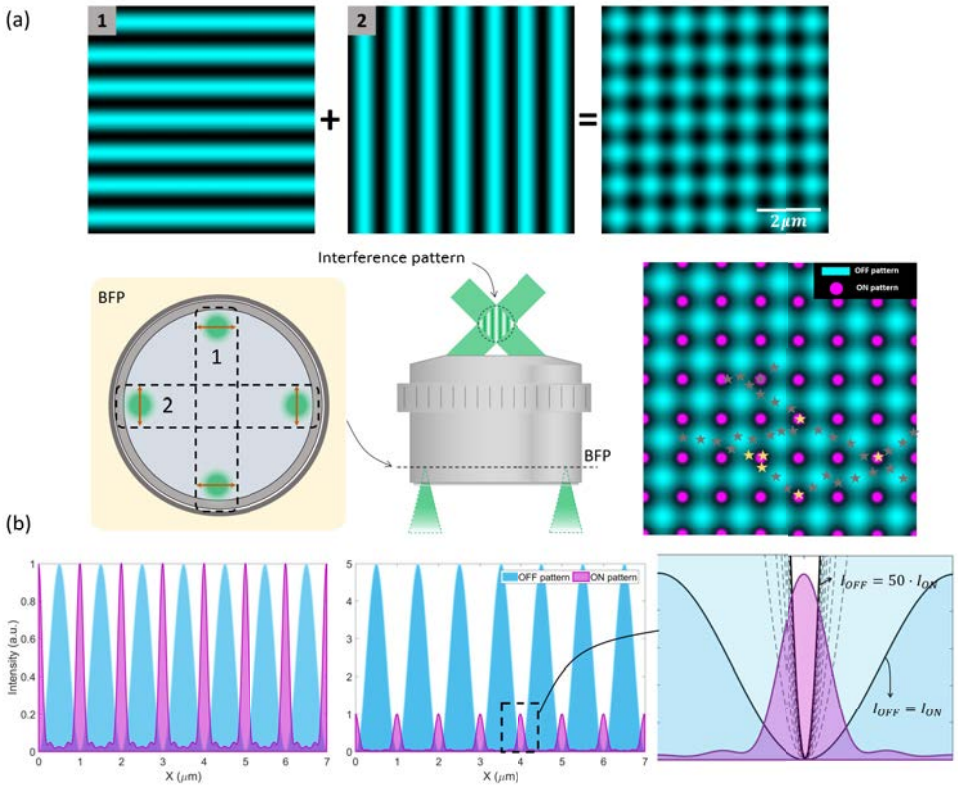


**Figure 7.2:** Description of the illumination patterns used in the MoNaLISA optical setup. The OFF pattern is the result of an interference between two plane waves. In order to achieve a complete destructive interference in the minima, it is very important for the polarization to be tangential to the back aperture. This way the interference contrast is always $\infty$. If instead we use the orthogonal polarization state (radially polarized), a strong z-component appears drastically reducing interference contrast. On the bottom we show how by increasing the OFF-pattern intensity, the overlapping area increases, and with it the depletion efficiency and final lateral resolution.

the emission in the z-axis at all, the use of focused spots to control the density of ON molecules, and the same for controlling the population of emitters, results in a confined axial region. Providing MoNaLISA with better resolution than a regular confocal microscope, similar to two-photon microscopy, improving both the lateral and axial resolution by a factor of $\sqrt{2}$. If the OFF-pattern is not used, the obtained image already provides sub-diffraction information. This image is referred as "enhanced confocal".

The alignment of a MoNaLISA setup is something laborious and due to thermal and mechanical drifts, is has to be repeated almost routinely. Note that all three patterns,

ON, OFF and readout, are generated with 3 different lasers (or 4, depending on how the OFF-pattern is generated). The alignment process consists on first, matching the periodicity and then center the focus of both ON and readout patterns, with the intensity minimum of the OFF-pattern. Regarding the periodicity values, as explained in section 5.3.1 (figure 5.19), the appearance of replicas along the z-axis establishes the minimum useful periodicity to be 600nm. For smaller values, replicas are so close that optical sectioning is lost.

The use of fixed optical components for the generation of these patterns, also makes it very difficult the implementation of a laser scanning approach. In MoNaLISA, the illumination patterns remain static and the sample is moved using a piezoelectric stage. For each position of the stage, the fluorescence readout signal is captured with a camera, ending up with a similar image stack as in the SCREAM unit. Note that, due to the stage scanning procedure, the emission focus are always at the same position. So, before composing all frames into a final super-resolution reconstruction, each frame has to be shifted the corresponding amount. In terms of acquisition speed, the MoNaLISA setup is mainly limited by the piezoelectric stage rise time, as well as the periodicity used. As in the SCREAM setup, a solution to increase speed is to decrease periodicity, however this is not possible due to replicas in z.

Here we propose the use of the AOSLM developed through this thesis, for the implementation of all three illumination patterns. The incorporation of a fully programmable single element, responsible for the generation of all patterns, supposes (according to us) several advantages over the MoNaLISA setup based on fixed optics. First, instead of 4 different lasers, here we only need 2, since both the OFF and readout patterns (488nm both) can be generated by simply changing the modulating acousto-optic hologram. Secondly, by implementing the scanning procedures described in section 5.4 (see figure 5.22), it allows the future transition from stage driving to a laser driving approach, with all the benefits that it entails, in terms of increased acquisition speed and positioning accuracy.

And third, since all patterns are generated using the same programmable element, the alignment protocol becomes a totally digital process, being able to even implement automatic routines. Moreover, the flexibility of the setup allows the user to change the pattern periodicity in a continuous and digital manner. Being all three patterns intrinsically aligned, no matter the periodicity value. This ability to change the periodicity would allow MoNaLISA to: reduce acquisition time by bringing excitation points closer, or in contrary, image deeper into thick samples by increasing periodicity, hence reducing point-to-point crosstalk.

Regarding the intrinsic "self-alignment" capabilities, figure 7.3 shows all three (ON, OFF and readout) patterns we designed for the implementation of MoNaLISA with AODs, demonstrating perfect alignment between them. As can be seen, the ON and readout patterns correspond to the same multi-point patterns deeply described and explained in previous chapters. For the OFF pattern, in this particular example, we use an XY separable approximation to an ideal Laguerre-Gauss vortex beam. In the optical setup, both 405nm and 488nm were aligned collinear before entering the AOD window. As explained in section 5.2.2 (figure 5.5), the custom pair of AODs were

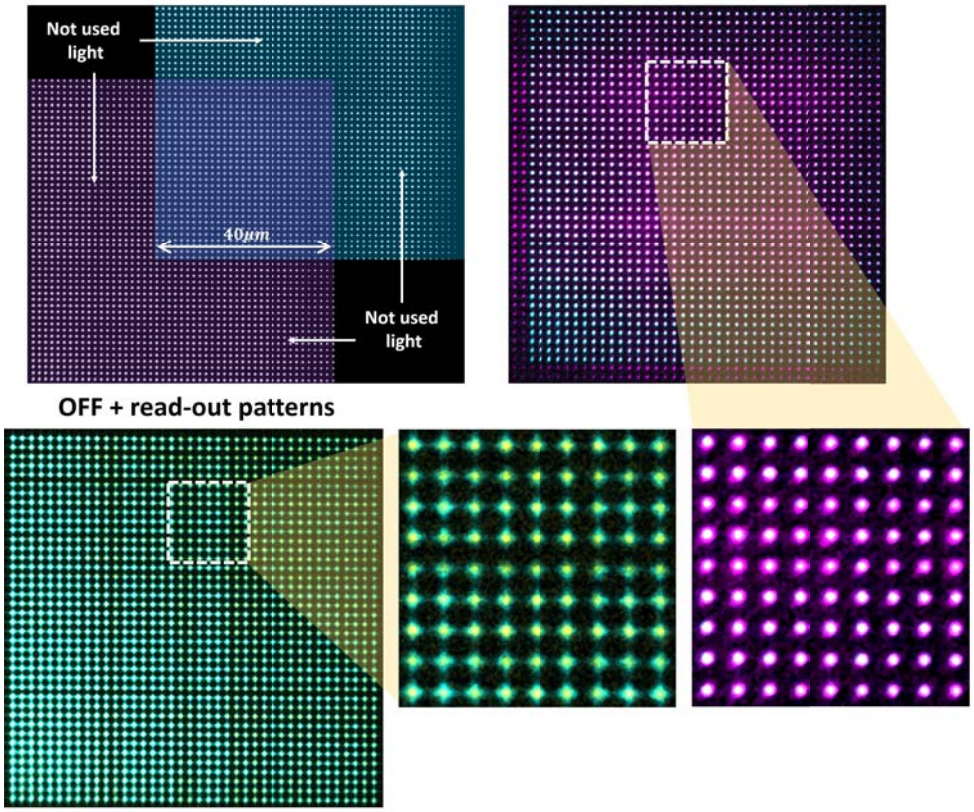


**Figure 7.3:** Experimental images of all the intensity patterns generated with the AOSLM to parallelize RESOLFT microscopy. Even though the custom AODs are designed for 488 and 561nm, modulation with the 405nm laser was also possible. This figure also demonstrates how the continous periodicity change (demonstrated in figure 5.16), allows us to compensate for the different $\lambda_0 \cdot f_{obj}$ scaling factor for both wavelengths.

designed to diffract efficiently 488nm and 561nm wavelengths. Resulting in a non-ideal performance for the 405nm laser, responsible for the ON-switch. The characterization of our custom AOD set at 405nm showed a diffraction efficiency of $< 8\%$ and a maximum deflection angle of 39mrad, compared to $> 60\%$ and 43/41mrad for the 473 and 488nm. Moreover, the area overlapping between 405 and 488 reconstructions is less than 40%.

To increase the overall FOV, we used a driving frequency $f_d$ different than the central frequency $f_c$ for each wavelength. Such that, as seen in figure 7.3 the 488nm pattern is shifted to the lower left part of the FOV, and the 405 to the upper right, increasing the overlapping area. Mention that working under this conditions is not ideal. For

the 405nm reconstruction, the central frequency used was 105MHz, falling outside of the Bragg window, resulting in a non-flat intensity distribution, something that was not corrected.

The low diffraction efficiency at 405nm was compensated by concentrating all the laser energy just at the common area between both wavelengths. As can be seen in figure 7.3, due to this AODs are not designed for 405nm, the FOV is reduced to 38x38$\mu m$, but AODs are able to diffract up to $\sim 70\mu m$. By just generating the spots that fall inside the common FOV, the energy density increases, allowing a more efficient process. Otherwise more than 70% of diffracted light will go outside of the imaging region.

For the alignment process, mention that since the OFF and readout patterns are generated by modulating the same 488nm laser, they are intrinsically aligned as long as the driving frequency for both acousto-optic holograms is the same. The most difficult part is to align the ON pattern with either the OFF or readout, that share the same center of coordinates. In order to match the ON and OFF patterns, the acousto-optic hologram has to compensate for the wavelength-dependent $\lambda_0 \cdot f_{obj}$ scaling factor of the OFT. This is done by slightly changing the hologram size $D_h$ for one of the two lasers, as explained in section 5.3 (figure 5.16), which offers continuous control over the pattern periodicity. In other words, assuming the same hologram, the fact that we are using two different lasers result in two identical reconstructions but with different periodicities. The periodicity for the 405nm is $\frac{405}{488}$-times smaller than the 488 reconstruction. It is worth mentioning that such difference can not be compensated with an SLM, since it only allows to change periodicity in discrete steps. With an SLM, the only possible way is to use a periodicity value corresponding to the least common multiple between $\frac{\lambda_1 f}{L}$ and $\frac{\lambda_2 f}{L}$.

### 7.2.1 Custom illumination patterns for depletion

The ON and readout illumination patterns are generated exactly as the multi-point excitation patterns in our SCREAM unit (sections 5.3 and 5.3.1). This section presents different approaches we implemented for the OFF pattern, which is the responsible for the lateral resolution improvement.

When it comes to the OFF pattern, the ideal solution would be to generate an array of Laguerre-Gauss vortex beams, the same used in any STED or point-scanning RESOLFT setup, in such a way that the "zero" of each doughnut is aligned with each excitation and ON-switch focus. In terms of image quality, a vortex beam offers the same resolution improvement in all directions, all molecules at a given radius $r$ are switched OFF equally. Whereas with the interference pattern used in MoNaLISA, the effective depleted area is an square rather than a symmetrical circle.

However, due to the mathematical constrain that holography with AODs offers (XY separability), a Laguerre-Gauss vortex beam is impossible to generate just with the AOSLM. In general, a doughnut beam is the result of a plane wave diffracted by a phase-only diffractive optical element (DOE) of the form:

$$\phi_{vortex}(x,y) = e^{iL\theta} = e^{iL\cdot\arctan\left(\frac{x}{y}\right)} \tag{7.2}$$

As can be seen in the equation, $\phi_{vortex}$ corresponds to a radially increasing phase, where $\theta$ is the angular coordinate, and $L$ the vortex's topological charge, responsible for the radius of the doughnut. The higher the topological charge, the wider will be the doughnut, and thereby the less efficient depletion. From equation 7.2 one can deduce that $\phi_{vortex}(x,y)$ can not be expressed as the product of two functions such that $\phi_{vortex}(x,y) = \phi_x(x) \cdot \phi_y(y)$. The $\arctan(x/y)$ function is not XY separable.

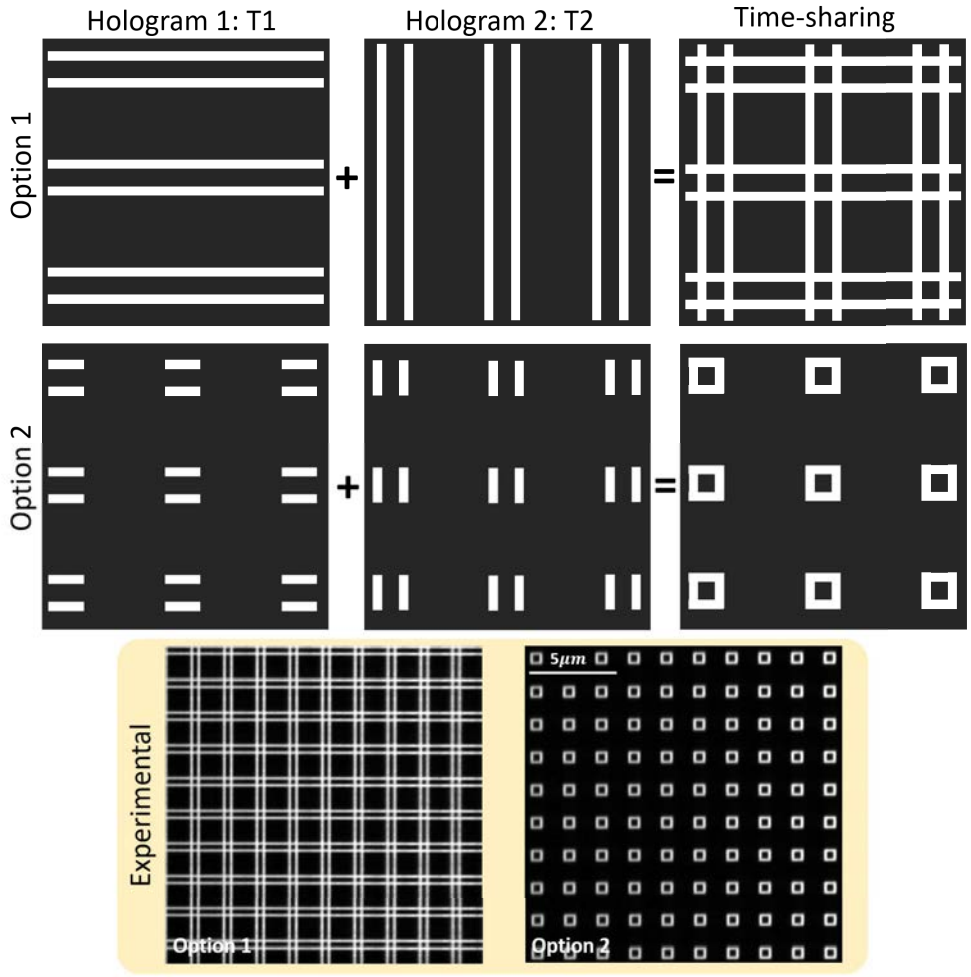


**Figure 7.4:** Scheme of the generation of two proposals for OFF-patterns with AODs. Presenting two options: a grid of double lines and a small square array. Being the array of squares a more efficient solution, since light is distributed over less positions. An experimental image for each option is also shown.

It is worth mentioning that if this phase distribution could be displayed by the AOSLM, the parallelization of this array of doughnuts would be straight forward. The corresponding vortex phase $\phi_{vortex}$ would be directly added to the previously calculated multi-point hologram $H(x,y) = A(x,y) \cdot e^{i\phi(x,y)}$, such that $H'(x,y) = H(x,y) \cdot e^{i\phi_{vortex}(x,y)} = A(x,y) \cdot exp(i(\phi(x,y) + \phi_{vortex}(x,y)))$. This way the multiplication of both contributions at the AOD plane, the multi-point hologram and the vortex's phase, will result on the convolution between a 2D Dirac's delta array and a doughnut beam at the sample plane.

In this section two different approximations to the ideal vortex array pattern are described. In both cases the pattern is divided in two XY separable terms that are displayed at kilohertz rates. In such a way that, on average, the effect is very similar to an array of doughnuts.

The first option is based on projecting an intensity pattern with a very similar geometry to a doughnut, but separable in XY. Instead of a circle we came up with the idea of an array of small squares. Figure 7.4 shows an scheme of the two terms needed to generate such array of squares. They can be generated by intersecting double-lines, or using short segments. In both cases, the final pattern is the non-coherent superposition (sum of intensities) of two intensity distributions, that are encoded in two separable holograms, H1 and H2 respectively. Each of them is taking care, in principle, to the resolution improvement in one direction. Even though the first option based on double lines is inspired on the MoNaLISA OFF pattern, for a given periodicity, the second option is much better in terms of light efficiency. Since all diffracted photons are used for depletion, light is distributed over less positions.

In figure 7.5 we show experimental images of such array of squares. Which, as demonstrated in the figure, the programmabilitiy of the AOSLM allows us to change the square size. Note that, using this approach, the transition from the OFF pattern to the readout pattern is done by changing the hologram. Figure 7.5 shows the superposition of both the OFF square pattern and the corresponding readout pattern, displayed just afterwards in 1 hologram transition ($1t_h$). Demonstrating how both patterns are intrinsically aligned.

Regarding the intensity value at the center (quality of the zero), due to diffraction through the objective lens, we find it of low quality and not suitable for improving lateral resolution. As shown in the intensity plot of figure 7.4, for small square sizes, the PSFs of both sides add up in intensity, contributing to a higher the value at the center. That increases as both sides approach. Even when the edges of the square are far apart, the same effect happens with the tails of both PSFs, they overlap, resulting in a shallow contrast compared to the interference pattern used in MoNaLISA.

The main problem in the generation of these squares is that both sides of the square contribute constructively, adding the intensities of both sides. Under this approach, the only case in which the central intensity is strictly zero, occurs when the minima of both PSFs coincide in the center. However, when this happens, both PSFs are more than 1 Airy unit apart. The effect of the OFF pattern will be minimal, forcing the use of very high laser powers to achieve a detectable increase in resolution.

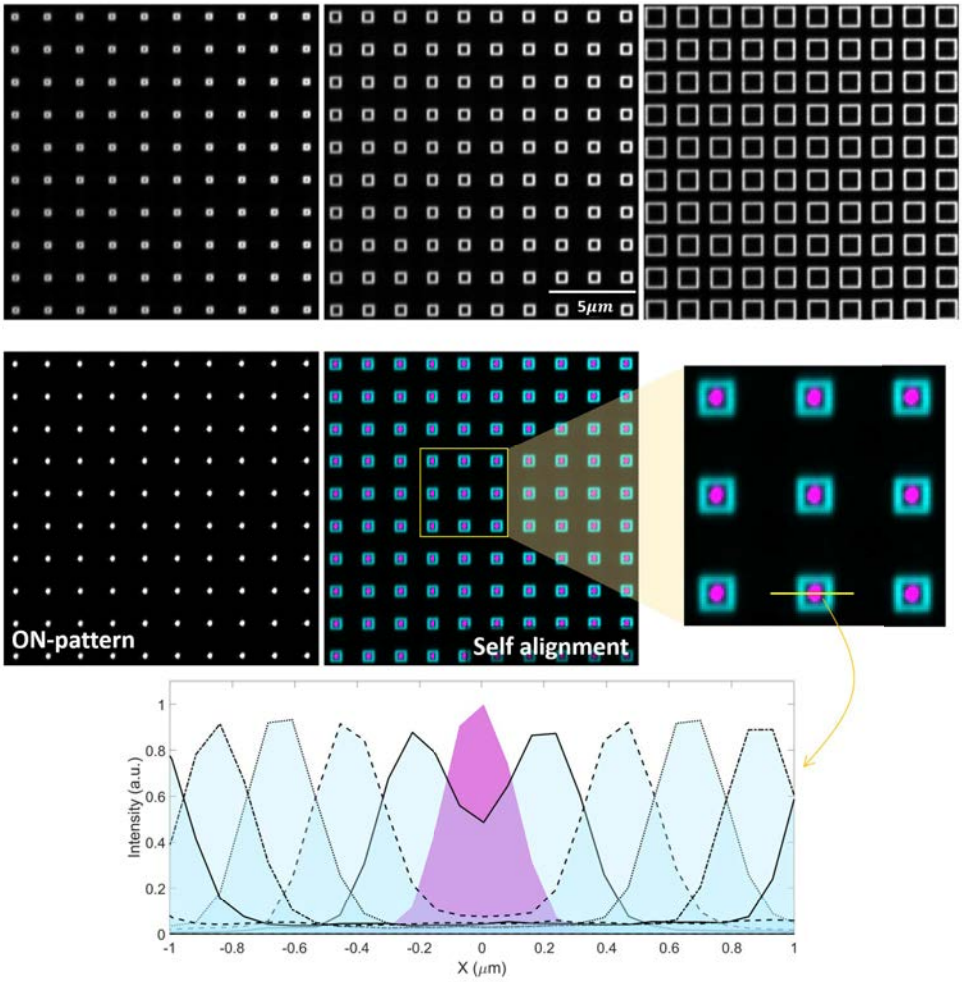


**Figure 7.5:** Experimental images for the array of squares, demonstrating the programmability of the AOSLM by changing the square size. The corresponding ON/readout pattern is also shown. The fact that all patterns are generated using the exact same device, makes all patterns inherently aligned and perfectly centered.

The main reason to such low contrast is because any pattern generated by means of the AOH algorithm (described in chapter 4) is also diffraction limited. With this method of superposing multiple spots, is not possible to introduce sub-diffraction-limit features in the illumination pattern. No diffraction-limited intensity distribution is able to enhance lateral resolution efficiently.

In STED or MoNaLISA, such small features are generated by means of a destructive interference at the center of the pattern. Analyzing carefully $\phi_{vortex}(x, y)$ expression, we note that the destructive interference at the center is the result of a mathematical

singularity in $\phi_{vortex}(x, y)$. At the center of such phase-only distribution, the light wavefront phase is not well defined, resulting in the appearance of a shallow zero at the center.

Diffraction theory and Fourier optics say that the intensity distribution at the center of the reconstruction will be an strict zero, as long as the sum of all complex values in the hologram $H(x, y) = A(x, y)e^{i\phi(,xy)}$ is also zero. Analyzing the STED vortex beam case, we see that such condition is only achieved when the intensity distribution inciding the phase-only plate is symmetric and centered with the DOE. This way, after the phase plate, any electric field value $E(x, y)$ will find its corresponding complex conjugate at a diametrically opposite position $E(-x, -y) = E(x, y)*$. When focusing the laser, all this values merge into the same spot, canceling out the intensity at the center of the PSF.

Even though $\phi_{vortex}(x, y)$ can not be displayed by the AODs, figure 7.6 shows an scheme of the second solution proposed for the OFF pattern. Instead of decomposing the intensity distribution of the doughnut in two different intensity terms, we propose the decomposition of its phase distribution. Analyzing the vortex's phase distribution we see that, in any diameter line, the phase remains constant $\phi 1$ for the first half and then changes to $\phi 1 + \pi$. There is an abrupt phase jump from 0 to $\pi$, located at the center of the laser. This way, instead of a vortex phase plate, we generate a "half-moon" phase distribution, which basically consists on codifying a $\pi$ phase jump at the center of the AOD aperture. Half of the wavefront will take $e^{i0}$ and the other half $e^{i\pi}$.

As can be seen in figure 7.6, the result of such phase distribution is a totally destructive interference in one dimension, whereas in the orthogonal view the pattern is not affected. Applying this $0 - \pi$ phase distribution in only AODx, will result on a resolution enhancement just in the X direction. To solve that, one possible option is to apply the same $0 - \pi$ phase jump in both AODx and AODy. However, due to the telescope T1, responsible for the optical product between both holograms ($Hx(x)$ and $Hy(y)$), both phase distributions will add, resulting in a cross-like destructive interference.

The implementation we propose in this thesis is to time-share both $0 - \pi$ phase distributions. At first, the $0 - \pi$ is applied only at AODx and not at the AODy, resulting in two intensity lobes with an strict destructive interference at the center, a zero-line in the Y direction. Then, the $0 - \pi$ phase jump is switched from AODx to AODy, generating the same reconstruction but in the orthogonal direction. After repeating this procedure at kilohertz rates, the average effect is an intensity distribution almost identical to the one generated by a real vortex phase plate, given by equation 7.2.

Obviously, such $0 - \pi$ phase jump $\phi_{0-\pi}(x, y)$ can be codified on top of any previously calculated hologram $H(x, y)$, either a multi-point os multi-line hologram $H(x, y) \cdot e^{i\phi_{0-\pi}(x,y)}$. Automatically, this "pseudo-doughnut" is replicated around each foci, as shown in figure 7.6. By re-calculating $H(x, y)$ the periodicity can be changed to adapt to new experiment needs. Moreover, the whole pattern distribution can be shifted with sub-nanometer precision by changing the hologram driving frequency $f_d$

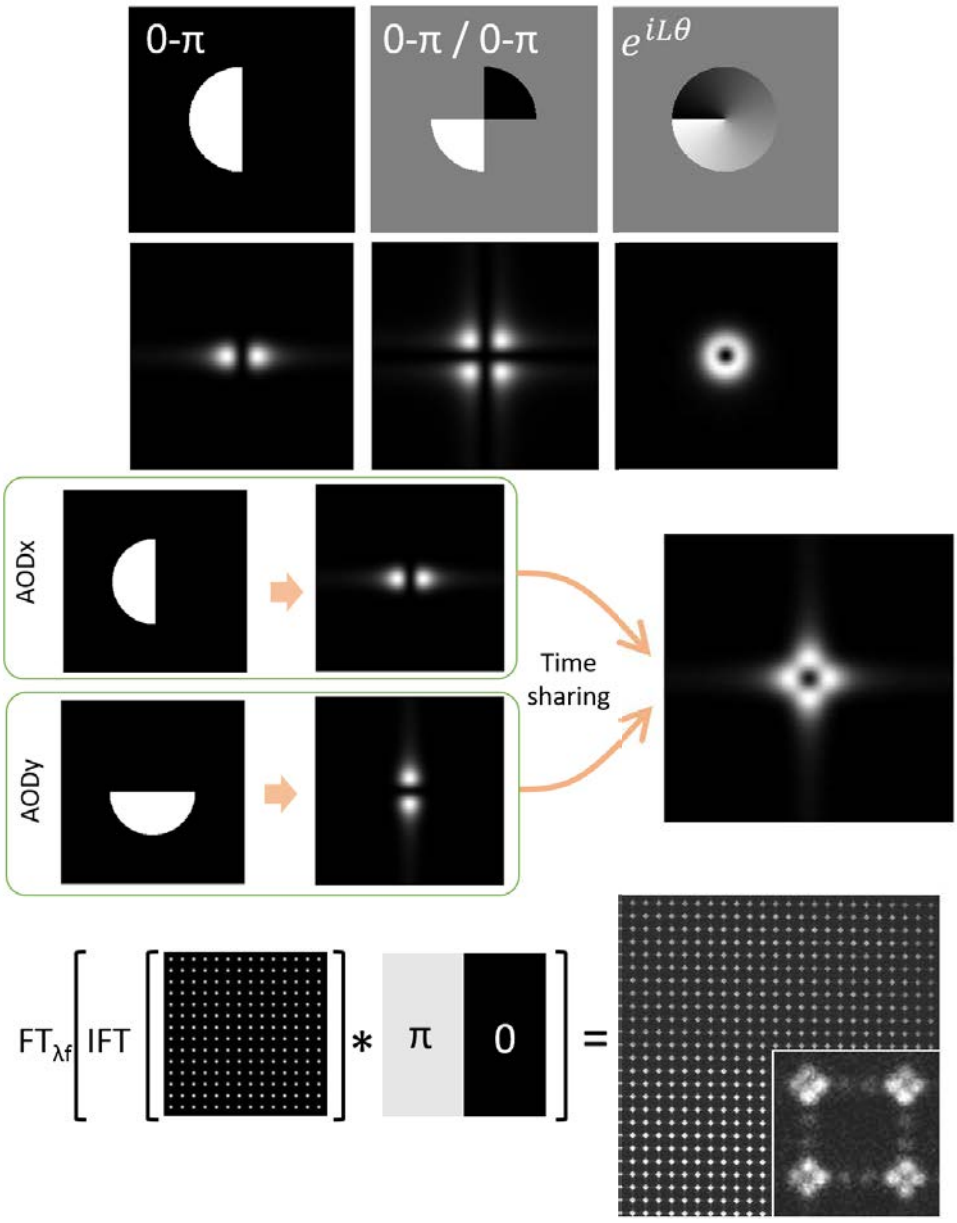


**Figure 7.6:** Description of different strategies to achieve destructive interference in the center. The corresponding phase distributions are added to the respective acousto-optic hologram, in such a way that the patterns are automatically replicated. The separability constrain introduced by the two AODs, forces us to approximate the ideal Laguerre-Gauss beam in two one-dimensional terms.

or introducing an extra linear phase term (as seen in section 5.4).

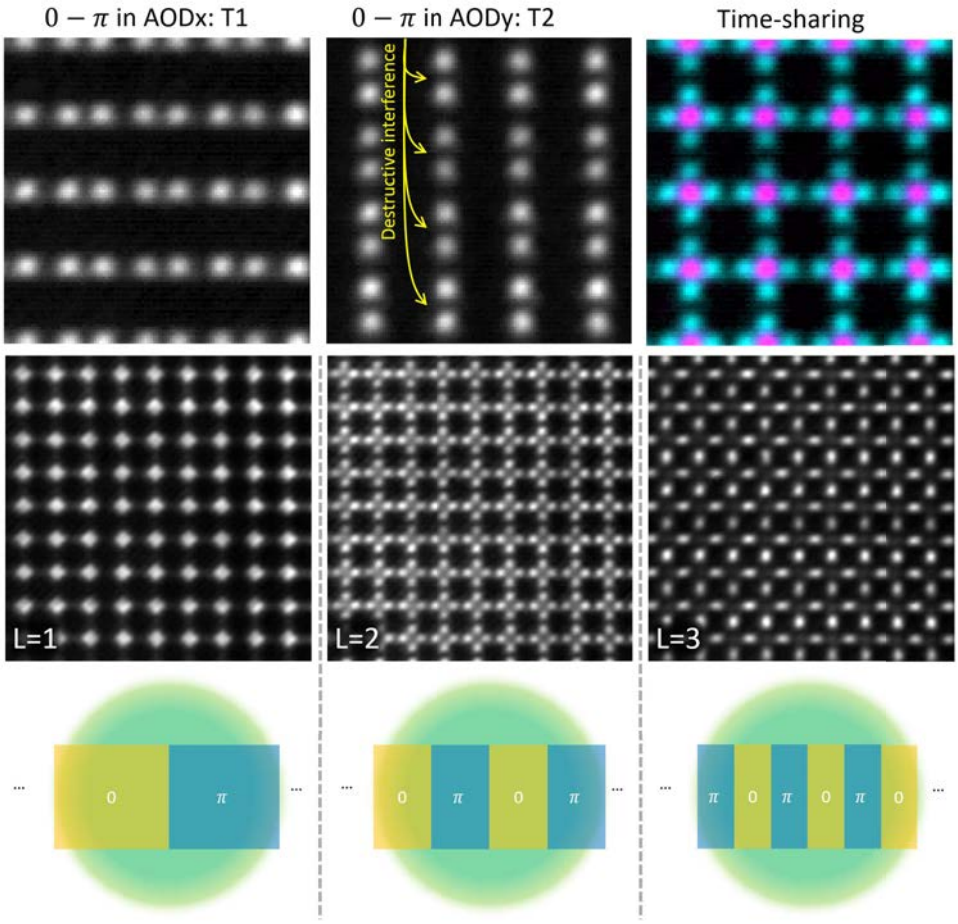


**Figure 7.7:** Experimental images of the $0-\pi$ OFF-pattern. Since all three illumination patterns are generated with the same AOSLM, the OFF-pattern and the multi-point readout pattern are intrinsically aligned. By changing the topological charge $L$ of the phase distribution the separation between lobes increase.

The experimental implementation of this solution is shown in figure 7.7. Where we present present each individual $0-\pi$ reconstructions in X and Y, and the superposition of both by means of a time-sharing scheme. The ON multi-point pattern is also presented in purple to demonstrate perfect intrinsic alignment between all patterns. Another interesting aspect is that, in the same way as in a real doughnut beam, the size of this pseudo-doughnut can also be changed with the corresponding topological charge $L$. In this particular case, the topological charge indicates the number of $0-\pi$ phase jumps codified within the AOD window. For L=1, each half of the beam is taking 0 and $\pi$ phase. Whereas for $L > 1$, the AOD window is divided in two different 1D masks that are interleaved. Note that in all cases the sum of phases is

zero, fulfilling the condition for a destructive interference at the center. The intensity value at the center will be zero as long as L is an integer, otherwise the part of the beam taking $e^{i0}$ phase will be different than the same taking $e^{i\pi}$, resulting in a $\neq 0$ center value.

### 7.2.2 Experimental results of the SCREAM unit for RESOLFT microscopy

In this section we show different experimental images taken with the custom $0-\pi$ OFF-pattern, and the corresponding multi-point arrays for the ON-switch and fluorescence readout. All images correspond to the vimentin intermediate filament network of U2OS cells endogenously expressing the rsEGFP2 photoswitchable green fluorescent protein.

Regarding the imaging procedure, the holograms for the three patterns ($H_{ON}(x,y)$, $H_{OFF}(x,y)$ and $H_{RD}(x,y)$ respectively) were calculated and stored into the AWG internal memory for later display. The AWG was configured such that the two output RF signals (one for each channel) are triggered with the same TTL controlling both 405 and 488nm lasers. Due to limitations in the AWG used in this case (RIGOL DG5102) the whole sequence of holograms was concatenated into one long acoustic signal. The time-duration for the ON, OFF and readout steps was controlled by repeating each hologram the appropriate number of times. Every time the piezoeletric stage changes to a new scanning position, the same TTL signal controlling the 405nm shutter (ON-switch) initiates the display of the whole time sequence. Due to limitations on the 405nm diffraction efficiency, and limited RF power of the AWG, the ON, OFF and readout display times were 0.5, 1.5 and 0.5 miliseconds respectively. The camera shutter was opened during the last 0.5 miliseconds, coinciding with the corresponding fluorescence emission readout.

Finally, for the wide-field images shown for comparison, this ones were taken by modulating two constant intensity squares, one for the ON-switch and the other responsible for the fluorescence readout. Comment that this wide-field mode becomes very useful for a quick and first inspection of the sample. It allowed us to visualize and choose the best looking cell before switching to "super-resolution mode".

As can be seen in figures 7.8 and 7.9, the use of such reversible fluorophores enhances the image quality and lateral resolution. Remember that in all these cases all the patterns are generated by means of the same programmable AOSLM. The AODs here, are responsible for either the pattern creation, the pattern switch, and also the laser power. Both lasers were set at the maximum output power and the ON/OFF/RD power was controlled by the amplitude of the complex RF signal.

By looking at the obtained RESOLFT images we can clearly observe filaments impossible to see on the wide-field case. In all these images, the most noticeable characteristic is the huge improvement in optical sectioning. Due to the use of focused spots for both the ON-switch and readout, the emitting volume is confined axially a factor of $\sqrt{2}$. There is no need for a virtual pinhole process.

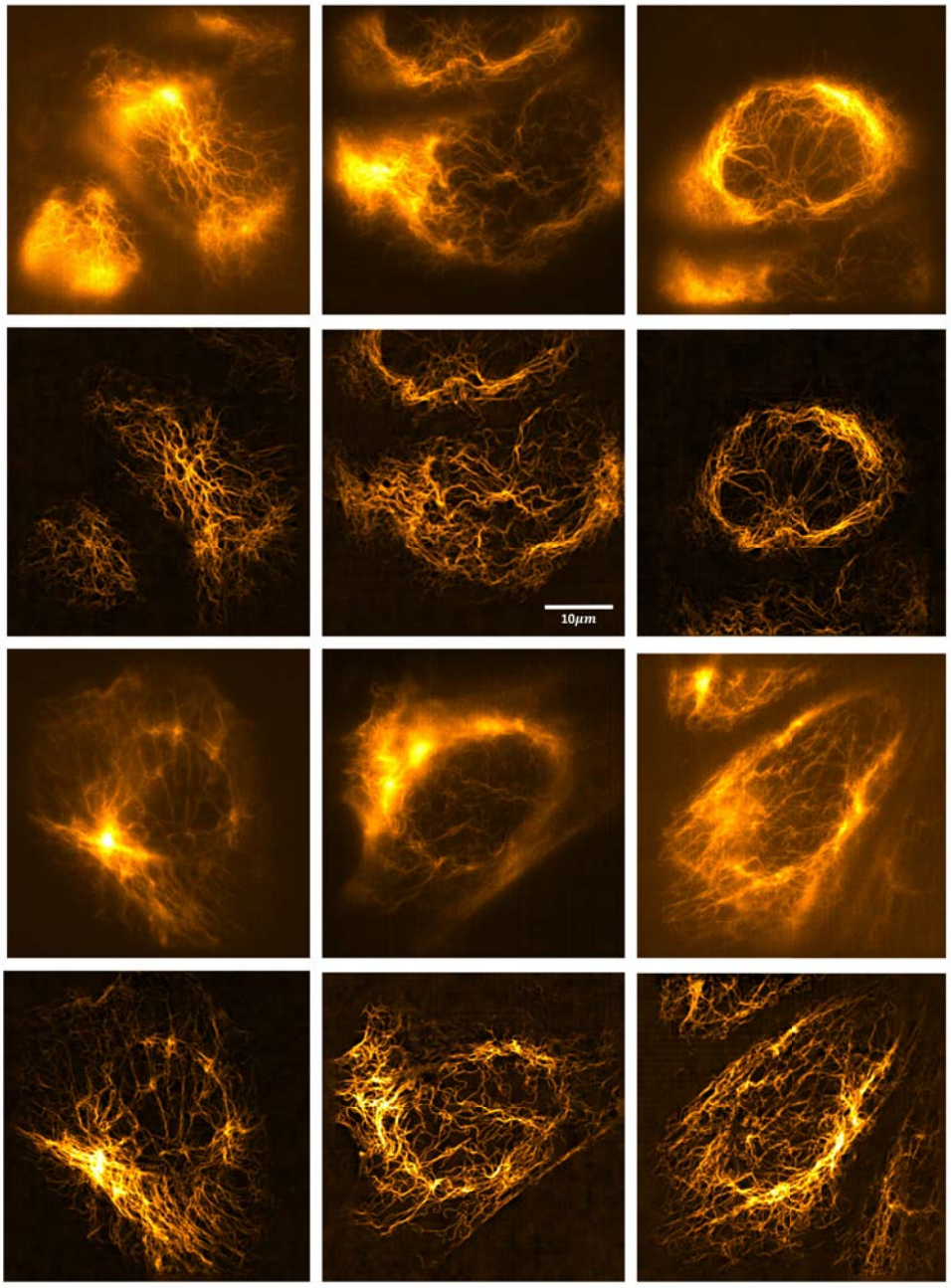


**Figure 7.8:** Set of experimental images using the $0-\pi$ OFF pattern. The wide-field epifluorescence image is shown for comparison.

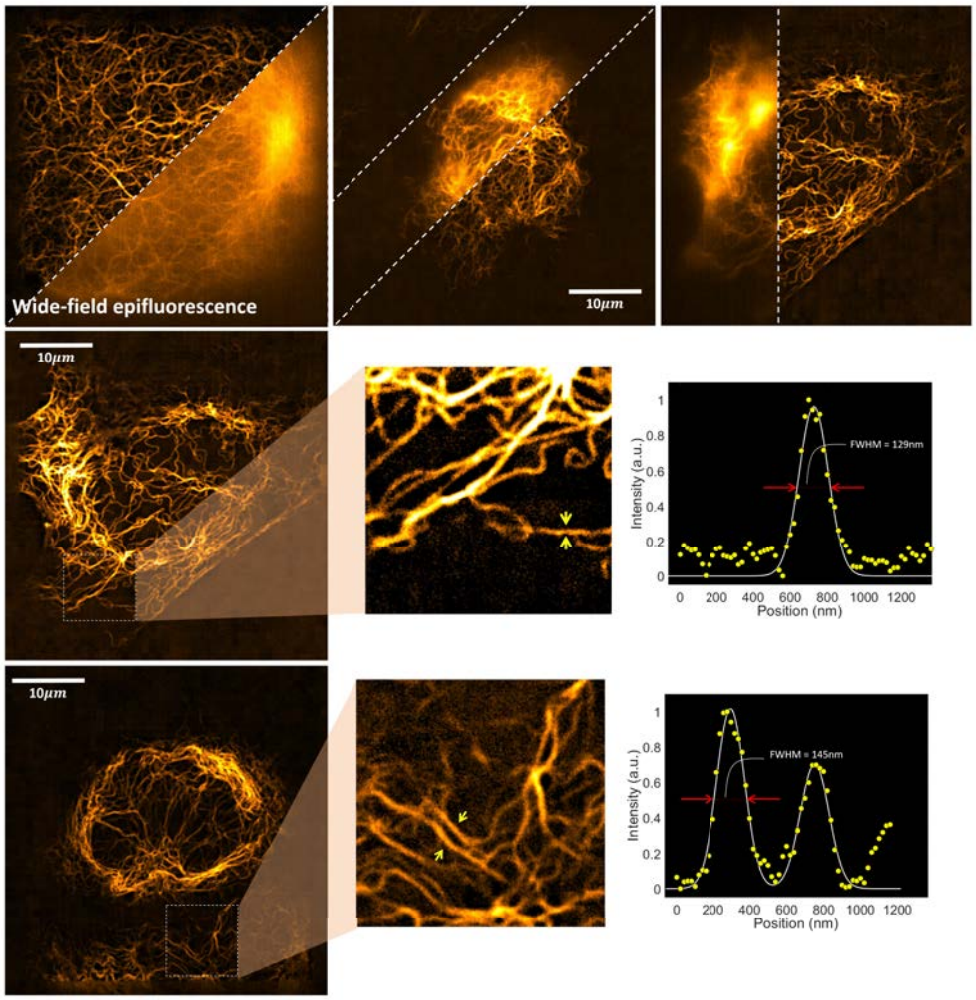


**Figure 7.9:** Experimental images using the AOSLM unit to project all three ON, OFF and readout patterns. The resolution improvement is around $\sqrt{2}$ over the diffraction limit, indicating that the $0 - \pi$ OFF pattern was not efficient enough. However, due to the use of two multi-foci patterns for both the ON-switch and fluorescence readout, the images offer an astonishing optical sectioning, showing a drastic improve over the wide-field case.

One of the main problems regarding the lateral resolution is that, due to we are using special fluorophores, is very difficult to give an exact value of the lateral FWHM. There are no resolution tests for such fluorophores. In practice, lateral resolution is measured by thoroughly analyzing a huge number of vimentin filaments where a line plot, and a further Gaussian fit, can be done. The resolution value then is the minimum fitted FWHM. However, this FWHM value depends on either the effective PSF and also the filament thickness itself. For this reason, it is very important to measure isolated filaments, close to the coverslip-cell interface, where all vimentin filaments are spread out and the probability of finding single filaments is higher.

Two examples of the achieved resolution are shown in figure 7.9, where we measured filaments between 120 and 165nm. This resolution is far from the 50-60nm achieved by the MoNaLISA setup, but represents an improvement of $> \sqrt{2}$ factor over the wide-field case, and slightly better than the enhanced confocal case. If no OFF pattern is used for imaging, the two step process (ON and readout) already improves lateral resolution a factor $\sqrt{2}$. In the laboratory, we observe that switching on the OFF pattern reduces the amount of captured light, a good indicator that fluorophores are being depleted. However, it does not contribute to enhance the lateral resolution. This is attributed to a low zero quality of the $0 - \pi$ OFF pattern, that switches-OFF also molecules at the center of the pseudo-doughnut.

### 7.2.3 Future work and possible solutions

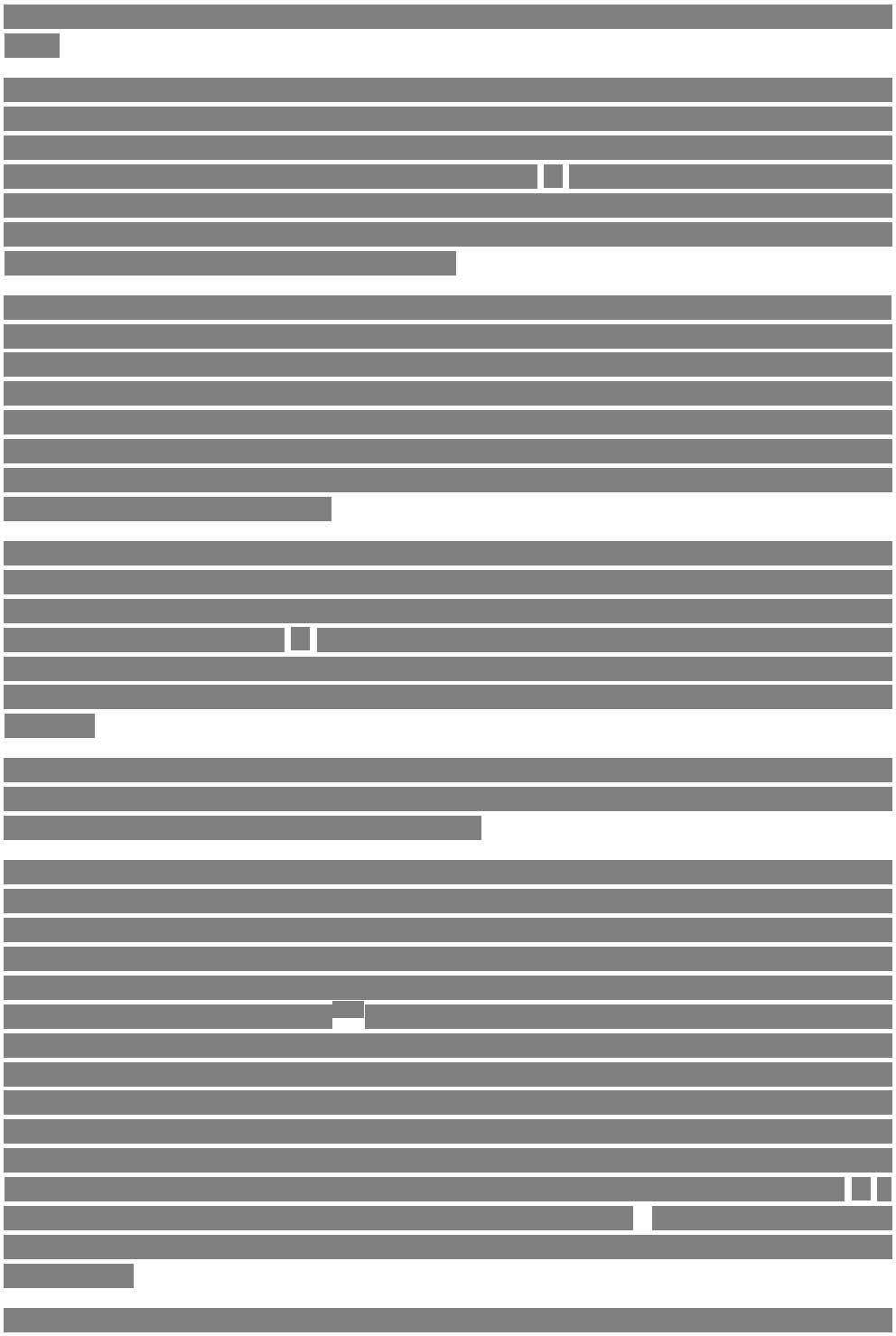

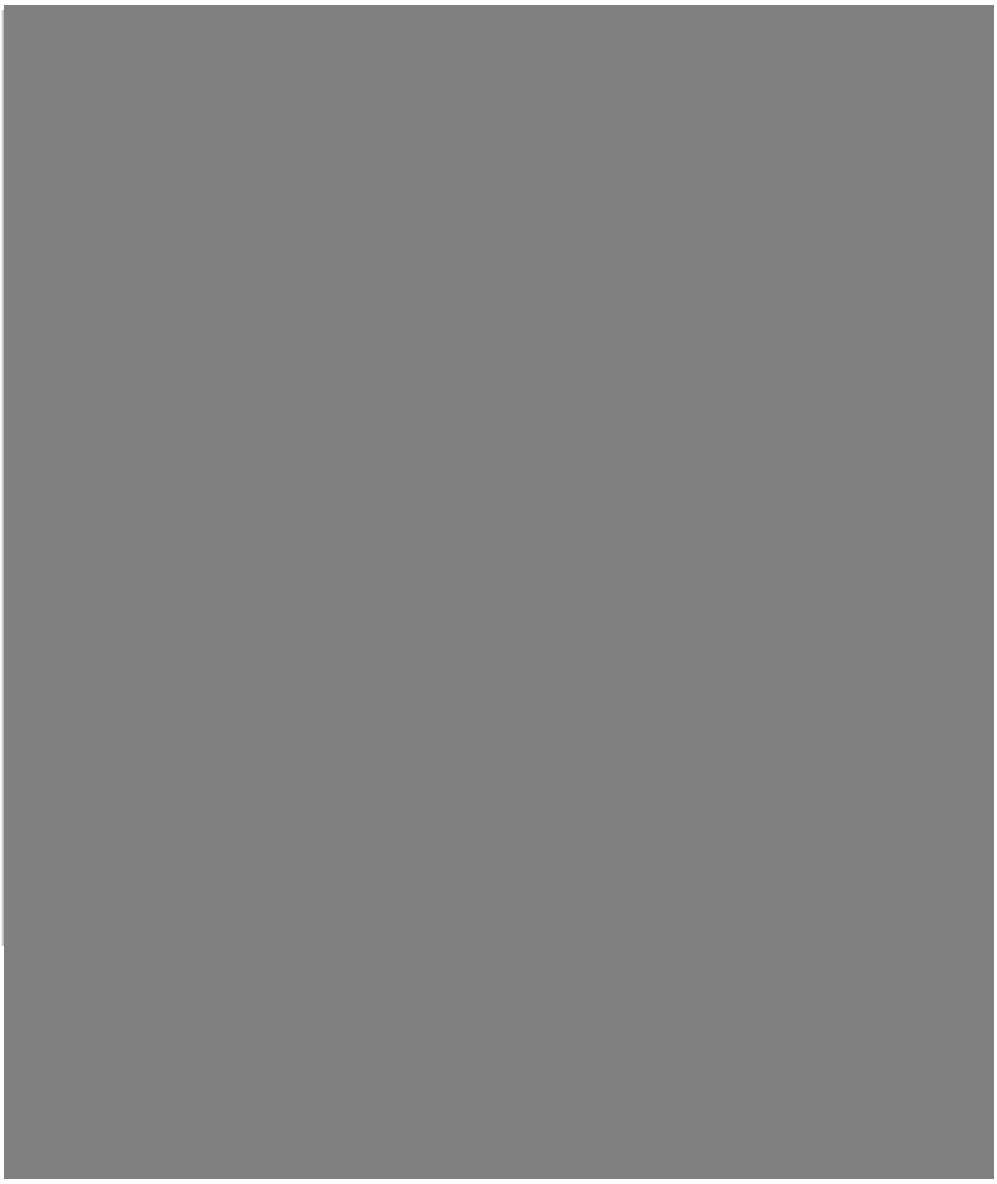

## 7.3 The SCREAM device for super-resolution microscopy: a deep learning approach

### 7.3.1 Extracting super-resolution information from a fine scan: algorithmic solution in simulations

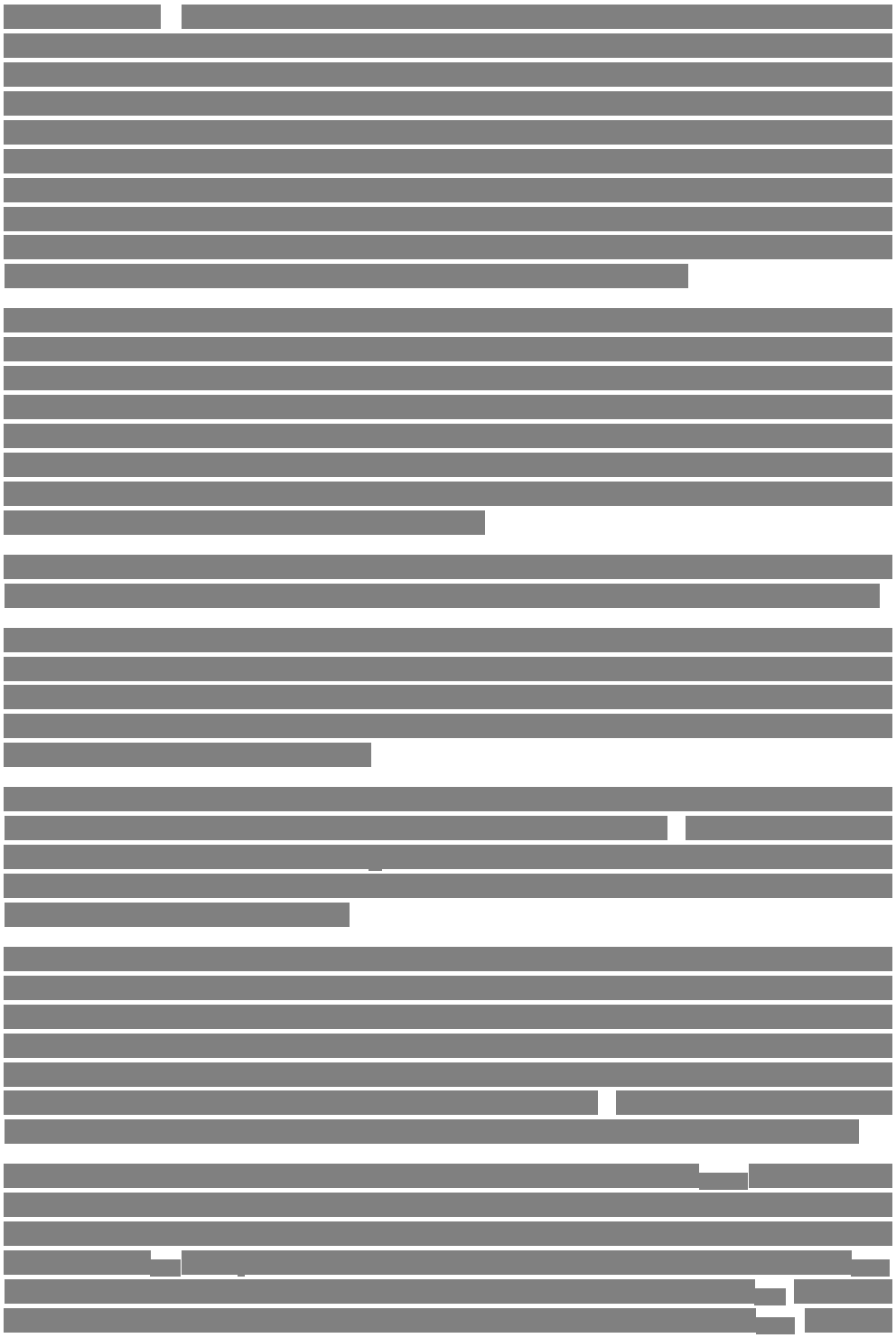

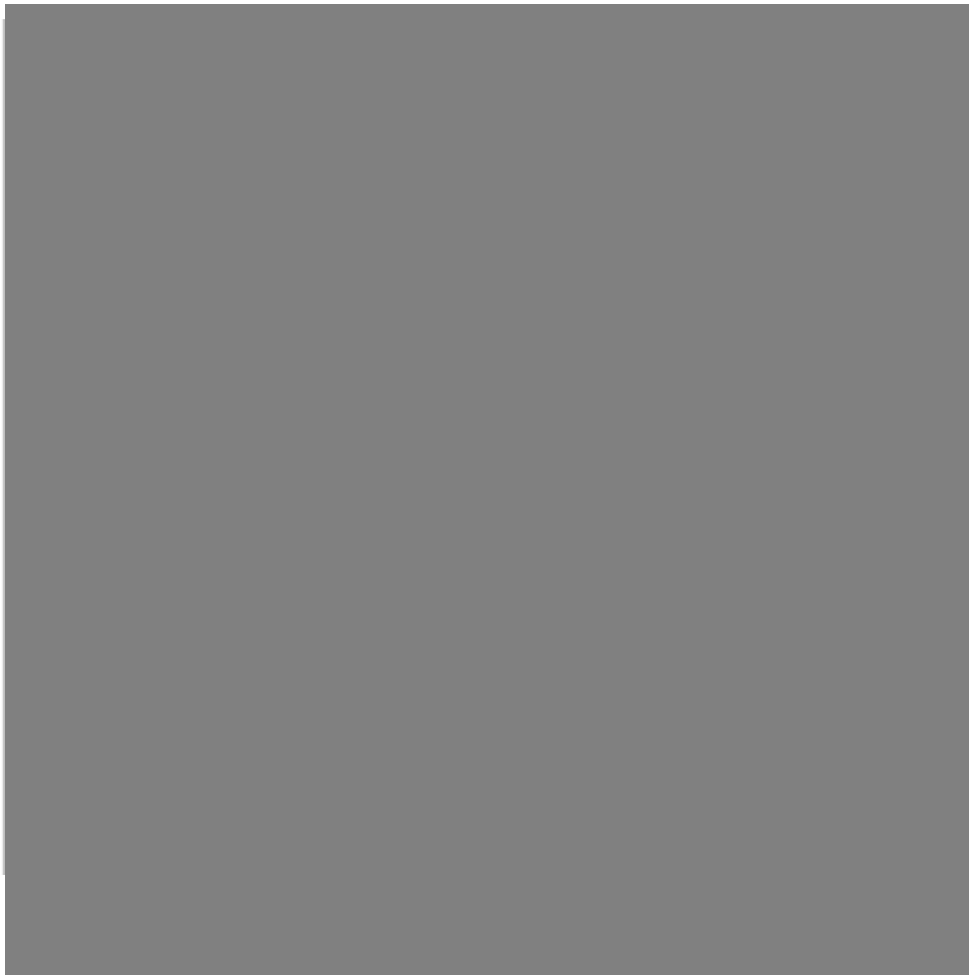

### 7.3.2 Processing the image stack by means of a convolutional neural network

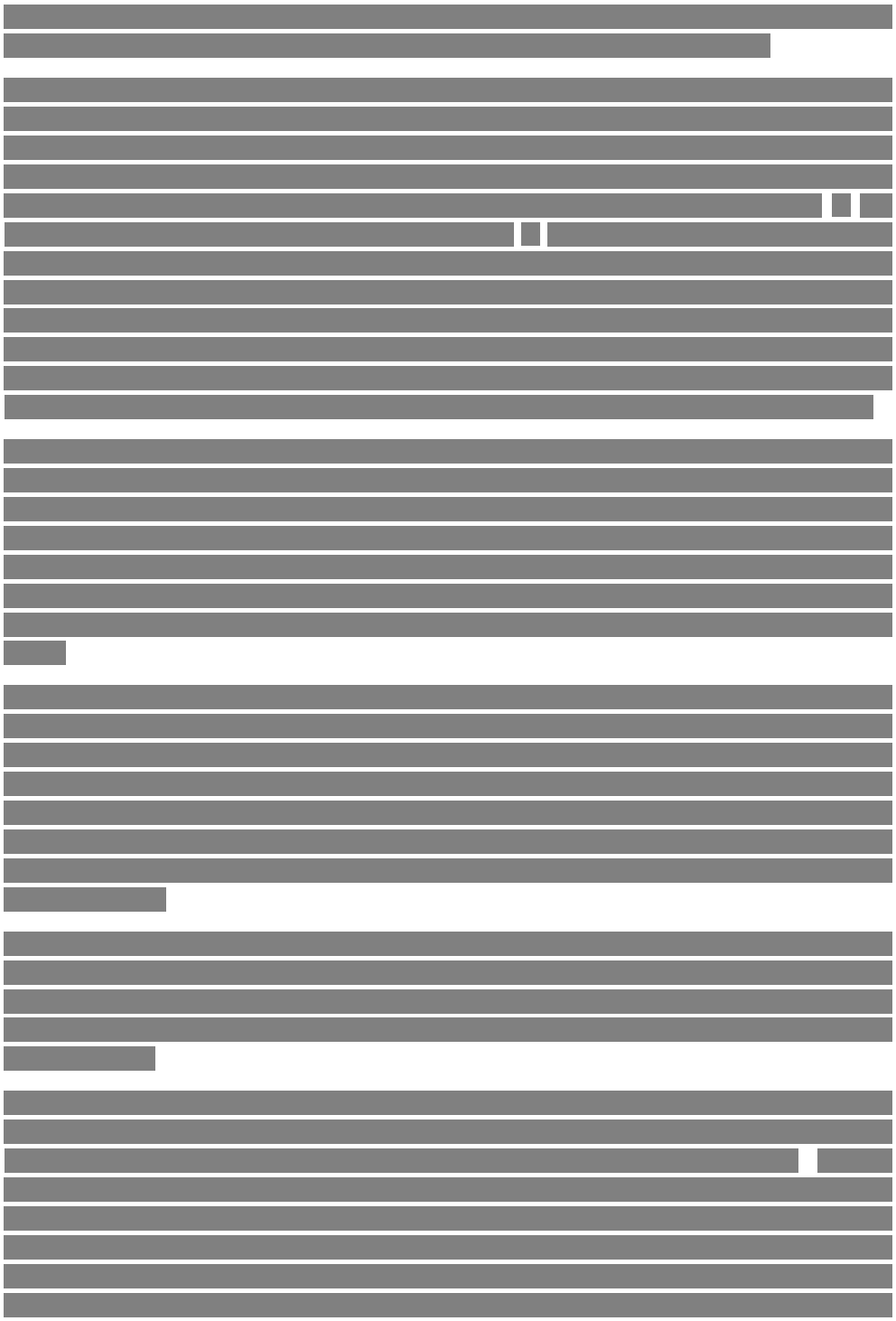

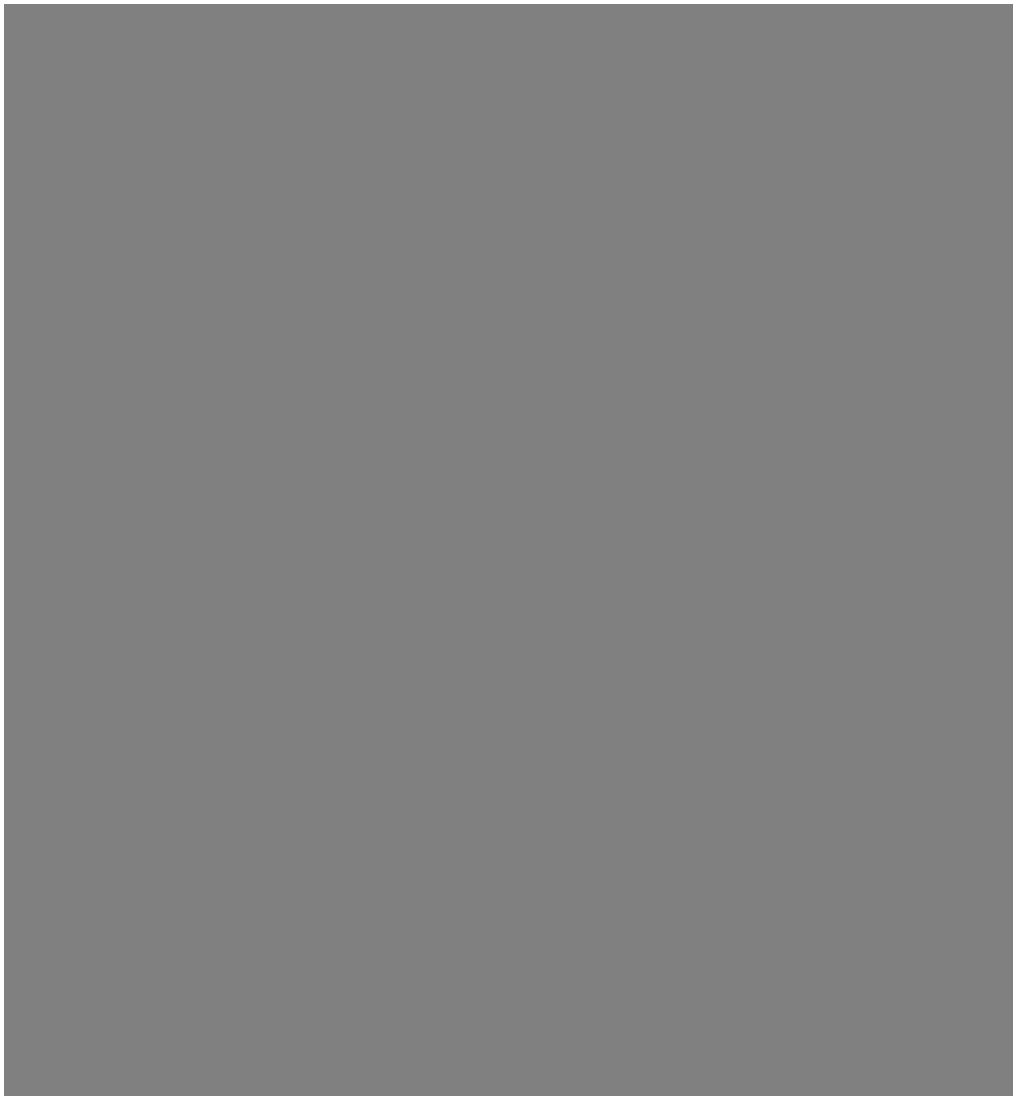

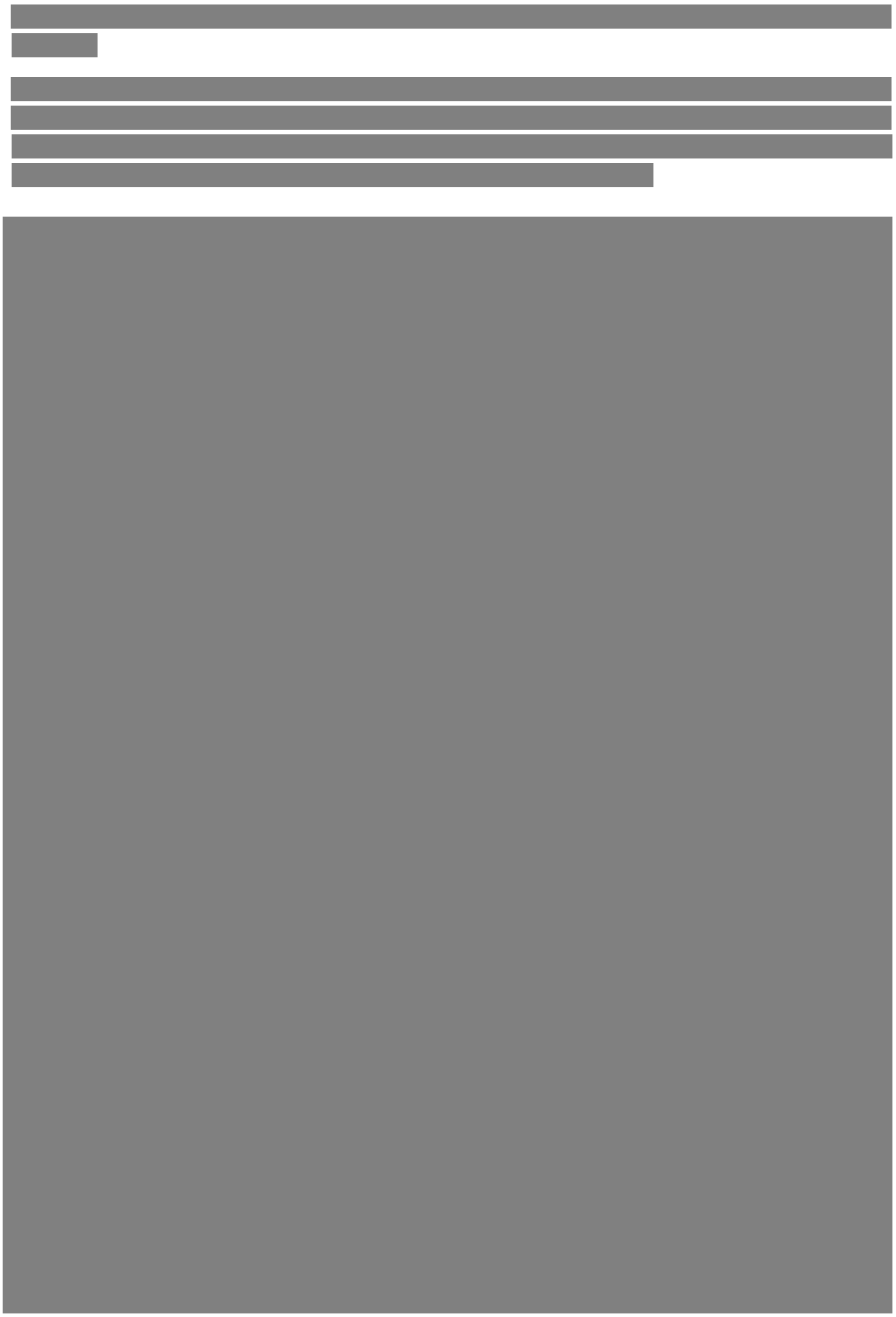

# Chapter 8

# Conclusions

The extensive work carried out during these five years has been reflected in the creation of two flexible optical systems with great applicability in cell biology. As a result of the whole development process, I hereby depict the main conclusions of this thesis, divided into the different topics:

Regarding the design of the AOD-based optical trapping setup:

- AODs have been thoroughly analyzed for the further incorporation into the optical tweezers design. The diffraction efficiency dependence on input polarization, angle of incidence, wavelength, RF power and other parameters has been characterized.

- A time-sharing approach has been implemented by fast switching the laser position, demonstrating both theoretically and experimentally that it is possible to stably trap and manipulate multiple objects at the same time.

- The acoustic-wave propagation inside the AOD crystal is responsible for the appearance of intensity artifacts, known as "ghost traps". Different solutions for its elimination are given, demonstrating their complete removal.

- A custom modification has been made to the direct force measurement system to make it compatible with a time-sharing approach. Allowing force measurements at multiple sites simultaneously. It is essential to take care of all the acustic-wave transitions, as well as PSD charge time, to ensure precise measurements.

- A new AOD-based optical trapping setup has been designed, built, aligned, characterized and tested its performance in many different situations. The process also involved developing the RF generation and control electronics and a final user interface, allowing real-time manipulation and force measurements in multiple objects the same time. A detailed alignment protocol is described.

- The presented optical system is fully compatible with force measurements based on light's momentum changes. We presented a back-aperture stationary beam-steering system that ensures a null and constant force offset over the whole field of view.

Regarding the experiments performed with the optical trapping setup:

- The implementation of a time-sharing scheme and its synchronization with the direct force measurement device, allows to measure forces in multiple sites at the same time. Single object position and force information can be measured without previous calibration of the trap stiffness.

- Apart from individual trap control, AODs offer the possibility of controlled oscillations. By moving the trap position instead of the piezoelectric stage, we benefit from more precise and individual control over the exerted forces.

- It is possible to trap organelles inside living cells and use them as probes to measure the viscoelastic properties of the cell cytoplasm. Thanks to the active-passive method, trap stiffness can be calibrated in such visco-elastic environments.

- Laser driving active-passive calibration has been implemented. The transition from stage-driven to laser-driven calibration allows us to extend rheological measurements over a wider frequency range, improving the stiffness accuracy, due to an improved $\beta$ ($\mu m/V$) factor, to precise oscillations and to the non-existing inertial term.

- The fluctuation-dissipation theorem breakdown affects the active-passive calibration, making impossible trap calibration inside living cells, where organelles are out-of-equilibrium, specifically affecting calibration at low frequencies

- The direct force momentum apparatus can be used to quantify the FDT breakdown or "how far from thermodynamic equilibrium the system is". We present a new methodology to measure rheological properties based on direct force measurements.

- A new method is presented for directly measuring the complete force profile, by means of two different time-shared optical traps. This method has proven to be more robust than simple scanning.

- This force profiling method has been used to analyze how back-scattered light affects force measurements. Force profiles have been measured in particles of different sizes, materials and under controlled aberrations, observing that for large particles and of high refractive index the committed error is higher. Regarding aberrations, we observe that only affect near the escape force, while stiffness remains constant.

- It is possible to manipulate and measure forces in tubulin bundles, without the need for additional beads for handling. Force measurements show a very low trapping efficiency that makes impossible to manipulate the bundles while being active. When consuming ATP, forces exerted by the collective motion of kinesins are orders of magnitude higher than optical forces.

- An original experiment is presented to measure the mechanical properties of tubulin bundles. Preliminar results of tubulin Young's modulus are reported for three different bundles, being consistent with measurements in single filaments.

Regarding enhanced acousto-optic modulation:

- A new way of understanding and treating the AODs is presented, the acousto-optic holography (AOH). It is possible to display a computer generated hologram with a pair of orthogonally arranged AODs.

- The variety of intensity reconstructions that can be displayed by an acousto-optic spatial light modulator (AOSLM) is limited. Patterns are restricted to be mathematically separable, due to the use of two 1D AODs.

- We have implemented an algorithm to encode any intensity distribution into a complex RF signal, demonstrating that the amplitude and phase modulation of any complex RF driving signal is directly translated into an identical modulation of the first diffracted order of the AODs.

- A deep study on the discretization effects and reconstruction efficiency has been carried out, providing solutions to optimize both the reconstruction efficiency and completely removing reconstruction artifacts.

- Compared to an SLM only capable of modulating phase, an AOSLM provides better reconstruction quality and positioning precision, and much faster response time. The developed AOSLM provides twice the modulation depth, full complex modulation and variable pixel size. We demonstrated that amplitude modulation is a must to produce perfect, artifact free, reconstructions.

- AOH has been experimentally demonstrated by generating multiple static and stable optical traps. It is possible to generate trap arrays and switch them at kilohertz (kHz) rates, allowing independent control of each trap group. We name the technique acousto holographic optical tweezers (AHOTs).

- We experimentally demonstrate the compatibility of AHOTs with direct force measurements. Thanks to a precise synchronization with the force sensing device, it is possible to measure the force acting over the whole set of traps. Instead of single object force, AHOTs provide the sum of components in the same group. We report precise force measurements for different trap groups.

Regarding the development of the fully programmable microscope:

- Using an AOSLM as key element, a new confocal microscopy unit has been designed, built, aligned, characterized and tested its performance. The unit combines the benefits of both single-point and multi-point scanners in a very simple and compact optical setup. The SCREAM unit has been designed as an accessory to any existing inverted microscope, demonstrating diffraction limited performance both on the excitation and detection arms.

- The two main limitations of AODs for microscopy applications are: the very small deflection angle and the limited working wavelengths.

- AODs only work efficiently for one particular wavelength. For the SCREAM device we presented a custom modified AOD pair especially designed for 488 and 561nm simultaneously, capable of diffracting both wavelengths in a common FOV. This allows miniturization of the optical setup.

- In order to increase the common FOV, we designed and implemented a dichroic mirror system which increases the that parameter by $\sim 25\%$ in dual channel images.

- For future expansion to 4 wavelengths, two solutions to the optical design have been presented, based on either an ideal single AOD pair, or a more conservative but more expensive solution based on two already existing AOD pairs.

- We presented different illumination patterns for sample excitation, composed of multiple points, multiple lines or a constant intensity illumination for quick sample inspection. The illumination patterns are of extremely high-quality.

- We have demonstrated that the analog nature of the AOSLM offers continuous control over the pattern periodicity, as well as pattern offset. Neither of these two parameters are limited by pixel discretization, offering enormous control to adapt for different sample thicknesses.

- The acoustic-wave propagation inside the AOD, and the hologram optimization algorithm, turned out to enhance the sectioning capabilities of the excitation pattern. Homogeneously distributing the energy in out-of-focus planes.

- Different smart scanning strategies have been presented, demonstrating also the flexibility of the SCREAM unit. We have introduced two new imaging modes: a random scanning based on multi-point illumination and a double-line scanning approach. Both reduce the acquisition time over regular raster scanning.

Regarding the confocal filtering solutions:

- We have implemented a virtual pinhole algorithm to track the excitation centers and filter the out-of-focus light. The algorithm offers full control over the pinhole size and thereby the sectioning capabilities. Optionally, an additional photon reassignment processing can increase lateral resolution a $\sqrt{2}$ factor.

- It is possible to filter the out-of-focus light more efficiently than simulating a pinhole. We presented a set of pixel-based calculations that offer better sectioning capabilities than virtual pinholing. The presented algorithms are based on very simple mathematical operations and they do not require previous knowledge of the laser position.

- A physical interpretation to each of the image processing algorithms has been provided. Their optical sectioning capabilities have been thoroughly studied and compared, both in simulation as well as in experimental images. The conclusion is that superconfocal processing and homodyne detection work extremely well filtering out background flare and removing camera noise.

- Apart from removing out-of-focus light, some pixel-based calculations offer high-resolution capabilities. Concretely, superconfocal processing is able to unveil sub-diffraction-limit features.

- The readout of individual pixels from the camera has the same effect as a physical pinhole. We experimentally demonstrate that the rolling shutter readout can be used to filter out-of-focus light. Precise synchronization between AODs and the camera is crucial to achieve good optical sectioning. However, light is only filtered in one direction.

- A new concept of "hybrid confocal" has been presented. In this hybrid mode, the out-of-focus light is physically filtered in the Y direction (by the rolling shutter itself) and in the X direction, the remaining background flare is removed by software.

- It is possible to design a camera module with arbitrary row reading. By means of an FPGA modification and a new firmware, we have implemented a custom readout mode. The sensor is read in the same way as the sample is scanned, adapting to different excitation patterns and scanning schemes. With this custom mode, the sensor already offers confocal images, without the need for a post-processing step.

And finally, regarding super-resolution:

- We demonstrated that it is possible to use AODs for the parallelization of RESOLFT microscopy. The flexibility offered by AOH allows the design of custom illumination patterns for the ON-switch, OFF-switch and fluorescence readout.

- The programmability of the AOSLM reduces the complexity of an equivalent setup based on fixed optical components. Moreover, it simplifies the time-consuming alignment task. Because of all illumination patterns are created with the same device, all patterns are intrinsically aligned.

- A multi-point illumination pattern has been used for switching ON the molecules, as well as for fluorescence readout. For the OFF pattern we have presented two

different approaches: creating an array of small squares and inducing a destructive interference by means of a $0 - \pi$ phase jump.

- RESOLFT experimental images in living cells have been obtained using the AOSLM for all three steps. The results show a modest resolution improvement higher than $\sqrt{2}$ over the diffraction limit, indicating that the OFF pattern is not working properly. However, due to the use of focused light (multi-foci patterns) for both the ON-switch and fluorescence readout, images offer astonishing optical sectioning.

- The fact that lateral resolution is well above the 60-70nm achieved by RESOLFT, is attributed to an incomplete destructive interference at the center of each focus, resulting in a shallow contrast. Two hypothesis regarding such low contrast are provided: the appearance of an axial component and the acoustic-wave propagation.

- We concluded that the AOSLM works extremely well for the generation of intensity patterns. However, the continuously moving wave makes them inappropriate as wavefront coders. For this reason, we have proposed a new scheme for RESOLFT microscopy by combining an AOSLM with a physical vortex plate. We propose the use of the same multi-doughnut pattern for all three ON, OFF and readout steps.

- The random access nature of the AOSLM allows a very fine scanning of the sample, which allows the extraction of super-resolution information. We implemented an optimization algorithm that extracts high-resolution information from the stack of images obtained after a fine scanning. The results on simulations show an improvement over photon reassignment, slightly better than $\sqrt{2}$ over wide-field.

- We have presented a CNN model able to extract high-frequency components from the image stack, training it exclusively with synthetic and simulated data. Apart from an improvement in lateral resolution, results in experimental samples show a complete noise removal, increasing the SNR. Regarding the achieved resolution, different synthetic resolution tests have been generated. Results demonstrate that the CNN model is able to resolve structures smaller than 80nm. This values are then confirmed in experimental samples where a 3.7-fold improvement over the wide-field image is achieved.

# List of publications

Part of the work carried out during the development of this thesis is presented in the publications listed below.

## Articles in scientific journals

- R. Bola, D. Treptow, A. Marzoa, M. Montes-Usategui, and E. Martín-Badosa, "Acousto-holographic optical tweezers," Optics Letters, 45, 2938-2941 (2020).
- D. Treptow, R. Bola, M. Montes-Usategui, and E. Martín-Badosa, "Artifact-free holographic light shaping through moving acousto-optic hologram". Paper submitted to Light Science and Applications.

## Conferences

- R. Bola, D. Treptow, A. Marzoa, S. Lumbreras, E. Martín-Badosa, M. Montes-Usategui. "Development of a superfast confocal microscopy technique through enhanced acousto-optic modulation". Poster at IN2UB anual meeting, Barcelona, May 2019.
- A. Marzoa, R. Bola, D. Treptow, E. Martín-Badosa, M. Montes-Usategui. "Optical design of the illumination and imaging train of SUFFICE Microscope". Poster at ESODM 2019, Tenerife, March 2019.
- R. Bola, D. Treptow, A. Marzoa, S. Lumbreras, E. Martín-Badosa, M. Montes-Usategui. "Superfast confocal microscopy through enhanced acousto-optic modulation". Oral presentation at 4th Reunión Española de Microscopía Óptica Avanzada (REMOA), Granada, October 2018.
- R. Bola, D. Treptow, A. Marzoa, S. Lumbreras, E. Martín-Badosa, M. Montes-Usategui. "Superfast confocal microscopy through enhanced acousto-optic modulation". Poster at 4th Reunión Española de Microscopía Óptica Avanzada (REMOA), Granada, October 2018. **Best poster award**.

- D. Treptow, R. Bola, E. Martín-Badosa, M. Montes-Usategui. "Acousto-optic devices as spatial light modulators". Oral presentation at spanish national optics meeting (Reunion Nacional de Óptica), Castellón, July 2018.
- R. Bola, D. Treptow, A. Marzoa, E. Martín-Badosa, M. Montes-Usategui. "Multifocal confocal microscopy using AODs". Oral presentation at spanish national optics meeting (Reunion Nacional de Óptica), Castellón, July 2018.
- R. Bola, A. Marzoa-Domínguez, D. Treptow, E. Martín-Badosa, M. Montes-Usategui. "Holographic Optical Tweezers with Acousto-Optic Devices". Oral presentation at spanish national optics meeting (Reunion Nacional de Óptica), Castellón, July 2018.
- R. Bola, F. Català, R. Serrano, E. Martín-Badosa, M. Montes-Usategui. "Force profile and backscattered light loss determination in an Optical trap using momentum change method". Poster at IN2UB anual meeting congress, Barcelona, June 2018.
- R. Bola, F. Català, R. Serrano, E. Martín-Badosa, and M. Montes-Usategui, "Light momentum measurements for force determination in an optical trap". Poster at Sympossium on New Frontiers in Optical Trapping and Optical Manipulation (ICFO), Barcelona, July 2017.
- R. Bola, E. Martín-Badosa, and M. Montes-Usategui, "Rheological studies inside living cells with optical tweezers: from calibration-based methods to direct force measurements". Poster at IN2UB 10th Anniversary, Barcelona, January 2017.
- R. Bola, E. Martín-Badosa, and M. Montes-Usategui, "Intracellular Rheological Studies with Optical Tweezers". Poster at NanoBio & Med 2016, Barcelona, November 2016.
- R. Bola, F. Català, M. Montes-Usategui, and E. Martín-Badosa, "Optical tweezers for force measurements and rheological studies on biological samples". Poster at 15th Workshop on Information Optics, Barcelona, July 2016.

## Patents

- Patent application: "Programmable multiple-point illuminator, confocal filter, confocal microscope and method to operate said confocal microscope". Inventors: Mario Montes-Usategui, Raúl Bola Sampol, Estela Martín-Badosa, Dorian Treptow. This patent went through PCT in August 2019. And in January 2020 is going to national phase in Europe, United States, Japan and China.

# Acknowledgments

This extense manuscrit is the result of five years of hard work and joined efforts of many people that helped me to achieve all the results. This thesis would not have been possible without the help of all people I met during these years. All of you have made me a better scientist, but more importantly, a better person. I acknowledge my four year predoc fellowship from the Spanish Ministerio de Ciencia e Innovación (FPI program).

I gratefully thank my directors Mario and Estela for giving me the opportunity to start in this beautiful world of research five years ago, for teaching me everything I know about optics, and for trusting me from the beginning. The doors of Mario and Estela's offices have always been open when I wanted to discuss the innumerable topics covered in this thesis. I deeply appreciate the endless discussions with Mario about new experiments and ideas, and for his passion to innovate and develop new technology.

I really thank all the help and support from all the members of the Optical Trapping Lab - Grup de Biofotònica (BiOPT). I thank Dr. Josep Mas for kindly introducing me into the active-passive calibration and his priceless help in cell culture during my first months. I appreciate Dr. Frederic Català for sharing with me all his knowledge about force measurements, trap calibration and especially the light momentum method. I also thank him for endless discussions on optical trapping experiments and simulations. I thank Sara Lumbreras for her priceless work on developing the microscope simulator tool and helping me to push the microscope prototype project from the beginning. I also thank her for the design and training of the neural network model presented in this work. I thank Dorian Treptow for discussion about AODs and learning together how this incredible devices work. I also thank Tony Marzoa and Rafa Serrano for his help when needed.

I thank all Impetux Optics S. L. people for sharing with me his knowledge about optical trapping and force measurements. I especially thank Dr. Arnau Farré for helping me when needed. I will always be in debt with Ferran Marsà for sharing with me all his experience and meticulous work in the design and alignment of optical systems, as well as programming automated experiments.

I honestly appreciate Professor Ilaria Testa from the Science for Life Laboratory (KTH Royal Institute of Technology, Stockholm, Sweeden) for accepting my proposal

for the PhD stay and introducing me into the amazing world of super-resolution microscopy. I really thank all members of the TestaLab (Xavi, Andreas, Jonatan, Francesca, Giovanna and Martina) for their warm welcome and sharing their expertise and knowledge on building such complex microscopes.

Finally, I must express my very profound gratitude to my parents, my sister Emma, and to you Sara, for always being there, providing me with unfailing support and continuous encouragement throughout all these years. I owe it all to you, this thesis is more yours than mine, none of this would have been possible without you. Gràcies a tothom, vus estim!

# Bibliography


[1] P. A. Sharp, C. L. Cooney, M. A. Kastner, J. Lees, R. Sa, and T. T. Revolution, *The Third Revolution: The Convergence of the Life Sciences, Physical Sciences, and Engineering*, 2011. [Online]. Available: http://dc.mit.edu/sites/dc.mit.edu/files/MITWhitePaperonConvergence.pdf

[2] K. Schütze, H. Pösl, and G. Lahr, "Laser micromanipulation systems as universal tools in cellular and molecular biology and in medicine." pp. 735–746, 1998.

[3] K. E. Sheetz and J. Squier, "Ultrafast optics: Imaging and manipulating biological systems," *Journal of Applied Physics*, vol. 105, no. 5, 2009.

[4] S. Chattopadhyay, R. Moldovan, C. Yeung, and X. L. Wu, "Swimming efficiency of bacterium Escherichia coli," *Proceedings of the National Academy of Sciences of the United States of America*, vol. 103, no. 37, pp. 13 712–13 717, 2006.

[5] N. Khatibzadeh, A. B. Stilgoe, A. A. Bui, Y. Rocha, G. M. Cruz, V. Loke, L. Z. Shi, T. A. Nieminen, H. Rubinsztein-Dunlop, and M. W. Berns, "Determination of motility forces on isolated chromosomes with laser tweezers," *Scientific Reports*, vol. 4, pp. 1–9, 2014.

[6] S. N. Olof, J. A. Grieve, D. B. Phillips, H. Rosenkranz, M. L. Yallop, M. J. Miles, A. J. Patil, S. Mann, and D. M. Carberry, "Measuring nanoscale forces with living probes," *Nano Letters*, vol. 12, no. 11, pp. 6018–6023, 2012.

[7] T. Wilson, "Optical sectioning in fluorescence microscopy," *Journal of Microscopy*, vol. 242, no. 2, pp. 111–116, 2011.

[8] Q. S. Hanley, P. J. Verveer, M. J. Gemkow, D. Arndt-Jovin, and T. M. Jovin, "An optical sectioning programmable array microscope implemented with a digital micromirror device," *Journal of Microscopy*, vol. 196, no. 3, pp. 317–331, 1999.

[9] W. Caarls, B. Rieger, A. H. De Vries, D. J. Arndt-Jovin, and T. M. Jovin, "Minimizing light exposure with the programmable array microscope," *Journal of Microscopy*, vol. 241, no. 1, pp. 101–110, 2011.

[10] A. G. York, S. H. Parekh, D. D. Nogare, R. S. Fischer, K. Temprine, M. Mione, A. B. Chitnis, C. A. Combs, and H. Shroff, "Resolution doubling in live, multicellular organisms via multifocal structured illumination microscopy," *Nature Methods*, vol. 9, no. 7, pp. 749–754, 2012.

[11] D. Cojoc, F. Difato, E. Ferrari, R. B. Shahapure, J. Laishram, M. Righi, E. M. Di Fabrizio, and V. Torre, "Properties of the force exerted by filopodia and lamellipodia and the involvement of cytoskeletal components," *PLoS ONE*, vol. 2, no. 10, 2007.

[12] M. C. Noom, B. van den Broek, J. van Mameren, and G. J. Wuite, "Visualizing single DNA-bound proteins using DNA as a scanning probe," *Nature Methods*, vol. 4, no. 12, pp. 1031–1036, 2007.

[13] M. Polin, D. G. Grier, and S. R. Quake, "Anomalous vibrational dispersion in holographically trapped colloidal arrays," *Physical Review Letters*, vol. 96, no. 8, pp. 1–4, 2006.

[14] M. Schwingel and M. Bastmeyer, "Force Mapping during the Formation and Maturation of Cell Adhesion Sites with Multiple Optical Tweezers," *PLoS ONE*, vol. 8, no. 1, 2013.

[15] H. Turlier, D. A. Fedosov, B. Audoly, T. Auth, N. S. Gov, C. Sykes, J. F. Joanny, G. Gompper, and T. Betz, "Equilibrium physics breakdown reveals the active nature of red blood cell flickering," *Nature Physics*, vol. 12, no. 5, pp. 513–520, 2016.

[16] S. B. Smith, Y. Cui, and C. Bustamante, "Optical-trap force transducer that operates by direct measurement of light momentum," *Methods in Enzymology*, vol. 361, no. 1994, pp. 134–162, 2003.

[17] A. Farré and M. Montes-Usategui, "A force detection technique for single-beam optical traps based on direct measurement of light momentum changes," *Optics Express*, vol. 18, no. 11, p. 11955, 2010.

[18] A. Farré, F. Marsà, and M. Montes-Usategui, "Optimized back-focal-plane interferometry directly measures forces of optically trapped particles," *Optics Express*, vol. 20, no. 11, p. 12270, 2012.

[19] F. Català, F. Marsà, M. Montes-Usategui, A. Farré, and E. Martín-Badosa, "Extending calibration-free force measurements to optically-trapped rod-shaped samples," *Scientific Reports*, vol. 7, no. February, pp. 1–10, 2017.

[20] J. Turunen, "Acousto-optic devices," *Perspectives for Parallel Optical Interconnects*, pp. 221–234, 1993.

[21] A. Ashkin, "Acceleration and Trapping of Particles by Radiation Pressure," *Physical Review Letters*, vol. 24, no. 4, pp. 156–159, 1970.

[22] A. Ashkin, J. M. Dziedzic, J. E. Bjorkholm, and S. Chu, "Observation of a single-beam gradient force optical trap for dielectric particles," *Optics Express*, vol. 11, no. 5, pp. 196–198, 1986.

[23] G. Gouesbet, B. Maheu, and G. Gréhan, "Light scattering from a sphere arbitrarily located in a Gaussian beam, using a Bromwich formulation," *Journal of the Optical Society of America A*, vol. 5, no. 9, p. 1427, 1988.

[24] Y. Harada and T. Asakura, "Radiation forces on a dielectric sphere in the rayleigh scattering regime," *Optics Communications*, vol. 124, no. 5, pp. 529 – 541, 1996. [Online]. Available: http://www.sciencedirect.com/science/article/pii/0030401895007539

[25] E. J. Peterman, F. Gittes, and C. F. Schmidt, "Laser-induced heating in optical traps," *Biophysical Journal*, vol. 84, no. 2 I, pp. 1308–1316, 2003.

[26] F. Català, F. Marsà, M. Montes-Usategui, A. Farré, and E. Martín-Badosa, "Influence of experimental parameters on the laser heating of an optical trap," *Scientific Reports*, vol. 7, no. 1, pp. 1–9, 2017.

[27] S. P. Gross, "Application of Optical Traps in Vivo," *Methods in Enzymology*, vol. 361, no. 1998, pp. 162–174, 2003.

[28] K. Svoboda and S. M. Block, "Biological applications of optical forces," *Annual Review of Biophysics and Biomolecular Structure*, vol. 23, pp. 247–285, 1994.

[29] I. A. Favre-Bulle, A. B. Stilgoe, E. K. Scott, and H. Rubinsztein-Dunlop, "Optical trapping in vivo: Theory, practice, and applications," *Nanophotonics*, vol. 8, no. 6, pp. 1023–1040, 2019.

[30] P. L. Johansen, F. Fenaroli, L. Evensen, G. Griffiths, and G. Koster, "Optical micromanipulation of nanoparticles and cells inside living zebrafish," *Nature Communications*, vol. 7, pp. 1–8, 2016. [Online]. Available: http://dx.doi.org/10.1038/ncomms10974

[31] A. Gennerich and R. D. Vale, ""Walking the walk: how kinesin and dynein coordinate their steps", Gennrich, Vale, Current Opinion in Cell Biology 2009, 21:59–67," *Cell*, vol. 21, no. 1, pp. 59–67, 2009.

[32] K. Svoboda and S. M. Block, "Force and velocity measured for single kinesin molecules," *Cell*, vol. 77, no. 5, pp. 773–784, 1994.

[33] M. A. Welte, S. P. Gross, M. Postner, S. M. Block, and E. F. Wieschaus, "Developmental regulation of vesicle transport in Drosophila embryos: Forces and kinetics," *Cell*, vol. 92, no. 4, pp. 547–557, 1998.

[34] K. Bambardekar, R. Clément, O. Blanc, C. Chardès, and P. F. Lenne, "Direct laser manipulation reveals the mechanics of cell contacts in vivo," *Proceedings of the National Academy of Sciences of the United States of America*, vol. 112, no. 5, pp. 1416–1421, 2015.

[35] K. Sugimura, P. F. Lenne, and F. Graner, "Measuring forces and stresses in situ in living tissues," *Development (Cambridge)*, vol. 143, no. 2, pp. 186–196, 2016.

[36] F. Gittes and C. F. Schmidt, "Interference model for back-focal-plane displacement detection in optical tweezers," *Optics Letters*, vol. 23, no. 1, p. 7, 1998.

[37] K. C. Vermeulen, J. Van Mameren, G. J. Stienen, E. J. Peterman, G. J. Wuite, and C. F. Schmidt, "Calibrating bead displacements in optical tweezers using acousto-optic deflectors," *Review of Scientific Instruments*, vol. 77, no. 1, pp. 1–6, 2006.

[38] G. M. Gibson, J. Leach, S. Keen, A. J. Wright, and M. J. Padgett, "Measuring the accuracy of particle position and force in optical tweezers using high-speed video microscopy," *Optics Express*, vol. 16, no. 19, p. 14561, 2008.

[39] K. C. Neuman and S. M. Block, "Optical trapping," *Review of Scientific Instruments*, vol. 75, no. 9, pp. 2787–2809, 2004.

[40] K. Berg-Sørensen and H. Flyvbjerg, "Power spectrum analysis for optical tweezers," *Review of Scientific Instruments*, vol. 75, no. 3, pp. 594–612, 2004.

[41] M. Ribezzi-Crivellari, J. M. Huguet, and F. Ritort, "Counter-propagating dual-trap optical tweezers based on linear momentum conservation," *Review of Scientific Instruments*, vol. 84, no. 4, 2013.

[42] W. Grange, S. Husale, H. J. Güntherodt, and M. Hegner, "Optical tweezers system measuring the change in light momentum flux," *Review of Scientific Instruments*, vol. 73, no. 6, p. 2308, 2002.

[43] M. T. Valentine, N. R. Guydosh, B. Gutiérrez-Medina, A. N. Fehr, J. O. Andreasson, and S. M. Block, "Precision steering of an optical trap by electro-optic deflection," *Optics Letters*, vol. 33, no. 6, p. 599, 2008.

[44] J. Liesener, M. Reicherter, T. Haist, and H. J. Tiziani, "Multi-functional optical tweezers using computer-generated holograms," *Optics Communications*, vol. 185, no. 1-3, pp. 77–82, 2000.

[45] R. M. Simmons, J. T. Finer, S. Chu, and J. A. Spudich, "Quantitative measurements of force and displacement using an optical trap," *Biophysical Journal*, vol. 70, no. 4, pp. 1813–1822, 1996. [Online]. Available: http://dx.doi.org/10.1016/S0006-3495(96)79746-1

[46] Y. Ren, J. Wu, M. Zhong, and Y. Li, "Monte-carlo simulation of effective stiffness of time-sharing optical tweezers," *Chin. Opt. Lett.*, vol. 8, no. 2, pp. 170–172, Feb 2010. [Online]. Available: http://col.osa.org/abstract.cfm?URI=col-8-2-170

[47] W. H. Guilford, J. A. Tournas, D. Dascalu, and D. S. Watson, "Creating multiple time-shared laser traps with simultaneous displacement detection using digital signal processing hardware," *Analytical Biochemistry*, vol. 326, no. 2, pp. 153–166, 2004.

[48] F. Marsà, A. Farré, E. Martín-Badosa, and M. Montes-Usategui, "Holographic optical tweezers combined with back-focal-plane displacement detection," *Optics Express*, vol. 21, no. 25, p. 30282, 2013.

[49] D. Ott, S. Nader, S. Reihani, and L. B. Oddershede, "Simultaneous three-dimensional tracking of individual signals from multi-trap optical tweezers using fast and accurate photodiode detection," *Optics Express*, vol. 22, no. 19, p. 23661, 2014.

[50] A. G. Hendricks, E. L. Holzbaur, and Y. E. Goldman, "Force measurements on cargoes in living cells reveal collective dynamics of microtubule motors," *Proceedings of the National Academy of Sciences of the United States of America*, vol. 109, no. 45, pp. 18 447–18 452, 2012.

[51] M. Fischer and K. Berg-Sørensen, "Calibration of trapping force and response function of optical tweezers in viscoelastic media," *Journal of Optics A: Pure and Applied Optics*, vol. 9, no. 8, 2007.

[52] M. Fischer, A. C. Richardson, S. N. S. Reihani, L. B. Oddershede, and K. Berg-Sørensen, "Active-passive calibration of optical tweezers in viscoelastic media," *Review of Scientific Instruments*, vol. 81, no. 1, 2010.

[53] J. Mas, A. C. Richardson, S. N. S. Reihani, L. B. Oddershede, and K. Berg-Sørensen, "Quantitative determination of optical trapping strength and viscoelastic moduli inside living cells," *Physical Biology*, vol. 10, no. 4, 2013.

[54] E. Moeendarbary, L. Valon, M. Fritzsche, A. R. Harris, D. A. Moulding, A. J. Thrasher, E. Stride, L. Mahadevan, and G. T. Charras, "The cytoplasm of living cells behaves as a poroelastic material," *Nature Materials*, vol. 12, no. 3, pp. 253–261, 2013. [Online]. Available: http://dx.doi.org/10.1038/nmat3517

[55] Y. A. Ayala, B. Pontes, D. S. Ether, L. B. Pires, G. R. Araujo, S. Frases, L. F. Romão, M. Farina, V. Moura-Neto, N. B. Viana, and H. Moysés Nussenzveig, "Rheological properties of cells measured by optical tweezers," *BMC Biophysics*, vol. 9, no. 1, pp. 1–11, 2016. [Online]. Available: http://dx.doi.org/10.1186/s13628-016-0031-4

[56] P. A. Pullarkat, P. A. Fernández, and A. Ott, "Rheological properties of the Eukaryotic cell cytoskeleton," *Physics Reports*, vol. 449, no. 1-3, pp. 29–53, 2007.

[57] C. López-Quesada, A.-S. Fontaine, A. Farré, M. Joseph, J. Selva, G. Egea, M. D. Ludevid, E. Martín-Badosa, and M. Montes-Usategui, "Artificially-induced organelles are optimal targets for optical trapping experiments in living cells," *Biomedical Optics Express*, vol. 5, no. 7, p. 1993, 2014.

[58] J. R. Staunton, B. Blehm, A. Devine, and K. Tanner, "In situ calibration of position detection in an optical trap for active microrheology in viscous materials," *Optics Express*, vol. 25, no. 3, p. 1746, 2017.

[59] A. E. Wallin, H. Ojala, G. Ziedaite, and E. Hggstrm, "Dual-trap optical tweezers with real-time force clamp control," *Review of Scientific Instruments*, vol. 82, no. 8, 2011.

[60] R. S. Dutra, N. B. Viana, P. A. Maia Neto, and H. M. Nussenzveig, "Absolute calibration of forces in optical tweezers," *Physical Review A - Atomic, Molecular, and Optical Physics*, vol. 90, no. 1, pp. 1–13, 2014.

[61] P. Guillamat, J. Ignés-Mullol, and F. Sagués, "Control of active liquid crystals with a magnetic field," *Proceedings of the National Academy of Sciences of the United States of America*, vol. 113, no. 20, pp. 5498–5502, 2016.

[62] P. Guillamat, J. Ignés-Mullol, S. Shankar, M. C. Marchetti, and F. Sagués, "Probing the shear viscosity of an active nematic film," *Physical Review E*, vol. 94, no. 6, pp. 1–5, 2016.

[63] B. Martínez-Prat, J. Ignés-Mullol, J. Casademunt, and F. Sagués, "Selection mechanism at the onset of active turbulence," *Nature Physics*, vol. 15, no. 4, pp. 362–366, 2019. [Online]. Available: http://dx.doi.org/10.1038/s41567-018-0411-6

[64] O. Krivosudský, P. Dráber, and M. Cifra, "Resolving controversy of unusually high refractive index of a tubulin," *Epl*, vol. 117, no. 3, 2017.

[65] F. Gittes, B. Mickey, J. Nettleton, and J. Howard, "Flexural rigidity of microtubules and actin filaments measured from thermal fluctuations in shape," *Journal of Cell Biology*, vol. 120, no. 4, pp. 923–934, 1993.

[66] M. Kikumoto, M. Kurachi, V. Tosa, and H. Tashiro, "Flexural rigidity of individual microtubules measured by a buckling force with optical traps," *Biophysical Journal*, vol. 90, no. 5, pp. 1687–1696, 2006. [Online]. Available: http://dx.doi.org/10.1529/biophysj.104.055483

[67] H. Felgner, R. Frank, and M. Schliwa, "Flexural rigidity of microtubules measured with the use of optical tweezers," *Journal of Cell Science*, vol. 109, no. 2, pp. 509–516, 1996.

[68] G. Xu, K. S. Wilson, R. J. Okamoto, J. Y. Shao, S. K. Dutcher, and P. V. Bayly, "Flexural Rigidity and Shear Stiffness of Flagella Estimated from Induced Bends and Counterbends," *Biophysical Journal*, vol. 110, no. 12, pp. 2759–2768, 2016. [Online]. Available: http://dx.doi.org/10.1016/j.bpj.2016.05.017

[69] M. Capitanio, R. Cicchi, and F. Saverio Pavone, "Continuous and time-shared multiple optical tweezers for the study of single motor proteins," *Optics and Lasers in Engineering*, vol. 45, no. 4, pp. 450–457, 2007.

[70] D. L. Vossen, A. Van Der Horst, M. Dogterom, and A. Van Blaaderen, "Optical tweezers and confocal microscopy for simultaneous three-dimensional manipulation and imaging in concentrated colloidal dispersions," *Review of Scientific Instruments*, vol. 75, no. 9, pp. 2960–2970, 2004.

[71] J. Goodman, *Introduction to Fourier Optics*, ser. Electrical Engineering Series. McGraw-Hill, 1996. [Online]. Available: https://books.google.es/books?id=QllRAAAAMAAJ

[72] E. Tervonen, J. Turunen, M. R. Taghizadeh, A. T. Friberg, and J. Westerholm, "Programmable optical interconnections by multilevel synthetic acousto-optic holograms," *Optics Letters*, vol. 16, no. 16, p. 1274, 1991.

[73] D. W. Prather and J. N. Mait, "Acousto-optic generation of two-dimensional spot arrays," *Optics Letters*, vol. 16, no. 22, p. 1720, 1991.

[74] H. Andrews and C. Patterson, "Singular value decomposition (svd) image coding," *IEEE Transactions on Communications*, vol. 24, no. 4, pp. 425–432, 1976.

[75] W. Akemann, J.-F. Léger, C. Ventalon, B. Mathieu, S. Dieudonné, and L. Bourdieu, "Fast spatial beam shaping by acousto-optic diffraction for 3D non-linear microscopy," *Optics Express*, vol. 23, no. 22, p. 28191, 2015.

[76] P. Bechtold, R. Hohenstein, and M. Schmidt, "Beam shaping and high-speed, cylinder-lens-free beam guiding using acousto-optical deflectors without additional compensation optics," *Optics Express*, vol. 21, no. 12, p. 14627, 2013.

[77] R. W. Gerchberg, "A practical algorithm for the determination of the phase from image and diffraction plane pictures," *Optik*, vol. 35, pp. 237–246, 1972. [Online]. Available: https://ci.nii.ac.jp/naid/10018865349/en/

[78] L. A. Shaw, R. M. Panas, C. M. Spadaccini, and J. B. Hopkins, "Scanning holographic optical tweezers," *Opt. Lett.*, vol. 42, no. 15, pp. 2862–2865, Aug 2017. [Online]. Available: http://ol.osa.org/abstract.cfm?URI=ol-42-15-2862

[79] W. Akemann, J.-F. Léger, C. Ventalon, B. Mathieu, S. Dieudonné, and L. Bourdieu, "Fast spatial beam shaping by acousto-optic diffraction for 3d non-linear microscopy," *Opt. Express*, vol. 23, no. 22, pp. 28 191–28 205, Nov 2015. [Online]. Available: http://www.opticsexpress.org/abstract.cfm?URI=oe-23-22-28191

[80] T. Čižmár, H. I. C. Dalgarno, P. C. Ashok, F. J. Gunn-Moore, and K. Dholakia, "Optical aberration compensation in a multiplexed optical trapping system," *Journal of Optics*, vol. 13, no. 4, p. 044008, mar 2011. [Online]. Available: https://doi.org/10.1088%2F2040-8978%2F13%2F4%2F044008

[81] V. Ljosa and A. E. Carpenter, "Introduction to the quantitative analysis of two-dimensional fluorescence microscopy images for cell-based screening," *PLoS Computational Biology*, vol. 5, no. 12, pp. 1–10, 2009.

[82] M. J. Sanderson, I. Smith, I. Parker, and M. D. Bootman, "Cold Spring Harb Protoc," *Physiology & behavior*, vol. 2014, no. 10, pp. 1–36, 2016.

[83] J. B. Pawley, Ed., *Handbook Of Biological Confocal Microscopy*. Springer US, 2006. [Online]. Available: https://doi.org/10.1007/978-0-387-45524-2

[84] J. A. Conchello and J. W. Lichtman, "Optical sectioning microscopy," *Nature Methods*, vol. 2, no. 12, pp. 920–931, 2005.

[85] M. Minsky, "Memoir on Inventing the Confocal Scanning Microscope," *Scanning*, vol. 10, no. 1 988, pp. 128–138, 1987.

[86] R. H. Webb, "Confocal optical microscopy," *Reports on Progress in Physics*, vol. 59, no. 3, pp. 427–471, mar 1996. [Online]. Available: https://doi.org/10.1088%2F0034-4885%2F59%2F3%2F003

[87] G. M. De Luca, R. M. Breedijk, R. A. Brandt, C. H. Zeelenberg, B. E. de Jong, W. Timmermans, L. N. Azar, R. A. Hoebe, S. Stallinga, and E. M. Manders, "Re-scan confocal microscopy: scanning twice for better resolution," *Biomedical Optics Express*, vol. 4, no. 11, p. 2644, 2013.

[88] O. E. Olarte, J. Andilla, E. J. Gualda, and P. Loza-Alvarez, "Light-sheet microscopy: a tutorial," *Adv. Opt. Photon.*, vol. 10, no. 1, pp. 111–179, Mar 2018. [Online]. Available: http://aop.osa.org/abstract.cfm?URI=aop-10-1-111

[89] J. Oreopoulos, R. Berman, and M. Browne, *Spinning-disk confocal microscopy. present technology and future trends*, 1st ed. Elsevier Inc., 2014, vol. 123, no. June. [Online]. Available: http://dx.doi.org/10.1016/B978-0-12-420138-5.00009-4

[90] A. G. York, P. Chandris, D. D. Nogare, J. Head, P. Wawrzusin, R. S. Fischer, A. Chitnis, and H. Shroff, "Instant super-resolution imaging in live cells and embryos via analog image processing," *Nature Methods*, vol. 10, no. 11, pp. 1122–1130, 2013.

[91] W. Denk, J. Strickler, and W. Webb, "Two-photon laser scanning fluorescence microscopy," *Science*, vol. 248, no. 4951, pp. 73–76, 1990. [Online]. Available: https://science.sciencemag.org/content/248/4951/73

[92] J. Girkin, "Optical sectioning microscopy and biological imaging," pp. 165–195, Feb. 2015. [Online]. Available: https://doi.org/10.1002/9781119011804.ch5

[93] S. Ganguly, A. H. Clayton, and A. Chattopadhyay, "Fixation alters fluorescence lifetime and anisotropy of cells expressing EYFP-tagged serotonin1A receptor," *Biochemical and Biophysical Research Communications*, vol. 405, no. 2, pp. 234–237, 2011.

[94] P. P. Laissue, R. A. Alghamdi, P. Tomancak, E. G. Reynaud, and H. Shroff, "Assessing phototoxicity in live fluorescence imaging," *Nature Methods*, vol. 14, no. 7, pp. 657–661, 2017. [Online]. Available: http://dx.doi.org/10.1038/nmeth.4344

[95] F. P. Martial and N. A. Hartell, "Programmable illumination and high-speed, multi-wavelength, confocal microscopy using a digital micromirror," *PLoS ONE*, vol. 7, no. 8, 2012.

[96] A. H. B. de Vries, N. P. Cook, S. Kramer, D. J. Arndt-Jovin, and T. M. Jovin, "Generation 3 programmable array microscope (PAM) for high speed large format optical sectioning in fluorescence," *Emerging Digital Micromirror Device Based Systems and Applications VII*, vol. 9376, no. June 2016, p. 93760C, 2015.

[97] P. Theer, C. Mongis, and M. Knop, "PSFj: know your fluorescence microscope," *Nature Methods*, vol. 11, no. 10, pp. 981–982, Sep. 2014. [Online]. Available: https://doi.org/10.1038/nmeth.3102

[98] E. Riba, D. Mishkin, D. Ponsa, E. Rublee, and G. Bradski, "Kornia: an open source differentiable computer vision library for pytorch," in *Proceedings of the IEEE/CVF Winter Conference on Applications of Computer Vision (WACV)*, March 2020.

[99] H. Kirshner, D. Sage, and M. Unser, "3D PSF models for fluorescence microscopy in ImageJ," in *Proceedings of the Twelfth International Conference on Methods and Applications of Fluorescence Spectroscopy, Imaging and Probes (MAF'11)*, Strasbourg, French Republic, September 11-14, 2011, p. 154.

[100] C. B. Müller and J. Enderlein, "Image scanning microscopy," *Physical Review Letters*, vol. 104, no. 19, pp. 1–4, 2010.

[101] J. Dreier, M. Castello, G. Coceano, R. Cáceres, J. Plastino, G. Vicidomini, and I. Testa, "Smart scanning for low-illumination and fast RESOLFT nanoscopy in vivo," *Nature Communications*, vol. 10, no. 1, pp. 1–11, 2019. [Online]. Available: http://dx.doi.org/10.1038/s41467-019-08442-4

[102] J. M. Ede and R. Beanland, "Partial Scanning Transmission Electron Microscopy with Deep Learning," *Scientific Reports*, vol. 10, no. 1, pp. 1–10, 2020.

[103] J. M. Ede, "Adaptive Partial Scanning Transmission Electron Microscopy with Reinforcement Learning," *arXiv*, vol. 37, 2020.

[104] E. Nehme, L. E. Weiss, T. Michaeli, and Y. Shechtman, "Deep-storm: super-resolution single-molecule microscopy by deep learning," *Optica*, vol. 5, no. 4, pp. 458–464, Apr 2018. [Online]. Available: http://www.osapublishing.org/optica/abstract.cfm?URI=optica-5-4-458

[105] X. Ye and M. D. McCluskey, "Modular scanning confocal microscope with digital image processing," *PLoS ONE*, vol. 11, no. 11, pp. 1–14, 2016.

[106] L. Li, C. Kuang, Y. Xue, and X. Liu, "Nano-displacement measurement based on virtual pinhole confocal method," *Measurement Science and Technology*, vol. 24, no. 3, 2013.

[107] E. Sánchez-Ortiga, C. J. R. Sheppard, G. Saavedra, M. Martínez-Corral, A. Doblas, and A. Calatayud, "Subtractive imaging in confocal scanning microscopy using a CCD camera as a detector," *Optics Letters*, vol. 37, no. 7, p. 1280, 2012.

[108] E. Sánchez-Ortiga, G. Saavedra, M. Martínez-Corral, A. Doblas, and A. Calatayud, "Confocal scanning microscope using a CCD camera as a pinhole-detector system," *2011 10th Workshop on Information Optics, WIO 2011*, pp. 2–4, 2011.

[109] R. Heintzmann, V. Sarafis, P. Munroe, J. Nailon, Q. S. Hanley, and T. M. Jovin, "Resolution enhancement by subtraction of confocal signals taken at different pinhole sizes," *Micron*, vol. 34, no. 6-7, pp. 293–300, 2003.

[110] R. Heintzmann and P. A. Benedetti, "High-resolution image reconstruction in fluorescence microscopy with patterned excitation," *Applied Optics*, vol. 45, no. 20, pp. 5037–5045, 2006.

[111] P. Křížek, I. Raška, and G. M. Hagen, "Flexible structured illumination microscope with a programmable illumination array," *Optics Express*, vol. 20, no. 22, p. 24585, 2012.

[112] S. Roth, C. J. Sheppard, K. Wicker, and R. Heintzmann, "Optical photon reassignment microscopy (OPRA)," *Optical Nanoscopy*, vol. 2, no. 1, pp. 1–6, 2013.

[113] M. A. A. Neil, R. Juškaitis, and T. Wilson, "Method of obtaining optical sectioning by using structured light in a conventional microscope," *Opt. Lett.*, vol. 22, no. 24, pp. 1905–1907, Dec 1997. [Online]. Available: http://ol.osa.org/abstract.cfm?URI=ol-22-24-1905

[114] A. Thendiyammal, G. Osnabrugge, T. Knop, and I. M. Vellekoop, "Model-based wavefront shaping microscopy," *Opt. Lett.*, vol. 45, no. 18, pp. 5101–5104, Sep 2020. [Online]. Available: http://ol.osa.org/abstract.cfm?URI=ol-45-18-5101

[115] M. G. Gustafsson, "Surpassing the lateral resolution limit by a factor of two using structured illumination microscopy," *Journal of Microscopy*, vol. 198, no. 2, pp. 82–87, 2000.

[116] B. Bailey, D. Farkas, D. Taylor, and F. Lanni, "Enhancement of axial resolution in fluorescence microscopy by standing-wave excitation," *Nature*, vol. 366, no. 6450, p. 44—48, November 1993. [Online]. Available: https://doi.org/10.1038/366044a0

[117] M. G. Gustafsson, L. Shao, P. M. Carlton, C. J. Wang, I. N. Golubovskaya, W. Z. Cande, D. A. Agard, and J. W. Sedat, "Three-dimensional resolution doubling in wide-field fluorescence microscopy by structured illumination," *Biophysical Journal*, vol. 94, no. 12, pp. 4957–4970, 2008.

[118] L. Schermelleh, P. M. Carlton, S. Haase, L. Shao, L. Winoto, P. Kner, B. Burke, M. C. Cardoso, D. A. Agard, M. G. L. Gustafsson, H. Leonhardt, and J. W. Sedat, "Subdiffraction multicolor imaging of the nuclear periphery with 3d structured illumination microscopy," *Science*, vol. 320, no. 5881, pp. 1332–1336, 2008. [Online]. Available: https://science.sciencemag.org/content/320/5881/1332

[119] S. W. Hell and J. Wichmann, "Breaking the diffraction resolution limit by stimulated emission: stimulated-emission-depletion fluorescence microscopy," *Opt. Lett.*, vol. 19, no. 11, pp. 780–782, Jun 1994. [Online]. Available: http://ol.osa.org/abstract.cfm?URI=ol-19-11-780

[120] T. A. Klar and S. W. Hell, "Subdiffraction resolution in far-field fluorescence microscopy," *Opt. Lett.*, vol. 24, no. 14, pp. 954–956, Jul 1999. [Online]. Available: http://ol.osa.org/abstract.cfm?URI=ol-24-14-954

[121] V. Westphal and S. W. Hell, "Nanoscale resolution in the focal plane of an optical microscope," *Phys. Rev. Lett.*, vol. 94, p. 143903, Apr 2005. [Online]. Available: https://link.aps.org/doi/10.1103/PhysRevLett.94.143903

[122] M. Dyba and S. W. Hell, "Focal spots of size $\lambda/23$ open up far-field florescence microscopy at 33 nm axial resolution," *Phys. Rev. Lett.*, vol. 88, p. 163901, Apr 2002. [Online]. Available: https://link.aps.org/doi/10.1103/PhysRevLett.88.163901

[123] X. Chen and P. Xi, "Hundred-Thousand light holes push nanoscopy to go parallel," *Microscopy Research and Technique*, vol. 78, no. 1, pp. 8–10, 2015.

[124] M. Hofmann, C. Eggeling, S. Jakobs, and S. W. Hell, "Breaking the diffraction barrier in fluorescence microscopy at low light intensities by using reversibly photoswitchable proteins," *Proceedings of the National Academy of Sciences*, vol. 102, no. 49, pp. 17 565–17 569, 2005. [Online]. Available: https://www.pnas.org/content/102/49/17565

[125] M. G. L. Gustafsson, "Nonlinear structured-illumination microscopy: Wide-field fluorescence imaging with theoretically unlimited resolution," *Proceedings of the National Academy of Sciences*, vol. 102, no. 37, pp. 13 081–13 086, 2005. [Online]. Available: https://www.pnas.org/content/102/37/13081

[126] M. J. Rust, M. Bates, and X. Zhuang, "Sub-diffraction-limit imaging by stochastic optical reconstruction microscopy (STORM)," *Nature Methods*, vol. 3, no. 10, pp. 793–795, 2006.

[127] E. Betzig, G. H. Patterson, R. Sougrat, O. W. Lindwasser, S. Olenych, J. S. Bonifacino, M. W. Davidson, J. Lippincott-Schwartz, and H. F. Hess, "Imaging intracellular fluorescent proteins at nanometer resolution," *Science*, vol. 313, no. 5793, pp. 1642–1645, 2006. [Online]. Available: https://science.sciencemag.org/content/313/5793/1642

[128] S. T. Hess, T. P. Girirajan, and M. D. Mason, "Ultra-high resolution imaging by fluorescence photoactivation localization microscopy," *Biophysical Journal*, vol. 91, no. 11, pp. 4258–4272, 2006.

[129] N. Gustafsson, S. Culley, G. Ashdown, D. M. Owen, P. M. Pereira, and R. Henriques, "Fast live-cell conventional fluorophore nanoscopy with ImageJ through super-resolution radial fluctuations," *Nature Communications*, vol. 7, pp. 1–9, 2016.

[130] T. Dertinger, R. Colyer, R. Vogel, J. Enderlein, and S. Weiss, "Achieving increased resolution and more pixels with superresolution optical fluctuation imaging (sofi)," *Opt. Express*, vol. 18, no. 18, pp. 18 875–18 885, Aug 2010. [Online]. Available: http://www.opticsexpress.org/abstract.cfm?URI=oe-18-18-18875

[131] B. Wang, Z. Liu, L. Zhou, Y. Fei, C. Yang, L. Mi, Q. Mu, and J. Ma, "Active-modulated, random-illumination, super-resolution optical fluctuation imaging," *Nanoscale*, vol. 12, no. 32, pp. 16 864–16 874, 2020.

[132] Z. Qiu, R. S. Wilson, Y. Liu, A. R Dun, R. S. Saleeb, D. Liu, C. Rickman, M. Frame, R. R. Duncan, and W. Lu, "Translation Microscopy (TRAM) for super-resolution imaging," *Scientific Reports*, vol. 6, no. January, pp. 1–11, 2016.

[133] L. A. Masullo, A. Bodén, F. Pennacchietti, G. Coceano, M. Ratz, and I. Testa, "Enhanced photon collection enables four dimensional fluorescence nanoscopy of living systems," *Nature Communications*, vol. 9, no. 1, 2018. [Online]. Available: http://dx.doi.org/10.1038/s41467-018-05799-w

[134] F. Pennacchietti, E. O. Serebrovskaya, A. R. Faro, I. I. Shemyakina, N. G. Bozhanova, A. A. Kotlobay, N. G. Gurskaya, A. Bodén, J. Dreier, D. M. Chudakov, K. A. Lukyanov, V. V. Verkhusha, A. S. Mishin, and I. Testa, "Fast reversibly photoswitching red fluorescent proteins for live-cell RESOLFT nanoscopy," *Nature Methods*, vol. 15, no. 8, pp. 601–604, 2018. [Online]. Available: http://dx.doi.org/10.1038/s41592-018-0052-9

[135] D. P. Kingma and J. L. Ba, "Adam: A method for stochastic optimization," *3rd International Conference on Learning Representations, ICLR 2015 - Conference Track Proceedings*, pp. 1–15, 2015.

[136] A. Krull, T. Buchholz, and F. Jug, "Noise2void - learning denoising from single noisy images," *CoRR*, vol. abs/1811.10980, 2018. [Online]. Available: http://arxiv.org/abs/1811.10980

[137] W. Ouyang, A. Aristov, M. Lelek, X. Hao, and C. Zimmer, "Deep learning massively accelerates super-resolution localization microscopy," *Nature Biotechnology*, vol. 36, no. 5, pp. 460–468, 2018.

[138] P. Isola, J. Zhu, T. Zhou, and A. A. Efros, "Image-to-image translation with conditional adversarial networks," *CoRR*, vol. abs/1611.07004, 2016. [Online]. Available: http://arxiv.org/abs/1611.07004

[139] O. Ronneberger, P. Fischer, and T. Brox, "U-net: Convolutional networks for biomedical image segmentation," *CoRR*, vol. abs/1505.04597, 2015. [Online]. Available: http://arxiv.org/abs/1505.04597